Old Dominion University

ODU Digital Commons

Summer 2012

Modeling, Visualizing, and Understanding Complex Tectonic Structures on the Surface and in the Sub-Surface

Steven Wild
Old Dominion University

MODELING, VISUALIZING, AND UNDERSTANDING COMPLEX TECTONIC STRUCTURES ON THE SURFACE AND IN THE SUB-SURFACE

by

Steven Wild
B.S. Physics June 1996, Baldwin-Wallace College
M.S. Chemistry June 2000, Indiana University
M.S. Physics June 2009, Old Dominion University

A Dissertation Submitted to the Faculty of
Old Dominion University in Partial Fulfillment of the
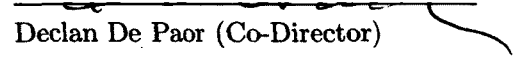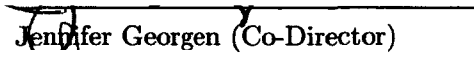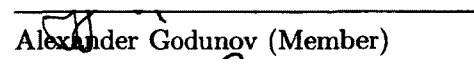Requirements for the Degree of

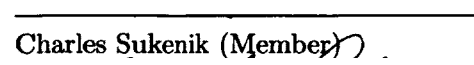DOCTOR OF PHILOSOPHY

PHYSICS

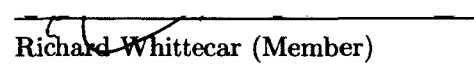OLD DOMINION UNIVERSITY
August 2012

Approved by:

Declan De Paor (Co-Director)

Jennifer Georgen (Co-Director)

Alexander Godunov (Member)

Charles Sukenik (Member)

Richard Whittecar (Member)

ABSTRACT

MODELING, VISUALIZING, AND UNDERSTANDING COMPLEX TECTONIC STRUCTURES ON THE SURFACE AND IN THE SUB-SURFACE

Steven Wild
Old Dominion University, 2012
Co-Directors: Dr. Declan De Paor
Dr. Jennifer Georgen

Plate tectonics is a relatively new theory with many details of plate dynamics which remain to be worked out. Moving plates can interact by divergence, lateral sliding, convergence, or collision. At a convergent plate boundary, a lithospheric slab of oceanic crust and upper mantle is subducted at a trench and dips down under a magmatic arc - either oceanic or continental. Textbooks show a static view of convergent boundaries but plate dynamics require that subduction zones and magmatic arcs must migrate with time. Therefore I develop animated models to help convey this motion. Also, convergent plate boundaries cannot continue along strike or down dip indefinitely without changing. Subduction zones change orientation and eventually terminate. They may bend and shear or tear and open a window for asthenospheric flow.

Two different convergent plate boundaries are the primary focus of my studies: the Tonga subduction zone where the Pacific plate moving beneath an island arc is torn along the Samoan Island Archipelago, and the Andean subduction zone in central South America where the Nazca plate moves beneath a continental arc. I choose these zones because they exhibit tears or shears, where subduction stops, or changes dip suddenly. To examine these features I use several modeling and visualization techniques. COLLADA (COLLabrative Design Activity) models in Google Earth and Google Earth Application Programming Interface (API) are used for visualizing and teaching of plate boundary systems. The testing of COLLADA models for geoscience concepts showed positive learning gains. Kinematic models are made to study strain rates and possible methods of plate evolution. Dynamic COMSOL numerical models are created to probe temperature and flow fields in the subduction zone. Animated COLLADA models are designed for different models of subduction initiation and development for the Tonga trench for both research and educational

purposes. The development of these models led to a new hypothesis of this region's formation. Using these models and Google Earth materials studies in undergraduate classes tested the effectiveness of Google Earth based lab activities for enhancing student understanding of geoscience.

In the central Andean subduction zone, emergent COLLADA models are made from mining GeoMapApp (http://www.geomapapp.org) and published contour data to demonstrate the unique geometry of the Nazca plate having adjacent subduction angles of 10° and 30°. This led to the research question, can the Nazca plate support this geometry by shearing without tearing? A literature review shows efforts to explore this topic by means of hypocenter, teleseismic, and thermal data to have no consensus on the topic. To this end a new approach is taken to examine this region by applying the methods of kinematic and dynamic modeling to further explore this question. These different models of the Andean system lead to the conclusion that no major magmatic window could have opened between the flat and steep subduction areas given the time and deformation mechanisms available.

ACKNOWLEDGMENTS

I would first like to thank my thesis committee members, especially Dr. Declan De Paor and Dr. Jennifer Georgen who gave many hours of their time to help me along in my graduate career. I also want to thank Dr. Georgen for allowing me to use her computer and software for the simulation work. I would also like to thank Dr. De Paor for allowing me to attend many conferences and events to enrich my graduate experience. I want to thank my wife, Alisha, for all her love and support.

TABLE OF CONTENTS

LIST OF TABLES

LIST OF FIGURES

CHAPTER 1

INTRODUCTION

The Earth's outer shell, or lithosphere, is broken into approximately twelve major tectonic plates that are in constant motion over the underlying asthenosphere. In general, motion at plate boundaries can be divergent (where plates move apart), convergent (where one plate is subducted beneath another), conservative (such as along a transform fault), or collisional (where the continental portions of two plates interact, such as India and Eurasia forming the Himalayas). Evidence of these interactions and motions can be seen in the surface topography of the Earth, such as in mountain belts and mid-ocean ridges. Earthquakes are the result of a release of energy when two plates or crustal blocks move against each other and are a good indicator of plate boundaries.

This thesis focuses on subduction plate boundaries. A series of kinematic calculations, as well as two-dimensional and three-dimensional numerical models, are used to investigate the dynamics of subduction zones in locations where the downgoing plate is believed to have tears or discontinuities. Also, COLLaborative Design Activity (COLLADA) models are created using hypocenter earthquake data to better visualize the geometries of subduction zones, to develop possible research questions, and to create educational models for teaching tectonic processes. The feasibility of COLLADA models in Google Earth and the Google Earth Application Programming Interface (API) as an effective learning tool in the geosciences is additionally examined. Overall, all of these investigations were facilitated by significant improvements in data quantity and quality in the study regions, such as seismic hypocentral depths (e.g. *Anderson et al.* [2007]).

Two different subduction zones are the primary focus of these studies, the Tonga trench near the American Samoa islands, and the central Andes in South America where the Nazca plate moves beneath continental South America. In the Tonga trench there is a tear point near the Samoan islands. On one side of the tear, north of Samoa, the Pacific plate continues without subducting, whereas on the other side, south of Samoa, it subducts beneath the Australian plate [*Sykes*, 1966; *Frohlich*, 1989]. The trench is also in the process of rollback, wherein the line along which the

plate bends into the subduction zone migrates eastward, against the western migration of the material of the plate, resulting in a marginal basin - the Lau Basin [*Uyeda and Kanamori*, 1979; *Moores and Twiss*, 1995; *Rosenbaum and Lister*, 2004].

In South America, there are regions of the Nazca plate where subduction occurs at an angle of 30° juxtaposed against regions subducting at 10° [*Isacks et al.*, 1968; *Barazangi and Isacks*, 1976; *Jordan et al.*, 1983]. The boundaries between these segments may involve tears or shears [*Barazangi and Isacks*, 1976; *Isacks et al.*, 1968; *Jordan et al.*, 1983; *Cahill and Isacks*, 1992]. The question of the whether the transition zone at S33° is a torn slab or a slab in a state of continuous deformation was first addressed by *Barazangi and Isacks* [1976], who suggested the plate is torn. However, later efforts to explore this question by means of hypocenter [*Hasegawa and Sacks*, 1981; *Anderson et al.*, 2007], teleseismic [*Bevis and Isacks*, 1984; *Bevis*, 1986], and thermal [*Springer*, 1999; *Gutscher*, 2002] data have no clear consensus. Thus, one of the primary goals of this thesis is to investigate the nature of slab deformation in the Nazca subduction region using kinematic, two-dimensional (2D), and three-dimensional (3D) models.

1.1 KINEMATIC AND DYNAMIC MODELS

Kinematic modeling is a method used to examine regional geological development and to investigate deformational processes. Two kinematic models are developed for the Andean subduction transition zone. The first method is to model the region with a tear which approximates the zone as two different slabs moving with different dip angles. If the bottom of the shallow subducting slab clears the top of the steep slab, a window may open and allow material to flow. The size of the window will be determined based on the model as constrained by plate age [*Syracuse and Abers*, 2006]. The second method is to model the transition zone as a region of continuous shear deformation, without the development of a "slab window". In both models a matrix incorporating general shear and translation is used to describe material motion of the system shown by *Ramsay* [1967]; *Simpson and De Paor* [1993]; *De Paor* [1994]. Though the methodology of kinematic models has been developed through earlier works, it has not been previously applied to study the Nazca plate geometry.

The second type of modeling used in this thesis is dynamic numerical modeling. Subduction zone modeling can be performed to examine scales from whole Earth

[*Schubert*, 1992; *Tackley*, 2000] to very local systems [*Wada and Wang*, 2009; *Syracuse et al.*, 2010]. These models often employ a finite element method to calculate system solutions for temperature, flow field, and strains [*Springer*, 1999; *Eberle et al.*, 2002; *Billen and Hirth*, 2005, 2007; *Wada et al.*, 2008; *Wada and Wang*, 2009]. For this research, a multi-physics finite element code called COMSOL is used to solve the non-dimensionalized, steady-state conservation equations for mass, momentum, and energy. The use of the dynamic models is two-fold. First, 2D models are created to explore the impact of three parameters (subduction rate, subduction angle, and coupling distance) on subduction zone dynamics. The results of this 2D study form a framework to create a multi-angle 3D model. These 2D studies are unique in that they include a 10° angle which has not been previously studied within a parameter space framework. The 10° model results are necessary for creating the 3D model to study the Nazca subduction system.

The second step in the dynamical modeling is the creation of a multi-angle 3D model to study the transition zone between 10 and 30° slabs. Although other studies have modeled 3D subduction zone flow patterns (e.g.*Billen and Gurnis* [2001]; *Behn et al.* [2007]), this is, to the author's knowledge, the first multi-angle model to solve fully coupled Navier Stokes and conduction-convection equations for predicted temperature and flow fields for the Nazca plate subduction system. The model-predicted temperatures are used to create brittle-ductile maps and first-order approximation deformation mechanisms for the slab in the dip angle transition region. Possibilities for future work in this modeling effort include adding variable viscosity, allowing the boundary conditions of the overriding plate to take different thicknesses, extending the geological applications of the 3D models by using different angles in the multi-angle model to simulate different subduction zones, and comparing the 3D flow field results to existing seismic anisotropy data to examine trench-parallel flow.

1.2 VISUALIZATIONS AND EDUCATIONAL STUDIES

In addition to studying the geophysics and geodynamics of subduction zones, this thesis also includes a study of subduction zone visualization. It is a policy of the Geospatial Visualization Research Group at ODU to combine theoretical and numerical studies with classroom-tested visualizations in order to ensure that research results translate into learning outcomes. Subduction zones are a natural choice for creating visualization tools because the sub-surface nature of the zones are not easily

accessible and the time scales on which processes occur is very large, while movement rates are on the order of cm/yr. *Gobert and Clement* [1999]; *Gobert* [2000] showed that plate tectonics is a difficult topic for students to learn because it involves hidden mechanical processes that are outside of their direct experience, as well as several types of knowledge including spatial, causal, and dynamic. Many concepts must be combined to build a rich four-dimensional mental model of the system [*Gobert and Clement*, 1999; *Gobert*, 2000].

Emergent and animated COLLADA models [*Arnaud and Barnes*, 2006; *De Paor*, 2007a,b, 2008a; *De Paor et al.*, 2009, 2010a] in Google Earth and Google Earth API are tools that will help researchers to investigate questions about the 3D structure of the Tonga region and its evolution with time. Such modeling is important for understanding earthquakes and tsunami processes in regions like Tonga. For example, plate tectonic processes are responsible for natural disasters like the September 2009 tsunamigenic earthquake which occurred south of the Pacific islands of Western Samoa and American Samoa [*Okal et al.*, 2009; *Lay et al.*, 2010]. Emergent COLLADA models are also a good tool to use for displaying data, such as earthquake hypocenter data, in a manner that allows the user to examine data from different perspectives, an advantage over paper images.

In addition to being a useful data displaying tool, the animated subduction zone models are also tested for use in the classroom and learning outcomes. Google Earth as a geoscience learning tool has been shown to have potential by *Cruz and Zellers* [2006]; *Whitmeyer et al.* [2009]. However, there has been little done to study the effectiveness of this tool, and this thesis reports on the results of one such study. Future work in the area of educational testing could include developing modules for multi-user interfaces, and using multi-user interface modules with students to measuring learning outcomes to measure effectiveness in teaching geosciences concepts. Future work in the general use of COLLADA models could be to visualize not only other subduction zones but also spreading ridges, transforms faults, and mantle plumes as well. The models could also be used for other data types and numerical model outputs, like tomography [*Tarantola*, 1984; *Dordevic et al.*, 2011], heat flow, and deep mantle convection.

CHAPTER 2

EMERGENT AND ANIMATED COLLADA MODELS OF THE TONGA TRENCH AND SAMOA ARCHIPELAGO: IMPLICATIONS FOR GEOSCIENCE MODELING, EDUCATION, AND RESEARCH

In this chapter the creation method and use of COLLaborative Design Activity (COLLADA) models for research and as a visualization tool are introduced. The main emphasis of this chapter is on the emergence of a new hypothesis by exploring various methods in which the Tonga trench region may have developed. My main contribution are in developing and creating the 3D time evolved and data models for Google Earth and the Google Earth Application Programming Interface (API). I was the first to develop animated COLLADA for this purpose. In addition to the animated controls GeoMapApp data (http://www.geomapapp.org) is mined to build the slab models. The work reported in this chapter has been published in the peer-review journal Geosphere (see *De Paor et al.* [2012a]). As a co-author of this paper I contributed 40%.

2.1 ABSTRACT

We report on a project aimed at developing emergent animated COLLADA models of the Tonga-Samoa region of the western Pacific for teaching and outreach use with Google Earth. This is an area of historical importance to the development of plate tectonic theory and is important today owing to neotectonic activity including a 29 September, 2009 tsunamigenic earthquake. We created three types of models: an emergent digital elevation model of the Tonga Slab with associated magmatic arc and back-arc basin based on GeoMapApp data-mining (http://www.geomapapp.org); animated models of alternative plate tectonic scenarios; and a large scale model

that permits users to view the subsurface down to lower mantle levels. Our models have been deployed in non-science-major laboratory classes and positive learning outcomes have been documented in an independent study by *Gobert et al.* [2012]. The models have also been made available to colleagues and the public via ODU's Pretlow Planetarium and via an outreach and dissemination web site, http:// www.digitalplanet.org. In the process of constructing a complete set of tectonic models for the area of interest, we added cases which have not been described in the research literature. Thus this study spans the three functions of modern academia - research, teaching, and outreach - and the multifaceted aspects of creating, using, testing, and disseminating electronic geospatial learning resources.

2.2 INTRODUCTION

On 29 September, 2009, a deadly tsunamigenic earthquake occurred south of the Pacific islands of Western Samoa and American Samoa, drawing the attention of the world to a region of complex oceanic plate tectonics [*Okal et al.*, 2009; *Lay et al.*, 2010]. The magnitude 8.1 earthquake [*USGS*, 2009a] occurred near the point where the Pacific plate's active western margin turns sharply from a northerly-trending convergent boundary to a westerly-trending transverse boundary (Figure 1).

Historically, tsunamis in this region are associated only with convergent tectonics. The extensional event [*USGS*, 2009b] on 29 September was in a part of the plate subject to significant lithospheric flexure and tangential longitudinal strain, close to but not on the active plate boundary.

Because of the nature of the tectonic setting we created a set of emergent and animated COLLADA models [*Arnaud and Barnes*, 2006; *De Paor*, 2007a,b, 2008a; *De Paor et al.*, 2009, 2010a] in Google Earth that would clearly illustrate the three-dimensional structure and its temporal evolution. Our purpose was principally instruction and outreach, since visualizations have been demonstrated (e.g. *Gobert* [2000, 2005a]) to play a key role in many novices' conceptualization of tectonic movements. In the process of designing instructional visualizations, however, we found that attempting to cover all multiple working hypotheses lead us to additional models not previously described in the tectonic literature of the region. Our target audience was three-fold: (i) the large number of non-major students who study courses involving plate tectonics as part of their general education requirements in the US undergraduate education system; (ii) visitors to the Pretlow Planetarium who can view

Figure 1. A view of the Tonga - Samoa region from our data-mining source, GeoMapApp (see text) (http://www.geomapapp.org). Red star marks the epicenter of the Sept. 29, 2009 tsunamigenic earthquake south of Samoa. Yellow line marks the Tonga trench. Red line is center of Lau marginal basin. Blue line is Vitiaz Lineament. Principle emergent island names are in green.

our models beside models of lunar and planetary structures in a museum-style informal education setting; and (iii) visitors to our web site http://www.digitalplanet.org which is sponsored by the NSF for the purpose of disseminating results of our funded research. Learning outcomes were tested with the first category only and are reported by an independent study (*Gobert et al.* [2012] see summary below). Given the positive learning gains they recorded, the visualizations could well prove beneficial to other groups, including geoscience majors taking courses in structural geology and tectonics, geophysics, or geodynamics, and also to citizens ranging from first responders in earthquake- and tsunami-prone regions to casual museum visitors.

We chose to create COLLADA models because they can be viewed with the highly popular Google Earth virtual globe [*De Paor*, 2007a], the basic version of which is free (the commercial Google Earth Pro can be used to view our models but it is not required). Google Earth is both a desktop application and a web browser plug-in that

contains many built-in geoscience data sets in its primary database, including surface imagery, water bodies, volcanoes, and earthquakes, all of which can be used to study subduction zones and marginal basins. In general, Google Earth is most suited for studying processes at or above the surface (e.g. *De Paor et al.* [2007]; *Mc Donald and De Paor* [2008]), however we have developed several techniques for visualizing the sub-surface as outlined in detail below (see *De Paor and Pinan-Llamas* [2006]; *De Paor and Williams* [2006]; *Whitmeyer and De Paor* [2008]; *De Paor and Whitmeyer* [2010]).

This paper is aimed towards readers with an interest in the tectonics of the region, as well as those who would wish to use the models we have created in their classrooms or informal education settings, and also towards those who wish discover how to create their own 3D COLLADA models of global scale processes elsewhere for viewing on Google Earth. In the past, modeling was done mainly by computer programmers. However just as non-technical people are increasingly contributing to Web content (especially via social media such as Facebook that facilitate easy uploading of custom content), so also the old distinctions between teacher, researcher, and programmer are breaking down as increasing numbers of academics create, test, and disseminate their own computer-base learning, research, and outreach resources.

2.3 GEOLOGICAL BACKGROUND

The Pacific plate (Figure 2) is formed by the tectonic processes of mantle upwelling, partial melting, crustal magmatism, and sea-floor spreading on a network of current (East Pacific Rise) and past spreading ridges. Unlike the Mid-Atlantic Ridge which is symmetrically positioned roughly equidistant from the Atlantic Ocean Basin's eastern and western passive margins, the East Pacific Rise is located much closer to (in places actually on) the Pacific's eastern active margin along the Americas. The Pacific plate thus extends westward across thousands of kilometers of Earth's surface before encountering the various plates and micro-plates that mark the western active margin of the Pacific Ocean Basin. As it moves away from the spreading ridge, the plate becomes older, colder, thicker, and denser [*Parker and Oldenburg*, 1973; *Yoshii*, 1975] and eventually is subducted along the western part of the so-called "Pacific Ring of Fire". Owing to variations in strike of the western active margin, tectonism varies in style from convergent to transverse, and associated marginal basins commonly undergo minor divergent tectonism.

Figure 2. Google Earth representation of tectonics of Pacific Ocean Basin.
Red lines mark East Pacific Rise. Northern Tonga trench is shown in yellow and the
Samoan transform boundary in cyan. Island of Tonga is indicated in green. Modified
from KML file downloaded from USGS website.

In this paper, we focus on a study area (Figure 3) covered by longitudes from
W170° to the Anti-meridian 180°, and by latitudes from S13° to the Tropic of Capri-
corn (S23.5°). The overall structure of the region consists of:
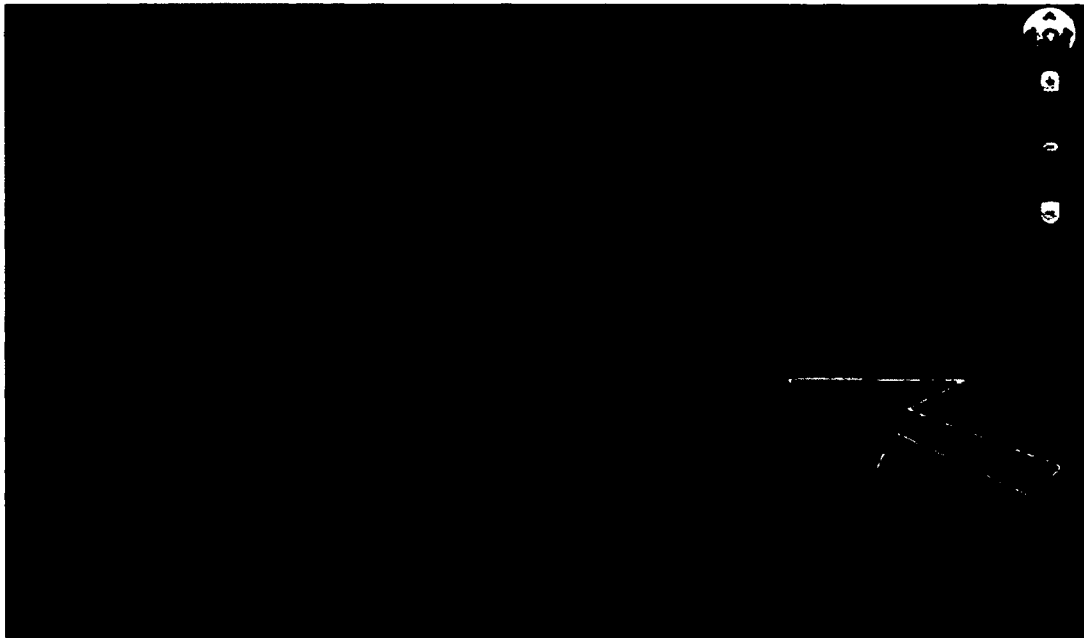
Figure 3. Current study area outlined in green. Pacific plate motion direction in white. Yellow line marks Tonga trench. Cyan line is Vitiaz Lineament. Red line represents a complex region of back-arc spreading.

- the westward spreading Pacific plate,

- the older extension of that plate north of American Samoa,

- The Tonga-Kermadec trench,

- The Tonga volcanic Arc,

- The Lau Back-arc Basin,

- The Lau remnant arc, and

- the South Fiji Basin.

A complication occurs south of this study region where a line of seamounts are currently subducting near Monowai, resulting in the differentiation of the northern Tonga and southern Kermadec trenches. To avoid this complexity, our study is confined to the region north of Monowai. To the west, the Lau Back-arc Basin meets the South Fiji Basin which is influenced by subduction of opposite polarity coming from

the New Hebrides convergent zone further west. Our study area is thus strategically chosen to avoid unnecessary complications.

In all but the northernmost part of our study area, the $\sim$ 100 million year old Cretaceous crust of the Pacific plate meets the recently formed edge of the Indo-Australian Plate along a 6-10 kilometers bathymetric depression called the Tonga trench [*Muller et al.*, 2008]. A 100 kilometer-thick descending lithospheric slab dips westwards under the Lau Basin to form the Tonga Subduction Zone. Slab morphology has been determined to various mantle depths by *Gudmundsson and Sambridge* [1998]; *Syracuse and Abers* [2006] and data are readily available in the GeoMapApp on-line database [*Ryan et al.*, 2009; *GeoMapApp*, 2012] (http://www.geomapapp.org). The chosen study area is of interest for several reasons. It is important for the scientific history of the theory of plate tectonics because seismic studies in this region were the basis for the original identification of subduction by *Isacks et al.* [1968]. The relationships illustrated within the dotted parallelogram of Figure 4 (modified slightly from that paper's famous figure) were inspired by the Tonga - Samoa region. Furthermore, the Lau Basin is a classic teaching example of back- arc spreading due to trench rollback and trench suction [*Uyeda and Kanamori*, 1979; *Moores and Twiss*, 1995; *Rosenbaum and Lister*, 2004]. In the rollback process, the immaterial line of maximum lithospheric flexure entering the trench migrates horizontally eastward as material in the plate continues to travel westward and turn downwards. This creates a so-called trench suction force that extends the overlying arc and causes divergence in the back-arc basin (Figure 5). Roll-back is a spatio-temporal concept involving different directions and rates of movement of material versus immaterial geometries and is thus potentially difficult to visualize, even by experts.

Towards the north, the Tonga trench ends abruptly along the Vitiaz Lineament just south of the approximately east-west trending Samoan Archipelago of islands and seamounts (Figures 1, 3). Here, the strike of the convergent plate boundary turns sharply from north to west, to become parallel to the plate movement vector, and the boundary therefore transitions into a transform boundary. North of this latitude and continuing beyond the study area, the Pacific plate forms the ocean floor for thousands of kilometers westward, progressively aging from Cretaceous to Jurassic before subducting at locations such as the Mariana trench, whereas to the south of the Vitiaz Lineament, a six million-year-old Cenozoic marginal basin called the Lau
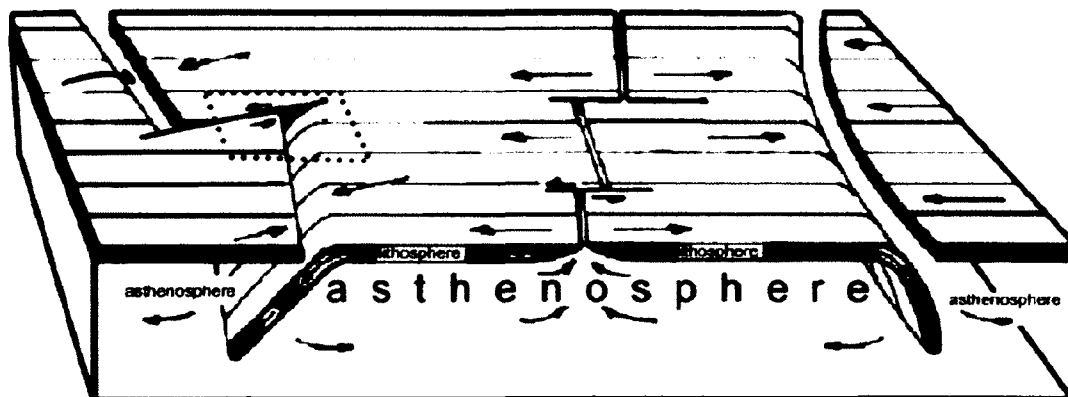
Figure 4. Plate tectonics explained in famous illustration (slightly modified) from *Isacks et al.* [1968] (their-Figure 1). Width of Pacific plate not to scale. Asymmetric position of East Pacific Rise not shown. Dotted parallelogram marks present study area.

Basin overlies the subducting Tonga Slab [*Lupton et al.*, 2003; *German et al.*, 2006], dividing the active Tonga Volcanic Arc to its east from the extinct Lau Arc to its west.

The change from convergent to transform plate margin correlates with geophysical evidence from *Smith et al.* [2001] that the lithosphere is in the process of tearing just southwest of American Samoa (Figure 6). An instructional analogy can be created easily, either by cutting partially through a sheet of paper or wood panel, or by holding ones fingers as shown in Figure 6-inset. However, the transition is complicated and obscured because the Vitiaz Lineament has been alternately interpreted as a dormant compressional structure dating from times when plate movement vectors were different [*Pelletier and Auzende*, 1996] or a product of rapid eastward tearing of the lithosphere [*Hart et al.*, 2004].

At the northern end of the Tonga trench, rates of subduction exceeding 20 centimeters per year are amongst the highest documented anywhere on Earth by *van der Hilst* [1995]; *Muller et al.* [2008]; *Bonnardota et al.* [2009]. *Holt* [1995] notes a south-to-north increase in down-dip velocities of the slab and the widening of the Lau Back-arc Basin is consistent with a northward increase in the rate of rollback, reaching as high as 10 centimeters per year. The trench continues along strike to the south beyond the study area, where it is known as the Kermadec trench. However, the character of the downgoing slab varies along strike as revealed by seismic tomography

Figure 5. COLLADA models raised above Google Earth surface showing structure of study region. Arc, basin, and slab can be selectively shown or hidden.

(Figure 7). Tomography shows a lithospheric slab dipping steeply all the way down to mid-mantle levels (1,600 kilometers out of the mantle total of 2,981 kilometers) south of Tonga, whereas in the current study area a shallow segment is imaged in the 410-660 kilometers transition zone [*van der Hilst*, 1995; *Mussett and Khan*, 2008]. These depths correspond to the olivine-spinel and spinel-perovskite phase transitions which are thought to affect slab density and kinematics. *Bonnardota et al.* [2009] present evidence of slab detachment at intermediate depths.

The Samoan Archipelago of islands and seamounts that forms the northernmost strip of the study area has been interpreted alternatively as attributable to drift of the Pacific plate over a deep-seated Samoan hotspot analogous to the Hawaiian
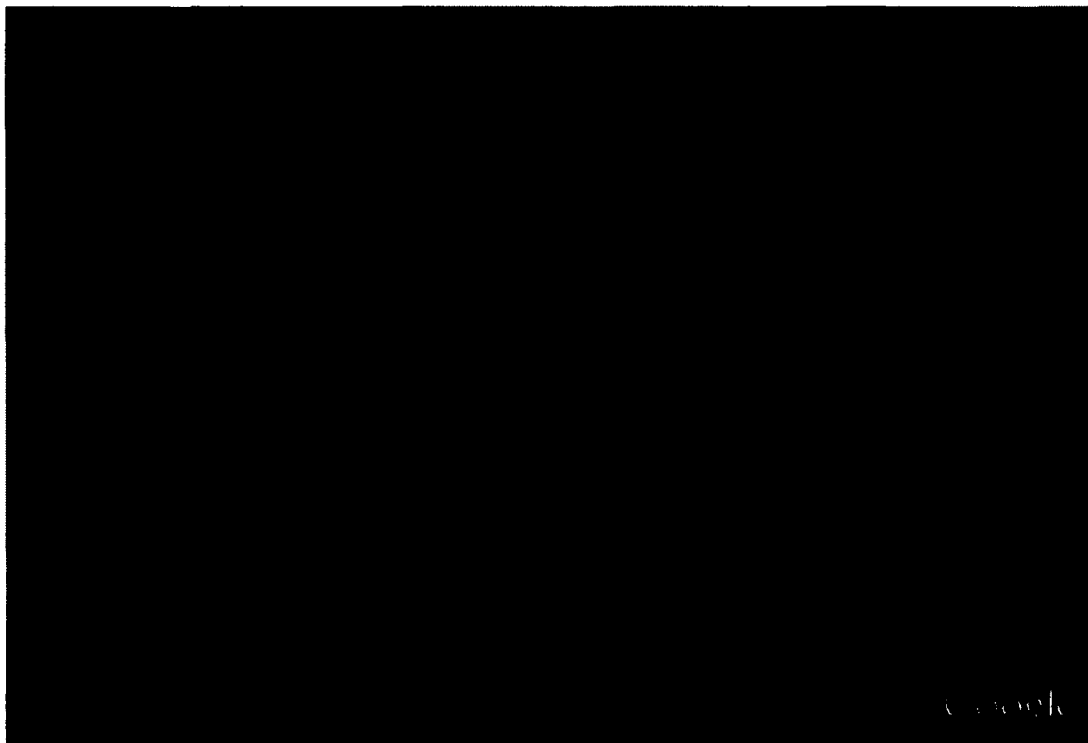
Figure 6. Hiding Tonga Arc and Lau Basin reveals how southern (nearer) portion of Pacific plate subducts along Tonga trench whilst northern part continues westward on Earth's surface. Inset: hand analogy helps some students visualize situation.
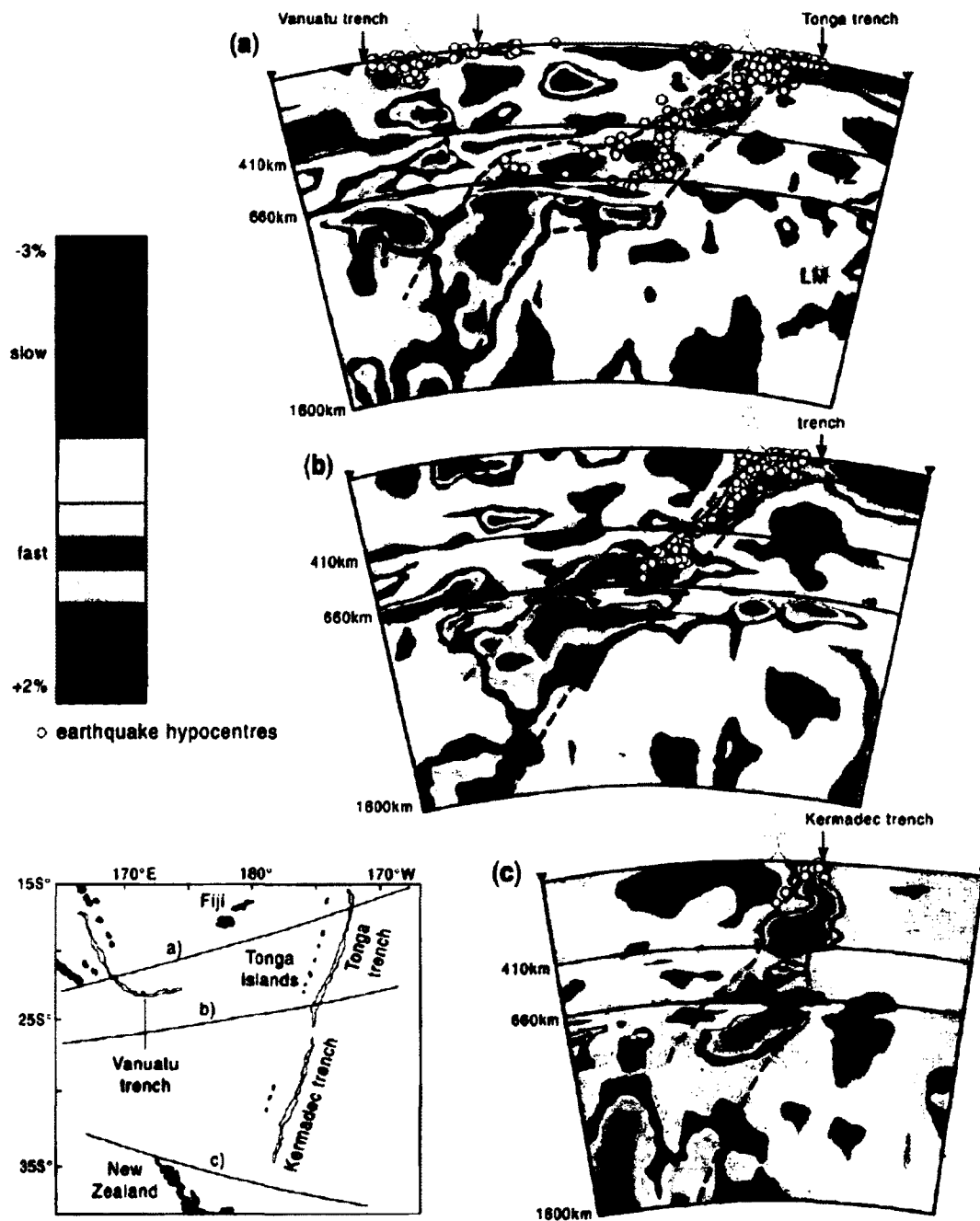
Figure 7. Seismic tomography of Tonga-Kermadec slab from *Mussett and Khan* [2008]. Note mid-mantle flat-slab developed in north but not in south.

hotspot [*McDougall*, 2010] or as a result of warping and stretching along an east-west-trending lithospheric monocline in the proximity of the transform boundary and tear point [*Hart et al.*, 2004]. In either case, the volcanic lineament adds complexity and intrigue to the story of this region.

2.4 COLLADA MODELS IN THE GOOGLE EARTH DESKTOP APP

To aid with visualization of complex tectonics, we constructed interactive emergent and animated COLLADA models of the Tonga - Samoa region. We include a description of the model coding process here both for those readers who are interested in how COLLADA works and for those those who might wish to create similar models elsewhere. The authors' recent experiences in co-presenting several over-subscribed Geological Society of America short courses and workshops on the topic of Google Earth modeling with COLLADA point to growing interest in this approach amongst geoscience researchers and educators. The following account should be accessible to readers without experience in programming languages such as FORTRAN or C. If readers can format a Web page with HTML, they can modify the types of scripts discussed below to work in their own area of interest (for more details of scripting for Google Earth, see *Wernicke* [2009]; *De Paor et al.* [2010a]).

One of the more powerful features of Google Earth is the ability it offers users to display their own content [*Goodchild*, 2008]. Custom content can be added using Google Earth's menus or by creating a file written in the Keyhole Markup Language (KML), a dialect of XML designed specifically for virtual globes. The basic structure of a KML file is shown in Figure 8. This script places a default yellow map pin in the center of North America. The custom content we are most interested in here consists of 3D COLLADA models. Like KML, COLLADA is another dialect of XML and is used mainly to add 3D buildings to Google Earth, for example using the SketchUp modeling program. Fortunately, the dimensions of COLLADA models can be set to regional or global in magnitude so that a program intended for modeling buildings can be used to create crustal blocks on the scale of mountains [*De Paor*, 2008b,c] or even continents [*Dordevic et al.*, 2009, 2011; *De Paor and Whitmeyer*, 2011]. COLLADA models saved in Digital Asset Exchange (DAE) files are recognized and imported by Google Earth. The example in Figure 9 adds a model of the Tonga slab as seen in Figure 6.

To create Figure 6, we digitally mined data from *Syracuse and Abers* [2006] which

```
<?xml version="1.0"?>
<kml>
      <Document>
            <Placemark>
                  <Point>
                        <coordinates>-95.45, 37.68, 0</coordinates>
                  </Point>
            </Placemark>
      </Document>
</kml>
```

Figure 8. An example of code for creating a Placemark in KML.

```
<?xml version="1.0"?>
<kml>
      <Placemark>
            <Model>
                  <altitudeMode>relativeToSeaFloor</altitudeMode>
                  <Location>
                        <longitude>85.935848221848</longitude>
                        <latitude>-18.36255792927627</latitude>
                        <altitude>200000</altitude>
                  </Location>
                  <Orientation>
                        <heading>21.732</heading>
                        <tilt>0</tilt>
                        <roll>0</roll>
                  </Orientation>
                  <Scale>
                        <x>0.816</x>
                        <y>0.776</y>
                        <z>0.796</z>
                  </Scale>
                  <Link>
                        <href>files/TongaSlab.dae</href>
                  </Link>
            </Model>
      </Placemark>
</kml>
```

Figure 9. An example of code for a COLLADA model in KML.

is openly available on GeoMapApp [*GeoMapApp*, 2012] (http://www.geomapapp.org). GeoMapApp is a free desktop application that gives the user a Google Maps-style interface with a wide-range of geological data (Figure 1 is a screen shot). Among the global data sets made accessible in GeoMapApp are earthquake hypocenters (http://www.geomapapp.org). The first step to creating our models was to select a rectangular region in GeoMapApp, export the hypocenter points, and load them into an Excel file. This file was used to create points with correct depth tags for compatibility with KML. Once the points were in the KML file, a snapshot of the region of interest was taken in Google Earth. This picture was saved as a PNG image file which was then edited with photographic editing software. We used the free open-source application called GIMP [*GIMP*, 2011], however owners of a commercial application such as Adobe Photoshop could use it equally well. In SketchUp, a rectangle was created with the same dimensions as the area from which the Google Earth terrain image was taken. The edited PNG file was then used as a so-called texture pasted on the rectangle (that is, an image covering a model surface like wallpaper). In the case of the GeoMapApp data, to aid computer memory management, several small sections were exported onto six different rectangles. Next, points were dropped to the correct depth beneath the surface. If several data were clustered together the deepest one was selected (usually the depths were within five kilometers of one another). After all the points were correctly located in the z-dimension, the regions were stitched together using geological markers and longitude/latitude lines. The data points were then connected into depth profile lines. An outline of the surface slab was copied and offset 5 kilometers to simulate ocean crustal thickness and a second copy of the slab was offset 100 kilometers to create a bounding surface at the bottom of the lithosphere. These slab surfaces were intersected by vertical planes on the sides using a SketchUp 'intersect' command to complete a solid model. The geo-referenced slab was saved in a DAE file which was imported into Google Earth.

A similar process was used to create 3D models of the arcs and back-arc basin, except that these were constrained by the subducting slab geometry, not by seismic data. Finally, a KML Placemark containing the model (Figure 9) was replicated and a KML TimeSpan element was added to each replica Placemark (Figure 10). The begin and end time tags of the Timespan and the model's altitude tag were incremented in unison (in KML, the altitude is in meters so "200000" represents an

altitude of 200 kilometers.) As the Google Earth slider is moved and a slider value is reached, the code responds by changing the elevation of the COLLADA model. All tectonic domains were elevated in unison but different domains were placed in separate KML Folders so that they could be selectively shown or hidden.

```
<?xml version="1.0"?>
<kml>
    <Placemark>
        <TimeSpan>
            <begin>-100</begin>
            <end>-200</end>
        </TimeSpan>
        <Model>
            ...
            <Location>
                <longitude>...</longitude>
                <latitude>...</latitude>
                <altitude>200000</altitude>
                ...
                ...
                ...
    </Placemark>
    <Placemark>
        <TimeSpan>
            <begin>-200</begin>
            <end>-300</end>
        </TimeSpan>
        <Model>
            ...
            <Location>
                <longitude>...</longitude>
                <latitude>...</latitude>
                <altitude>300000</altitude>
                ...
                ...
                ...
```

Figure 10. Sample code for emergent COLLADA model in KML.

Two difficulties were encountered in the above process. First, the study area bordered the Earth's Anti-meridian and Google Earth was found to behave erratically in this region. We overcame this by draping the famous NASA Blue Marble image of the Earth [NASA, 2005] over the Google Earth surface imagery and moving the origin of longitude so that the models were safely away from the Anti-meridian (a second ground overlay snapped from the Google Earth terrain was superimposed in the Tonga region in order to provide local detail) (Figure 11). A side-effect of this solution is that the lat/lon grid must be left turned off. The second difficulty was that

the time slider technique gave the viewer only one slider control whereas we wanted to be able to both elevate and animate the block. Initially, we animated blocks that were already elevated to a fixed altitude (see *De Paor et al.* [2012b] - Movie1) but later we switched to the Google Earth API (see next section).
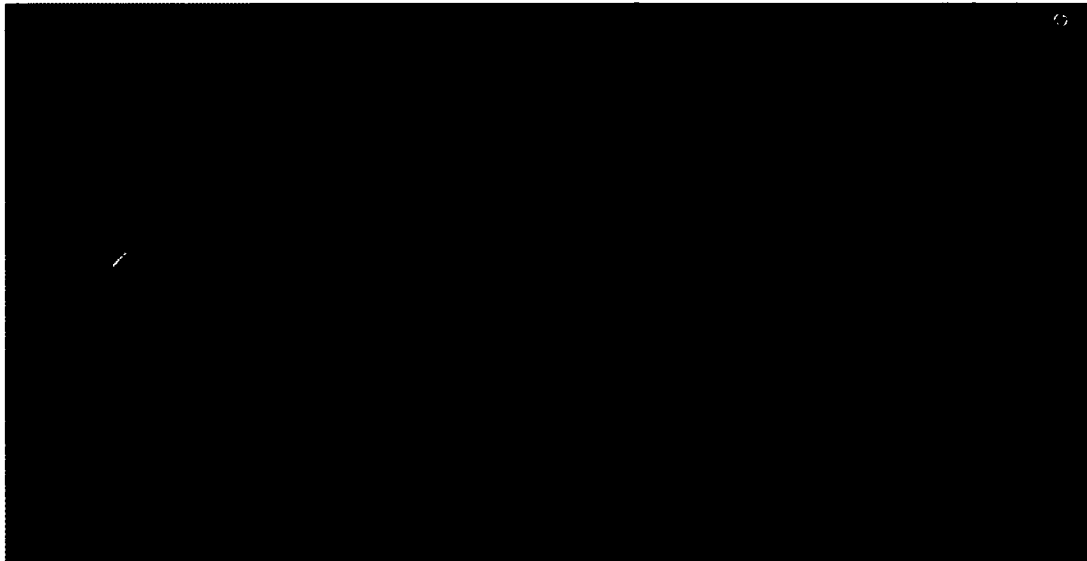
Figure 11. Sea-floor detail for Tonga region snapped from Google Earth and draped over NASA Blue Marble image of Earth. Both were moved through longitude to get away from the Anti-meridian, a region where Google Earth has difficulty handling models (see text).

Animating models in Google Earth (Figure 12) was similar to elevating emergent models (Figure 10). Instead of incrementing the altitude of a single model, we created a sequence of gradually differing models at a constant altitude (a marker was used to ensure that models were all exported from the same spot to prevent unwanted jittering or wobble) and we changed the name of the linked model file in the KML Placemark sequence. This introduced an unanticipated problem. Although the images used as textures were relatively small (under 100 Kb), the long sequence of models used in this animation proved to be hesitant to load even on a fast computer. Google Earth displayed the blank, white-sided model frame first and applied texture images after a brief interval. Even though this was less than a second in most cases, white flashes interrupted the immersive effect of the animation. Our solution was to wait for all frames to load before playing the animation, however this approach

is tedious. Hopefully, future versions of Google Earth will cache textures before displaying models or build visualizations in an off-screen bitmap and only move them on-screen with completely loaded; this is standard practice in other applications.

```
<?xml version="1.0"?>
<kml>
    <Placemark>
        <TimeSpan>
            <begin>-100</begin>
            <end>-200</end>
        </TimeSpan>
        <Model>
            ...
            ...
            ...
            <Link>
                <href>files/200.dae</href>
                ...
                ...
                ...
    </Placemark>
    <Placemark>
        <TimeSpan>
            <begin>-200</begin>
            <end>-300</end>
        </TimeSpan>
        <Model>
            ...
            ...
            ...
            <Link>
                <href>files/300.dae</href>
                ...
                ...
                ...
```

Figure 12. Animated COLLADA model in KML.

2.5 THE GOOGLE EARTH API AND JAVASCRIPT CONTROLS

In addition to the well known stand-alone desktop application, Google Earth is available as a web browser plug-in that allows one or more instances of the virtual globe to be embedded in a Web page and controlled with client-side JavaScript (an example of script is shown in Figure 13) or by means of server-side scripts written with a scripting language such as PHP, Python, or Ruby. All features do not transfer over from the Google Earth desktop application to the Google Earth API - for example, there is no sidebar with Places and Layers. However individual features such as

tools in the application toolbar may be coded in JavaScript. Content control using JavaScript is an advantage to the API. Maps, cross-sections, COLLADA models, etc. can be independently controlled and modified. Ease of viewing content is a big plus to the Google Earth API. A person wishing to display content no longer has to download and launch a file, but can view Google Earth directly in their web browser. The Google Earth API is controlled by standard controls found in HTML forms (buttons, sliders, menus, text boxes, etc.). This style of control enables the creation of more robust user interaction with the content. Thus, in the Google Earth API a new control may be added for every user interaction needed. The main controls used in our time-evolved models are the elevation control with a slider and visibility and time/motion controls with buttons. The slider works by allowing the user to vary any KML element over a range of values. It would not be difficult for readers to add their own spot quizzes or text areas for gathering student responses, for example.

```
<!DOCTYPE html ...>
<htmL>
        <head>
                <script language="JavaScript" type="text/javascript" src=
"http://www.lions.odu.edu/org/planetarium/steve/Tonga_API/tonga_roll_js/openfile.js">
                </script>

        </head>
        <body>
                <form>
                        <input type="button" value="Load Case 1" onclick="openfile(1)">

                </form>
        </body>
</html>
```

Figure 13. API JavaScript interface.

For our elevation slider we used an inexpensive commercial product called TigraSlider Control [*SoftComplex*, 2010]. A free version is offered but does not have necessary functionality. Were we starting afresh we would use the free native slider input built into HTML5 and supported by all new browsers. Such a slider can be added to a web page with the single line:

<input name="slider" type="range " min= "0" max="10" value="5"> and its value

can be read with the JavaScript function document.getElementById('slider').value. The visibility controls are standard HTML form buttons which enable model components to be shown or hidden, thus revealing or obscuring sections of the model behind them. A quick method used to accomplish this task was to change the HTML href hyperlink to the .dae file. If a model component needed to be invisible, the href link was pointed to a non-existent .dae file, thus nothing was loaded.

2.6 IMPLEMENTATION

Since 2008 we and our colleagues [*Whitmeyer et al.*, 2011] have been distributing geological COLLADA models to a cohort of educators in a variety of universities and colleges and we have made them freely available for download both from our academic web sites and from www.digitalplanet.org. The animated emergent models described here, along with similar models in a variety of tectonic settings, have been used by us in several undergraduate courses at four east coast universities and are available to visitors to the ODU Pretlow Planetarium in an informal education setting. During leave-of-absence by De Paor in 2010, co-author Wild developed a set of Google Earth API-based laboratory activities including animations using the above technique (see Figures 14, 15,16,[*Wild et al.*, 2011], and movies 1, 2, 3 [*De Paor et al.*, 2012b,c,d]. These were combined in a single laboratory class along with similar activities addressing the Iceland spreading ridge and hot spot, and presented as a test with IRB compliance to 127 non-science-majors as part of a broad survey of the solar system. Pre- and post-tests were administered by Wild and analyzed by NSF-sponsored independent assessor Gobert, and results are reported by *Gobert et al.* [2012]. Quoting their abstract, these authors "found: 1) overall learning gains; 2) no differences in learning gains when comparing those with prior coursework in Geology or geography to students without this prior coursework; and 3) no differences in learning gains when comparing males and females." They report a gender difference favoring males in terms of items completed during the class period and a correlation between students' pre-test and embedded laboratory scores.

Testing in the informal education setting of a planetarium has not yet been attempted. Here, models can be displayed on a portion of the dome using a peripheral LCD projector during planetarium shows and on peripheral computer screens that visitors can casual browse. Future plans include eye-tracking studies of such browsing as we have recently acquired the necessary equipment.

24

Figure 14. Google Earth API, COLLADA models manipulated in Google Earth instance embedded in web page. Slider, buttons controlled using JavaScript.
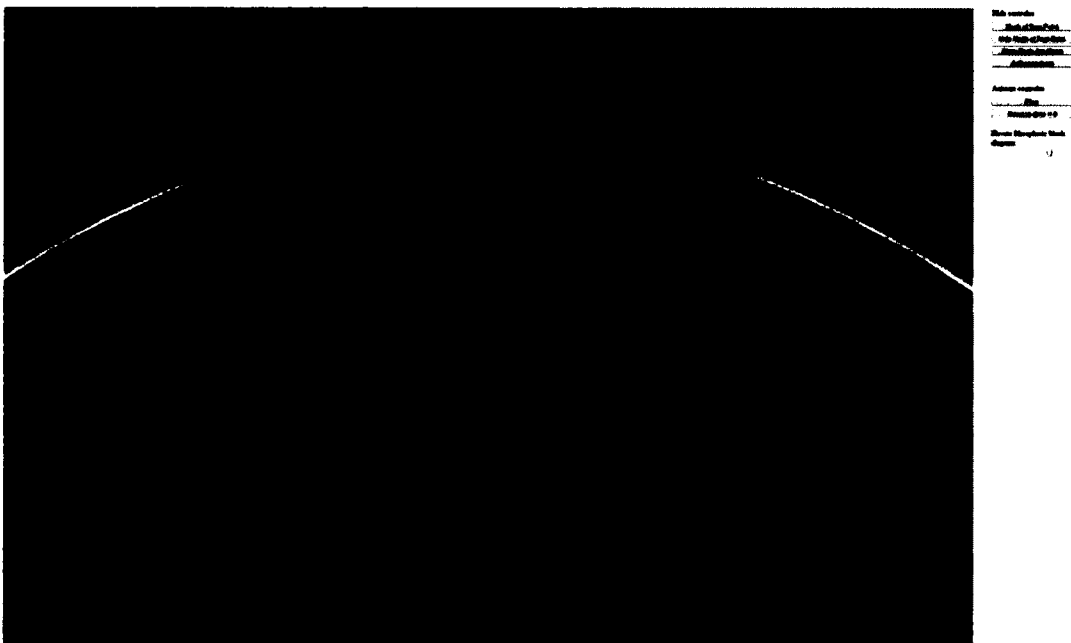
Figure 15. Alternative models of trench rollback and slab kinematics. See text.

Figure 16. Block model that can be raised and reorientated while animation is running using multiple JavaScript controls.

2.7 ENHANCED VISUALIZATION USING GOOGLE MARS

In addition to the emergent COLLADA models described above, we developed methods of viewing sub-surface tectonic structures in situ. The radius of Earth's outer core (3,500 kilometers) is within 3% of the mean radius of Mars. Consequently we can use the Google Mars virtual globe to represent Earth's core- mantle boundary. The Martian 3D terrain is turned off and a plain image overlay is used to cover all of the built-in Martian surface imagery. At the Earth's core-mantle boundary depth of 2,900 kilometers, the peak black-body radiation is white-hot, however white is not a suitable color for modeling, therefore we use red or gray overlay images (Figure 17) to convey temperature or metallicity respectively (an informal poll taken by *De Paor and Whitmeyer* [2011] revealed that ten of the fourteen voters favored the red core whereas three favored gray and one white). A spherical COLLADA model representing Earth's surface to scale is draped with a semi- transparent PNG image of the NASA Blue Marble. Figure 18 shows the core with three slices of the mantle under Tonga. The upper part of each slice is textured with seismic tomography from *Mussett and Khan* [2008]. The lower part is colored purple to emphasize the relative

proportion of the mantle not reached by the tomographic data. Elements of Figures 17 and 18 are combined in Figure 19, with a circular cut-out revealing the interior. All three models can be downloaded from our Web site [*Digital-Planet*, 2011].
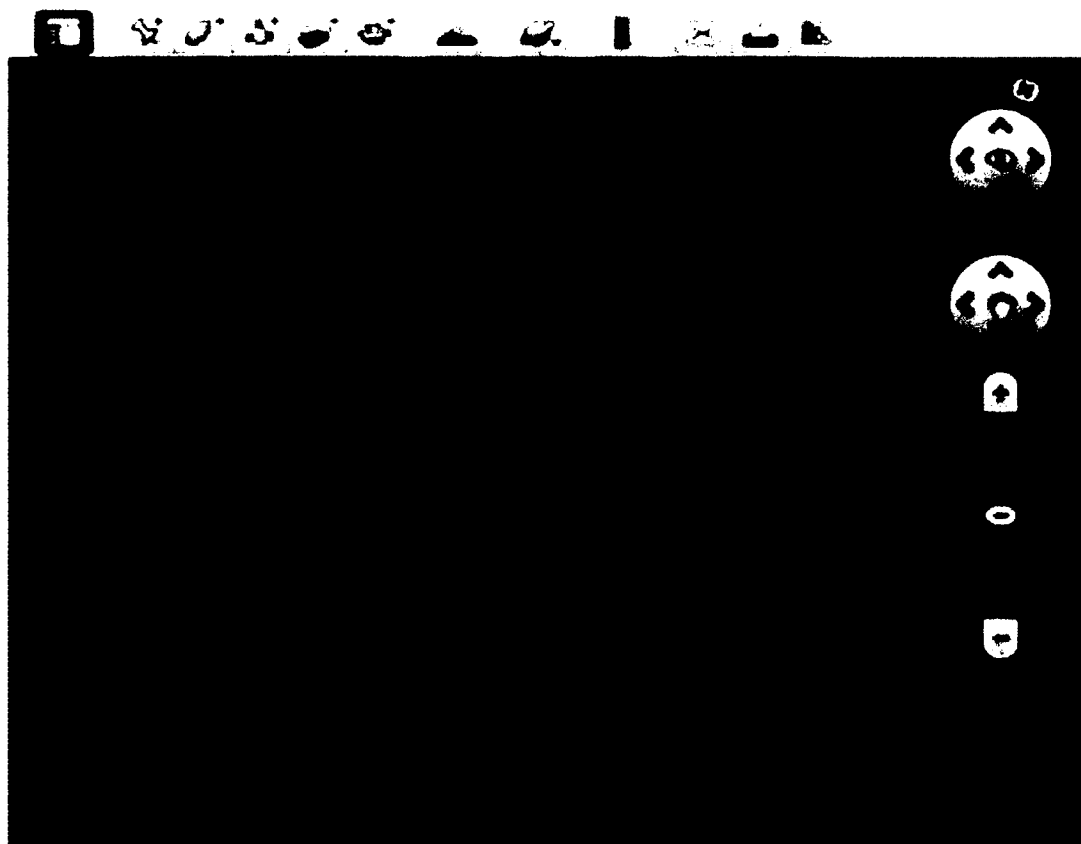
Figure 17. Visualizing subsurface using Google Mars with plain red image overlay and Blue Marble COLLADA model of Earth's surface.

Specific to this study area, inclusion of deep mantle tomography lead us to consider tectonic models of the Tonga subduction system extending beyond the depth of the *Syracuse and Abers* [2006] data. The feature of particular interest in the tomographic section is the region of shallow or 'flat' slab dip between 430 kilometers and 670 kilometers as discussed below.
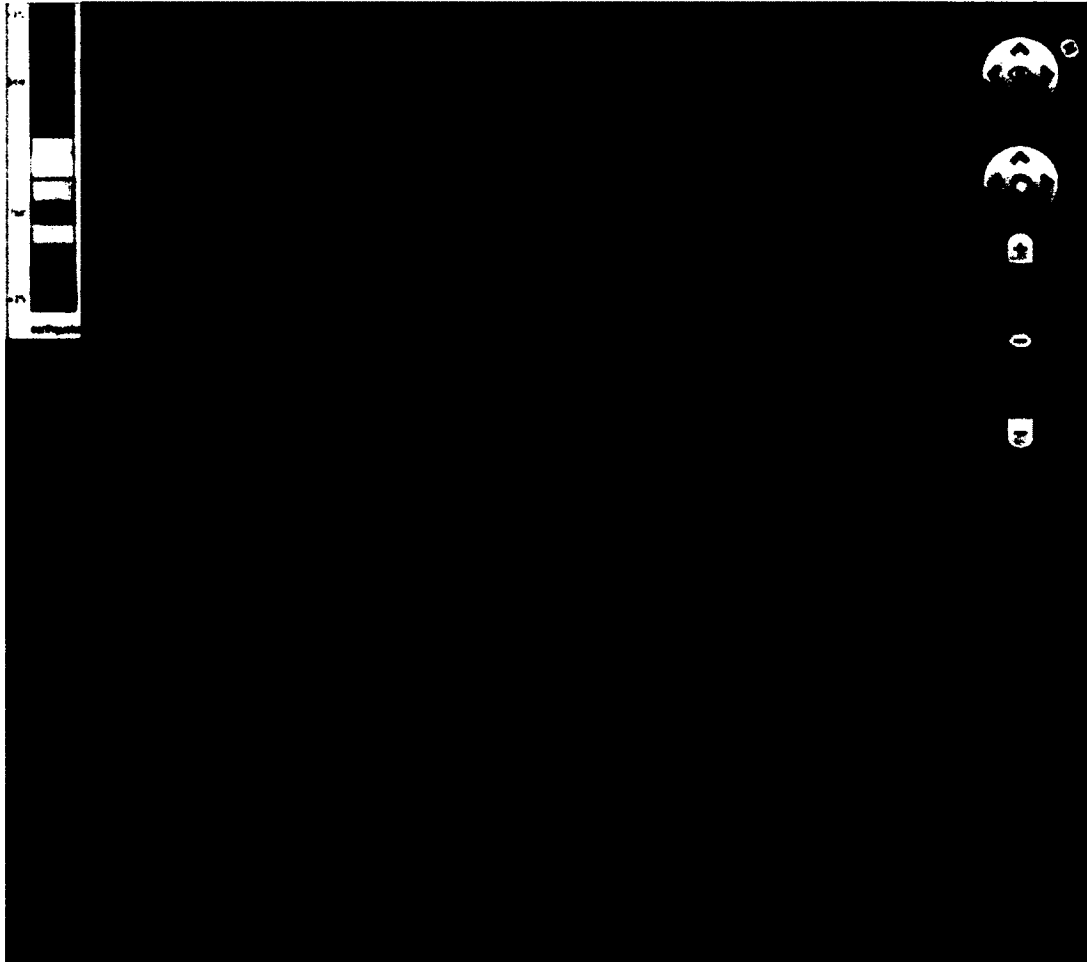
Figure 18. Slices of crust and mantle shown with seismic tomography from *Mussett and Khan* [2008]. Note flat subduction at mid-mantle levels. Purple represents lowermost mantle below limit of tomographic data. Red sphere representing Earth's core.

Figure 19. Visualization with circular cut-out revealing underlying mantle. Yellow, red, and blue lines mark surface tectonic lineaments. Note that Arctic, North America, and Russia are seen inverted on inner surface of sphere behind core.

2.8 TECTONIC MODELS OF THE TONGA REGION

Creating learning and outreach resources for the Tonga-Samoa region required the assembly of six alternate plate tectonic models including mostly well- established but also some novel ideas. To a casual observer, this might seem excessive. Geologists are so used to viewing two-dimensional cross sections of subduction zones that they may not ponder how such zones must change in four dimensions of space and time. On a finite spherical Earth, a subduction zone cannot continue along strike forever and neither Andean-style magmatic arcs nor Lau-style back arc basins can be understood in terms of a steady-state subduction system akin to a descending escalator. Yet plate tectonics texts tend to skimp on discussion of complications such as lateral terminations or rollback and static illustrations strongly suggest a steady-state process of subduction at a fixed trench location. By presenting over-simplified models of subduction to students and the public we make it impossible for them to truly understand the genesis of arcs.

The rigid Pacific plate is contiguous east of the study area, and its absolute Euler pole of rotation lies far away (Figure 20), so the velocity of the sea- floor approaching the Tonga trench must be approximately the same as its velocity along the Samoan Archipelago north of the subduction zone (web reference [*GSI*, 2004]). Consequently the variables of interest are the absolute and relative velocities of the tear point. Absolute velocities may be stated relative to the global hotspot reference frame whereas relative velocities are stated with reference to an arbitrary material point in the lithospheric plate.

2.8.1 MODEL 1: NO TEARING OR SLOW TEARING.

In this end-member case (Figure 21), the tear point southwest of American Samoa is not currently active but rides along passively with the plate, a scenario that results in horizontal absolute velocity vectors for all points both on the surface and on the slab. This end-member case cannot be the whole story because it does not allow subduction to get started in the first place, however, it is a temporary condition which is possible at some later time. In order for the slab to move horizontally westward, the arc material in front of it must either 1) move west at an equal or greater pace, or else 2) deform to form a contractional forearc accretionary wedge or a foreland thrust belt, or both (Figure 21). If the tear point propagates eastward
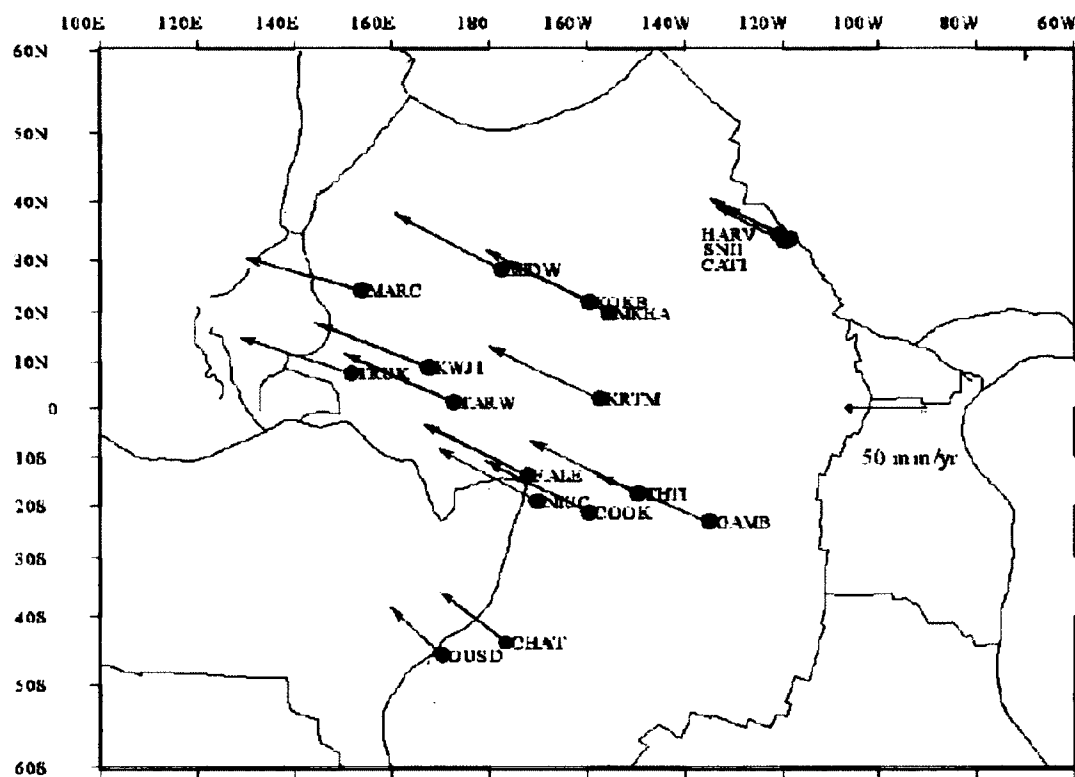
Figure 20. Velocity vectors for the Pacific plate from GPS measurements. Web reference [*GSI*, 2004].

more slowly than the plate moves westward then the movement vectors for material in the slab will dip westward more shallowly than the dip of the slab itself and the scenario will also correspond to Model 1 (Figure 22).

Figure 21. Structure of Andean Arc oriented to correspond to polarity of Tonga Subduction Zone, view north. Green denotes forearc and foreland sedimentary basins. Black lines are thrust faults near surface and shear zones at depth. Red denotes magmatism.

The structure of the lithosphere above the Tonga Subduction zone in Model 1 depends on the absolute velocity of the Australian Plate west of the study area. Back-arc spreading west of Tonga could be compatible with Model 1 if the Australian Plate drifted west faster than the Pacific plate or if rollback of the opposite-polarity New Hebrides Subduction Zone west of Fiji created the necessary extension. As

Figure 22. Tear point migrating slowly eastward (white arrow) resulting in dipping absolute movement vectors (black).

it happens, the direction of absolute plate motion of the Australian Plate is northward, approximately perpendicular to the Pacific plate [*Kreemer*, 2009; *Stadler et al.*, 2010], therefore it does not have a significant orthogonal component of movement relative to the trench and is equivalent to a stationary block for the purposes of this model. Furthermore, the New Hebrides structure cannot be responsible for all back-arc spreading because its influence does not extend beyond the northern end of the Lau Basin. Thus, if Model 1 were valid, there ought to be a mountainous magmatic arc bordered by forearc and foreland thrust belts, which are shown in Figure 22 but not seen in ground truth. If there were ever a period during which the tear point drifted passively with the plate or ripped slowly, it could not have lasted long, else a large compressional arc would have grown and endured.

Despite the obvious unlikeliness of Model 1 to an expert (professor), we included it amongst our alternatives in order to challenge novices (students) to think of reasons to reject it, or equivalently, to envisage the type of data that would support it but are not seen.

2.8.2 MODEL 2: BAND SAW TEARING.

Our second model requires an immaterial tear point fixed in an external reference frame (Figure 23). The western drift of the Pacific plate can then be compared to pushing a sheet of plywood westward through a band saw and holding the north side level (Figure 23 inset) whilst letting the south side sag (to include the Samoan Archipelago in the analogy, one would add a candle in a fixed location under the north side of the sheet close to the band saw).

The absolute velocity vector of any material point in the slab in this case would be directed down-dip, i.e., parallel to the top and bottom of the slab, consequently the arc forming above the slab would be under no lateral stress, neither forming an Andean-style compressional structure such as a thrust belt nor an extensional structure such as a back-arc spreading ridge. Nevertheless, the the model would lead to a prediction of gradual magmatic arc build up to significant size.

It is not intuitively obvious that there are two independent questions to be addressed in this scenario. First, is the Samoan Archipelago a hot-spot trail caused by the Pacific plate drifting slowly westward over a fixed hot-spot? And second, has the tear point always been located close to the hotspot? If the latter were true, the tear point southwest of the youngest island - American Samoa - today would have

Figure 23. Model 2: Tear point fixed in external reference frame. Velocity (white arrow) equal and opposite to plate velocity. Velocities in slab parallel to dip (black arrows).

been southwest of the older Western Samoa in the recent past and southwest of the oldest Wallis and Futuna Islands before that, with each of these islands presumed to have formed over the stationary deep mantle hot-spot before the younger ones existed. Thus a test of the hot-spot trail model would be a progression of island ages and thermally induced decreasing altitudes or bathymetries, comparable to the Hawaiian chain. The hot-spot answer was in doubt because of the occurrence of recent vulcanism at both the west and east end of the Samoan volcanic lineament. However, studies by *Mahoney and Spencer* [1991]; *Koppers et al.* [2003]; *Hart et al.* [2004] have shown plume hot spot activity similar to Hawaii. Recent volcanism along the Samoan lineament is seen by them as a separate phenomenon superposed on the hot-spot progression and therefore requiring a separate explanation.

2.8.3 MODEL 3: RAPID ROLLBACK.

Our third model involves the eastward relative migration of the tear point at a faster rate than the westward absolute movement of the Pacific plate over the hotspot, resulting in eastward absolute movement of the tear point and absolute velocity vectors for material in the slab that are steeper than the slab dip (Figure 24). An analogy would be the act of cutting cloth by moving a scissor forward whilst pulling the cloth backwards towards oneself (students have also suggested a comparison with the Michael Jackson moon-walk). In this case, the original tear point would have been at the western end of the Samoan Volcanic Lineament, well west of the fixed mantle hot-spot and would have migrated rapidly east so that it happens to be close to Vailulu'u today. Rapid migration of the tear point could account for the superposition of recent vulcanism on the age progression of the Samoan Archipelago as discussed above by flexure of the lithosphere close to the line of tearing. If we could see into the future, the tear point might continue to migrate east of the current hotspot. On the other hand, its current proximity to the hotspot might trap the tear in a steady-state phase in the future as represented by Model 2.

Since relative motion of the tear point is key, Model 3 can also result from modest tear velocities in combination with slow plate velocities. In the end- member case there is no horizontal component of plate motion and the slab vectors are vertical (Figure 25). Clearly the Pacific plate does have a significant horizontal velocity, so the end-member case is not practical.

Figure 24. Model 3: Rapid eastward migration of tear point (white arrow). Absolute slab velocity vectors steeper than slab dip. Stress in arc causes extension and dike intrusions, opening Lau Basin.
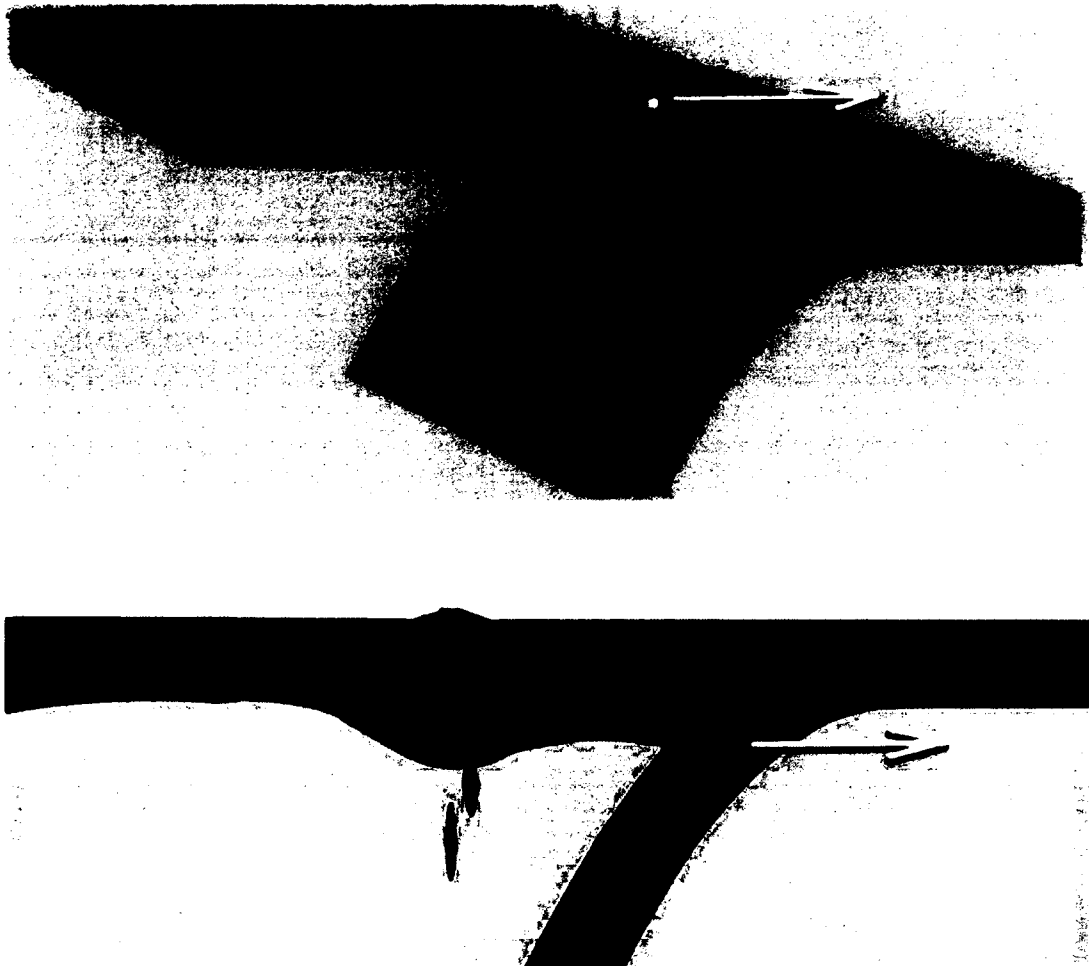
Figure 25. Model 3 (contd.): Dominance of rollback over horizontal plate motion. Steep to vertical absolute velocities in slab (black arrows). Stress in back arc region is tensional.

2.8.4 MODEL 4: DEEP MANTLE ROLLBACK MODEL.

Model 3 can account for the development of a subduction zone and extensional back-arc basin, but we also need to account for the flattening of the slab dip approximately between 400 and 600 kilometers depth. *Kincaid and Olson* [1987] suggested that the subduction system may have initially followed Model 2 (no rollback) and that rollback and back-arc spreading may have ensued when the slab hit the 430-670 kilometers mantle discontinuity after about 10 million years at 7 centimeters per year. In this scenario, the slab encounters resistance to subduction due to mid-mantle phase and viscosity changes (430 kilometers is marked by the olivine-spinel transition whereas the spinel-perovskite transition occurs at 670 kilometers) and it develops a bend that itself rolls back (lower white arrows in Figure 26).

2.8.5 MODEL 5: FOUNDERING FLAT-SLAB MODEL.

As far as we can ascertain, this fifth model (Figure 27) is not previously described in the tectonic literature. In this scenario, the western Pacific plate first cracked along the Tonga trench and tore at a point to the west of the Samoan Archipelago causing the southern portion to subduct. A magmatic arc built but there was no significant back-arc spreading. The seamounts and islands of the Samoan Archipelago pierced the plate progressively along a line to the east of the tear point. Islands and seamounts aged and subsided as they drifted westward. At about 6 million years, the tear point ripped rapidly eastward as in Model 3, superimposing recent volcanism of the Vitiaz Lineament and ending in proximity with the hotspot. This rapid rollback resulted in a shallow-dipping slab segment at shallow depth with steep-dipping absolute movement vectors. The flat slab then continued to founder to its present mid-mantle level. In the third dimension, the structure involves a near-pole rotation (cf. *De Paor et al.* [1989]) resulting in the narrowing of Lau Basin towards the south and widening to the north. At about 2 million years ago, trench rollback started a near-pole rotation process about an Euler pole located around S 24. The rotation occurred at a rate of 7° per million years.

2.8.6 MODEL 6: SUBDUCTION STEP-BACK.

Our final model is one in which subduction initiates in the west under the Lau Arc and then instantaneously steps back to the longitude of the Tonga Arc (Figure
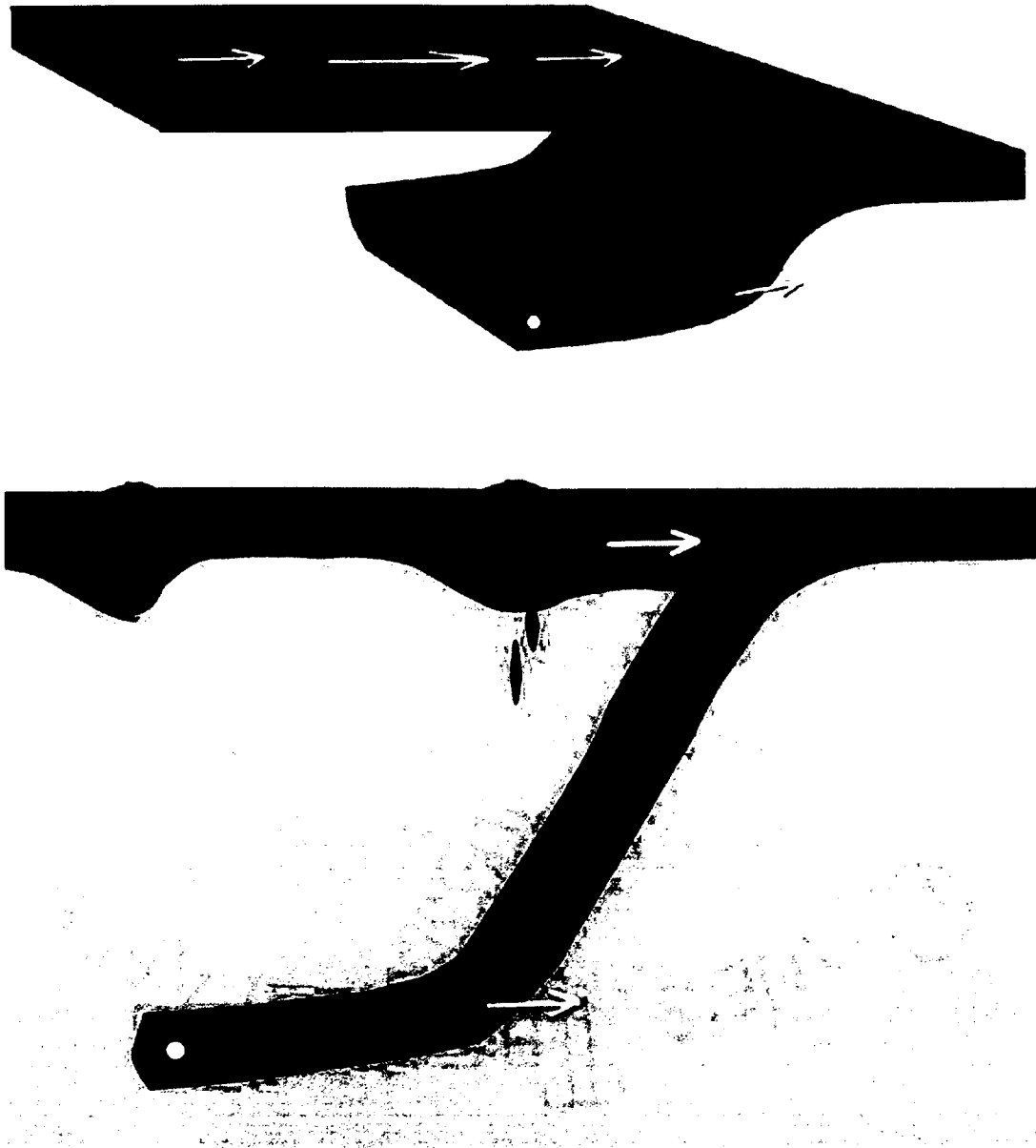
Figure 26. Deep Mantle Rollback (lower white arrow) may have created flat slab segment at about 600 km and also driving surface rollback (upper white arrow). White spot marks point where slab started to go flat due to mid-mantle resistance.

Figure 27. Model 5. Foundered flat slab. See text for discussion.

28). There is no back-arc spreading, rather the marginal basin is floored by a broken off and abandoned segment of the Pacific plate. This model is established elsewhere: it has been proposed to explain part of the evolution of the Mariana system, among others. However, diffuse magnetic patterns in the Lau Basin imply [*Lawver and Hawkins*, 1978] that it formed by distributed back-arc spreading driven by trench rollback [*Uyeda and Kanamori*, 1979] and trench suction [*Chase*, 1978] rather than by entrapment of normal oceanic lithosphere behind a newly formed Tonga Arc to its east (these different models of marginal basin formation are discussed by *Karig* [1974]).
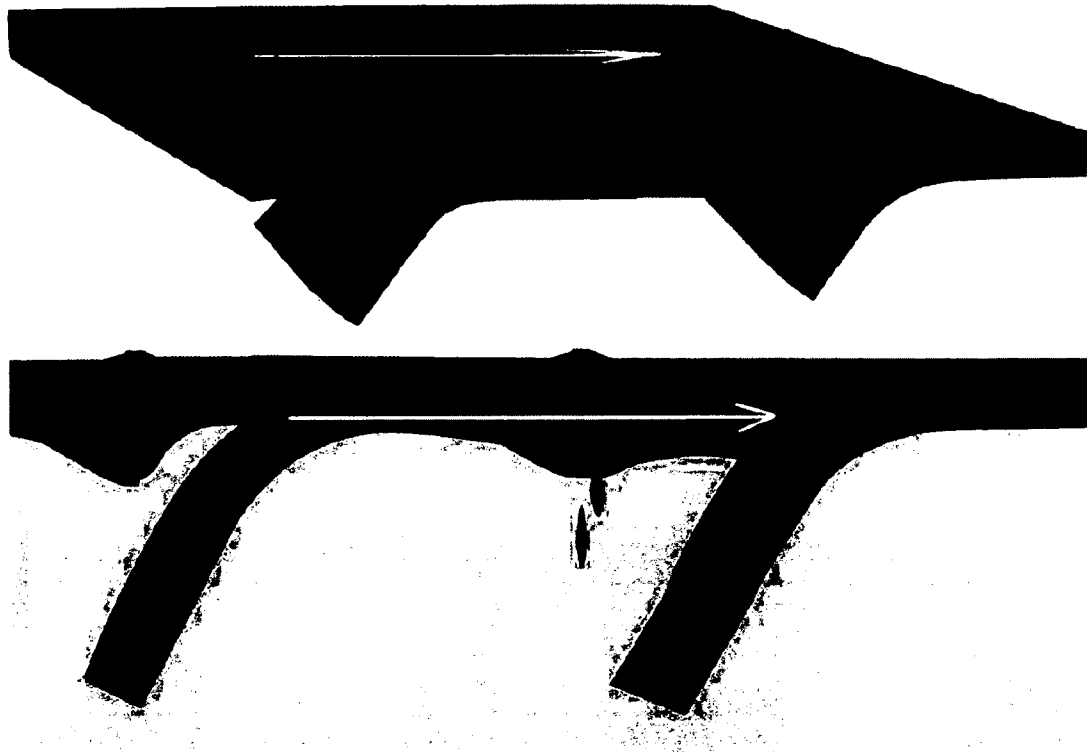
Figure 28. Model 6. Subduction step-back. Subduction initiates in west, then steps instantaneously to east (oceanward). See text for discussion.

We leave the task of debating the fine details of alternate models to regional tectonic experts. As usual, there are end-member cases that can be rejected but no single hypothesis that trumps all others. Under-constrained alternatives help guide tectonic experts towards the types of data that need to be collected in the future. For instructional purposes, it is useful to present these multiple working hypotheses

as an example of the oft-misunderstood process of science (e.g. *Brickhouse* [1990]; *Handelsman et al.* [2004]).

2.9 DISCUSSION AND CONCLUSIONS

Ever since its inception, Google Earth has been adopted with great enthusiasm by geoscientists (e.g. *Butler* [2006]) and it has been widely used in geographical and geological education (e.g. *Stahley* [2006]; *Patterson* [2007]; *Rakshit and Ogneva-Himmelberger* [2008, 2009]). *Cruz and Zellers* [2006] have established its efficacy for the study of landforms. COLLADA models have been used in conjunction with Google Earth by *De Paor and Whitmeyer* [2008]; *De Paor et al.* [2009]; *Selkin et al.* [2009]; *Brooks and De Paor* [2009]; *Pence et al.* [2010]; *Whitmeyer et al.* [2011]; *Gobert et al.* [2012]. Anecdotally, students in several of our classes have reacted positively to the tactile nature of the process of lifting blocks out of the subsurface. They seem to "get it." However, in order to spur further evaluation studies, there needs to be a greater cohort of academics who create and distribute learning resources for Google Earth using COLLADA and KML.

Previous studies have documented the benefits of learning with visualizations in general by *Kali et al.* [1997]; *Orion et al.* [1997]; *Reynolds et al.* [2005] and specifically with Geographic Information Systems by *Hall-Wallace and McAuliffe* [2002]. There are also many studies of the positive role of student research projects in undergraduate education by *Libarkin* [2001]; *Jenkins et al.* [2007]. In some cases, instructors already know the right answers and by mentoring student inquiry rather than just lecturing, they help students to discover those answers. In other cases, questions are more open-ended and students discover new findings thereby acting as genuine researchers as well as learners. This paper presents a case where construction of engaging instructional resources blurred the boundary between academic education and research at the instructor level. It is commonly stated that one does not truly understand any topic until one is asked to teach it. Clearly, the process of preparing course materials is an important aspect of research and with modern methods of data mining and data visualization, teachers who are not topic experts have the opportunity to help promote not only their own comprehension but the research community's understanding also.

We a keenly aware of: 1) the potential of complex 3D visualizations such as Google Earth to cause visual overload and loss of attention [*Rensink et al.*, 1997; *Parkhurst*

et al., 2002; *Martin and Treves*, 2008]; and 2) the ease with which students can wander off task given simple mouse controls and a whole earth to explore. Adding emergent blocks to Google Earth helps solve the first problem by creating salience and a focal point for student attention. In separate lab exercises, we use the KML NetworkLink and FlyToView elements as a means of geo-fencing (e.g. *Rashid et al.* [2006]); when a student wanders away from the region the KML script automatically resets the view angle. Serendipitously, our solution to the Anti- meridian rendering problem in Google Earth (above) reduces visual overload by replacing the complexly overprinted surface imagery and 3D DEM with the simple NASA Blue Marble image of the Earth. *Simpson et al.* [2011] have taken the concept further by draping a plain beige image over all of the Google Earth surface except for the Archean Kaapvaal Craton which is their area of interest.

Given our recent courses, our classroom use of COLLADA models and Google Earth have been mainly with non-science majors, *Goodchild* [2006] has promoted the notion that general education requires geospatial reasoning as a "fourth R" in addition to reading, writing and arithmetic. Furthermore, there is no reason to believe that students majoring in geosciences and other geospatial disciplines would not benefit also. In a previous small (eight student) class of geoscience majors studying structural geology, a student questioned two weeks after the laboratory activity was able to correctly estimate crustal thickness as a proportion of the width of a block. This student might also have been able to give a numerical answer but evidently had developed a useful visually-based mental concept of scale.

We hope that the electronic media linked this paper will lead to widespread dissemination, implementation, and testing of our models in many settings and to the development of new COLLADA models in Google Earth by our colleagues in many second and third level educational institutions. Since Google Inc. handed control of KML to the open-source community, its free availability is ensured for the foreseeable future and it has the potential to be truly transformative in the field of geoscience modeling, education, and outreach [*De Paor*, 2011a,b; *De Paor and Whitmeyer*, 2011].

Having created and developed these visualization tools for exploring tectonic processes the next step is to develop and implement tests to study the validity of using Google Earth as an educational tool. Only by testing to measure learning outcomes can one determine if the visualizations have merit.

CHAPTER 3

TESTING GEOSCIENCE LEARNING WITH GOOGLE EARTH

In this chapter the process of measuring learning outcomes using the COLLADA models and Google Earth is described from the creation, implementation, and measuring learning gains. My involvement in the project was in developing the tests for the Tonga region, administration of both exams, and helping to develop and score the exams. The work reported in this chapter has been published in a GSA Special Paper on Google Earth and Virtual Visualizations (see *Gobert et al.* [2012]). As a co-author of this paper I contributed 35%.

3.1 ABSTRACT

Two sets of learning activities in Google Earth were developed for use by geoscience majors and non-science majors. The first activity aimed to foster undergraduate students' understanding of the geography and basic geology of Iceland. We tested the efficacy of this activity for learning with 300 undergraduates from a university in the southeastern part of the United States. In terms of post- versus pre-test scores we found: 1) overall learning gains when collapsing over type of prior knowledge and gender, 2) no differences in learning gains when comparing those with prior coursework in Geology or geography to other students without such prior coursework, and 3) no differences in learning gains when comparing males and females. In terms of items completed during the lab exercise, again we found no differences by prior coursework (prior Geology, prior geography, or None) and no differences by gender. Lastly, moderate positive correlations were found between students' pre-test and post-test scores, as well as between students' embedded lab scores and post-test scores.

For the second activity, we developed a laboratory activity about the classic Tonga region of the west Pacific in order to support undergraduate students' understanding of: 1) the physical geography of the Tonga Subduction System, 2) the dynamic

geological processes involved in plate movement, subduction, magmatic arc evolution, and trench rollback, and 3) geological processes resulting from subduction, including volcanism, and earthquake formation. Using the program called Google Sketch-Up, we created 3D COLLADA models that are viewable as 4D animations in the Google Earth API (a web based version of Google Earth) to help demonstrate several geophysical processes. These animations potentially have a wide range of learning application from basic to more abstract ideas. Specifically, the learning objects created involve the Pacific plate subducting underneath the Australian Plate in the Tonga Region; these are designed to help show subduction, active and dormant volcanoes, back-arc spreading, trench rollback, and migration of the tear point that marks the northern termination of the subduction system. We tested the efficacy of this activity with 127 undergraduates from a university in the southeastern part of the United States. In terms of post- versus pre- test scores we found: 1) overall learning gains, when collapsing over type of prior knowledge and gender, 2) no differences in learning gains when comparing those with prior coursework in Geology or geography to other students without this prior coursework; and 3) no differences in learning gains when comparing males and females. For the lab activity itself, we found no differences by prior coursework (Geology/geography versus None) but found a gender difference, favoring males, however this learning did not show up as statistically significant at post-test (as previously mentioned). Lastly, moderate positive correlations were found between students' pre-test and lab scores.

Data is discussed with respect to Google Earth's utility to convey basic geoscience principles to non-geology undergraduates and its potential impact on public understanding. This is important and aligned with many current educational reform efforts [*American Association for the Advancement of Science*, 1993; *National Research Council*, 1996], which call for broader scientific literacy.

3.2 INTRODUCTION

3.2.1 LEARNING IN THIS DOMAIN: WHY IS IT DIFFICULT?

The domain chosen for this study is plate tectonics, the lead paradigm for understanding the origin and evolution of Earth's surface features including continents, oceans, and island arcs. This is a difficult topic to learn both because of the hidden mechanical processes, which are outside our direct experience, and because it involves

several different types of knowledge including spatial, causal, and dynamic knowledge [*Gobert and Clement*, 1999; *Gobert*, 2000]. Specifically, conceptual understanding in this domain requires understanding the spatial arrangement of the various material components of the earth (i.e., spatial/static information) as well as understanding the movements within these layers and their dynamic causes (i.e., primordial Core) and radioactive sources of heat (i.e., mantle) that must escape the earth's deep interior [*KamLAND Collaboration*, 2011], convection of solid material through the mantle [*Wilson*, 1973], plate movements, divergence and convergence at plate boundaries, and the interaction of surface plates with deep mantle plumes [*Morgan*, 1972]. In addition to acquiring two types of knowledge (spatial/static and kinematic/dynamic), several concepts need to be integrated into a complex causal chain to build a rich four-dimensional mental model of the system [*Gobert and Clement*, 1999; *Gobert*, 2000]. From these mental models, predictions and inferences can be made about the system's behavior: in the case of plate tectonics, explaining or depicting locations of earthquakes and volcanoes, sea-floor spreading, mountain-building, and island arc evolution.

Among the most difficult concepts that we present to students are (i) plate-plume interaction as in Iceland [*Ito and Lin*, 1995], and (ii) trench rollback as in the Tonga region [*Isacks et al.*, 1968]. Iceland stands high above sea-level because it marks the intersection of the Mid-Atlantic Spreading Ridge and a Deep Mantle Plume emanating from the core-mantle boundary. Students thus have to visualize two processes with very different length and time scales; time scale is particularly difficult to understand, even for graduate students of Geology [*Jacobi et al.*, 1996]. Tonga is the type locality for the process of trench rollback whereby the line along which the plate bends into a subduction zone migrates in the opposite direction to the material of the plate [*Uyeda and Kanamori*, 1979; *Moores and Twiss*, 1995; *Rosenbaum and Lister*, 2004]. At Tonga, for example, the rocks of the Pacific plate move westward whilst the trench marking the initiation of subduction migrates east.

3.2.2 RELEVANT WORK ON LEARNING IN GEOSCIENCE

Google Earth, a fairly new program (version 1 was released in 2005), constructs pictures of the earth by downloading satellite data from a remote terabyte server [*Lisle*, 2006] and rendering them on a virtual globe in real time. The program is interactive so that the location and size of the region viewed is under full control of

the learner/user; the user can zoom in, pan, and tilt the terrain from any desired viewpoint, and the surface imagery communicates information in a format that is more intuitive and realistic than paper maps and cross-sections [*Whitmeyer et al.*, 2010]. This last feature makes them useful for learning and reasoning for experts in the domain, as well as for students and lay people, e.g. non-science majors (this is addressed more fully later in the paper).

It is argued that Google Earth is a tool that can help build scientific literacy on a broad scale because it and other geo-technologies are ways to give citizens basic knowledge of geography [*Sanchez*, 2009] and geoscience [*Thompson et al.*, 2006]. Secondly, in addition to basic content knowledge, some researchers claim that working in Google Earth can hone one's data analysis and interpretation skills, which, many argue, are becoming increasingly important in scientific and industrial fields. As an extension to this latter point, it has been further argued that the ability to use images and spatial technologies is necessary in order to participate in modern society [*Bednarz et al.*, 2006] since information and data tends to be displayed in spatially-oriented formats.

To date, there have been a fairly large number of studies that address learning in geoscience, but most of these have been conducted with a pre-college population [*Libarkin and Anderson*, 2005], and studies on college students or other adults only emerged within the last decade or so [*DeLaughter et al.*, 1998; *Trend*, 2000; *Libarkin*, 2001; *Libarkin and Anderson*, 2005; *Dahl et al.*, 2005]. Amongst the research on this topic with an adult population, the research that is most closely related to the present research is the research on learning with visualizations in geoscience [*Hall-Wallace and McAuliffe*, 2002; *Thompson et al.*, 2006; *Whitmeyer et al.*, 2009].

With respect to training students in geoscience specifically, recent reform efforts emphasize the need to utilize technology in teaching and learning [*Stout et al.*, 1994; *National Research Council*, 1996], which has translated into greater demand for technology-based teaching methods [*Cruz and Zellers*, 2006]. In parallel, there also have been demands for greater instructor accountability for students' learning at all levels, as decreasing enrollment trends continue in the STEM disciplines [*McConnell et al.*, 2006]. Although learning with Google Earth has been touted as having great potential for improving students' knowledge about geological phenomena, spatial skills, problem-solving, etc., and the fact that, intuitively it appears to have many affordances for geoscience learning [*Cruz and Zellers*, 2006; *Whitmeyer et al.*, 2009],

there are relatively few studies that either characterize the learning processes that students engage in while learning with Google Earth, or that address the efficacy of learning with Google Earth.

Characterizing learning processes with Google Earth, it has been noted that Google Earth (GE) offers a benefit over more traditional GIS in that Google Earth can be implemented into classrooms at any level because it has relatively few tools and thus less overhead for the teacher in learning it [*Patterson*, 2007; *Bodzin et al.*, 2012]. In terms of the utility of Google Earth for college professors and high school teachers, Google Earth only requires a basic knowledge of scripting languages in order to construct materials [*Whitmeyer et al.*, 2010]. For example, Google Earth has been used in high school classrooms for virtual exploration of geologic features to support students' understandings of geological processes [*Fermann*, 2006; *Stahley*, 2006]. Similarly, [*Sanchez*, 2009] describes implementations in which a teacher developed a geological map that encompasses layers of data about earthquakes and volcanoes. Here, it was suggested that these help students to identify different aspects of oceanic crust formation and understand the mid ocean ridge system. Lastly, [*Patterson*, 2007], who has used Google Earth for middle school instruction, suggested that Google Earth's interactive exploration capacity helps students understand the spatial context of their location and engage in spatially-oriented learning in an entertaining and meaningful manner.

In terms of studies that have addressed the efficacy of Google Earth, one study compared GE to traditional textbook materials for undergraduates' learning of landforms [*Cruz and Zellers*, 2006]. Findings revealed that students in the GE condition gained deeper understanding of the content compared to those in the traditional textbook condition. Furthermore, those students who had previous exposure to GE performed better than those who did not. Similarly, *Martin and Treves* [2008] showed that GE is effective to help students and the general public (i.e., non-majors) visualize both scientific data and science content in 3D. Martin and Treves stressed the importance of promoting active learning, and dissuaded the development of "flashy " 3D animations, since students, who by definition lack expertise, do not know what is salient in order to engage in knowledge acquisition from information sources [*Gobert*, 2005a]. *Bodzin and Cirucci* [2009] similarly, noted that resources such as GE, when used in conjunction with appropriately designed instructional materials, show much potential in promoting students' spatial thinking.

In two innovative studies in which students constructed their own materials using GE, learning gains were obtained. First, *Whitmeyer et al.* [2009] had undergraduates use handheld computers to collect lithologic and structural data, and then analyze it in order to construct geologic maps of their field areas. This approach, according to the authors, familiarizes students with GE tools, and in turn, can be useful in improving students' interpretations of field geology. Similar results have been found in which students constructed their own representations of geoscientific phenomena [*Gobert and Clement*, 1999; *Gobert*, 2000; *Gobert and Pallant*, 2004; *Gobert*, 2005b]. In another study, *Thompson et al.* [2006] showed students how to create their own content in GE. Here, not only did students learn important design elements and skills; students reported that these skills were amongst the most important that they learned in their geoscience program.

These last studies described address an important issue underlying learning with visualizations; that is, that deep learning with visualizations typically requires accompanying materials, scaffolds, etc., in order to support and guide students in their learning processes. This is critical since students often do not know what is salient within these rich visual information sources [*Lowe*, 1993] since they present all information simultaneously (see *Larkin and Simon* [1987]; *Gobert* [2005a] for more on this topic).

3.3 RATIONALE

In our project, we address the learning gains for two different units developed in Google Earth. In particular, in each study we address their efficacy for those with prior coursework in Geology and geography, compared to non-majors with no prior coursework in these domains. Secondly, although it was not part of the original design of the research, we compare the learning gains of both males and females, since many studies have shown that females lag behind males in their learning of geoscience concepts due to their inherent spatial nature and females' oft-reported diminished spatial skills [*Kahle et al.*, 1993; *Burkam et al.*, 1997; *Dabbs et al.*, 1998; *Britner*, 2008].

3.4 STUDY 1

3.4.1 PURPOSE

In the first study we developed a Google Earth activity to support students' understanding of the geography and basic geology of Iceland. We tested the efficacy of this activity in terms of post- versus pre-test scores for: 1) overall learning gains as measured by pre- post-tests, 2) differences in learning gains when comparing those with prior coursework in Geology or geography to other students without such prior coursework, and 3) differences in learning gains when comparing males and females. Lastly, we also compared students' learning on the lab activity itself, i.e., the pedagogical activities that were completed as part of the lab.

3.4.2 METHOD

Participants. A total of [N = 225] undergraduate students from a southeastern university participated in this study as part of their coursework[1]; age data for the participants was not collected. All students were part of the same large lecture; there were nine sections of the lab that corresponded to the lecture, from which our data was drawn.

3.4.3 MATERIALS

3.4.3.1 PRE-TEST/ POST-TEST

The pre-test and post-test consisted of the same set of 10 questions on basic geological and geographical knowledge of Iceland as well as one question asking about prior experience studying this topic. Of these questions, 9 were multiple choice, and one asked participants to locate Iceland on a provided map. The pre-test served to determine a baseline of prior knowledge that a participant had coming into the activity, while the post-test determined what knowledge was gained as a result of participating in the lab activity. All items were developed by experts in the area of geoscience as part of three on-going projects (NSF-CLLI #0837040 [*De Paor and*

---

[1]Data were collected, coded, and stored in compliance with the requirements as outlined by Federal Policy for the Protection of Human Subjects under JMU IRB #11-0114 and ODU IRB #10-186.

Whitmeyer, 2008], NSF-GEO #1034643 [*De Paor et al.*, 2010a], NSF-DUE #1022755 [*De Paor et al.*, 2010b]). Some examples of items on the pre- and post-test are given below; the full set of items is included in Appendix A.

Q8 What is the principle rock type seen in Iceland?

    (i) limestone
    (ii) basalt
    (iii) granite
    (iv) marble

Q9 Which best describes the geological origins of Iceland?:

    (i) Iceland sits on top of both a deep mantle plume and a divergent plate boundary
    (ii) Iceland is a fragment of continental crust, like Britain and Ireland, that detached from the European margin during North Atlantic spreading
    (iii) Iceland is a volcanic island arc forming above a subduction zone
    (iv) Iceland is a huge floating mass of ice drifting very slowly away from Greenland

Figure 29. An example of two questions from the pre- and post-test, Iceland activity.

3.4.3.2 LAB ACTIVITIES FOR ICELAND

The Iceland lab activity consisted of a series of tasks that were designed to develop students' understanding of the geography and Geology of Iceland. Tasks included: locating Iceland in Google Earth, specifying its relationship geographically with respect to the Arctic Circle, using the time slider to observe the horizon, asking students what they would expect to see here at the Winter Solstice, observing the landscape, geological features (e.g. rock types), and other characteristics of Iceland's urban and rural landscapes by driving around in a virtual car, observing the formation of the Mid-Atlantic ridge by using a time slider, noting how the Mid-Atlantic ridge is displaced across the Gibbs Fracture Zone, and observing the deep mantle plume under Iceland.

3.4.4 PROCEDURE

Students initially were given consent forms, with verbal explanation, and a tracking ID assigned. ID numbers were based on the course lab number, the beginning five digits, and then some digits after that given by the lab teaching assistant. Students were informed to not use their university identification numbers. Labs and pre/post

> 18.1 Wait for the images to load, then drag the time slider in order to reveal the deep mantle plume under Iceland. (Fig. 15).
>
> ● Compare the height (thickness) of the plume the the thickness of the lithosphere:
>
> ....
>
> ● Estimate how deep does the plume extend
>
> ....

Figure 30. An example of a question asked in the Iceland lab activity.

tests with university identification numbers were not used and removed from the study. Once the consent forms were completed and tracking identification numbers administered, each student was given a pre-test. If students finished their pre-test early, they were asked to wait quietly while others finished.

The students worked in groups of 2-4 depending on the lab section, with lab sections having different numbers of students. Students were encouraged, sometimes with help from instructors, to take turns working on the computers. Instructors were only allowed to help if students had technical problems but not with lab material itself. The students were informed that the lab itself would not be graded as part of their lab score, which may have had an effect on the way students answered questions or participated during lab. As students completed the labs, they were collected and the students were asked to wait for their fellow classmates to finish.

The last part of the lab consisted of the post-test. The post-test is the same as the pre-test. Each student was given a post-test and upon completion was allowed to leave the lab. No collaboration was allowed during the pre/post tests. The pre-test, lab activity, and post-test were all completed in one, two- hour lab period.

3.4.5 DATA SCORING

3.4.5.1 PRE- AND POST-TEST SCORING

The pre- and post-tests consisted mainly of multiple choice questions and were scored on a partial- or full-credit basis. A participant could earn a maximum of 2 points on each question for choosing the correct answer, 1 point for choosing a

partially correct answer, and 0 for choosing an incorrect answer. Some questions had more than one possible answer worth 1 point, as shown in Figure 31 below. Answer "iii" is worth 2 points, answers "i," "iv," or "v" are each worth 1 point, and answer "ii" is worth 0 points.

Q2 Where is Iceland relative to the Arctic Circle?	Scoring Q2	
(i) Iceland lies entirely south of the Arctic Circle	i.	1
(ii) Iceland lies entirely north of the Arctic Circle	ii.	0
(iii) The Arctic Circle touches the northern coast or offshore islands	iii.	2
(iv) The Arctic Circle touches the southern coast or offshore islands	iv.	1
(v) The Arctic Circle goes through the center of Iceland	v.	1

Figure 31. Question 2 and its coding scheme for the Iceland activity.

3.4.5.2 LAB ITEMS SCORING

The lab activity consisted of 7 open response or "yes/no" questions, which were scored on a partial credit basis out of a possible 1, 2, or 3, depending on the question. The scoring scheme for a 3-point question is shown below in Figure 32. Each correctly circled answer earned 1 point, and the open response portion was scored as 0, .5, or 1 point based on accuracy and detail.

4.4 Visit various parts of Iceland and record your first impressions of the country here:
Outside of Reykjavik, is Iceland heavily populated / developed? ● [Yes / No]
Do you see a lot of large-scale agricultural or industrial plant? ● [Yes / No]
● How would you describe the terrain?
un-developed or under-developed or poor land or barren or isolated or partly farmed or grassland or tundra or equivalent

Figure 32. Question 4.4 and its coding scheme for the Iceland activity.

3.4.6 RESULTS

Data were analyzed to address overall learning gains from the Iceland lab, as measured by pre- and post-tests, as well as to test whether there were any learning

gain differences due to prior coursework in Geology/geography. Gender differences were also analyzed although this was not part of the original design of the study. Lastly, data were analyzed with respect to learning during the lab activity itself. Each analysis is presented and described in turn. The unit of analysis here was data from each individual student.

Were there differences by prior coursework or gender before the Iceland learning activity with Google Earth? First, we addressed if there were any differences on the pre-test both by prior coursework and by gender. A univariate analysis of variance was computed for each of these analyses. First, the difference between the total scores on the pre-test was not statistically different when comparing those with prior coursework to those with no prior coursework (F = 1.838, p = .162). Secondly, the difference on the total pre-test score was not statistically different when comparing males and females (F = 1.890; p = .154). See Table 1 for means and standard deviations for each of these analyses[2].

Table 1. Average scores on pre-test by total, gender, and prior coursework for the Iceland activity

	Overall	Female	Male	Geolgeog	No Geo/Geog
Mean Pre-test Score	6.69	6.32	7.05	7.44	6.57
Standard Deviation (SD)	2.95	2.52	3.44	3.37	2.57

Did the Iceland activity yield differences in overall pre-post comparisons? Next we addressed if there were differences in overall post-test scores compared to pre-test scores collapsing over both prior coursework and gender categories. A paired t-test was computed for this analysis. The difference in overall pre-test score and overall post-test score was statistically significant, (t(224) = 13.33, p = .000; X pre = 6.69, SD = 2.95; X post = 9.68, SD = 3.58); this result demonstrates that on average, students had higher scores on the post-test than on the pre-test. See Table 2 and Figure 33.

Table 2. Comparing overall scores for pre- and post-test for the Iceland activity

	Pre-test	Post-test	t (df)	P
Mean Pre-test Score	6.69	9.68	13.329 (224)	.000
Standard Deviation (SD)	2.95	3.58		
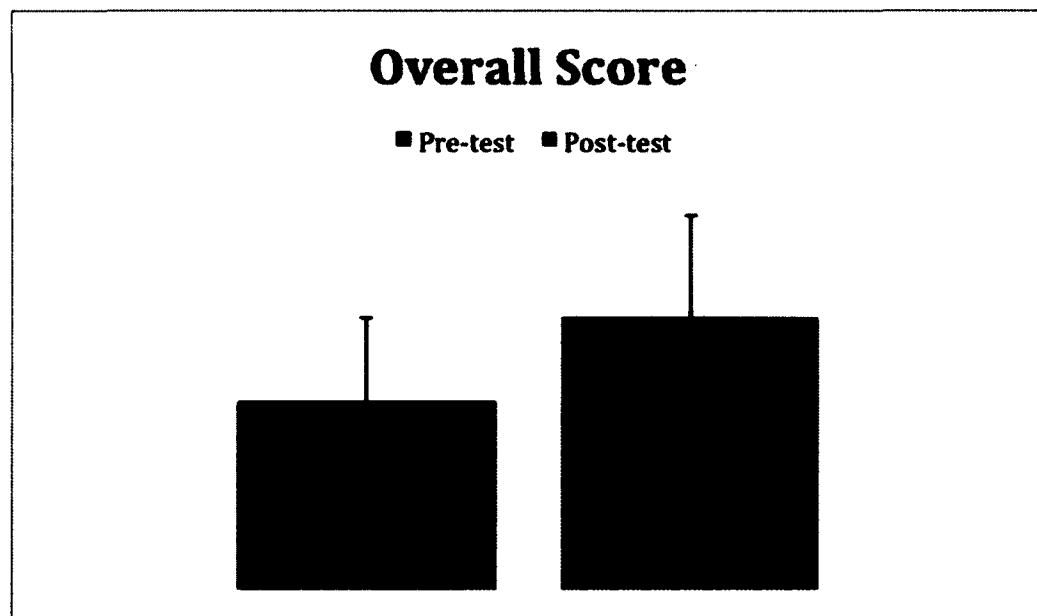
Figure 33. Overall scores on both pre-test and post-test for the Iceland activity.

Table 3. Average scores on pre-test and post-test for the Iceland activity by type of prior coursework

	Geolgeog	No Geo/Geog
Mean Pre-test Score	7.44	6.57
Standard Deviation (SD)	3.37	2.57
Mean Post-test Score	10.78	9.57
Standard Deviation (SD)	2.95	3.58

Did type of prior coursework influence learning in the Iceland activity? In order to address whether there were differences between the pre- and post-test scores when comparing those with prior coursework in Geology or geography to those with no relevant prior coursework, a univariate analysis of variance was conducted with the total post-test as the dependent variable and type of prior coursework as the independent variable; pre-test was used as a covariate. The difference in post-test score by level of prior coursework was not statistically significant ($F = 2.107$; $p = .124$). Thus, both students with prior Geology or geography coursework and those without this prior coursework learned approximately the same amount of content knowledge from the Google Earth Iceland activity, as measured by the post-test gains. The means and standard deviations can be seen in Table 3.

Were post-test differences by gender yielded for the Iceland activity? In order to address whether the overall pattern observed was when comparing males and females, a univariate analysis of variance was conducted with the total post-test as the dependent variable and gender as the independent variable; pre-test was used as a covariate. The difference in post-test minus pre-test scores by gender was not significant ($F = .436$; $p = .647$). Thus, both males and females learned approximately the same amount of content knowledge, as measured by the post-test, holding the effects of the pre-test score constant. The means and standard deviations can be seen in Table 4.

---

[2]Although the means appear different when both comparing males and females, and when comparing those with prior relevant coursework to those with no relevant prior coursework, the standard deviations associated with these means indicates that the dispersion of scores was large in both cases, thus no statistically reliable differences were found for either comparison.

Table 4. Average scores on pre-test and post-test for the Iceland activity by gender

	Female	Male
Mean Pre-test Score	6.32	7.05
Standard Deviation (SD)	2.52	3.44
Mean Post-test Score	9.37	10.21
Standard Deviation (SD)	3.30	3.84

Were there any differences on the lab scores for the Iceland activity when comparing by prior coursework or by gender? Next we addressed the differences on the lab activity scores both by prior coursework and by gender; in other words, whether there was a difference on students' performance in the lab activity by prior coursework in Geology/geography, or by gender. A univariate analysis of variance was computed for each of these analyses. There was no statistically significant difference found between the total scores on the lab activity when comparing those with prior coursework to those with no prior coursework (F = .069, p = 0.934). Additionally, the difference on the total score for the lab activity was not statistically significant when comparing males and females (F = 1.109, p = .332). This result demonstrates that on average, males and females scored similarly on the lab activity. See Table 5.

Table 5. Average scores on the Iceland lab activity by gender and prior coursework

	Female	Male	Geolgeog	No Geo/Geog
Mean Pre-test Score	4.36	4.69	4.51	4.55
Standard Deviation (SD)	1.62	1.87	1.52	1.77

Is there a relationship between the pre-test scores, the lab scores, and the post-test scores for the Iceland activity? In order to establish whether there was a relationship between these learning measures, a Pearson correlation analysis was conducted between all the measures, namely, the pre-test, the lab scores, and the post-test. A statistically significant correlation was found between the pre-test and post-test (r = 0.483, p = 0.000, (2-tailed)), indicating a moderate, positive relationship between the pre-test and the post-test. Another statistically significant correlation was found

between the lab scores and the post-test, r = 0.291, p = 0.000, (2-tailed). The Pearson correlation values can be seen in Table 6. No statistically significant correlation was found between the pre-test score and the lab scores (r =.101, p = .132, (2 tailed). The scatterplots for pre-test and post-test, and pre-test and lab scores can be seen in Figures 34 and 35, respectively.

Table 6. Pearson correlation values between pre-test, post-test, and lab scores for the Iceland activity. *Significant at the p < 0.01 level

	Pre-test	Post-test	Lab
Pre-test	1	0.483*	0.10
Post-test	0.483*	1.87	2.91*
Lab	0.101	.291*	1
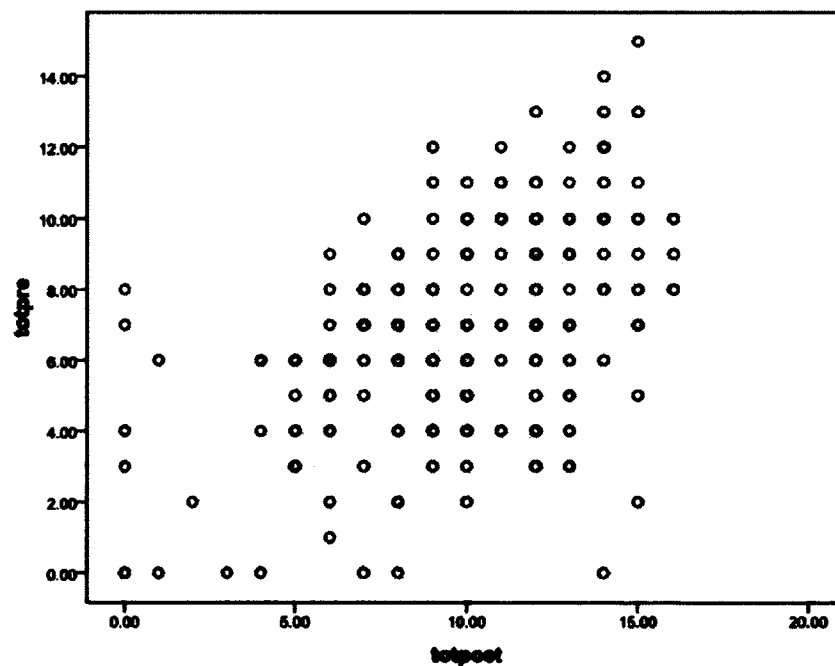
Figure 34. Scatterplot of correlation between total pre-test scores and total post-test scores for the Iceland activity.
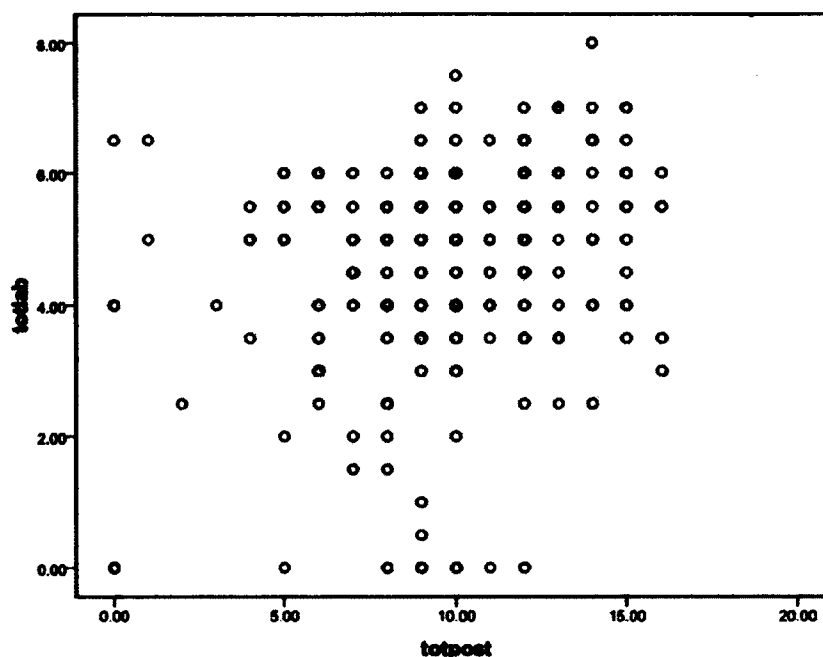
Figure 35. Scatterplot of correlation between total lab scores and total post-test scores for the Iceland activity.

3.5 STUDY 2

3.5.1 PURPOSE

In Study 2, we developed a laboratory activity focused on the classic Tonga region of the west Pacific in order to support undergraduate non-geology majors' understanding of: 1) the geographical layout of the Tonga Subduction System, 2) the dynamic geological processes involved in plate movement, subduction, magmatic arc evolution, and trench rollback, and 3) geological processes related to subduction, including volcanism, and earthquake formation.

3.5.2 METHOD

A total of [N = 138] undergraduate students from a southeastern university participated in this study[3]; age data for the participants were not collected. All students

---

[3]Data collected, coded, and stored in compliance with requirements outlined by Federal Policy for the Protection of Human Subjects under JMU IRB #11-0114 and ODU IRB #10-186.

were part of the same large lecture; there were nine sections of the lab that corresponded to the lecture, from which our data were drawn.

3.5.3 MATERIALS

3.5.3.1 PRE-TEST/POST-TEST

The pre-test and post-test consisted of the same set of 11 questions on basic geological and geographical knowledge of the American-Samoa/Tonga region as well as one question asking about prior experience studying this topic. Of these questions, 9 were multiple choice, one asked for the order of four listed events, and one asked participants to locate American-Samoa/Tonga on a map that was provided to them. All items were developed by experts in the area of geoscience as part of three ongoing projects (NSF-CLLI #0837040 [*De Paor and Whitmeyer*, 2008] , NSF-GEO #1034643 [*De Paor et al.*, 2010a], NSF-DUE #1022755 [*De Paor et al.*, 2010b]). The pre-test served to determine a baseline of prior knowledge for each participant, while the post-test determined what knowledge gains were made after participating in the lab activity.
See Figures 36 and 37 for sample items; all items are shown in Appendix B.

3.5.3.2 LAB ACTIVITIES FOR TONGA

The Tonga lab activity consisted of a series of tasks that were designed to develop students' understanding of the geology of the Tonga region in the western Pacific Ocean. Tasks included: locating the Tonga Region with respect to the Tropic of Capricorn, viewing and manipulating virtual block diagrams to observe animations of subduction, island arc formation, and trench migration, answering questions about the relative location of volcanoes and earthquakes, and answering questions about plate movement, trench formation, and plate movement and trench rollback.

3.5.4 PROCEDURE

The process of gathering student performance was done in the following manner. Students initially were given consent forms, with verbal explanation, and a tracking ID assigned. Identification numbers were based on the course lab number, the beginning five digits, and then some digits after that given by the lab teaching assistant.

Figure 36. An example of a question from the pre- and post-test for the Tonga activity.

Figure 37. An example of two questions asked in the pre- and post-test for the Tonga activity.

Students were informed to not use their university identification numbers. Labs and pre/post tests with university identification numbers were not used and removed from the study. Once the consent forms were completed and tracking identification numbers administered each student was given a pre-test. If students finished their pre-test early, they were asked to wait quietly while others finished.

The lab only has 10 Mac books available for use, thus, students worked in groups of 2-4 depending on the lab section, with all lab sections having different numbers of students. Students were encouraged, sometimes with help from instructors, to take turns working on the computers. Instructors were only allowed to help if students had technical problems but not with lab material itself. The students were informed that the lab itself would not be graded as part of their lab score, which may have had an effect on the way students answered questions or participated during lab. As students completed the labs, they were collected and the students were asked to wait for their fellow classmates to finish.

The last part of the lab consisted of the post-test. The post-test is the same as the pre-test. Each student was given a post-test and upon completion was allowed to leave the lab. No collaboration was allowed during the pre/post tests. The pre-test, lab activity, and post-test were all completed in one, two-hour lab period.

3.5.5 DATA SCORING

3.5.5.1 PRE- AND POST-TESTS

The pre- and post-tests consisted mainly of multiple choice questions and were scored on a partial- or full-credit basis. A participant could earn a maximum of 2 points on each question for choosing the correct answer, 1 point for choosing a partially correct answer, and 0 for choosing an incorrect answer. Some questions had more than one possible answer worth 1 point, as shown in Figure 38 below. Answer "iii" is worth 2 points, either answers "i" or "ii" are worth 1 point, and answer "iv" is worth 0 points.

The four choices for the question asking about the participant's prior knowledge on the subject were coded for categorization purposes as either 0, 1, 2, or 3. This scheme is illustrated in Figure 39.

Q6 The Tonga Trench's motion relative to the Pacific Plate is		Scoring Q6	
(i)	Moves forward with the Pacific Plate	i.	1
(ii)	Stationary (trench does not move).	ii.	1
(iii)	Moves against Plate Motion.	iii.	2
(iv)	There is no such thing as the Tonga Trench.	iv.	0

Figure 38. Question 6 and its coding scheme for the Tonga activity.

Q 1 What is your previous experience of the geology or geography of American-Samoa/Tonga?		Scoring Q1	
	(i) I have no significant previous study experience	i.	0
	(ii) I did a class project about the geology or geography of American-Samoa/Tonga	ii.	1
	(iii) I participated in a real field trip or a holiday visit	iii.	2
	(iv) I am Native to or lived in the American-Samoa/Tonga region for an extended period	iv.	3

Figure 39. Question 1 and its coding scheme for the Tonga activity.

3.5.5.2 LAB ITEMS SCORING

The lab activity consisted of 13 open response or matching questions, which were scored on a partial- or full-credit basis out of a possible 1, 2, or 3, depending on the question. These questions ranged on topics covered in the activity including plate movement, subduction processes, and trench formation. See Figures 40 and 41.

Q4 On which side of the trench do we expect to see earthquakes on, the down-going plate (on the east side of the trench in this case) or the over-riding plate (on the west side of the trench in this case)?
over-riding plate or west side (1pt)

Figure 40. Question 4 and its coding scheme for the Tonga activity.

3.5.6 RESULTS

Data were analyzed to address overall learning gains from the Tonga lab, as measured by pre- and post-tests, as well as to test whether there were any learning gain differences due to prior coursework in geology/geography. Gender differences
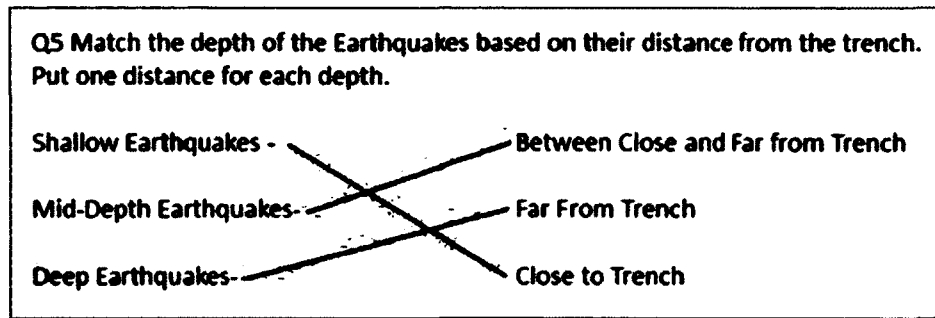
Figure 41. Question 5 and its coding scheme (1 point for each proper match) for the Tonga activity.

were also analyzed although this was not part of the original design of the study. The unit of analysis here was data from each individual student. Each analysis is presented and described in turn.

Were there differences by prior coursework or gender before the Tonga learning activity with Google Earth? We first addressed if there were any differences on the pre-test by prior coursework and by gender; in other words, whether there was a difference on students' knowledge going into the pre-test either by prior coursework in Geology/geography, or by gender. A univariate analysis of variance was computed for each of these analyses. The difference between the total scores on the pre-test was not statistically significant when comparing those with prior coursework to those with no prior coursework (F = 3.052, p = .051). Secondly, there was no statistically significant difference on the total pre-test score when comparing the males and females (F = 1.831; p = .179; see footnote 1 here). See Table 7 for means and standard deviations for each of these analyses.

Table 7. Average scores on pre-test by total, gender, and prior coursework for the Tonga activity

	Female	Male	Geolgeog	No Geo/Geog
Mean Pre-test Score	0.88	0.80	0.86	0.85
Standard Deviation (SD)	0.36	0.31	0.25	0.36
Mean Post-test Score	1.13	1.07	1.03	1.12
Standard Deviation (SD)	0.37	0.39	0.39	0.35

Were differences in overall pre-post comparisons found for the Tonga activity? Next we addressed if there were differences in overall post-test scores compared to pre-test scores collapsing over prior coursework and gender. A paired t-test was computed. The difference in overall pre-test score and overall post-test score was statistically significant, $(t(136) = 6.591, p = .000;$ X pre $= 0.82,$ SD $= 0.35;$ X post $= 1.09,$ SD $= 0.38);$ this result demonstrates that on average, students had higher scores on the post-test than on the pre-test. See Table 8 and Figure 42.

Table 8. Overall scores for pre- and post-test for the Tonga activity. *Significant at the p < .001 level

	Pre-test	Post-test	t (df)	P
Mean Pre-test Score	0.82	1.09	6.591 (136)	0.000*
Standard Deviation (SD)	0.35	0.38		

Overall Score
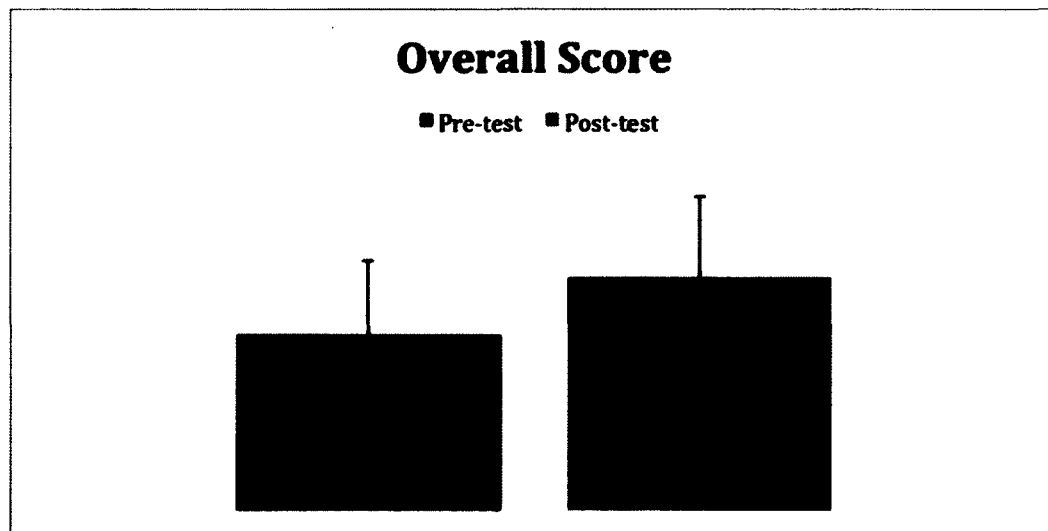
■ Pre-test ■ Post-test

Figure 42. Overall scores on both pre-test and post-test for the Tonga activity.

Were post-test differences by type of prior coursework found for the Tonga activity? We addressed whether there were differences between the pre- and post-test scores when comparing those with prior coursework in Geology or geography to those with no relevant prior coursework. To do this, we conducted a univariate analysis of

variance with the total post-test as the dependent variable and type of prior course-work as the independent variable; pre-test was used as a covariate. The difference in post-test score by type of prior coursework was not statistically significant (F = .692; p = .502). Thus, both students with prior coursework and those without prior coursework learned approximately the same amount of content knowledge from the Tonga lab, as measured by the post-test, when holding the pre-test scores constant. The means and standard deviations can be seen in Table 9.

Table 9. Average scores on pre-test and post-test for the Tonga activity by type of prior coursework

	Geolgeog	No Geo/Geog
Mean Pre-test Score	0.86	0.85
Standard Deviation (SD)	0.25	0.36
Mean Post-test Score	1.03	1.12
Standard Deviation (SD)	0.39	0.35

Were post-test differences by gender found for the Tonga activity? In order to address whether there were differences when comparing males and females on their post-test scores for the Tonga activity, a univariate analysis of variance was conducted with the total post-test as the dependent variable and gender as the independent variable; pre-test was used as a covariate. The difference in post-test score by gender was not significant (F = .545; p = .462). Thus, both males and females learned approximately the same amount of content knowledge, as measured by the post-test. The means and standard deviations can be seen in Table 10.

Table 10. Tonga activity results of average scores on pre-test and post-test by gender

	Female	Male
Mean Pre-test Score	0.88	0.80
Standard Deviation (SD)	0.36	0.31
Mean Post-test Score	1.13	1.07
Standard Deviation (SD)	0.39	0.39

Were there any differences on the lab scores for the Tonga activity when comparing groups by prior coursework or by gender? Next we addressed the differences on the lab activity scores both by prior coursework and by gender; in other words, whether there was a difference on students' performance in the lab activity by prior coursework in Geology/geography, or by gender. A univariate analysis of variance was computed for each of these analyses. The difference between the total scores on the lab activity was not statistically significant when comparing those with prior coursework to those with no prior coursework ($F = 0.738$, $p = 0.480$); however, the difference on the total scores on the lab activity was statistically significant when comparing males and females ($F = 8.463$, $p = 0.004$). This result demonstrates that on average, males outperformed females on the lab activity. See Table 11 and Figure 43.

Table 11. Average scores on the Tonga lab activity by gender. *Significant at the $p < 0.005$ level

	Female	Male	p
Lab Score	9.85	11.07	.004*
Standard Deviation (SD)	3.40	2.20	
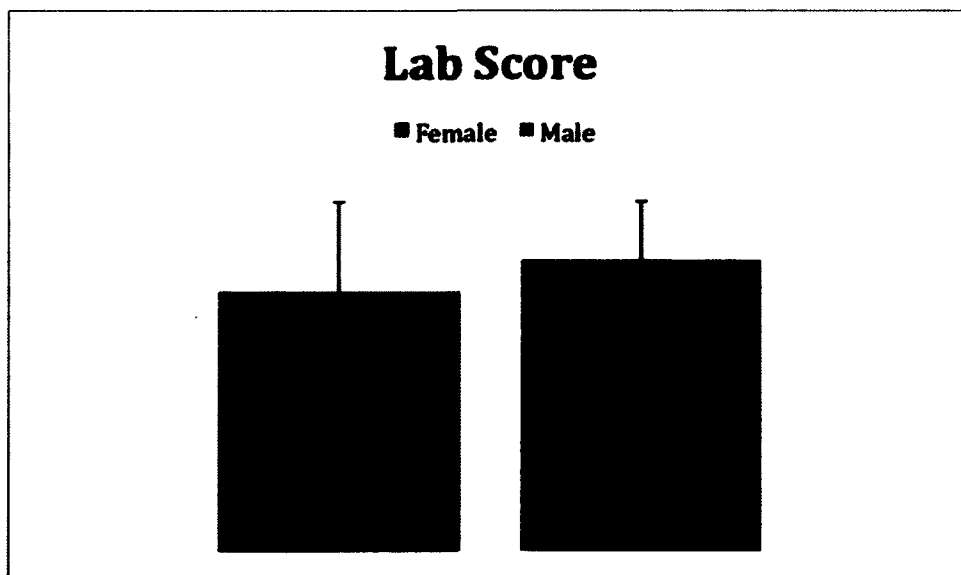
Figure 43. Total lab score by gender for the Tonga activity.

Were there any correlations between pre-, lab, and post-test scores? In order to establish whether there was a relationship between each of the three scores, a Pearson correlation analysis was conducted using the pre-test, post-test, and lab scores. A statistically significant correlation was found between the pre-test and lab scores (r = 0.384, p = 0.000, (2-tailed)), indicating a moderate, positive relationship between pre-test and lab scores. Pearson correlation values can be seen in Table 12. These results are depicted in Figure 44.

Table 12. Pearson correlation values between pre-test, post-test, and lab scores for the Tonga activity. *Significant at the p < 0.01 level

	Pre-test	Post-test	Lab
Pre-test	1	0.123	0.384*
Post-test	0.123	1	0.153
Lab	0.384*	0.153	1

3.6 DISCUSSION

3.6.1 SUMMARY OF GOALS AND APPROACH

In this research and development effort, we report on two studies that examined the efficacy for learning with Google Earth lab activities. This involved examining students' prior knowledge, their knowledge acquired during the lab activity, and their post-test learning gains, thereby examining both the processes (answers to the lab exercises) and products of learning (post-test compared to pre-test); an approach that is important since it has the potential to inform instruction in the geosciences [*Libarkin and Anderson*, 2005].

Our goal in these studies was to compare learning during the lab activity, as well as the resulting learning gains by comparing pre- and post-test scores for those with prior Geology and/or geography coursework to those with no such prior coursework. This research question is important in terms of addressing the efficacy of Google Earth as a learning tool for both majors and non-majors since Google Earth is potentially important to scientific literacy on a broad scale [*American Association for the Advancement of Science*, 1993; *National Research Council*, 1996]. Our findings suggest
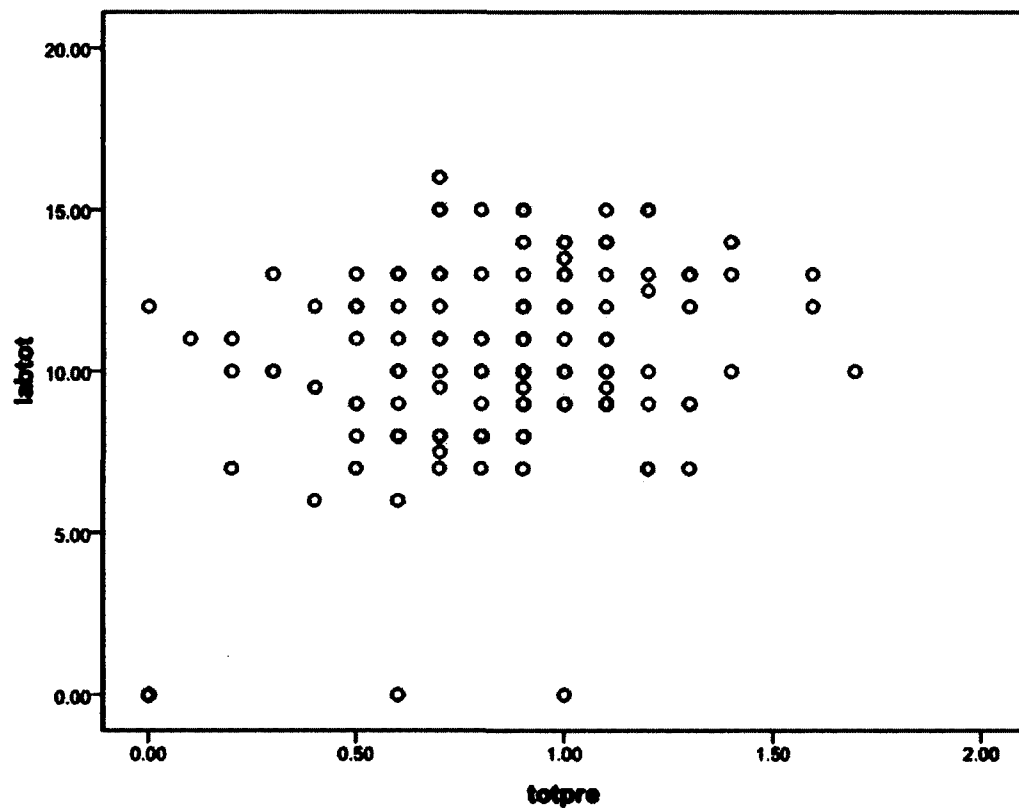
Figure 44. Scatterplot of correlation between total lab scores and total pre-test scores for the Tonga activity.

that Google Earth can be an effective learning tool for non-majors, and thus, it also has potential efficacy for scientific literacy on a broad scale.

We also compared learning gains of males and females, although it was not part of the original research design. That is, since there have been a plethora of studies that have reported gender differences in science by *Maccoby and Jacklin* [1974]; *McGee* [1979]; *Linn and Petersen* [1985]; *Halpern and LaMay* [2000], and in geoscience in particular by *Downs and Liben* [1991]; *Schofield and Kirby* [1994]; *Kali and Orion* [1996]; *Piburn et al.* [2002], it was a research question that we could address in the present studies. Similar to the issues around the type of prior knowledge students have coming into our studies, addressing whether there are differential learning gains yielded by males versus females allows us to address the efficacy of Google Earth as a teaching tool for both genders. If gender differences were to be borne out, we as a community of educators would need to begin to think about how to scaffold different learners to accommodate these differences.

3.6.2 OVERVIEW OF FINDINGS REGARDING PRIOR COURSEWORK

In the first study, we used an activity developed in Google Earth by Declan De Paor and his group (*De Paor and Whitmeyer* [2008] NSF CLLI #0837040). The goal of this activity was to deepen students' understanding of the geography and geology of Iceland. The concepts and knowledge targeted here were: specifying Iceland's relationship geographically with respect to the Arctic Circle, using the time slider to observe the horizon, asking students what they would expect to see here at the Winter Solstice, observing geological features (e.g. rock types), observing the formation of the Mid-Atlantic ridge by using a time slider, noting how the Mid-Atlantic ridge is displaced across the Gibbs Fracture Zone, and observing the plate-plume interaction under Iceland. In the second study, we used an activity, also developed by *De Paor et al.* [2008], which was more difficult than the first activity in terms of the geoscience content it targeted. Specifically, the activity consisted of: locating the Tonga region with respect to the Tropic of Capricorn; viewing and manipulating virtual block diagrams to observe animations of subduction; island arc formation and trench migration; and answering questions about the relative location of volcanoes, earthquakes, plate movement, trench formation, plate movement, and trench rollback.

Our results for the two studies were highly similar and thus will be summarized together, except for one measure for which significant differences exist.

Our data for both studies showed that there were overall gains in learning when comparing all students' scores. Collapsing over type of prior coursework and gender, all students, on average, had higher post-test scores compared to their pre-test scores for both the Iceland activity as well as the Tonga activity. Since there were no group differences on the pre-test by either type of prior coursework or by gender for either the Iceland or the Tonga activities, we can attribute our post-test gains as being due to the Google Earth labs for Iceland and Tonga, respectively.

When analyzing post-test gains by type of prior coursework (geology/geography versus no prior coursework in either of these areas), we found that there were no significant differences, on average, for those with prior coursework in geology or geography when compared to those with no prior coursework in these areas for either the Iceland lab or the Tonga lab. This suggests that the two Google Earth labs were effective as learning activities, regardless of type of prior coursework.

This finding is important because prior studies that have used traditional methods of geoscience instruction often do not yield large learning gains [Hall-Wallace and McAuliffe, 2002; Libarkin and Anderson, 2005]. Furthermore, our findings are commensurate with prior research that showed that rich dynamic visualizations such as GIS and Google Earth are successful at remediating students' misconceptions about three-dimensional geoscience phenomena such as ocean ridges and tsunamis [Hall-Wallace and McAuliffe, 2002] ocean ridges were targeted in our activities in both the Iceland and Tonga activity. Findings from our studies suggest that Google Earth appears to provide a means of deep learning for students that does not hinge on prior coursework, thus our data suggest that GE is a useful tool for undergraduate education, regardless of prior relevant coursework. Thus, in terms of promoting scientific literacy, Google Earth may also be very effective with the general public, but additional research would need to be conducted since students in this study were self-selected by virtue of signing up for the geoscience course from which this subject population was drawn, and thus may have been favorably predisposed to this content, etc.

3.6.3 OVERVIEW OF FINDINGS REGARDING GENDER

When analyzing our post-test gains for each Google Earth activity by gender, we

see that males and females gained, on average, about the same amount of content from the activities. Furthermore, because there were no differences due to gender on the pre-tests scores for either activity (see [1] here), our data suggests that this effect is not due to differences that the students had before the activity. One gender difference, favoring males, was found for the Tonga lab on the items that were answered as students worked through the lab activity. Specifically, on the Tonga lab, the more difficult of the two labs, males outperformed females in terms of the number of correct items they answered. However, since there were no significant differences by gender yielded on the post-test for the Tonga activity, the differences favoring males on the lab items were not robust enough to be reflected in the males' post-test understanding.

These findings are important since many studies have shown that males tend to outperform females on spatially-oriented tasks (cf. *Maccoby and Jacklin* [1974]; *McGee* [1979]; *Linn and Petersen* [1985]; *Halpern and LaMay* [2000]). In geoscience in particular, few studies regarding gender effects have been conducted by *Downs and Liben* [1991]; *Schofield and Kirby* [1994]; *Kali and Orion* [1996]; *Piburn et al.* [2002] although researchers have noted a need to address the relationship of spatial skills to specific sciences, rather than as science in the aggregate [*Lau and Roeser*, 2002]. In terms of such studies, *Dabbs et al.* [1998] found that basic spatial skills contribute to geographical knowledge and that men tended to excel at mental rotation, whereas women tended to excel at object location. *Black* [2005] found a relationship between specific types of spatial skills, namely mental rotation, and Earth science misconceptions [*Black*, 2005]. *Black* [2005] hypothesized that mental rotation is required to visualize the position of objects from varying vantage points, and further that this is the type of mental rotation needed for understanding both seasonal change and phases of the moon, two areas in which significant misconceptions have been found. In terms of the present study, we found only one gender difference of the several measures taken, and as previously stated, this difference favoring males was not robust enough to be maintained, as evidenced by the lack of differences due to gender on the post-test. Thus, from our data, it appears that Google Earth does not offer a differential bias for one gender over another. Furthermore, since Google Earth has features that permit students to manipulate the tilt of the Earth in order to view it from different vantage points, Google Earth may have provided a means to support learners on this difficult task; the study by *Black* [2005] suggests that this is a strong

possibility.

All told, our data suggest that Google Earth is a useful tool for learners regardless of level of prior coursework in geology or geography, and regardless of gender. As such, it has the potential to be used to address scientific literacy on a broad scale.

3.6.4 SCAFFOLDING LEARNING

As previously stated, all complex learning should be accompanied by orienting tasks or scaffolding in order to support students' learning processes. Students, unlike experts, typically do not know what is salient within rich information sources [Lowe, 1993] such as Google Earth, and thus, if unscaffolded i.e., unguided, they might not acquire the targeted information as intended. This is particularly true in domains in which the medium of information is visual-spatial in nature in which all information is presented to the learner simultaneously. This is in direct contrast to textual information sources in which the knowledge acquisition processes are guided by the structure of the text [Larkin and Simon, 1987; Gobert, 2005a]. In prior work, Bodzin and Cirucci [2009] noted that resources such as Google Earth, when used in conjunction with appropriately designed instructional materials, show much potential in promoting students' spatial thinking. Our data, which yielded learning gains, also support this. In the present study, a great deal of effort was taken to insure that the lab exercises both oriented and scaffolded the students in order to deepen their learning. It is doubtful that learning gains would have been found for both those with and without prior coursework if the learning activities had not been well designed, although the activity with and without its scaffolding and orienting was not tested as part of this study. Thus, for those using Google Earth as a pedagogical tool at any level of education (K-graduate school), it is important that care is taken to guide students' knowledge acquisition processes in order to deepen their learning; scaffolding is particularly important when novices are learning with visual information sources [Lowe, 1993]. The materials developed by De Paor, Whitmeyer, and their colleagues (NSF-CLLI #0837040, [De Paor and Whitmeyer, 2008]; NSF-GEO #1034643, [De Paor et al., 2010a]; and NSF-DUE #1022755, [De Paor et al., 2010a]) that were used used in the present research provide a good example for how such scaffolding is accomplished.

Though we demonstrated the validity of COLLADA models in Google Earth as a viable learning tool, there were still more possibilities for this tool. The current

version only allows for one user to interact at a time with the environment. So, the next step logical step in developing COLLADA models for education is to create multi-user environments where many users can explore and interact with each other and the surroundings. This topic will be explored in chapter 4.

CHAPTER 4

AVATARS AND MULTI-STUDENT INTERACTIONS IN GOOGLE EARTH - BASED VIRTUAL FIELD EXPERIENCES

In this chapter a discussion of the basic coding framework necessary for creating and developing a multi-user Google Earth environment is presented. We discuss some of the challenges or pitfalls encountered building the framework. My contribution concentrated on building an intuitive user interface and processing the input data. The work reported in this chapter has been published in a GSA Special Paper on Google Earth and Virtual Visualizations. (see *Dordevic and Wild* [2012]). As a co-author of this paper I contributed 50%.

4.1 ABSTRACT

We have developed object-oriented programming methods to enable avatar movement across the Google Earth surface in response to student actions, either on their own, or in groups attached to a field vehicle avatar (a Jeep). Students can communicate using text messages sent from their web page text field to balloons that pop up from the avatars' placemarks in Google Earth. Students can be located locally in a lab class or at great distances from one another, as in a distance education course.

Our programming methods help to create a more engaging virtual field trip in which the students take the lead and decide where to go rather than simply reading text and viewing graphics in a tour designed by their instructor. The user interactivity with avatar in web page embedded Google Earth is controlled by JavaScript and PHP. Since the position of each avatar is known it is possible to track their movements and offer text-message advice when they stray off-task or wander about aimlessly. Our methods will be included in new virtual field trips being developed for Iceland, Hawaii, and other locations.

4.2 INTRODUCTION

Google Earth [*Google*, a] comes in three forms: (i) a stand-alone application available for Windows, Macintosh, and Linux platforms, and (ii) a mobile device app available for iOS and Android operating systems, and (iii) a web browser plug-in compatible with a variety of JavaScript-enabled web browsers including Chrome, Firefox, and Safari [*Google*, b]. The plug-in permits the programmer to incorporate one or more instance of Google Earth in a web page and to control each with familiar Hypertext Markup Language (HTML) interface elements such as buttons, text fields, and sliders. This paper focuses on the web browser plug-in form of Google Earth because of its extensive JavaScript Application Programming Interface (API) and the possibility for client-server-client communication.

The majority of work done in the area of Google Earth-based virtual field trips involves a single person using a computer to view images, read text, etc. see *Simpson and De Paor* [2010]. Interaction includes following pre-recorded tours or clicking on placemarks and reading associated HTML content. Few tools are available for users (students, teachers, administrators, etc.) to actually interact with the virtual surroundings other than panning and zooming the camera view. What we have done is to simultaneously bring multiple users together and allow them to interact and explore on the same virtual globe, thereby simulating a real field experience where each user would be able to communicate with colleagues and collaborate on collective tasks. Interaction in a virtual environment or Google Earth is not new [*Roush*, 2007; *Google*, b]. However, the hybridization of Google Earth API for a virtual-interactive geological environment is.

To achieve the above goals, designing the client-side application is not sufficient. Being able to synchronize multiple client instances of Google Earth over the Internet requires server side programming as well. The server has to log and process incoming traffic from clients. For this purpose, the PHP scripting language was chosen for its flexibility. First, it has the ability to generate HTML pages. PHP scripts can also be embedded into HTML pages. Finally, PHP scripts can manipulate MySQL- type databases. We might equally have chosen Python or Ruby-on-Rails for this task instead of PHP.

The purpose of this paper is to demonstrate how to implement the programming tasks necessary to support user interaction on Google Earth. To this end, we will

present the client-server-client communication code with a web-chat example. Passing of other data, for example avatar location, will be discussed along with server polling. Data logging is an extra benefit gained whose usefulness for educators and programmers will be explored. The combination of these parts makes creating virtual field trips possible.

4.3 WEB-CHAT EXAMPLE USING AJAX AND PHP

The backbone of the interactive Google Earth programming is the client-server-client communication. Once communication is established data such as chat messages, latitudes, longitudes, etc., may be exchanged among users. Communication between client and server is done via Ajax [*Garrett*, 2011]. Ajax enables web pages to communicate with a server, send and receive data asynchronously without refreshing the page, and therefore avoid reloading Google Earth plug-in at every update. The code snippets that handle the Ajax interface (courtesy of *http://icodesnip.com/search/ajax/1*) are in the form of a function,

function Ajax_Send(GP,URL,PARAMETERS,RESPONSEFUNCTION).

The function's parameters are as follows:

- **GP** represents the type of request (POST or GET);

- **URL** is the address of the PHP script that will be executed;

- **PARAMETERS** is the string that contains variables and values stored in it (var1=value1&var2=value2&var3=value3);

- **RESPONSEFUNCTION** is the function that will be evaluated upon server response with XMLHttpRequest.responseText as its argument.

To help the reader understand this AJAX-based communication, we will first explain the data structure and data handling on the server. In the entry string, the tag <!@!> separated row variables, and '/n' denoted a new row. PHP retrieved variables values from a file containing this entry string with the explode() method (e.g. the example in Figure 45).

In our case, the single data packet from the client contains variables that tell the server the following:

```
/*example of data entry on the server in the data.txt file: */
1299265835.4478<!@!>mike<!@!>Hi<!@!>24.999<!@!>-
39.999<!@!>25494105.783<!@!>0<!@!>0.0000018/n


/*PHP script that checks if your chat box is up to date */
/*Takes the time (in UNIX format) from client when he did his last update and assigns it to
$lastreceived */
        $lastreceived = $_POST['lastreceived'];
        /*Finds the physical location of the file with the conversation from the server and assigns
it to a array variable $data where every new line is listed as the next element of array */
        $data = file("data.txt",FILE_IGNORE_NEW_LINES);
        /*Checks the number of lines in  $data, if 0, there is no need to continue execution */
        if(count($data) == 0){
            exit();
        }
        /*Start a loop over the $data line by line */
        for($line = 0; $line < count($data); $line ++){
            /*Separates the current line ( $data[$line]) into array wher ever he encounters the
string <!@!>, in this case we will have $messageArr[0] = "1299265835.4478" and $messageArr[1] =
"mike<!@!>Hi<!@!>24.999<!@!>-39.999<!@!>25494105.783<!@!>0<!@!>0.0000018" */
            $messageArr = explode("<!@!>",$data[$line]);
            /*If there is new entry in data.txt, send it to the client */
            if($messageArr[0] > $lastreceived) echo $messageArr[1]."<+newline+>";
        }
        /*else, only send the time of the last entry from the data.txt */
        echo "<SRVTM>".$messageArr[0];
```

Figure 45. Code snippet for data entry on server.

- what action is required;

- the integer value of the last received row from the table that contains chat messages and locations of the other avatars;

- the user name of the client making a chat request;

- the user's group. Upon arrival of the data packet from the client, the server first decides what action to perform.

For example, if user1 (refer to here as the sender) starts a web-chat by sending a new message to user2 (the receiver), the data sent from the sender are:

- user name of the message receiver (can be a single other user or a whole group);

- content of the message;

- the name of the sender.

The code on the client side is a function defined as in Figure 46:

```
function sendMessage(){
    /*Define string that is being sent to the server */
    data = "action=send&to_who=william&content=" +
document.getElementById("message").value +
    "&sender=" + Avatar.userName;
    /*Function invoking XML HttpRequest */
    Ajax_Send("POST", "site/index_ch.php", data, sentOk);
}
```

Figure 46. Code for client side sender function.

The sender makes a connection with the server using the standard XMLHttpRequest protocol [*van Kesteren*, 2012]. The server then:

- picks up the string with the variables mentioned above using the $_POST['variable name'] (in this case the string is called data) ;

- cleans it (a standard procedure of filtering clients input so that corrupted, incorrectly formatted, or harmful data are not stored in the database); and

- stores the string into the database.

The next step is to ensure that the receiver is notified of the new message. All clients periodically query the server for updates by sending their user name, group, and a number that tells what database row they last read (lastReceived). The frequency of queries is set by the native JavaScript function: setInterval(). The time interval between successive queries needs to be experimentally determined and fine-tuned. In our case, the function called updateInfo() queries every 800ms (see Figure 47.):

```
function updateInfo(){

    /*Define string that is being sent to the server*/

    var data = "action=updateStat&lastReceived=" + lastReceived + "&user="+Avatar.userName

+

    "&myGroup=allow";

    /*Function invoking XMLHttpRequest */

    Ajax_Send("POST","studindex_ch.php",data.sentOk);

}
```

Figure 47. Code snippet that checks for updates.

When the server receives an update request from a client, it passes the query to the database with values from the user making the update request:

- the number (lastReceived) must be smaller than the current queue number in the database table;

- the receiver name must match the client user name making a request for an update;

- the entry must have been posted with a maximum time interval (currently 50 minutes).

Entries matching the query are sent to the client who made the request in JSON format [json, 1999] by the procedure called echo(). The snippet of PHP code that the server uses to do this is shown in Figure 48:

```
/*One of the switches in if statement */

case "updatellist":

/*Checking to see are all variables in received string defined true: proceed, false: send error and
exit */

        if(isset($_POST['lastReceived'],$_POST['item'],$_POST['myGroup'])){

/*Assign received values to local variables after cleaning them to prevent corrupted data passing */

            $lastReceived=clean($_POST['lastReceived']);

            $item=clean($_POST['item']);

            $myGroup=clean($_POST['myGroup']);

/*Making the mySQL query */

            $res=mysql_query("SELECT * FROM chat WHERE lastReceived< id_chat AND
('myGroup'=to_who OR 'item'=to_who) AND (888>( NOW()+0. time_of_send+0.)");

/*Listing the results of query */

            while($row = mysql_fetch_array($res)) {

/*Filling the messageStr array with listed results */

                $messageStr[]= $row['sender'].": ".$row['content'];

                $lastReceivedNew=$row['id_chat'];

            }

            $res=mysql_query("SELECT username FROM user INNER JOIN online ON
online.id_user=user.id");

                while($row = mysql_fetch_array($res)) {

                $online[]= $row['username'];    }

/*If database query returned any result for new chat, echo it with the online user list */

            if(isset($messageStr)){

                $user_array(message'=>$messageStr,'lastReceived'=>$lastReceivedNew,'online'=>$online);

                echo json_encode($user);

            }

/*Just echo online user list */

            else{

                $user_array('online'=>$online);

                echo json_encode($user);

            }

            exit();

        }

        echo "Error: variables in updatelist not defined";

        exit();
```

Figure 48. Code snippet of switch statement.

Two functions are involved in processing the received data on a receiver's side. The first function is sentOk(), which is the fourth argument (RESPONSEFUNC-TION) of the Ajax_Send() operation in updateInfo(). See Figure 49:

```
function sentOk(){

    /*Make sure that received data from server is in JSON format */

    if(res.isJSON()){

        /*Convert received JSON string to the Object p */

        var p = res.evalJSON(sanitize = true);

    /*Check that fields are defined in Object p */

        if(typeof p.lastReceived != 'undefined' && typeof p.message != 'undefined'){

            /*Updates the last received row from the chat table */

            lastReceived = p.lastReceived;

        /*Run the function that dynamically populates the chat box with newly arrived messages */

            populatingTables(p.message,'chatBox');

        }

    /*... (more function) */

}
```

Figure 49. SentOk code snippet.

This function looks for the part of the sent data that contains the message (p.message) and passes it to a function called populatingTables(). See Figure 50.

Figure 52 shows two students chatting about differences in rocks in the Andes near S33°, which is the result of the completion of the above function that arrived from the server see Figure 51.

4.4 PASSING OTHER DATA: AVATAR MOVEMENT

Web chat information is not the only type of data that can be sent using the above approach. Avatar location and movement are other examples. There are two aspects of avatar movement. The first is controlling the movement of one's personal avatar using an approach adapted from the Google Earth API sample code called 'Monster Milk Truck' [*Wikipedia*, 2011]. Keyboard input controls the local avatar movement and a function responsible for sending of the user's avatar position even while the user is stationary is nested in setInterval().

The second part of the avatar movement is updating positions of non-local avatar's

```
/*arguments:    cont, array that contains messages to be applied to the chat box "User: message"
                who, string id of the field that the message is going to be be applied
function populatingTables(cont,who){
/*Goes through all the elements of the cont and passes them to the anonymous function as
argument n

    cont.filter(
        function(n){
        /*Creates the div element
        var el = document.createElement("div");
        /*Apply the text to that div
        el.innerHTML = n;
        /*Finds the element who and applies the div element to it
        var a = document.getElementById(who);
        a.appendChild(el);
        a.scrollTop = a.scrollHeight;
        }
    )

}
```

Figure 50. PopulatingTables code snippet.

or everybody but the local avatar. This is accomplished with the same approach for data handling used in the web-chat mentioned above. The same timing function that updates the avatar position is used to poll the server for updates to the non-local avatars' positions (latitude and longitude). The server responds with the changes and the data are parsed and all non-local avatar positions are updated on the Google Earth terrain accordingly. Figure 53 contains an initial screen shot of two avatars and the field vehicle exploring in the Andes. An advantage of the virtual environment is that vehicles can travel anywhere - alternatively, a set of horse icons could be substituted for the Jeep in this setting! Figure 54 shows an updated position of the "steva" avatar. This is the result of the "steva" user:

```
/*GE update with the new message that pops above the head of the avatar that send it
function balloonMessage(message, user) {
    /*Try to remove any existing balloons first
    try{
        ge.setBalloon(null)
    }
    catch(err){};
    /*Create balloon and set its content
    var balloon = ge.createHtmlStringBalloon();
    /*Select the avatar that balloon will be associated with
    var placemark = Avatar_holder[Avatar_names.indexOf(user)].placemark;
    balloon.setFeature(placemark);
    balloon.setMaxWidth(300);
    balloon.setContentString(message);
    ge.setBalloon(balloon);
    /*Remove the balloon after 2 second
    setTimeout( function(){try{ge.setBalloon(null)} catch(err){}},2000)
}
```

Figure 51. Code snippet for chat-message balloon.
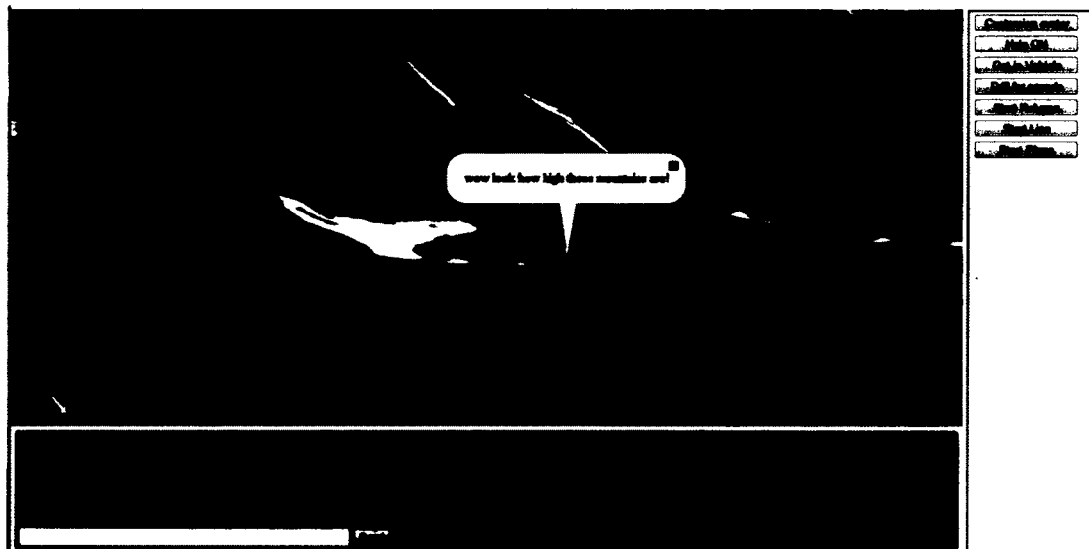
Figure 52. Two students discussing rocks in the Andes. Screenshot of "text balloon" after message is sent from one user to the server and then to the other user.

- moving locally;

- sending position update to the server;

- server processing update;

- second user "mladen" getting update from server;

- "mladen" locally parsing data and updates avatars.

The current iteration uses a MySQL database type instead of XML which was used in the web-chat example.

Figure 53. Screen shot of two students and the field vehicle. This is a reference shot taken on "mladen's" screen to see the "steva" avatar move in Figure 54. The region is in the Andes near S33°, as is the region for Figure 54.

4.5 DATA TRAFFIC

One challenge in client-server-client communications is polling, which relates to the timing of client-server or server-client communication. When the server receives more requests than in can fill, it stacks them and responds in order. During the response it hands out the most recent data set available. The issue that can arise at this moment is the update of the position. A local-user may miss an update of a non-local by being ahead in the queue or miss a non-local position update because

Figure 54. Second screen shot of user "mladen's" screen. This shot is taken after user "steva" has moved locally on his Google Earth. His movement is sent to the server and the server then sends the data to user "mladen" . The data are parsed locally and the "steva" avatar is moved. The "steva" avatar has moved many times to have noticeably changed.

a non-local user had his position updated twice before the local user received the update. The first problem is not so large while highly accurate positions of non-local avatars in some small time window are not vital to the virtual geology experience. The server is providing updates every 800 milliseconds. The second problem is handled by linear interpolation to move the avatars from update to update. The interpolation helps minimize skipping a missed point by moving them on a linear path from update to update.

In future iterations we will try to implement new technologies for communication that have become available with the draft release of HTML 5 Web socket [*Hickson*, 2012]. While currently in the testing phase, AJAX does not create any problems in terms of polling, but for scalability it may require migration to more efficient solutions that would cut back unnecessary traffic and server load.

4.6 DATA-LOGGING

One benefit gained in creating client-server-client communication is data-logging. The logging process occurs when users push their data to the server. The data recorded are latitude, longitude, and heading of every client (student in this case) with

a time stamp and a log of their chat conversations with other students. Recording the users' actions has the potential to be useful to both code developers and educators.

Helping developers debug and optimize the code and therefore enhance to the virtual field trip experience is another potential use of logging. Developers can also post-track users. Post-tracking is just reviewing the user activity on a map either sequentially or as a scatter plot. When developing it becomes important to know where and how much time the user spends on tasks. If a developed task is analyzed to not be useful in the given context it could be removed or adapted to better suit the user.

Data logging is potentially valuable for teachers as well. The available feedback could enable teachers to scaffold their student learning activities, assess learning outcomes, and evaluate students for credit if desired [*Buckley et al.*, 2010; *Horwitz et al.*, 2010; *Sao Pedro et al.*, 2010; *Jacobson and Reimann*, 2010]. Here again, post-tracking of users could be useful to help educators understand the ways in which students learn. In future iterations of the application, we will be recording students' submitted work such as locations of the sites they chose for data collection and their mapping efforts (identification of virtual specimens, drawing of contacts etc.). Also, as new tool sets become available for the client on different field trips, we will record their interactions within Google Earth.

4.7 CONCLUSIONS

Client-server-client communication enables virtual field trip developers to produce more interactive, efficient, and engaging learning experiences. Processes of communication were explored with example code for a web-chat. The first process involved a client sending information to the server, the server processing the information, and the server returning a result. The second process involved sending a request for information update to the server, the server processing the request, and the server returning the information requested. Our program has been demonstrated at national meetings by *Dordevic et al.* [2011] and beta testing with structural geology students at ODU took place during the Spring Semester 2012. From early user reactions, we are confident that it will be a useful addition to the tools available to instructors in the geosciences. We anticipate that in future years, instructors will move away from virtual field trips in which the students are passive observers of content created by the instructor, towards interactive alternatives that constitute active virtual field

work [*Ross et al.*, 2008].

In this chapter the uses of COLLADA models for multi-user education are explored with an emphasis on developing client-server-client communication which is critical for this to occur. In the next chapter the use of COLLADA models is continued but the application of kinematic modeling are also added. These two modeling types are used to examine the unique slab geometry of the Nazca plate.

CHAPTER 5

KINEMATIC AND STRAIN MODELING

My study of Tonga led to an exploration of other tears in subduction zones which led to the Nazca Plate that subducts beneath South America. The Nazca Plate has an interesting geometry because of transition zones between two different subduction angles. Can these zones accommodate the transition without tearing? In this chapter an approach to solve this question is taken by means of kinematic strain modeling. Calculations for the tear opening in the Nazca plate geometry at S33° are made. Also, strain rates are determined for the model and from earthquake separation distances. The strain-rates along with homologous temperatures are used to determine the deformation mechanism available based on a deformation mechanism map. This chapter will be submitted to a peer review journal in July with co-author D. De Paor.

5.1 ABSTRACT

In the central Andes, the Nazca Plate is subducted under western South America at an angle that varies along strike, suddenly changing from 30° to 10°. The transition from so called steep to flat slab subduction has been attributed to either tear faulting or distributed shear. Here, we investigate these alternatives using displacement and strain analysis and a deformation mechanism map.

Our conclusions are that (i) the strain rates calculated from subduction speeds are in agreement with general geological strain rates and are slow enough to allow plastic deformation given the right conditions; (ii) a deformation mechanism map for the system indicates relatively high stresses implying that the only plastic mechanism possible at the early stages of subduction would be cataclastic flow; (iii) even though the plate may deform by tearing initially, the thickness of the lithosphere precludes the opening of a window until the region near the end of the flat slab is reached, by which time, plastic processes may inhibit the opening of a window.

5.2 INTRODUCTION

On the curved surface of the Earth, subduction zones cannot continue along strike indefinitely - they must terminate against other tectonic structures. Terminations sometimes involve tearing of the oceanic lithosphere as at the northern end of the Tonga trench [*Isacks et al.*, 1968; *Millen and Hamburger*, 1998; *De Paor et al.*, 2012a]. Even within a single, continuous subduction zone, the dip of the downgoing lithospheric slab may change along strike, especially when inhomogeneities on the ocean crust such as fracture zones or ridges are involved, and tears have again been proposed in these settings by *Martinod et al.* [2010]. A vertical tear fault striking in the slab's dip direction may accommodate the change in slab dip and potentially open a window through which material and heat can flow from the hot asthenosphere beneath the shallow-dipping slab to the cooler mantle wedge above the steep-dipping slab [*Millen and Hamburger*, 1998; *Fowler*, 2005]. However, it has been suggested that lateral changes in slab dip might alternatively be accommodated by formation of a lithospheric shear zone involving continuous strain which would not open up such a mantle window nor permit lateral material transport [*Cahill and Isacks*, 1992]. This paper quantitatively examines the feasibility of lithospheric shear strain versus tear faulting in the central Andes.

5.3 THE ANDEAN OROGEN

The Pacific Ocean Basin's southeastern active margin extends the entire length of South American from western Venezuela to the Chilean province of Tierra del Fuego (Figure 55). Except for its northern and southern extremities, the Andean Orogen marks the convergent boundary between the Nazca Plate and the South American Plate. The northern end of the mountain range involves the Caribbean Plate as well as microplates that interact in a complex structure north of the Carnegie Ridge (an excellent animation of this is available at [*Carleton College*, 2012]). At the other end of the orogen, the Antarctic and Scotia Plates interact south of the Chilean Ridge. In both of these places, tears in the downgoing slab have been postulated by *Gutscher et al.* [1999]; *Espurt et al.* [2007]; *Russo et al.* [2010]; *Vargas et al.* [2011]; see Figures 56 and 57. Between these extremities, the present-day Nazca Plate is continuous, but its surface exhibits plateaus at sites of remnant ridges and fracture zones (Nazca Ridge, Iquique Ridge, Juan Fernandez Rise, etc.), consequently the

subduction geometry is far from cylindrical (Figure 58).
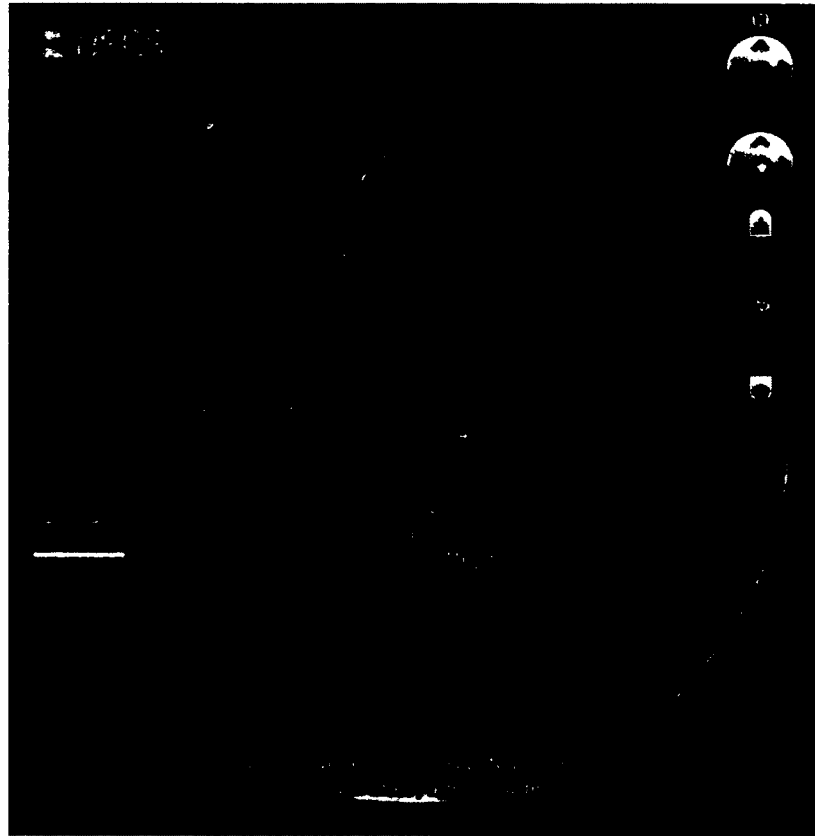
Figure 55. Volcanic gaps in the Andean Mountain Range correspond to regions of "flat slab" subduction (thick yellow lines). From north to south they are the Bucaramanga, Carnegie-Peruvian, and Pampean flat slabs. Plateaus on the Nazca plate are shown in orange. From north to south, they are the Carnegie, Nazca, and Juan Fernandez remnant ridges. Plate boundaries from the USGS. Volcanoes from the Google Earth volcanoes layer.

The Nazca Plate originates at the East Pacific Rise - the Pacific Ocean's main spreading ridge (Figure 55). In comparison with the vast Pacific plate to its west, the Nazca Plate travels a relatively short distance eastward before converging with and subducting under the western margin of the South American continent. Not having traveled far or for long, it is relatively warm, light, and buoyant, consequently we do not expect the steep dips nor the marginal basins associated with subduction of older, colder lithosphere as seen along the western Pacific margin in places such as the Marianas trench [*Isacks et al.*, 1968]. Slab dips of about 30° are common along the
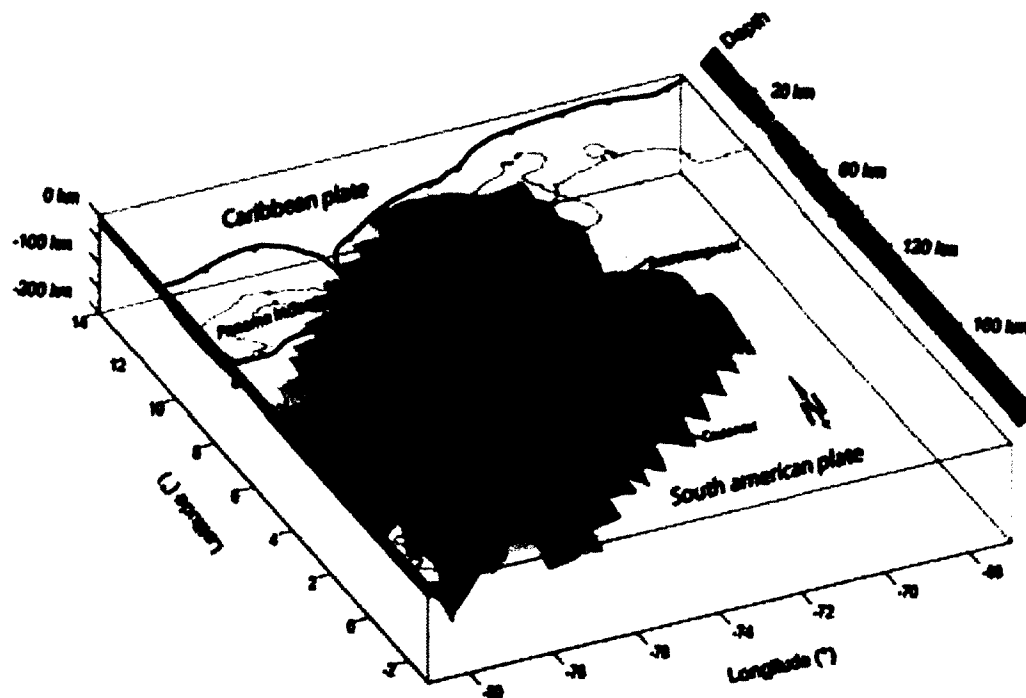
Figure 56. Model of the northern end of the Andean mountain chain where the Bucaramanga Flat Slab is bounded on the southern side by the seismically active Caldas Tear Fault. Source: http://www.revistas.unal.edu.co/index.php/ esrj/article/view/27208/28704#f1.
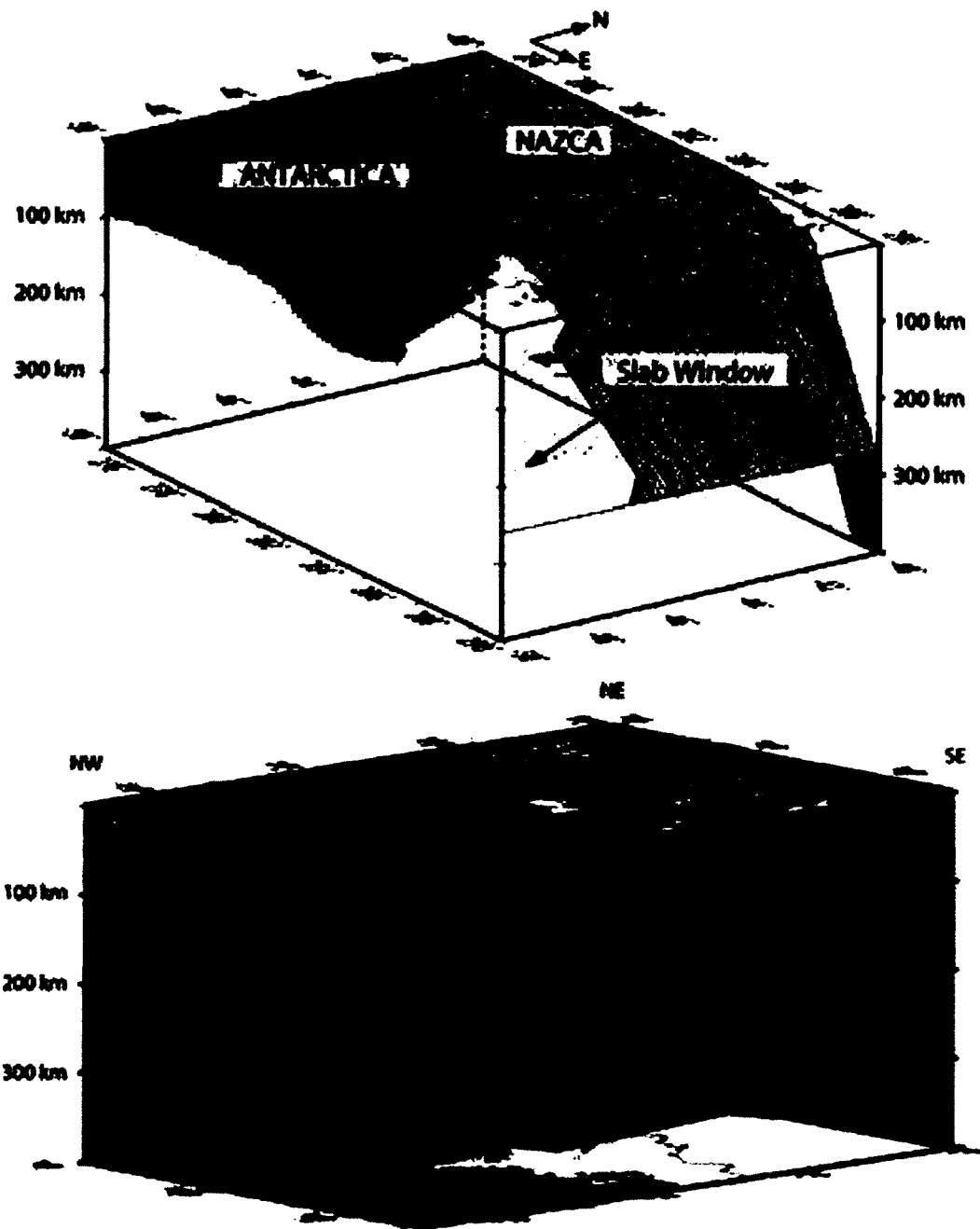
Figure 57. Proposed tear and mantle window associated with the subduction of the Chilean Ridge at the southern end of the Nazca Plate. From *Russo et al.* [2010].
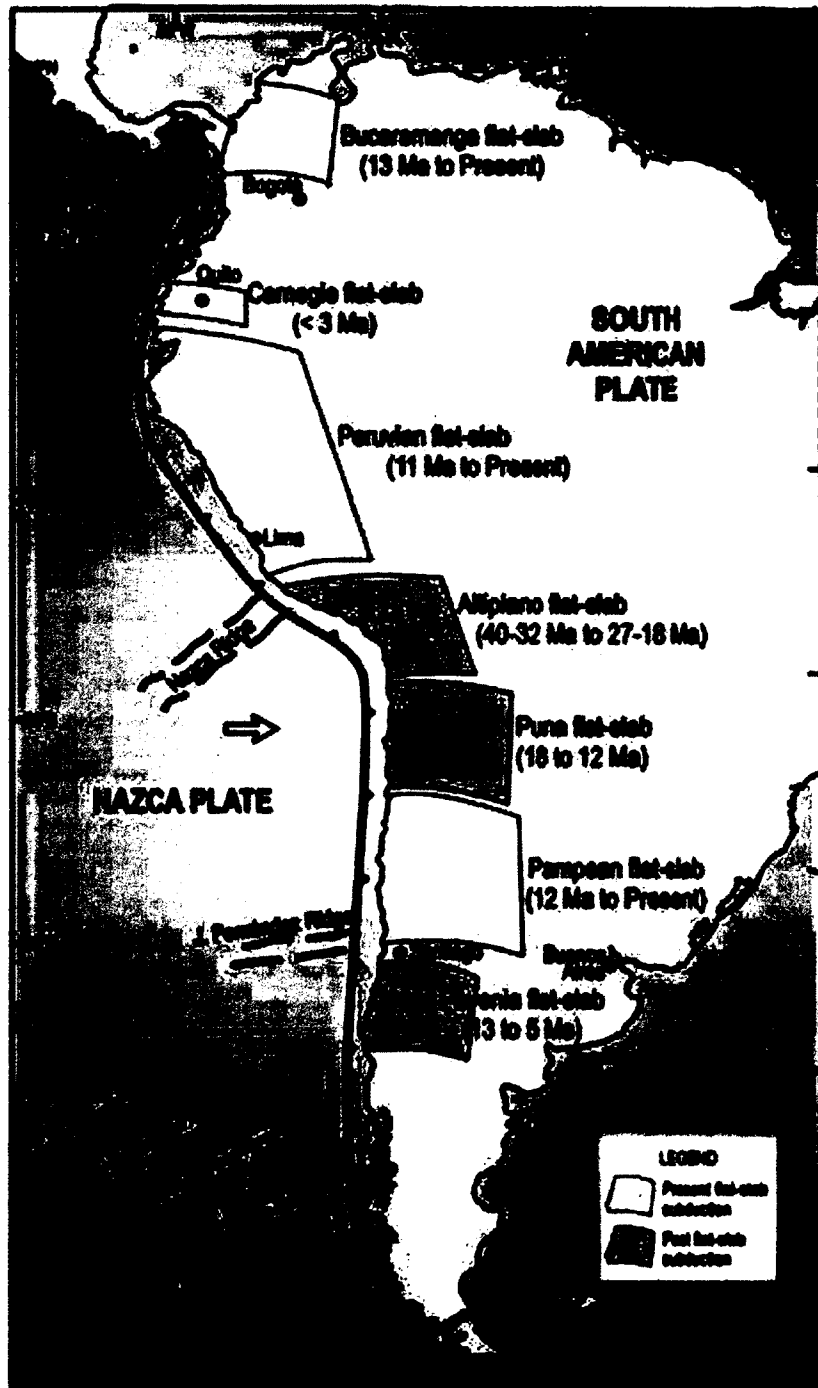
Figure 58. Remnant ridges in the Nazca Plate from *Ramos and Folguera* [2009].

Andean subduction zone, however in places the downgoing plate has been interpreted to have negative buoyancy resulting in shallow to horizontal dips by *Kelleher and McCann* [1976, 1977]; *Pilger* [1981]; *Espurt et al.* [2007, 2008]; *Manea et al.* [2012]. Steep and flat are thus relative terms and in the region of interest to this paper, 30° is considered steep subduction whereas a 10° dip is termed flat. Flat slab subduction was first proposed for the Laramide orogeny by *Dickerson and Snyder* [1978]; (see also http://www.geo.arizona.edu/geo5xx/geo527/Rockies/flatsub.html).

Although the Andes Mountains appear straightforward on a continental scale (e.g. *Moores and Twiss* [1995]), the tectonic scenario is quite complex. Much of the orogen is marked by active vulcanism as illustrated in Figure 55 where volcanoes are represented using the Google Earth™ "volcanoes" layer (see *Google* [2012]). Andesitic vulcanism (which is, of course, named after the Andes) occurs above steep east-dipping lithospheric slabs and is fed by partial melting in the mantle wedge beneath the continental arc as volatiles rise from the descending ocean floor [*Fowler*, 2005]. However, there are a number of present-day volcanic gaps in the orogen corresponding to regions where the slab dip is flat [*Schellart et al.*, 2010]. From north to south these are labeled (Figure 58) the Bucaramanga, Carnegie, Peruvian, and Pampean Flat Slabs [*Ramos and Folguera*, 2009]; note that the Pampean is also known as the Chilean Flat Slab - [*Manea et al.*, 2012]. In these regions, the shallow dip of the subduction zone does not permit a mantle wedge of sufficient volume to feed an overlying magmatic-volcanic system. The volcanic gaps coincide with relatively wide, Laramide-style, foreland fold and thrust belts verging towards the continental interior [*Jordan et al.*, 1983; *Allmendinger et al.*, 1990; *Alvarado et al.*, 2009].

The Bucaramanga Flat Slab (Figure 56) is bounded on its south side by the seismically active Caldas Tear Fault [*Vargas et al.*, 2011]. Tear faults have been proposed by *Gutscher et al.* [1999] for each side of the small Carnegie Flat Slab (Figure 59). *Espurt et al.* [2007] proposed a lithospheric tear and mantle window at the south end of the Peruvian Flat Slab, near Lima, which corresponds to the subduction of the Nazca remnant ridge (Figure 60). *Allmendinger and Gubbels* [1996] investigated crustal shortening by means of pure and simple shear strain as in influence on flat slab subduction.

We here confine our attention to the southernmost, Pampean Flat Slab in Central Chile and Argentina (Figure 58), an area where we and/or colleagues have previously carried out structural and tectonic field studies [*Simpson et al.*, 2001; *Ramos et al.*,
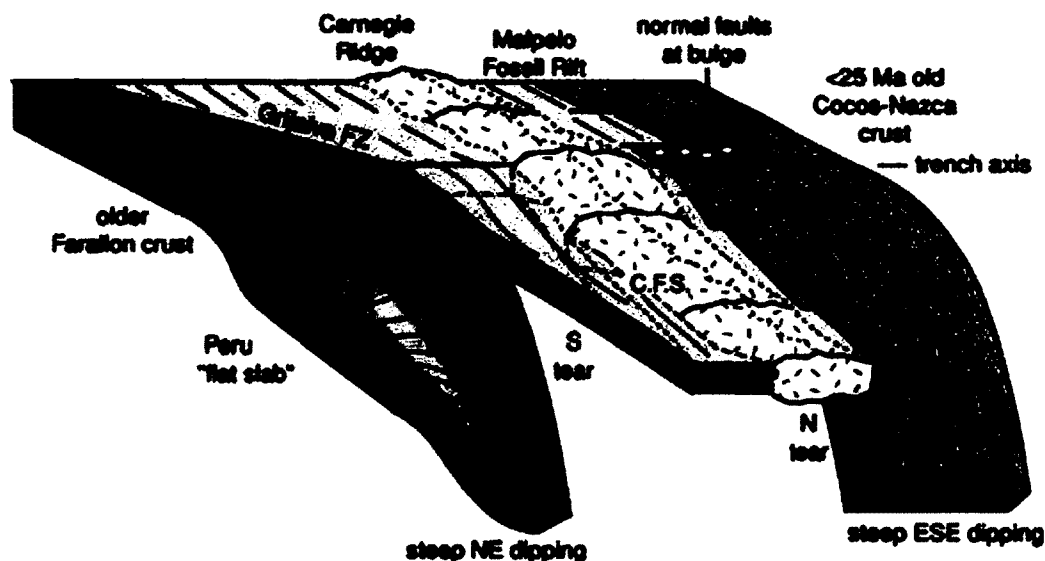
Figure 59. Proposed tears on either side of the subducted Carnegie Ridge. From *Gutscher et al.* [1999];
http://www.geo.arizona.edu/geo5xx/geos577/projects/flesch/
images/Gutscher%2099%20carnegie.gif.

2002; *Whitmeyer and Simpson*, 2003, 2004]. The current flat slab extends from S27° to S33° [*Isacks et al.*, 1968]. Its southern limit, near Santiago, coincides with the subduction of the remnant Juan Fernandez Ridge. *Wagner et al.* [2006] documents mantle evidence for eastward progression of a flattening slab. *Ramos and Folguera* [2009] suggested that the steep slabs north and south of the Pampean Flat Slab were flatter in the past (Figure 58). Evidently, flat slabs advanced and retreat with time.

5.4 3D VISUALIZATION

To visualize the Andean subduction zone interactively, we mined data from GeoMapApp [*GeoMapApp*, 2012] (http://www.geomapapp.org), a freely available application which gives the user a visual interface with a wide-range of geological data [*Ryan et al.*, 2009]. One database on GeoMapApp (http://www.geomapapp.org) contains earthquake hypocenters from the USGS. The first step was to select a geographical region and export hypocenter point data to an Excel file (because of their number, data were exported as six adjacent rectangular regions). Columns of opening and closing angle brackets and KML element names were inserted in the spreadsheet
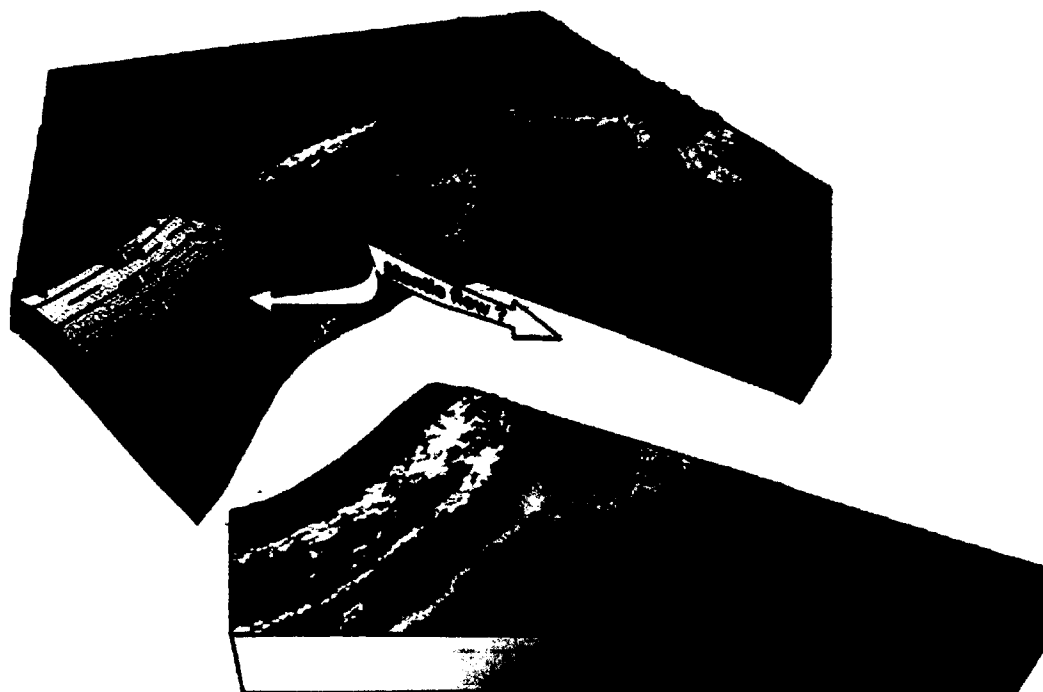
Figure 60. Lithospheric tear and mantle window associated with subduction of the Nazca Ridge. From *Espurt et al.* [2007]
http://geology.gsapubs.org/content/35/6/515/F4.large.jpg.

and exported as text, thus creating points with KML-formatted tags suitable for import into Google Earth as placemarks. These points were loaded into Google Earth and a vertical snapshot of the region was saved as a PNG file (Figure 61).

Next we launched Google Sketch-Up™(which is now Trimble SketchUp™) and created a three-dimensional rectangular block with the same top side dimensions as the PNG surface image saved in Google Earth. We applied the PNG as a texture on the top surface and left the sides transparent. Using the SketchUp 'move' tool, we dropped the GeoMapApp data points into the block until they were at their correct depth beneath the surface. If several points were clustered together the deepest one was selected (usually these depths were within 5 km of one another). After all hypocenter data points were positioned, the regions were grouped together using geological markers and longitude/latitude lines. Point data were then connected into depth profile lines and joined across similar depths as contours (Figure 62a). Polygons were added until the surface was closed to form a depth-profiled slab (Figure 62b).

Figure 61. Snapshot of the Pampean Flat Slab with hypocenter data from *Anderson et al.* [2007] (white spots).

The outline of this top surface of the slab was then copied and lowered orthogonally by 5 km to simulate ocean crust thickness. The approximate thickness of the Nazca plate can be determined from the age of the plate at the trench. *Syracuse and Abers* [2006] reports the age of the Nazca Plate between 10-40 m.y.. This age can be used with the half-space cooling equation for thickness [*Turcotte and Oxburgh*, 1967; *Parsons and Sclater*, 1977]

$$y_L = 2.32\sqrt{\kappa t} \tag{1}$$

where $\kappa = 1\ mm^2 s^{-1}$ is the coefficient of thermal conductivity and t is the age or time in seconds. Using the ages with Eqn 1 yields thickness values between 42-88 km. Due to uncertainties, we use a minimum value of approximately 50 km and a maximum of 100 km. A second copy was located 100 km below the top surface to represent the bottom of the lithosphere and vertical planes were added to create a slice of the lithosphere (Figure 63a). Gaps in the mesh were manually filled and painted gray for easy identification.

In addition to GeoMapApp (http://www.geomapapp.org), we mined data from publications. Two models were created - one from *Cahill and Isacks* [1992] and one from *Anderson et al.* [2007] hypocenter data. The Cahill and Isacks hypocenter data were taken from calculated databases. The Anderson data were determined from a hypocenter algorithm written by the first author. In both cases, the data were already separated into contours and these were loaded into Google Earth as described above. These two cases covered an area large enough to be concerned about Earth's curvature, so a spherical model was constructed and the textures draped in adjacent sub-segments. Points on contours were connected dot-by-dot to ensure that lines did not depart from the curved surface (this task has been made easier with recent additions of SketchUp ruby-scripts that can draw lines on curved surfaces - see *Trimble* [2012]).

After the contours were connected, contour lines were moved to the appropriate depth. The number of points in these cases was too great to permit filling in the space by connecting polylines manually, instead a feature called "contours" in the "SandBox" of the Sketch-Up application was used (Figure 62b). Lines of interest were highlighted and the program automatically filled in open spaces. Our models are consistent with models from (*Cahill and Isacks* [1992]-their Figure 6) but have the added advantage of interactivity - they can be, zoomed, panned, rotated, and
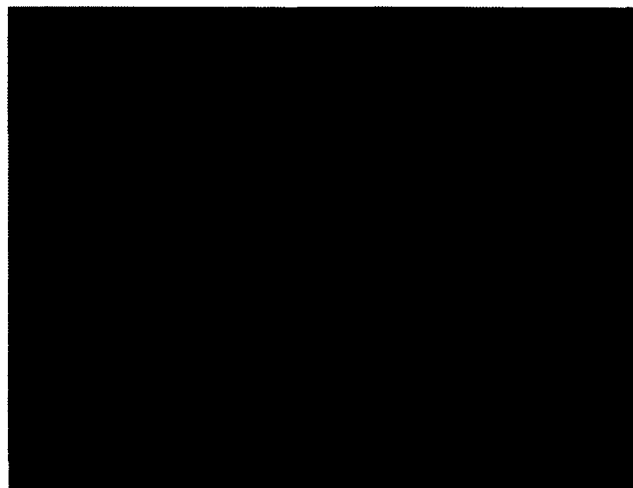
(a)
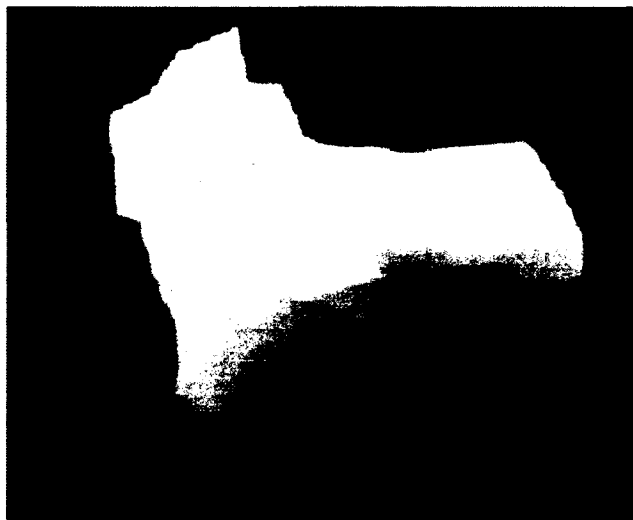
(b)

Figure 62. (a) SketchUp's Sandbox tool was used to create contours of hypocenter depths created in SketchUp. This is a 3D view. (b) Polygonization of (a).
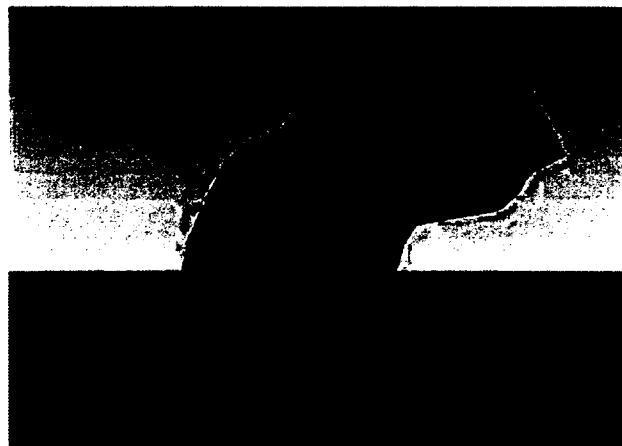
(a)
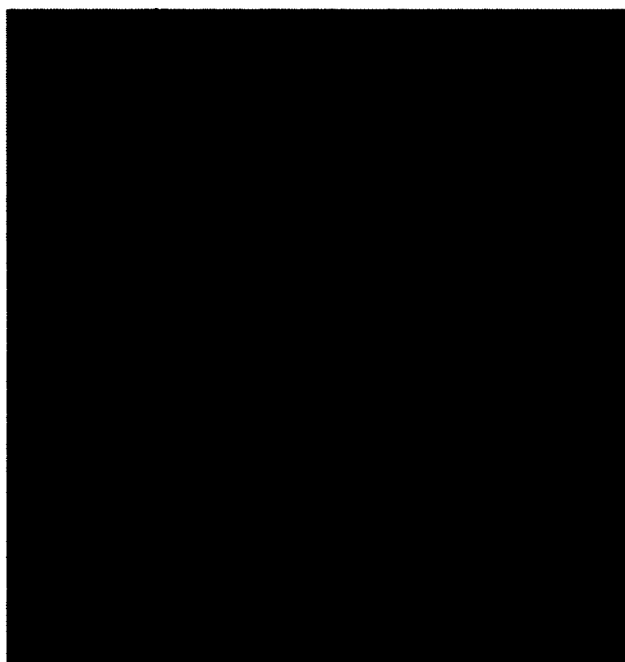
(b)

Figure 63. (a) SketchUp model of slice of Pampean Flat Slab, view southwest. Brown denotes crust, red denotes lithospheric mantle. Gray patch is gap in data. Region below dotted line omitted from 63b. (b) Steep-flat transition just south of 63a , view northwest. Blue is potential tear fault plane roughly at latitude of Santiago. Surface form lines show alternative shear interpretation. Gray is gap in data. Reference axes: east (green), north (red), up (blue).

viewed in any direction in SketchUp.

The first impression gained from these data-based interactive 3D models of the subducting slab is this: traveling down-dip, the flat slab region is a relatively short interruption of a dominantly steep-dipping subduction zone (Figure 63). In contrast, in other illustrations (e.g. *Fromm et al.* [2004]- their Figure 1; *Kay and Coira* [2009] p. 273- their Figure 8b; *Beck and Zandt* [2002] - their Figure 8) the flat portion dominates, only the top of the lithosphere is shown, and the deeper steep slab is omitted. When the full thickness of the lithosphere is shown, the flat slab is only moderately longer than thick. Its length is 300 km based on the estimates of *Barazangi and Isacks* [1976]; *Cahill and Isacks* [1992]; *Anderson et al.* [2007]. Note that *Jordan et al.* [1983] shows a flat slab extending to the 600 km tick mark on the horizontal axis but that is measured from the trench, not the point flat slab initiation.

5.5 TRANSITION ZONES - TORN OR SHEARED?

As outlined above, lateral boundaries between the Andean Flat Slabs and their steep neighbors have been interpreted alternately as tears or as zones of continuous shear deformation (Figure 63b). *Barazangi and Isacks* [1976] interpreted teleseismics as indicating discrete brittle tears in the Nazca Plate between the regions of different dip angle, similar to the tear in the Tonga-Samoa region of the western Pacific [*Bevis and Isacks*, 1984]. However, from local seismic data in the boundary region around latitude S15°, *Hasegawa and Sacks* [1981] interpreted the plate to be deformed by continuous flexure and not torn. *Bevis and Isacks* [1984]; *Bevis* [1986] strengthened that interpretation by analyzing the distribution of hypocenters using trend surface analysis. Tears were thought to be a possibility in aseismic areas within the central Andean subduction zone. The tears would occur as separate gaps lying within the space of the curved regional trend where no large seismic events are available to confirm tear fault activity [*Cahill and Isacks*, 1992]. *Zandt et al.* [2003] used teleseismic data to determine flow being aligned with fluid-filled cracks associated with normal faulting Using data from the CHile ARgentina Geophysical Experiment (CHARGE) broad-band network, and an earthquake relocation algorithm employed for the first time in this region, new hypocenter locations were determined and the possibilities for tears or gaps in the plate were presented by *Anderson et al.* [2007]. Recently, thanks to advances in seismology (including the number of stations and improved equipment), more earthquake data of higher quality have become available which

suggest that the plate does not tear but becomes sheared [*Millen and Hamburger*, 1998].

The alternative possibilities have implications for the thermal regime surrounding the slabs in regions of along-strike dip change (Figure 64a,b). If the slab is torn over a sufficient distance, then there is the opportunity for both heat and material transfer through a window from the hotter lower mantle below the flat slab to the cooler upper mantle above the steep slab. If the slab is not torn, no material flow occurs and heat flow is impeded by the relatively cool slab. Shear requires continuous, crystal-plastic deformation mechanisms, which raises the question whether temperature-pressure conditions and the slab's residence time at such conditions can accommodate crystal-plastic deformation. An intermediate case is possible if deformation in the transition zone leads to a boudinage-type structure. These different possibilities may be thought of as analogous to an open window that allows in heat and air, a glazed window that blocks the wind but allows some heat through, and a window with plantation shutters that inhibit but do not entirely block material and heat flow.

The nature of the lateral structures at locations of slab dip change will also affect the tectonic and volcanic structures visible on the Earth's surface. A tear may be expected to cause relatively rapid heat transfer and material flow into the triangular wedge of magma genesis above the steep slab and a spill-over of volcanism across the surface trace of the transition zone would be expected, whereas a continuous shear zone or boudinage structure would serve as either a full or partial barrier to material flow and convective heat transfer, resulting in a sharper boundary to the volcanic gap as the surface.

Of course, if the steep and flat parts of the slab diverged continuously with depth, then a tear somewhere in the $\sim$ 3,000 km-thick mantle would eventually become inevitable. However, seismic data suggest that, in the down-dip direction, the flat slab is confined to the region under the foreland thrust belt which is usually estimated to be about 300 km on the surface [*Ramos et al.*, 2002]. Farther east and at increasing depth, the dip switches back to 30° again (Figure 63a . Two steep segments- one that was always steep and one that was temporarily flat - thus have a constant offset and any lateral structure will become dormant in the sense that neither further tearing nor shearing is necessary to accommodate continued subduction into the lower mantle (Figure 64a,b- beyond the words turn down).
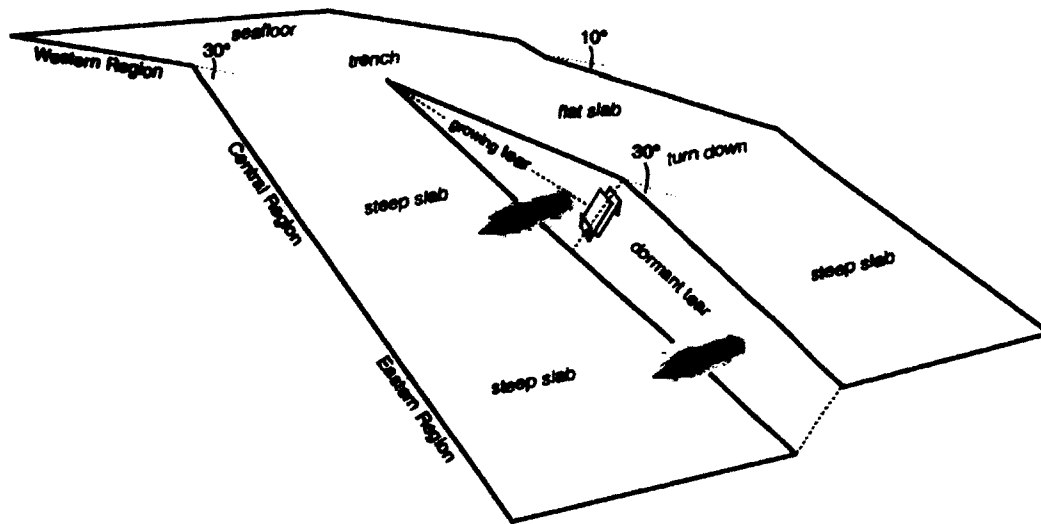
(a)
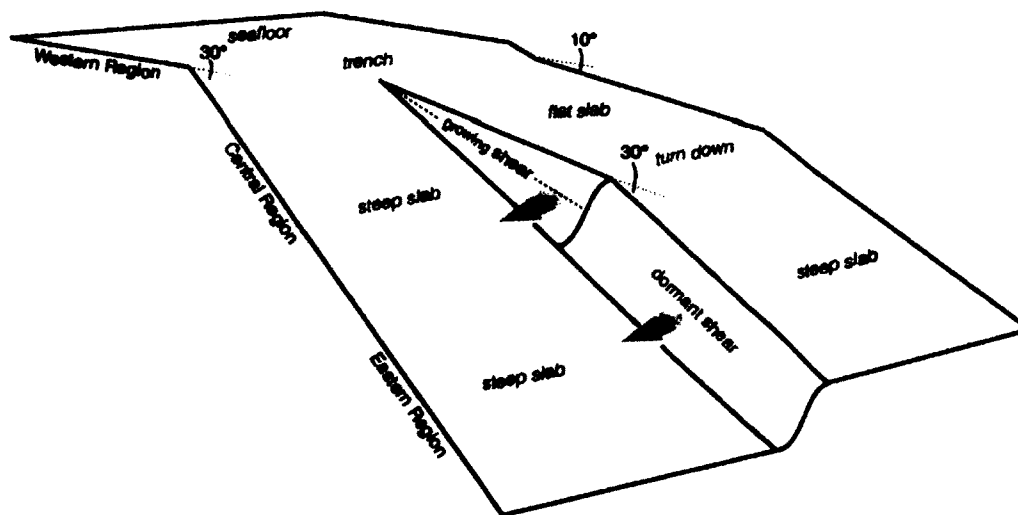
(b)

Figure 64. Tear vs shear at slab dip transition. a) Tear resulting in heat and material flow from lower mantle under flat slab to lithospheric mantle over steep slab (red arrows), b) Shear results in thinned sheet of lithosphere. Material flow is prevented, thermal flux is inhibited (semi-transparent red arrows). Thickness of slab not shown.

5.6 REFERENCE FRAMES

At first glance, the obvious geographical reference frame for our model would have an origin at the trench, a horizontal axis in the slab dip direction (approximately east), a horizontal axis parallel to strike (approximately north), and a vertical axis (up). A north-up plane would then contain horizontal traces of the steep and flat slabs at different elevations. The problems with this view are that (a) tearing or shearing begins after about 100 km of subduction has already taken place, so a better place for the origin is where the steep and flat slab begin to rip or shear, and (b) a vertical slice along strike does not contain the displacement vector for tearing or shearing, so this view would create an element of vertically exaggeration that is a function of particular slab dip angles, and the study would be difficult to apply elsewhere, especially to steeper dipping slabs. Instead, displacement vectors should join points that are equally far down-dip from the original point of tearing or shearing.

We therefore choose a reference frame with the origin approximately 100 km down dip from the trench, the x-axis in the direction of the average lithospheric dip $\bar{\delta}$, the y-axis along strike, and the z-axis in the average pole direction, orthogonal to x and y (Figure 65a). We call this x-y-z frame the *model reference frame-* it is related to a geographical reference frame (dip direction, strike, up) simply by a rotation about strike by an amount equal to the average lithospheric dip $\bar{d}$. Planes parallel to the non-vertical y-z reference plane are termed *profile planes* and the two-dimensional discussions that follow apply to these profile planes.

5.7 REGIONS

Given the discussion above, the problem can be addressed by defining three regions:

1. The Western Region. This extends from the Andean trench offshore of Chile to the point of tear or shear initiation approximately 100 km down the subducting slab. Segments of lithosphere that are destined to become flat and steep slabs are continuous and uniformly steep-dipping.

2. The Central Region. After approximately 100 km in the western region, the Nazca plate either tears or shears forming steep and flat slab segments. This region extends horizontally approximately 300 km perpendicular to strike and is the main region of interest. The tear fault offset in the z-direction is expressed

(a)

(b)
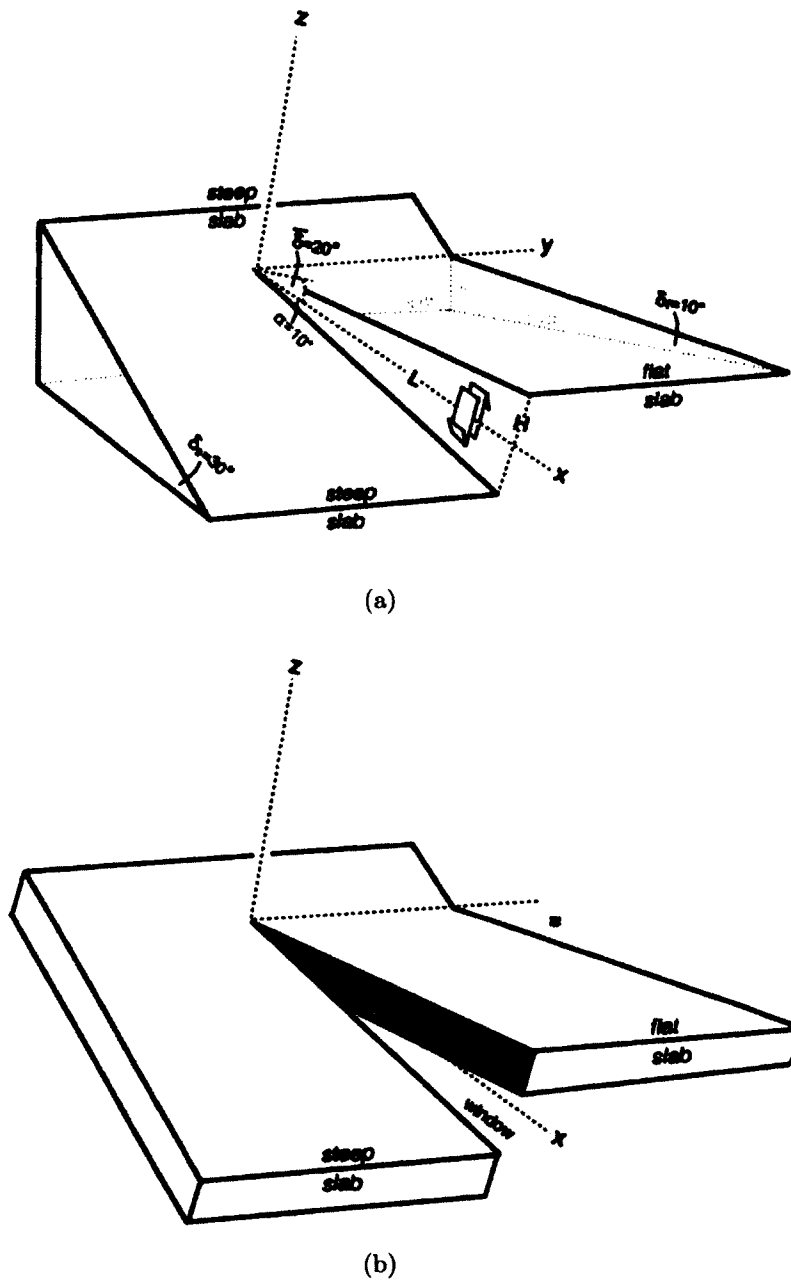
Figure 65. a) Geographical (east-north-up) and model (x-y-z) reference frames. δ_s and δ_f are the steep and flat slab dips. $\bar{\delta}$ is the mean slab dip. α is the half-wedge angle. L is the distance from the origin (initiation of the tear) to the profile plane. H is half the displacement in that profile plane. Sense-of-shear symbol straddles the vertical tear fault plane The origin is on the top of the slab - slab thickness not shown. b) Slab thickness shown.

as 2H, twice the magnitude of the displacement of either slab from the x-axis. This offset is a function of distance L along the x-axis and of the slab dip difference. In the present case, the steep slab dip is $\delta_s = 30°$ and the flat slab dip is $\delta_f = 10°$. We define the a as half the difference in these dips, so $\alpha = 10°$ in this case.

In the Central Region, the traces of the steep and flat slabs in the y-z profile plane are equally distant from the trench as measured along the surface of the slab in the down-dip direction, and the displacement vectors of the tear or displacement gradients of the shear are parallel to the y-z plane (ignoring slight displacement vector curvature due to the scissors effect).

3. The Eastern Region. Here, the flat slab steepens back up to 30° and is therefore parallel to, albeit permanently offset from, the slab segment that was always steep. The subducting Nazca Plate moves as a rigid unit in the down-dip direction, with no change in the extent of the tear or shear. Eventually, the lithosphere becomes plastic and losses its well-define slab geometry (see *Kellogg et al.* [1999]).

5.8 BASIC CALCULATIONS FOR TEAR

Tear faulting in the slab is easy to visualize by analogy with a band-saw. If a carpenter pushes a thin sheet of plywood through a band-saw, progressively slicing it into two parts, these parts may sag by different amounts, creating a very good analogy to the torn lithospheric slab. The tear occupies a discrete vertical plane striking in the slab dip direction. As subduction progresses, the gap between the steep and flat slabs widens linearly by an amount that depends on the difference in slab dip and the length of subducted slab since tear initiation.

If the torn slab were perfectly flat, then it would be a simple matter to determine tear fault displacement as a function of distance traveled, L (Figure 65), or as a function of time, given the subduction rate. Let α be the half-wedge angle - the difference between the steep and mean dip, which is $(1/2)(30° - 10°)$ or $10°$ in this case. If the speed of subduction is 7 cm/yr (Figure 66, see *Kendrick et al.* [2003]; *Schellart et al.* [2010]) and the mean slab length measured along the x-axis is approximately $L \approx 300$ km (its projection onto the x-axis in this case is equal to its projection onto the horizontal), then the duration of flat slab subduction t (i.e., the residence time

of material passing through the flat slab) is $(1/70)(300 \times 10^6)$ m.y. or approximately 4.3 m.y. In that time, the slabs undergo a displacement in the z-axis direction of H,

$$H = \pm L \sin \alpha = (300)(0.174)km \approx 52km \tag{2}$$
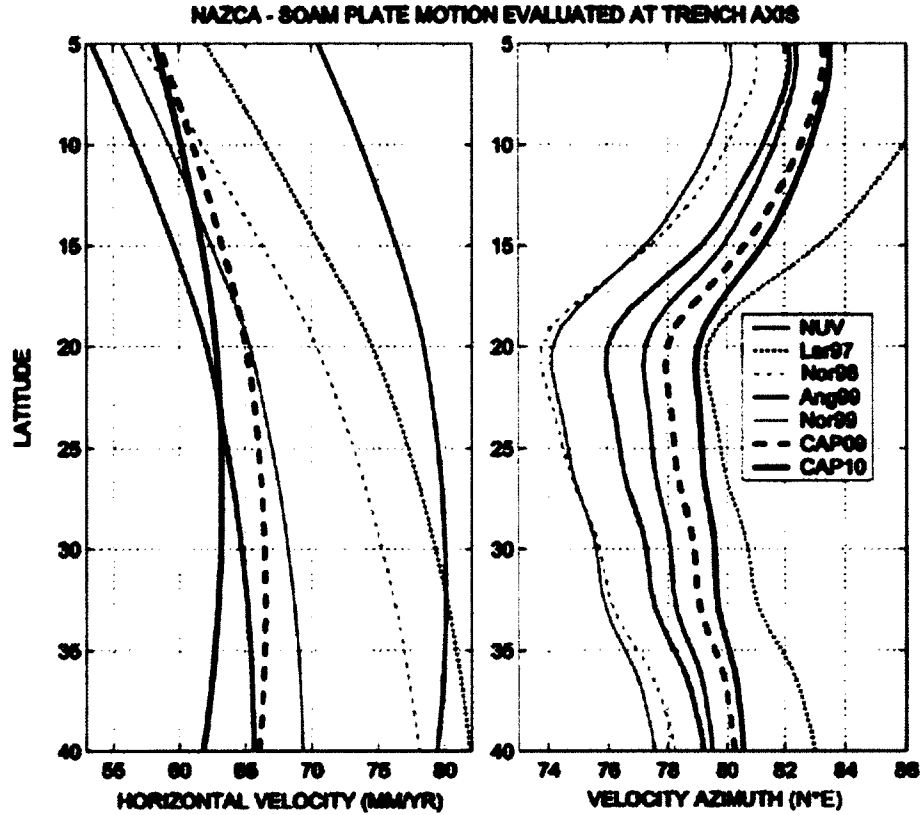
Figure 66. Nazca-South America relative plate velocities from *Kendrick et al.* [2003] - their Figure 4. For latitudes S23-30°, estimates range from 6.3-8.0 cm/yr.

Relative to the x-axis, the flat slab is offset upward and the steep slab downward, so the tear fault offset at the end of the flat slab is therefore twice H or roughly 104 km. This can also be found from the seismic data profiles reported by *Cahill and Isacks* [1992].

Let the flat and steep slabs have velocities v_f and v_s, respectively. They share a common speed s = 7 cm/yr, but diverge in direction by 2α. In a time t, the material has an x-direction component of motion L,

$$L = st \cos \alpha \tag{3}$$

Material points do not have a component of motion in the y-direction, but the sign of a point's y-coordinate determines the direction of its z-component of motion. Let b be a defined using a Boolean expression in square brackets

$$b = 1 - 2[y > 0] \tag{4}$$

Thus b has the value -1 when the Boolean expression [y > 0] is true (1) and b has a value 1 when the Boolean expression [y > 0] is false (0). Displacement in the z-direction is then expressed as

$$H = bL \tan \alpha = bst \sin \alpha \tag{5}$$

If the b-value is positive the material moves upward (positive z-direction) and if the b-value is negative the material moves downward (negative z direction). The distribution of material points through the region in space and / or time is then specified in a single matrix operation using homogeneous coordinates (see *De Paor* [1994]),

$$\begin{bmatrix} x' \\ y' \\ z' \\ 1 \end{bmatrix} = \begin{bmatrix} D_{xx} & D_{xy} & D_{xz} & U_x \\ D_{yx} & D_{yy} & D_{yz} & U_y \\ D_{zx} & D_{zy} & D_{zz} & U_z \\ 0 & 0 & 0 & 1 \end{bmatrix} \begin{bmatrix} x \\ y \\ z \\ 1 \end{bmatrix} \tag{6}$$

where D_{ij} (i,j = x,y,z) are elements of the deformation tensor and U_i are components of the displacement vector. In the tear model, there is no penetrative deformation, so the deformation tensor D_{ij} is the unit tensor, and the displacement vector is expressed in terms of time t, subduction speed s, and sense of displacement b,

$$\begin{bmatrix} x' \\ y' \\ z' \\ 1 \end{bmatrix} = \begin{bmatrix} 1 & 0 & 0 & st \cos \alpha \\ 0 & 1 & 0 & 0 \\ 0 & 0 & 1 & bst \sin \alpha \\ 0 & 0 & 0 & 1 \end{bmatrix} \begin{bmatrix} x \\ y \\ z \\ 1 \end{bmatrix} \tag{7}$$

The total tectonic window area A in the Central Region is approximately

$$A = (LH) - A' \tag{8}$$

where A' is the area of slab exposed in cross-section in Figure 65b

$$A' = 100(st - \frac{50}{\tan 20^0}) \tag{9}$$

Thus A works out at about 18,000 km^2.

The above matrix representation allows us to track points in the system for times when the material is in the central region. A MatLab™ script was written to generate the 2D time evolution for the tear in the profile plane. The result that is most interesting is for L = 300 km. This would represent the maximum amount of offset, while the plate no longer subducts at two different angles. In Figure 67, a plot of the deformation zone for a subduction dip = 10° and value of st = 100 km, 200 km, and 300 km are shown.
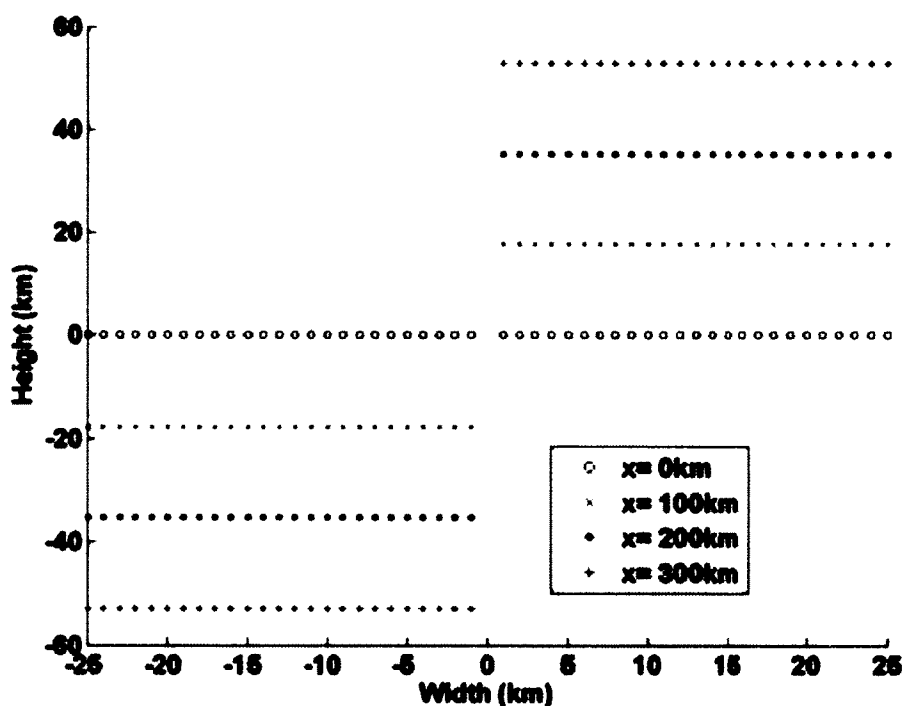
Figure 67. Tear evolution as distance increases down dip for a 50 km wide zone. After 300 km the tear height is 100 km.

5.9 THE SHEAR ALTERNATIVE

The important question is this: can the tear fault offset in Figure 65 be achieved instead by continuous shear strain in the 4.3 m.y. timespan available using crystal-plastic deformation mechanisms? A shear zone would create a curved monocline joining flat- and steep-dipping limbs (Figure 68). In profile, the fold is a Ramsay

Type II, or similar fold [*Ramsay*, 1967]. The fold's down-plunge direction is down-dip on the straight limbs so it would be called reclined in the nomenclature of structural geology (ibid.). It is a conical reclined monocline widening down-plunge for the length of the flat slab (Figure 68) and a cylindrical reclined monocline plunging at 30° thereafter (after 'turn down' in Figure 64b).
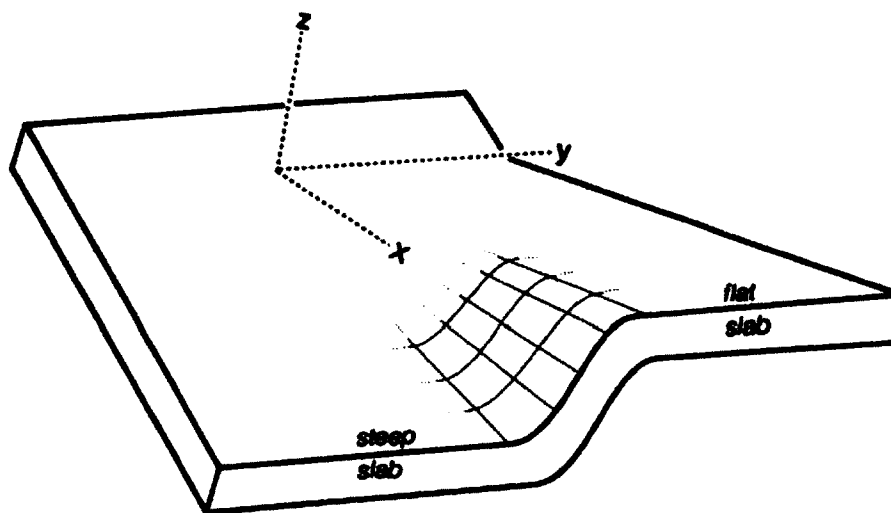
Figure 68. Shear in the form of a plunging monocline indicated by a curved lattice.

5.10 DISPLACEMENT AND STRAIN MODELING

To study shear as a mechanism of accommodating slab dip change, we need a strain model. Three different shear regimes are possible, simple, pure, and general [*Simpson and De Paor*, 1993] and in each case the strains may be either homogeneous or heterogeneous [*Ramsay*, 1967]. However a simple, parallel-sided shear zone is not possible as the size of shear zone must increase with distance down the subduction zone in order to accommodate progressively more offset. Consequently, the shear zone must start at zero width and gradually widen along the y-axis as one move in the x-direction (or as subduction / time progresses). New material from the adjacent borders of the steep and flat slabs gets incorporated in the shear zone progressively while material already in the shear zone is subject to further incremental strain. The result is a conical fold-shaped shear zone (Figure 68). The widening process is analogous to simpler classical models of kink band growth [*Weiss*, 1980].

To model strain in this fold, we approximated heterogeneous simple shear using symmetrically nested slices of homogeneous simple shear (Figure 69). Simple shear is not the most likely strain field as there is no mechanical reason for slip on xz-planes. A more physically realistic model would be tangential longitudinal strain, involving an element of pure shear with principal axes tangential to the slab [*Ramsay*, 1967]. Given the other approximations involved, however, we can reasonably approximate the heterogeneous shear zone by the three slices or if you like, card decks - a central slice with the maximum value of shear and two peripheral slices with half that value. By considering these slices separately and summing their net effects, we can treat the problem as one of homogeneous strain. Differences in stretch along the slab and consequently thinning across it will not vary significantly relative to the tangential longitudinal strain model.
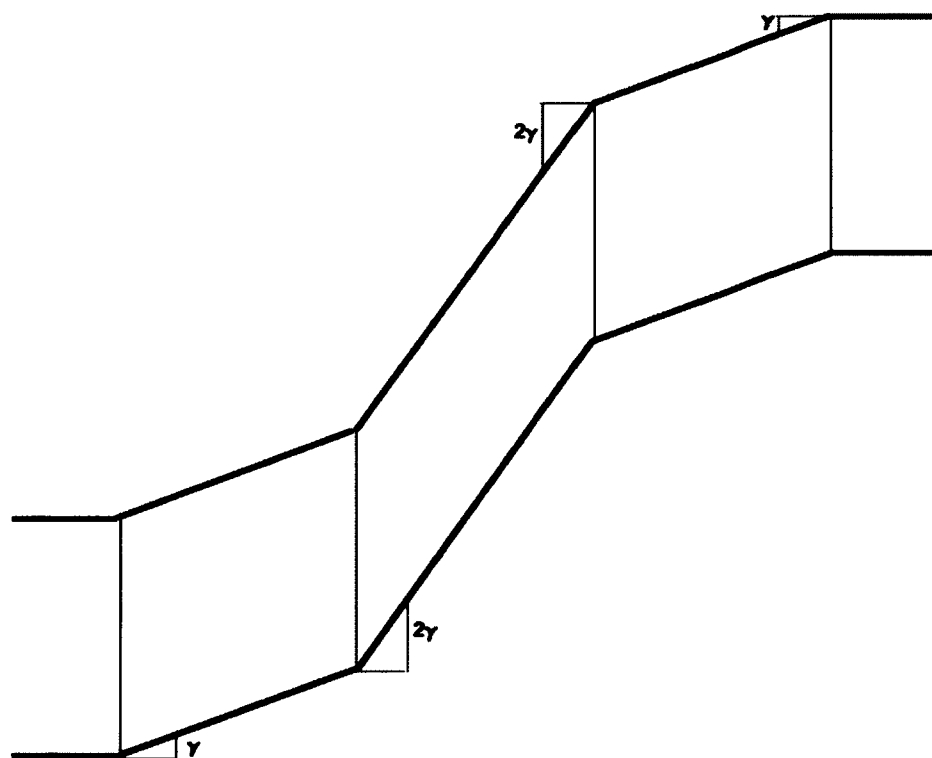
Figure 69. Approximation of heterogeneous shear by three slices of homogeneous shear. The central slice, representing material that has been in the shear zone longest, has undergone twice the shear strain γ of the marginal slices.

5.11 SLAB THICKNESS IN A SIMPLE SHEAR ZONE

In the current study, we need to consider slip in the z-direction on zy-shear planes happening as slab material is translated along the x-direction. A matrix combining these displacements and deformations [De Paor, 1994] is:

$$
\begin{bmatrix} x' \\ y' \\ z' \\ 1 \end{bmatrix} = \begin{bmatrix} 1 & 0 & 0 & U_x \\ 0 & 1 & 0 & 0 \\ 0 & \gamma_{zy} & 1 & 0 \\ 0 & 0 & 0 & 1 \end{bmatrix} \begin{bmatrix} x \\ y \\ z \\ 1 \end{bmatrix}
\tag{10}
$$

For simple shear in the profile plane, the stretch of the long side of the deformed square is $(1 + \gamma_{zy}^2)^{-1/2}$ from Pythagoras (Figure 70). This is the stretch of the lithospheric slab's top or bottom surface trace in the yz-plane. Simple shear does not change the area of the unit square, therefore the stretch perpendicular to the slab surface in the yz-plane is $(1 + \gamma_{zy}^2)^{-1/2}$. This corresponds to the change in thickness of a unit lithospheric slab. If the lithosphere is initially 100 km thick, then the final thickness zl is given by $100(1 + \gamma_{zy}^2)^{-1/2}$ km.

The amount of slab thinning is a simple function of shear but the amount of shear required to accommodate a change in slab dip depends not only on that change (from 30° to 10° in this case) but also on the width of the shear zone. The widening of the shear zone with distance along the x-axis can be expressed in terms of a semi-cone angle β (Figure 71). The geometry is directly analogous to the classical true/apparent dip issue in structural geology.

A semi-displacement H in the direction of the z-axis can be achieved by shear strain γ_{zy}, applied to the sides of the heterogeneous shear zone in Figure 69a and $2\gamma_{zy}$, applied in the central zone. This is equivalent to a homogeneous shear strain $\bar{\gamma}$

$$
\bar{\gamma} = \frac{4}{3}\gamma_{zy}
\tag{11}
$$

We can now express the semi-displacement H in terms of shear strain and shear zone width,

$$
H = \bar{\gamma}W
\tag{12}
$$

The width in turn depends on the slab length and the conical shear zone's semi-cone angle β.

$$
W = L \tan \beta
\tag{13}
$$
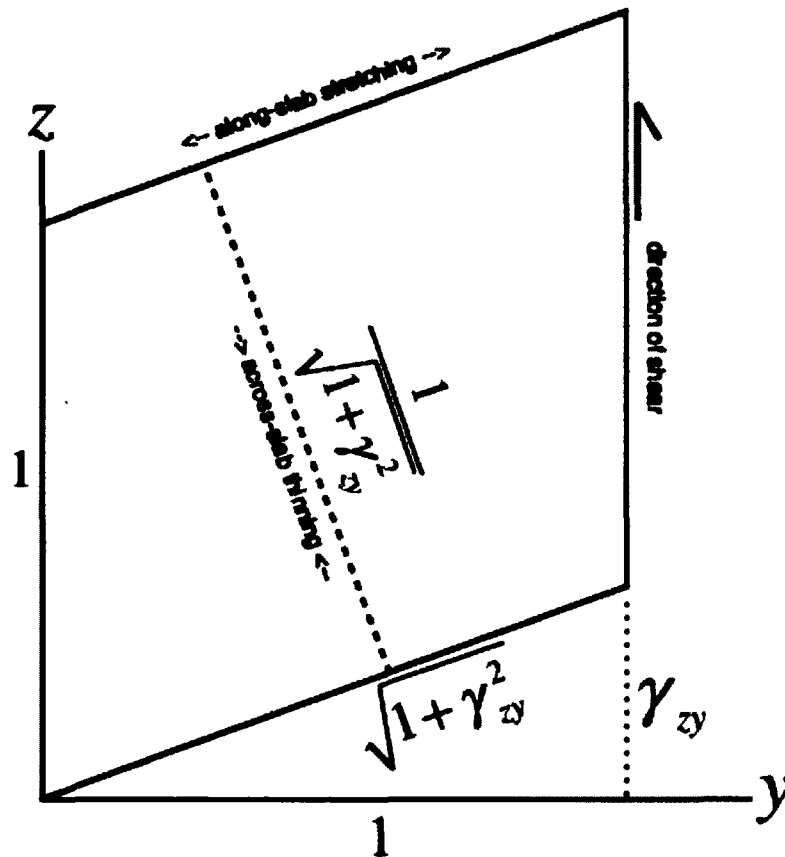
Figure 70. Calculation of slab stretch and thinning in the profile plane. Deformation is assumed to be by simple shear in the z direction on shear planes parallel to xz as in Figure 68. Stretching along the top or bottom of the slab is given by Pythagoras. Thinning of the slab is the inverse, assuming isochoric strain.
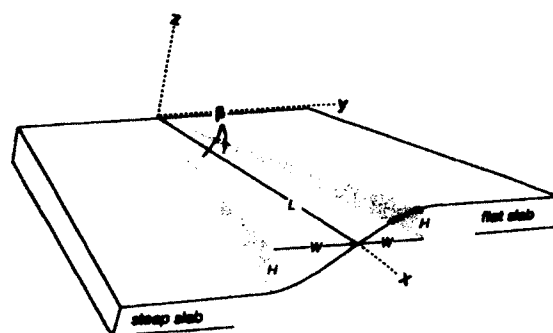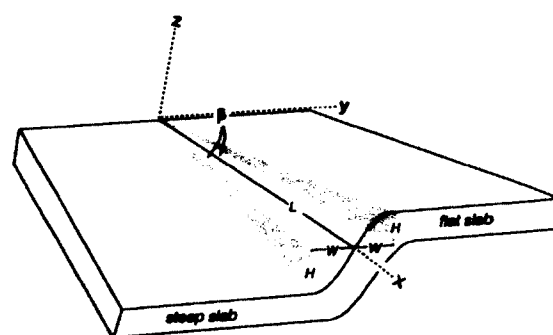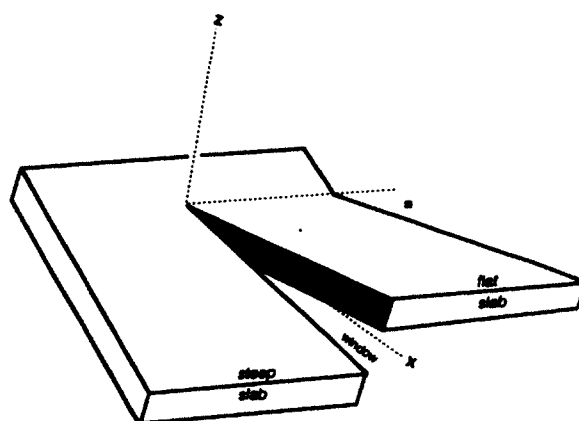
Figure 71. The amount of shear strain required to accommodate a given semi-offset H in the z-direction is a function of shear zone semi-width W in the y-direction as well as length L in the x-direction. a) wide zone requires low shear strain, b) narrower zone requires higher shear strain, c) a tear fault can be thought of as infinite shear strain corresponding to zero shear zone width. β is the semi-cone angle of the shear zone. Gray marks vertical boundaries.

If β is large, the zone widens rapidly with distance L along the x-axis (or equivalently with time given the subduction velocity) and relatively little shear strain is required to accommodate a given semi-offset H. A smaller cone angle β leads to a high shear strain $\overline{\gamma}$, the limiting case being a cone angle of zero which requires infinite shear strain and zero shear zone width, in other words a tear fault!

Analysis of the model in Figure 63b based on GeoMapApp data (http://www.geomapapp.org) plus the models of *Cahill and Isacks* [1992]; *Anderson et al.* [2007], suggests that a semi-cone angle of 10° is consistent with the 3D slab geometry.

With this 10° semi-cone angle, the shear zone semi-width W must be approximately 53 km after 300 km movement along the x-axis. To achieve the semi-offset H = 52 km in a zone of this width would require a homogeneous shear strain of about 1. In the heterogeneous shear model of Figure 69, the periphery of the shear zone would require a shear strain of $\frac{4}{3}$ and the center would require a shear strain of $\frac{3}{2}$. From Figure 70, the stretching along the slab d and the thinning across the slab d' would be given by the following equations

$$d = \sqrt{(1 + \gamma_{zy}^2)} \tag{14}$$

$$d' = \frac{1}{\sqrt{(1 + \gamma_{zy}^2)}} \tag{15}$$

For the periphery, this works out as d = 1.2; d' = 0.8, so a 100 km thick slab would be reduced to 80 km. In the center of the heterogeneous shear zone, the equivalent stretches are d = 1.8; d' = 0.55 so the 100 km slab is reduced to 55 km thick. Given suitable crystal plastic deformation mechanisms, it would certainly be possible for the slab to maintain continuity and not boudinage. However, it is questionable whether continuous brittle processes such as cataclastic flow could maintain slab cohesion during 50% thinning.

A 53 km wide shear zone is much wider than ductile shear zones recorded elsewhere in ophiolitic and continental crust that were formed at depth and later tectonically transport and exhumed at the surface. The latter are rarely more than 10 km in true thickness [*Simpson et al.*, 2001; *Whitmeyer and Simpson*, 2003, 2004]. However, their rocks employed deformation mechanisms such as basal slip in quartz which are not available in the present case.

Another constraint on shear zone width is provided by geophysical data - the contour data from *Cahill and Isacks* [1992]; *Anderson et al.* [2007]. The data were retrieved using C++ code to look at longitudinal stripes in a latitudinal box. The latitudes spanned from S32-34° and the longitudes were taken in 0.5 degree blocks from W67.5-69.5°. For example, for W68° the values examined were W67.25-68.25° and S32-34° for the latitudes. This approach was used to give profile-sections along the leading edge of the downgoing plate. Next, each earthquake hypocenter which fell into this range was compared to all the other hypocenters. The code compared separation distances and heights between all pairs.

Table 13. Values from earthquake data and calculations. Length is travel distance from trench

Source	W (km)	H (km)	L (km)	$\beta(°)$	$\alpha(°)$
Anderson S33	16.462	10	250	1.57	1.14
Anderson S33	42.621	20	250	4.06	2.29
CI S14	26.262	25	300	2.51	2.39
CI S14	90.747	50	300	8.60	4.76
CI S33	32.86	25	250	3.13	2.86
CI S33	89.453	50	250	8.48	5.71
x = 300	106	109	300	9.46	10.30

Useful results obtained from the search included (i) the shortest distance between two hypocenters with a non-zero height separation which can be used as the shortest width of the shear zone, and (ii) the smallest and largest values for shear strain (the ratio of the displacement in z to x). The same process is repeated for S14S-16° and W70-73° for the hypocenter data from *Cahill and Isacks* [1992]. The data region interpreted by *Anderson et al.* [2007] is S30.5S-32.5° for latitude with no restrictions for longitudes. The regions chosen were determined by visual examination of the contour maps. Results of the search are given in Table 13 where the x = 300 values are calculated from basic geometry.

5.12 DUCTILE DEFORMATION MECHANISMS

A deformation mechanism map can be used to understand how the system is deforming. The map is a plot of normalized stress versus homologous temperatures that is contoured for strain rate and divided into regions where different mechanisms are allowed. Thus, strain-rates and a homologous temperature are calculated to understand how the system may deform.

Evidence for ductile deformation in often seen in rocks of the continental crust that have been buried to 12 km depth or more, strained at a rate of about $1 \times 10^{-14} s^{-1}$ for millions of years, and exhumed as a result of contractional or extensional tectonics. A question that arises in this study is whether the temperatures and strain rates necessary for ductile deformation are present in the down going slab.

The strain rate can be calculated from the shear strain required to achieve the necessary semi-displacement H. In our heterogeneous shear zone model (Figure 69) the higher shear strain in the center of the zone is $\frac{3}{2}$. The time available has been estimated at 4.3 m.y. and given that there are 31,556,926 seconds in a year, the strain rate can be estimate at $1.1 \times 10^{-14} s^{-1}$. The average strain rate $2.35 \times 10^{-15} s^{-1}$ was also calculated using this procedure for the values given in Table 13. These values are within the geologically accepted range of realistic strain rates, [*Pfiffner and Ramsay*, 1982]. This number along with the homologous temperature can be used to determine the deformation mechanisms available.

The temperature of interest is the homologous temperature given by

$$T_H = \frac{T}{T_m} \tag{16}$$

with T being the temperature of the material, in this case olivine, and T_m representing the melt temperature of olivine given by *Turcotte and Schubert* [2002]

$$T_m = 2140 + d \cdot \frac{2}{1000} \tag{17}$$

The temperature of the system using a thermal structure for a subduction zone from *Turcotte and Schubert* [2002] gives the subducting material temperature of 873 K at a depth of 273 km. The melt temperature can be calculated for this depth using the above equation which gives $T_m = 2686.41$ K. This gives a homologous temperature of $T_H = .325$.

Using the strain-rates of $1.1 \times 10^{-14} s^{-1}$ and $2.35 \times 10^{-15} s^{-1}$ and the homologous temperature $T_H = .325$ a location on a deformation mechanism map can be

found (Figure 72). For the conditions given the location on the map is in the "plasticity" region which is the engineering term for "inelastic", so the plate can only maintain cohesion by cataclastic flow.
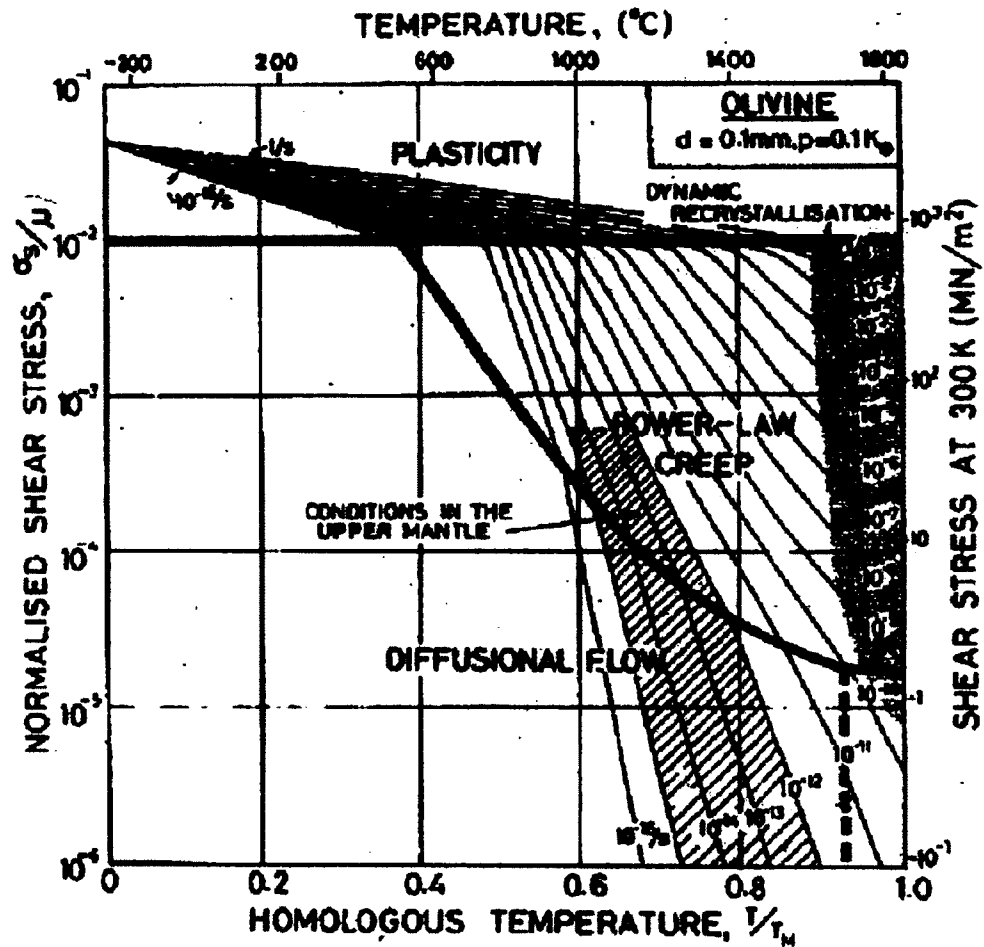
Figure 72. Deformation mechanism map for olivine. The points of interest (red dots) are for strain rates of $1.1 \times 10^{-14} s^{-1}$ and $2.35 \times 10^{-15} s^{-1}$ and a homologous temperature $T_m = .325$. Map is from *Ashby et al.* [1977].

5.13 DISCUSSION AND CONCLUSIONS

Results show that the slab can accommodate this two angle subduction between 10 and 30° for the 300 km distance while the slab may deform by cataclastic flow. The plate will be thinned to a thickness of 80 to 50 km as a result of this deformation but should still allow for a continuous plate to be maintained. *Segall and Simpson* [1986] concluded that ductile shear can nucleate on brittle fractures and we envisage such a transition as the slab is subduction. However, even if the deformation is initially brittle, the thickness of the plate (55 km) prevents a window from opening for a distance of 156 kilometers down dip.

To further our understanding of this subduction zone the goal of building a dynamic 3D model in COMSOL is the next step. This would allow for the two subduction angles to interact with minimal input, other than some physical parameters set by Geophysical conditions in the region. Before a 3D model can be built a thorough study using 2D models of the parameter space is done to understand which parameters influence the Geophysics of the region greatest. These 2D models also are also important because they will serve as initial conditions for parts of the 3D model.

CHAPTER 6

2D NUMERICAL MODELING OF SUBDUCTION ZONES

In this chapter 2D models are used to explore parameter space. This space includes three important parameters including the subduction angle, the subduction rate, and the coupling distance. By changing these variables over a suite of models their geophysical impact on the subduction process can be measured. These results will help lay a foundation to build a 3D multi-angle subduction model. This chapter will be submitted to a peer review journal in the Summer of 2012 with co-author J. Georgen.

6.1 ABSTRACT

The dynamics of subduction zones are influenced many factors including subduction angle, convergence rate, mantle viscosity structure, and coupling between the downgoing slab and mantle wedge. We use 2D finite element models to assess how temperature and velocity fields are affected by subduction angle, for slabs ranging from ~45° to ~10° dip. The model domain encompasses a downgoing slab, overriding plate, and upper mantle wedge. Models solve the steady-state equations of mass, momentum, and energy, neglecting heat production and thermal buoyancy and assuming isoviscous mantle flow. Flow in the wedge is driven by kinematic boundary conditions. The rigid, overriding plate is assumed to be stationary. As part of a parameter space exploration, convergence rate and frictional coupling between the slab and mantle wedge are also varied. The models help to better understand convergent geodynamics in a variety of settings. Three main conclusions can be drawn from the model suite. First, of the three parameters studied, subduction angle has the largest impact on model dynamics. Next, the second most important variable is the subduction rate, and the coupling distance influences the models least. Finally, in the subducting Nazca plate, where angles of 10° and 30° are adjacent, the juxtaposition of these different angles is likely to be an important control on the geodynamics of the convergent margin.

6.2 INTRODUCTION

The early beginnings of subduction zone investigations and models can be found with *Isacks and Molnar* [1969], who showed that earthquakes reflect the geometry of subducting slabs. Some of the first analytical models of subduction zones suggested that corner flow in the mantle wedge caused an upward force, but further work indicated that the forces balanced to give a realistic predicted subduction angle [*Batchelor*, 1967; *McKenzie*, 1969; *Stevenson and Turner*, 1977; *Tovish et al.*, 1978; *Reid and Jackson*, 1981]. The next improvement on the models was to incorporate variable viscosity. An early study by *Vassiliou et al.* [1984] used a wedge viscosity that ranged over two to three orders of magnitude. However, with improvements in computational power more recent studies using variable viscosity have ranges of four to six orders of magnitude [*Billen and Hirth*, 2005, 2007]. Time-dependent modeling was first implemented by *Gurnis and Hager* [1988] and helped to set the stage for dynamic modeling of subduction zones.

Generally speaking, subduction zone modeling can be performed on two scales. The first is global, wherein the modeler examines how subduction processes interact and influence one another on a long-wavelength scale [*Schubert*, 1992; *Tackley*, 2000]. The second is regional. Regional models may investigate generic small-scale zones, for example to quantify the effects of changing geodynamic parameters, or they may focus on a specific subduction zone. The regional scale is useful for examining properties that are more computationally intensive to investigate, including mantle layering, phase transitions, slab dehydration, wedge hydration, and mantle melting [*Wada and Wang*, 2009; *Syracuse et al.*, 2010].

Billen [2008] identified four general subduction model types: instantaneous, fully dynamic, dynamic with kinematic boundary conditions, and coupled kinematic/dynamic. The latter three types are time-dependent. The instantaneous model involves a solving the conservation equations for mass and momentum. The velocity field and pressure can be solved for, if density and viscosity are set and the boundary conditions are prescribed. From these solutions other physical quantities may be determined including plate motions, the geoid, stress orientations, and strain fields [*Hager*, 1984; *Zhong and Gurnis*, 1992, 1994; *Billen and Gurnis*, 2001; *Billen et al.*, 2003].

Time-dependent models incorporate the conservation of energy equation as well as the mass and momentum equations. Thus, the model may change with time by

conduction and advection of heat. In general, the system is solved in the following manner. First, the Navier-Stokes equations are solved, including variable viscosity and buoyancy, if applicable. Next, temperature structure is calculated using conservation of energy with the velocity field. Time-dependent models often differ from instantaneous models because they use simpler initial and boundary conditions.

Fully dynamic models have no prescribed velocity or applied force boundary conditions. The model is driven only by buoyancy forces [*Billen and Hirth*, 2007]. In dynamic models with kinematic boundary conditions, the top surface of the model often has an assigned direction and rate of subduction, with the goal of understanding how plate kinematics and mantle dynamics are related [*Kincaid and Sacks*, 1997; *Olbertz et al.*, 1997; *Schmelling et al.*, 1999; *Bellahsen et al.*, 2005; *Stegman et al.*, 2006]. Coupled kinematic/dynamic models are used for studying the interaction of the mantle wedge, subducting slab, and overriding plate. These models have a set velocity field for the downgoing slab, but the flow in the wedge is solved for dynamically. Coupled kinematic/dynamic models can be used to incorporate properties and processes that change on local scales, such as melting, dehydration, and variability in mineral composition [*Wada and Wang*, 2009; *Syracuse et al.*, 2010]. This study uses finite element, coupled kinematic/dynamic models to investigate how predicted temperature and velocity fields are affected by parameters like subduction angle, subducting plate velocity, and the frictional coupling between the downgoing slab and the mantle wedge.

6.3 GEOGRAPHICAL AREA

This study is motivated by the South American subduction zone. The Nazca plate, which is generated at the East Pacific Rise, travels a relatively short distance before reaching and subducting beneath the South American plate. The Nazca plate subduction zone is somewhat unusual because it possesses four distinct regions with contrasting downgoing slab angles. From S2-15° , the plate subducts at an angle of approximately 10° [*Cahill and Isacks*, 1992] (Figures 73 and 74). From S15-24°, the angle changes to 30°. For S27-33°, the angle returns to 10°. Finally, south of 33°, the subduction angle is again 30° [*Jordan et al.*, 1983].

Several studies have investigated the structure of the subducting slab in the regions of dip angle transition, but the nature of the transition zones remains to some degree an unresolved question. Initially the changes in subduction angle were first
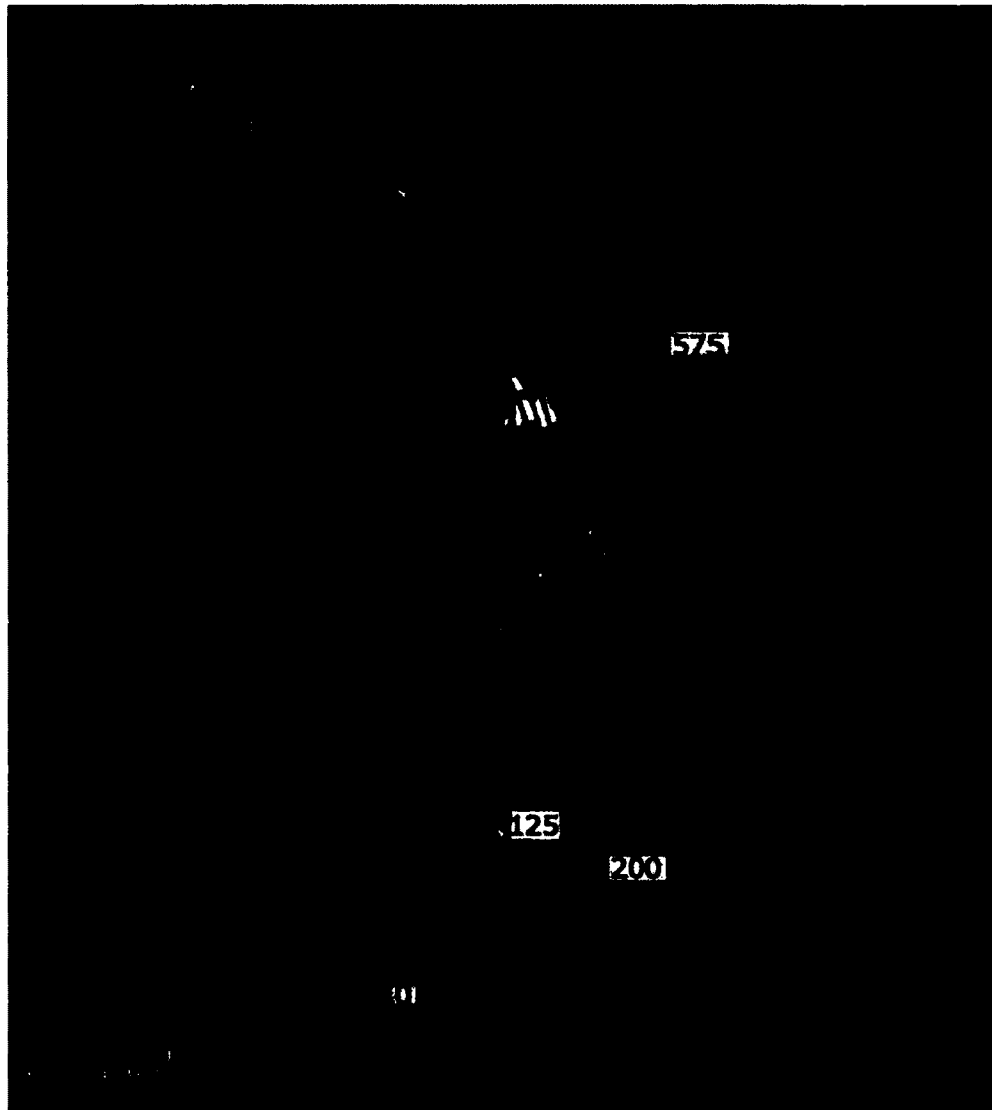
Figure 73. Contoured earthquake hypocentral depths from *Cahill and Isacks* [1992]. Contour interval is 25 km.
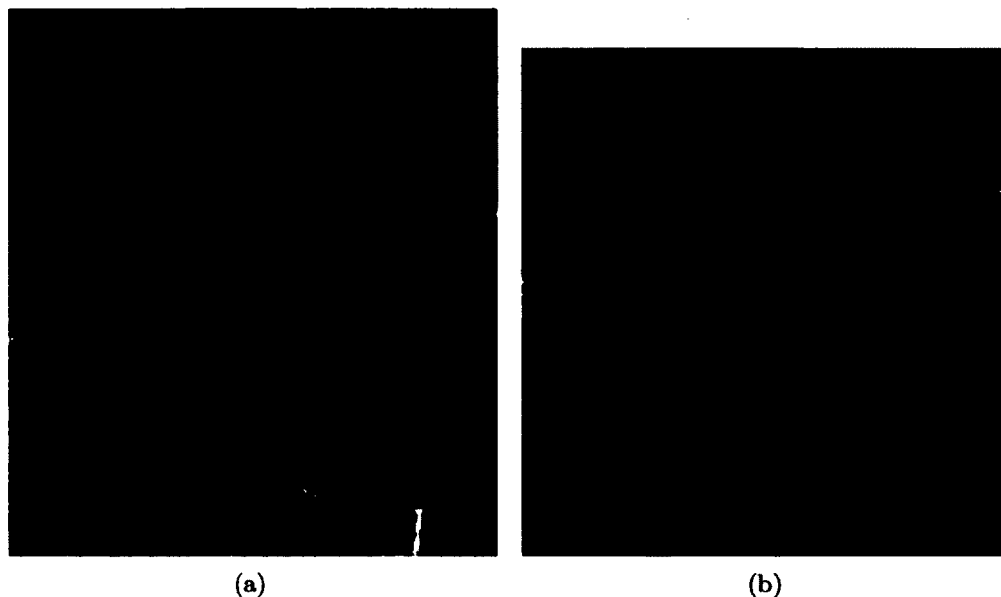
Figure 74. An elevated COLLADA model of a flat slab region using earthquake hypocentral depths from *Cahill and Isacks* [1992]. Gray region is interpolated.

interpreted by *Barazangi and Isacks* [1976] as tears in the Nazca Plate, similar to other areas like the Tonga trench in the western Pacific. However, local seismic data in the transition region around S15° suggested the plate could be deformed (i.e., in continuous flexure) and not torn [*Hasegawa and Sacks*, 1981]. The idea of the plate being deformed and not torn was reinforced by an analysis of teleseismic hypocenters using trend surface analysis, in the region of S2-40° by *Bevis and Isacks* [1984]; *Bevis* [1986]. However, tears were thought to be a possibility in aseismic areas within the central Andean Wadati-Benioff Zone [*Bevis and Isacks*, 1984; *Bevis*, 1986]. More recently, data from the Chile Argentina Geophysical Experiment (Charge) PASSCAL broad-band network, and an updated earthquake relocation algorithm, suggested the likelihood of tears or gaps in the plate between S30-36° [*Anderson et al.*, 2007].

The unique slab geometries in the South American subduction zone motivate this investigation, which uses a series of two-dimensional numerical models is used to explore how subduction zone geodynamics vary as the downgoing slab angle is changed. The parameters of coupling distance (the distance required for the subducting slab and the mantle wedge become fully frictionally coupled) and subduction rate are explored as well. This parameter space exploration guides construction of a

three-dimensional finite element model (Chapter 7), which calculates how juxtaposing different subducting geometries affects mantle temperature and flow fields. The calculated temperatures can then be used to make predictions about physical properties and the deformation style of the Nazca plate in the regions where subduction angle changes.

6.4 NUMERICAL MODEL

Similar to earlier studies (e.g. *Peacock* [1991]; *Davies and Stevenson* [1992]; *Furukawa* [1993]; *Peacock and Wang* [1999]; *van Keken et al.* [2002]; *Conder* [2005]; *van Keken et al.* [2008]) the model domain used in this investigation is a three-component system consisting of a rigid overlying plate, a subducting slab, and mantle wedge (Figure 75). The rigid overlying plate is held stationary, and flow in the mantle wedge is driven by a velocity assigned to the downgoing slab. In some previous studies, the overriding plate has been treated as a non-fixed boundary that dynamically interacts with the wedge through thermal ablation (e.g. *Eberle et al.* [2002]). In others, however, a rigid overriding plate has been used as a control mechanism to make heat flow predictions in the wedge corner region more consistent with observed values (e.g. *Conder* [2005]; *van Keken et al.* [2008]). The rigid plate treatment allows explicit definition of the shallow decoupled (or shear) zone for the downgoing slab [*van Keken et al.*, 2002; *Conder*, 2005; *van Keken et al.*, 2008]. In this investigation, the overriding plate is decoupled from the downgoing slab and it is used as a fixed surface layer that does not interact with wedge flow.

As aforementioned, downgoing slab velocity drives mantle flow in the wedge in this investigation. The subducting slab is treated as oceanic lithosphere. The motion of the downgoing slab induces corner flow in the mantle wedge [*Batchelor*, 1967; *McKenzie*, 1969; *Stevenson and Turner*, 1977; *Furukawa*, 1993; *van Keken et al.*, 2002]. Corner flow is responsible for the transport of hot material into the tip or corner of the wedge and along the subducting slab. Many studies have focused on the effects of using different methods to describe the properties of wedge material, such as by varying viscosity [*Zhong and Gurnis*, 1996; *Kincaid and Sacks*, 1997; *Eberle et al.*, 2002; *van Keken et al.*, 2002; *Billen et al.*, 2003; *Currie et al.*, 2004; *Billen and Hirth*, 2005; *Conder*, 2005; *Kneller et al.*, 2005; *Billen and Hirth*, 2007; *van Keken et al.*, 2008; *Wada et al.*, 2008; *Wada and Wang*, 2009]. In this investigation, the wedge is treated as isoviscous, density was assigned a constant value of 3300 kgm^{-3}, and
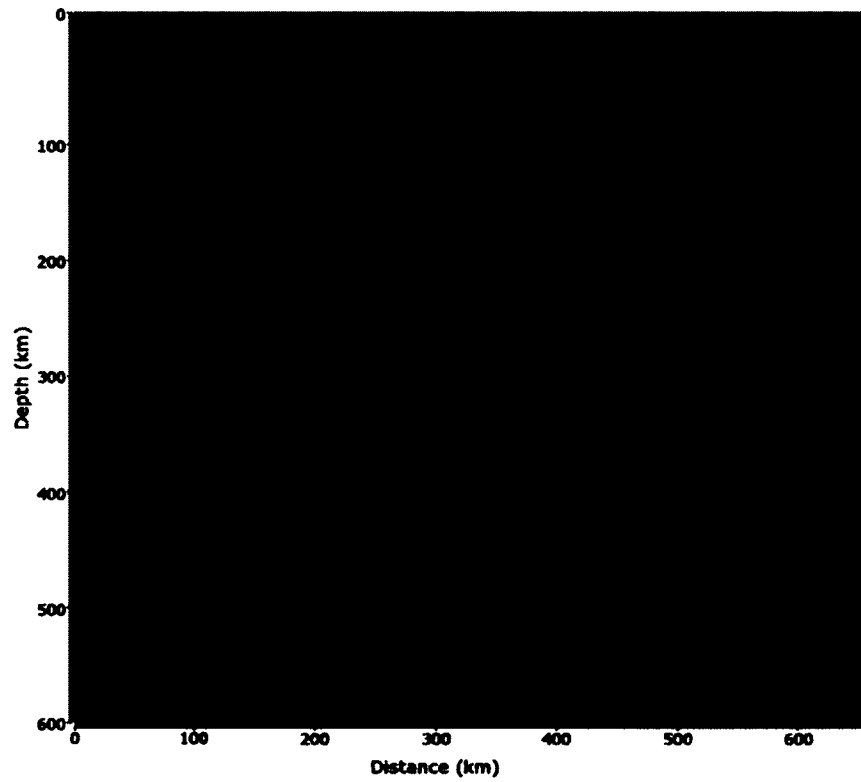
Figure 75. Set-up of model mesh and grid spacing for a 45° model.

sources of buoyancy variation (i.e., temperature dependence) were neglected. This approach allows the subducting slab to be the main driving force of material and heat flow, and permits the effects of varying parameters such as subduction angle to be isolated. The validity of the COMSOL code was checked against known solutions; see Appendix C for further details.

6.4.1 GOVERNING EQUATIONS, MESH, AND BOUNDARY CONDITIONS

The non-dimensionalized, steady-state conservation equations for mass, momentum, and energy were solved using COMSOL Multiphysics finite element software:

$$\nabla \cdot u = 0 \tag{18}$$

$$-\nabla p + \rho g = \nabla \cdot [\eta \nabla u] \tag{19}$$

$$\kappa \nabla^2 T = u \cdot \nabla t \tag{20}$$

where u is velocity, p is pressure, is density, η is dynamic viscosity, κ is thermal diffusivity, and T is temperature.

The spatial dimensions of the numerical domain (Figure 75) are similar to that of van Keken et al. [2008]. The depth (y) of the domain is fixed at 600 km. Domain length (x in km) is dependent on the subduction angle by dividing the depth with the tangent of the subduction angle and adding 60. The addition of an extra 60 km helps to minimize boundary condition effects in the solution. Grid resolution for all models varied from 1 to 5 km, with the upper wedge corner always being gridded with 1 km spacing. Resolution tests for model-predicted wedge temperatures indicate an increase in temperature with an increase of wedge resolution, from 623° C for 5 km resolution to 776°C for 1 km resolution. Increasing the model resolution below 1 km may increase the calculated temperature results somewhat (i.e., by a few degrees). However, these changes would not be large enough to have significant geodynamical implications when mantle temperatures range over 100-1000°C. The resolutions used in this investigation are consistent with Conder [2005]; van Keken et al. [2008]; Wada and Wang [2009], which range from 1 km to 15 km.

Figure 76 and Table 14 summarize the boundary conditions used in the calculations. In Table 14, continuity equation 1 is defined as:

$$\mathbf{n}(\eta_1(\nabla \mathbf{u}_1 + (\nabla \mathbf{u}_1)^T) - \eta_2(\nabla \mathbf{u}_2 + (\nabla \mathbf{u}_2)^T) - \mathbf{p}_1 \mathbf{I} + \mathbf{p}_2 \mathbf{I}) = 0 \tag{21}$$

and continuity equation 2 is

$$\mathbf{n} \cdot (\mathbf{q}_1 - \mathbf{q}_2) = 0; \mathbf{q}_i = -k_i \nabla T_i \qquad (22)$$

where $\mathbf{n}$ is the normal to the surface, $\mathbf{I}$ is the identity matrix, q is the heat flux and k is the thermal conductivity.

For the momentum equations, boundary 1 is a velocity inlet for the slab, with a rate of $u_0 = 3$, 5, or 7 cm/yr (see below for discussion of slab velocity). Boundary 2 is a velocity outlet for the slab, with a rate corresponding to the inlet velocity. Boundary 13 is a mantle wedge inflow boundary, while boundaries 10 and 12 are outflow boundaries. Boundaries 3, 4, 6, and 14 are no-slip and define the rigid overriding plate. The remaining boundaries 5 and 7 delineate the slab-wedge interface and are assigned a velocity defined by a coupling function:

$$u(x) = \left(\frac{x_s - x_c}{x_{fc} - x_c}\right) u_0 \qquad (23)$$

where x_c = corner location, which is the intersection of the bottom of the overriding plate and the downgoing slab; x_s = distance along the slab-wedge interface from the corner location; x_{fc} = location of full coupling, and u_0 = fully-coupled velocity, or the velocity of the downgoing slab. The coupling function, which is based upon the coupling equation of *van Keken et al.* [2008], prescribes a gradual build-up to a fully coupled velocity between the slab and the mantle wedge, at a defined distance down the slab.

The conduction-convection or energy equations use the following boundary conditions. Boundary 1 is assigned a temperature profile corresponding to 50 Myr oceanic lithosphere, using the half-space cooling equation [*Turcotte and Oxburgh*, 1967; *Parsons and Sclater*, 1977]

$$T(x = 0, y) = T_s + (T_0 - T_s) erf\left(\frac{y}{2\sqrt{\kappa T_{50}}}\right) \qquad (24)$$

where surface temperature T_s is the temperature at y = 0 (273 K), mantle reference temperature $T_0 = 1573$ K, and κ is thermal diffusivity ($0.7272 \times 10^{-6} m^2 s^{-1}$) [*van Keken et al.*, 2008]. Boundaries 2, 10, and 12 are heat flux outlets. The top of the model, boundary 4, is set to T_s. Boundaries 5, 6, 7, 8, 9, and 11 are internal boundaries and are set to maintain model continuity. Boundary 13 on the right side of the model is set to a temperature of T_0 to simulate hot mantle material entering the wedge. Boundary 14 is assigned a linear temperature gradient function that ranges between T_s and T_0.
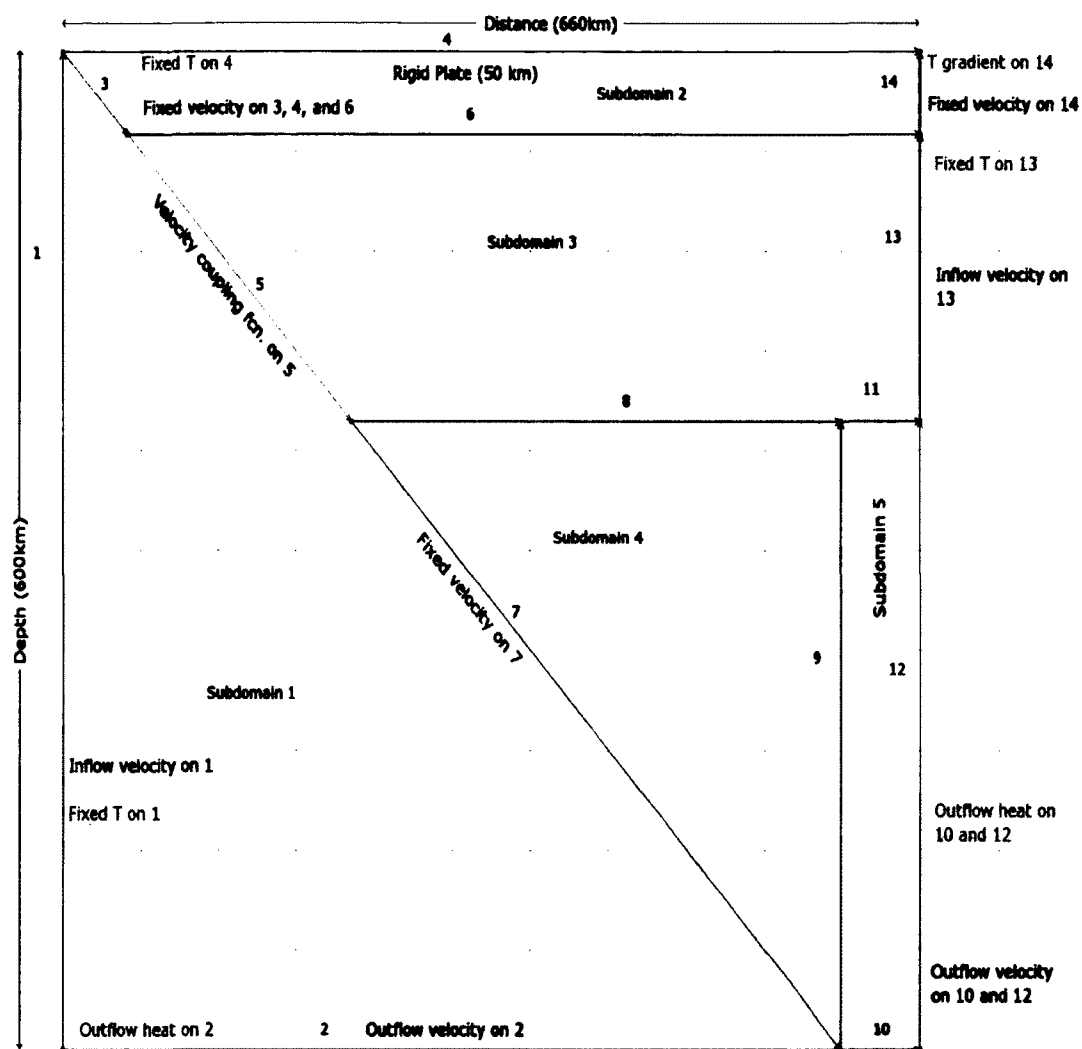
Figure 76. Set-up of model boundary conditions and sub-domains for a 45° model.

Table 14. General boundary conditions used for 2D subduction models in COMSOL

Boundary no.	Navier-Stokes	Conduction-Convection
1	$\mathbf{u} = 5\ \frac{cm}{yr}$	T = half-space cooling
2	$\mathbf{u} = 5\ \frac{cm}{yr}$	$-\mathbf{n} \cdot (-k\nabla T) = q_0$
3	$\mathbf{u} = 0$	$Continuity^2$
4	$\mathbf{u} = 0$	T = 273 K
5	$\mathbf{u} =$ coupling function	$Continuity^2$
6	$\mathbf{u} = 0$	$Continuity^2$
7	$\mathbf{u} =$ coupling function	$Continuity^2$
8	$Continuity^1$	$Continuity^2$
9	$Continuity^1$	$Continuity^2$
10	$\eta(\nabla \mathbf{u} + (\nabla \mathbf{u})^T) = 0,\ p = p_0$	$-\mathbf{n} \cdot (-k\nabla T) = q_0$
11	$Continuity^1$	$Continuity^2$
12	$\eta(\nabla \mathbf{u} + (\nabla \mathbf{u})^T) = 0,\ p = p_0$	$-\mathbf{n} \cdot (-k\nabla T) = q_0$
13	$\eta(\nabla \mathbf{u} + (\nabla \mathbf{u})^T) = 0,\ p = p_0$	T = 1573 K
14	$\mathbf{u} = 0$	T = linear gradient

6.5 PARAMETER SPACE

Many parameters, like subduction angle, convergence rate, coupling length, and viscosity, can influence the geodynamics of the subduction process. The three parameters that were varied in this study are the subduction angle, coupling length, and subducting slab velocity.

6.5.1 SUBDUCTION ANGLE

Previous studies have examined a variety of different subduction angles for specific zones, using parameters customized to the zone of interest (e.g. *Springer* [1999]; *Wada and Wang* [2009]; *Syracuse et al.* [2010]). Here, a general approach was used, so that geodynamic trends in subduction zone and wedge processes could be quantified as a function of slab angle. Subduction angles are varied from 10° to 45°, in 5° increments. This range encompasses the main angles of interest in the subducting Nazca plate, which are 10° and 30° at S15° and S33°.

6.5.2 COUPLING LENGTH

As aforementioned, the coupling length (x_{fc}) is the distance downslab from the corner location (x_c), where the slab and wedge velocities become fully coupled. The mechanism of coupling is an important factor in subduction zone geodynamics. In previous studies by *Zhong and Gurnis* [1996]; *Kincaid and Sacks* [1997]; *Gutscher* [2002]; *van Keken et al.* [2002]; *Billen et al.* [2003]; *Conder* [2005]; *Kneller et al.* [2005]; *Billen and Hirth* [2007, 2005]; *van Keken et al.* [2008]; *Wada et al.* [2008]; *Wada and Wang* [2009] the coupling length or method has been shown to play a key role in determining the wedge temperature and therefore subduction-related volcanism and mineral composition. In these studies, the coupling was incorporated by means of variable viscosity functions and/or by functions prescribing certain slab-wedge interactions through boundary conditions.

The method used in this study (equation 23) allows for a gradual increase of the velocity down-slab until the fully coupled velocity value is reached. This method is chosen because it allows the coupling distance to be changed while still maintaining a consistent dependence on subduction angle, so the model response to both of these parameters can be simultaneously explored. The coupling length distances x_{fc} are varied from 14 km to 99 km downslab.

6.5.3 SLAB VELOCITY

The third parameter examined was slab velocity (u_0), which is simply the rate at which the subducting slab descends into the mantle. Studies by various authors have shown differing results regarding the effect of the slab velocity on subduction zone geodynamics, with some finding the velocity changes the model little and others showing substantial velocity dependence (e.g. *Springer* [1999]; *Wada and Wang* [2009]). These differences can largely be attributed to the treatment of the wedge. *Wada and Wang* [2009] used a variable viscosity wedge while *Springer* [1999] controlled an isotherm in the wedge which was varied systematically to simulate different conditions. This study applies subduction velocities of 3, 5, and 7 cm/yr to three different subduction angles, 10, 30, and 45°. All models had a coupling length (x_{fc}) of 60 km.

6.6 QUANTIFICATION OF MODEL RESULTS

Three primary measures are used to quantify the differences between the various model runs. One measure focuses on the temperature at the corner of the mantle wedge, the second quantifies the temperature structure of the shallow portion of the subducting slab near the corner point, and the third describes the thermal structure of the wedge in a triangular zone near the corner point (Figure 77). All measures are similar to those used by *van Keken et al.* [2008].

The first measure used to quantify the temperature of the system is a singular point downslab of the corner point at a depth of 60 km, called the X60 point. *van Keken et al.* [2008] use a 45° slab angle, it is referred to as the (60,60) point. In this study, however, the description of the point needs to be redefined to account for the subduction angle (θ):

$$T_{X60} = T(\frac{60}{\tan(\theta)}, 60) \tag{25}$$

The points used in quantification of the slab temperature are determined as follows. At a given x-distance which depends on the subduction angle (θ), a vertical line is dropped from the slab-wedge interface, similar to a plumb line. The number of model grid points defining the line is set to be seven, so jmax = 7 in equation 26, below. The use of seven points extends the line for a distance of 36 km, through the region of maximum thermal variation at the top of the subducting slab. Depending on whether local or regional temperature variations are being quantified, a total of either one or seven lines are used. Thus, imax = 1 or 7 in equation 26, below. If one line is used then it is selected to be the first, or shallowest, plumb line in the model. The reported temperature measure, T_{slab}, is simply the square root of the sum of the squares of the temperatures along the line(s), divided by the number of points:

$$T_{slab} = \sqrt{\frac{\sum_{i=0}^{i=imax} \sum_{j=0}^{j=jmax} \left(T[\frac{60+i(9.6)}{\tan(\theta)}, (60 + i(9.6)) + j(6)] \right)^2}{(imax)(jmax)}} \tag{26}$$

The measure of the wedge temperature, T_{wedge}, is the square root of the sum of the squares of the temperatures in the portion of the wedge nearest the corner point. Across all models, the wedge temperatures are sampled to the same depth. A variable number of x-points were included, depending on the subduction angle (θ):

$$T_{wedge} = \sum_{i=0}^{i=11} \sum_{j=0}^{j=(xlim)} \sqrt{\frac{\left(T[\frac{(54+i(6))}{\tan(\theta)} + (j(6)), 54 + i(6)]\right)^2}{(11)(xlim)}} \qquad (27)$$

where xlim is the number of points per (i) that satisfy the condition $x \leq \left(\frac{0.2}{\tan\theta}\right) * 600$
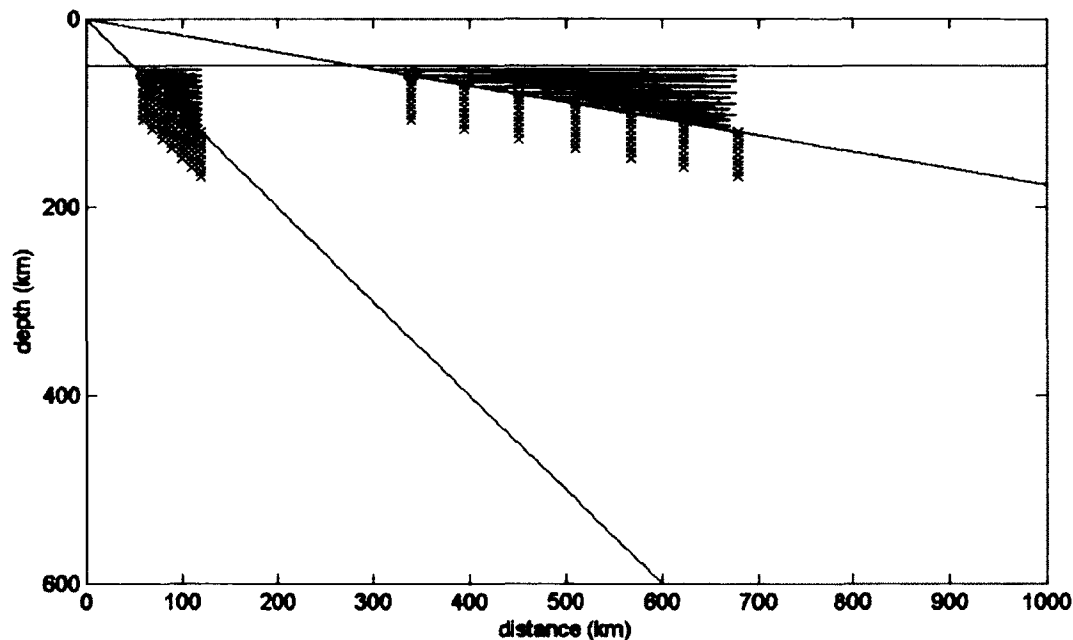
Figure 77. Data points used for calculating temperatures of interest for 45° and 10° models. Red x's = slab, blue regions are for wedges, and black circles are for X60.

6.7 RESULTS AND DISCUSSION

In this study, the two subduction angles of primary interest are 10° and 30°, because they are directly relevant to the Nazca plate and the dynamics of South American subduction. Thus, these subduction angles will be a focus for the discussion of model predictions. Another focus will be the 45° subduction angle, both for examining a more general case and for looking at the geodynamics of a higher-angle slab. *Syracuse and Abers* [2006] show 18 of 52 subduction systems studied had slab dips within 5° of 45°. In some ways, therefore, the 45° model temperature and flow fields can be taken to represent a more general subduction zone system. This Results section will first present a general overview of each of the three main

parameters (subduction angle, subduction velocity, and coupling distance). Then, summary plots of the entire suite of model results will be discussed.

6.7.1 SUBDUCTION ANGLE

Model-predicted temperatures vary strongly with subduction angle. For a 10° angle, temperatures in the mantle wedge near the corner point are very cold, less than 300°C (Figure 78). This is similar to the results found by *Gutscher* [2002], who predicted wedge temperatures of 350-400°C for a shallow subduction angle. The model temperatures are also in agreement with observed surface geographical features, mainly the lack of volcanism above the region with this shallow subduction angle [*Gutscher*, 2002]. *Gutscher* [2002] attributed the lack of volcanism to the colder temperatures, where the hot mantle material does not travel as far into the corner. In contrast, for the 30° subduction angle, wedge temperatures are significantly higher, varying between 600 and 700°C (Figure 79). In the 45° model (Figure 80), there are increased corner flow and higher temperatures in the wedge than the previous two, lower-angle models, suggesting the likelihood of active surface volcanism. *Syracuse and Abers* [2006], in fact, found frequent volcanoes near subduction zones of this type.
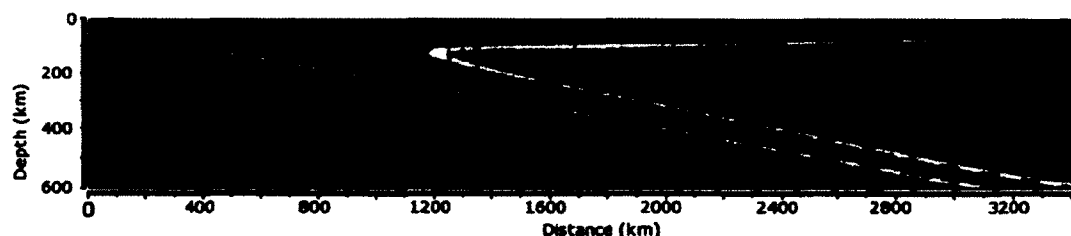

Figure 78. COMSOL model predicted temperature and flow-field for 10° subduction angle and couple distance of 60 km.
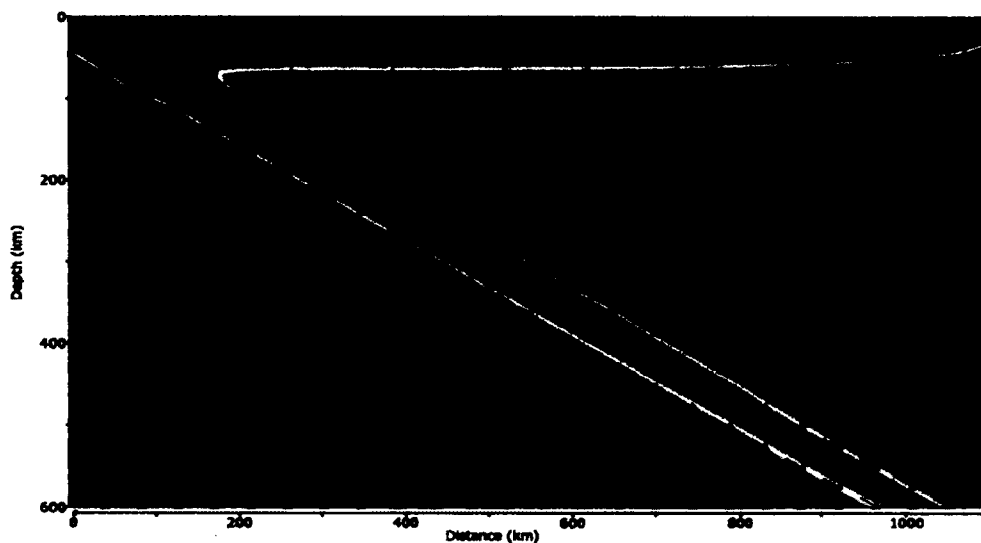
Figure 79. COMSOL model predicted temperature and flow-field for 30° subduction angle and couple distance of 60 km.

6.7.2 SUBDUCTION VELOCITY

Globally, subduction zone velocities vary from around 1 cm/yr to 9 cm/yr [*Schellart et al.*, 2007]. The segment of the Nazca plate which is of interest in this study moves at a rate of 7 cm/yr [*Schellart et al.*, 2007], so model runs for the 10° and 30° subduction angle with this slab velocity would best represent the dynamics of the Nazca-South American system (Figures 81c, 82c). The general trend observed due to a reduction in velocity (from 7 cm/yr to 3cm/yr or 5 cm/yr) is a decrease in the model-predicted wedge temperatures (Figures 81a-b-c and 82a-b-c), similar to work by *Wada and Wang* [2009]. For example, in the 30° models, the wedge temperature changes from ~600°C for 7 cm/yr to ~400°C for 3 cm/yr. The cooler wedge at slower subduction rates could increase earthquakes, because more cold material is available for interplate coupling and brittle failure to occur [*Gutscher*, 2002]. The general case of 45° exhibits the same trend as seen in the 30°Cases. That is, as the velocity decreases, so does the wedge temperature (i.e., from 850°C in the 7 cm/yr model to 680°C in the 3 cm/yr case) (Figure 83).

6.7.3 COUPLING DISTANCE

The method used to examine the role of the coupling distance is to take the

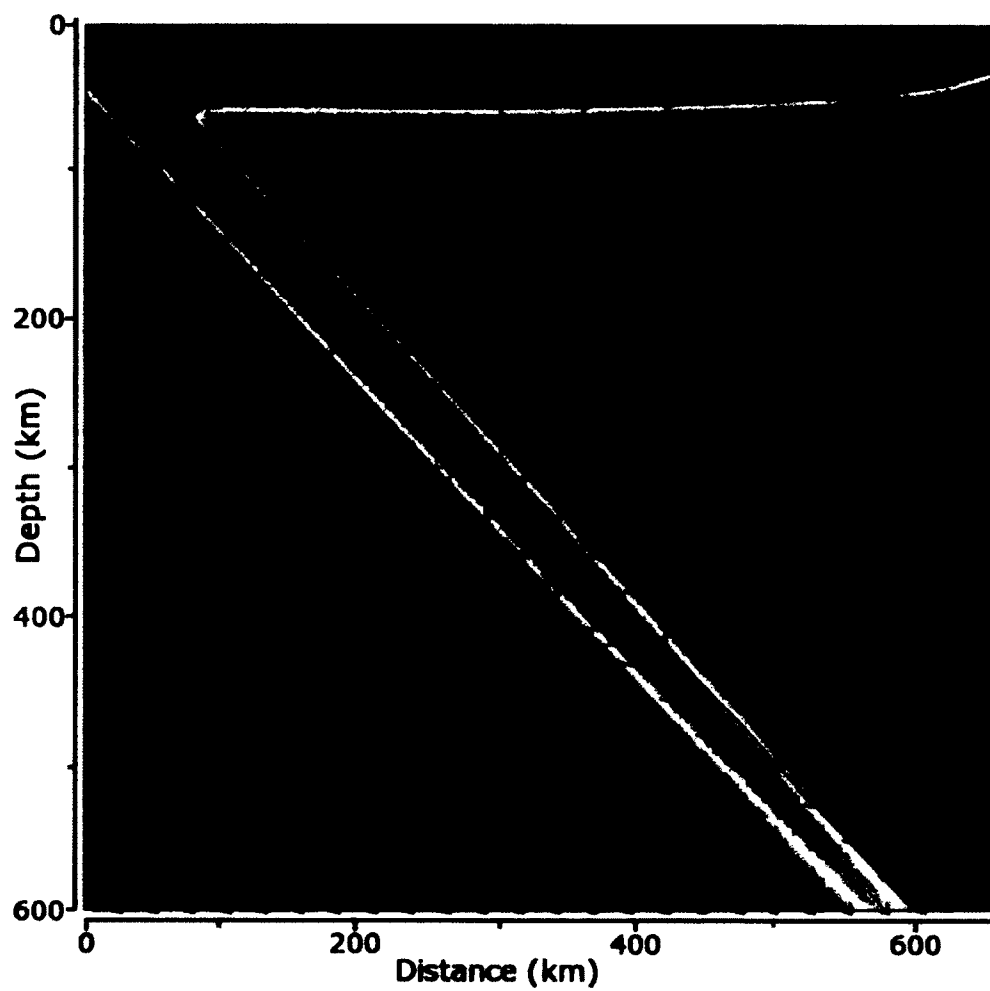**Figure 80.** COMSOL model predicted temperature and flow-field for 45° subduction angle and couple distance of 60 km.
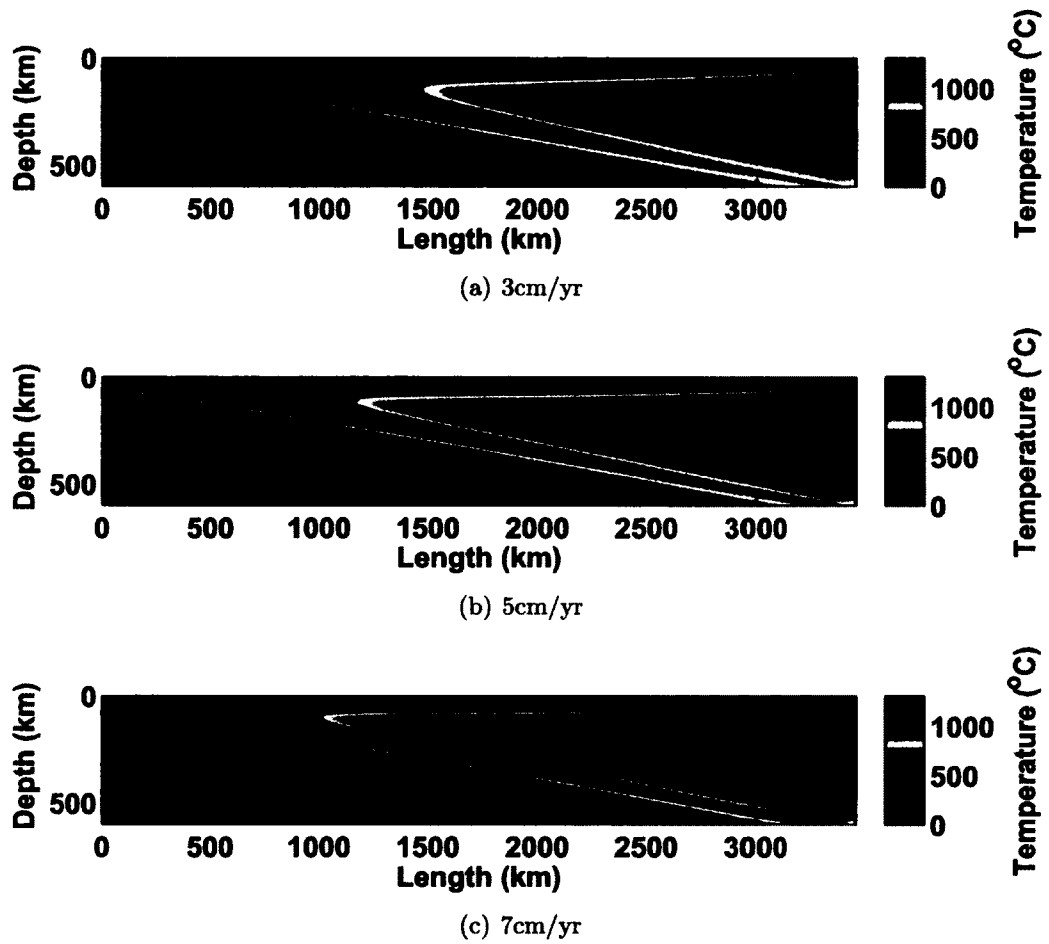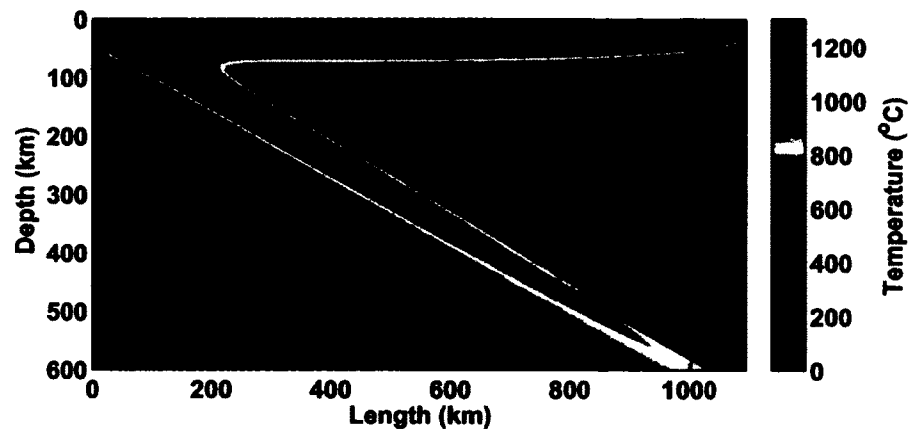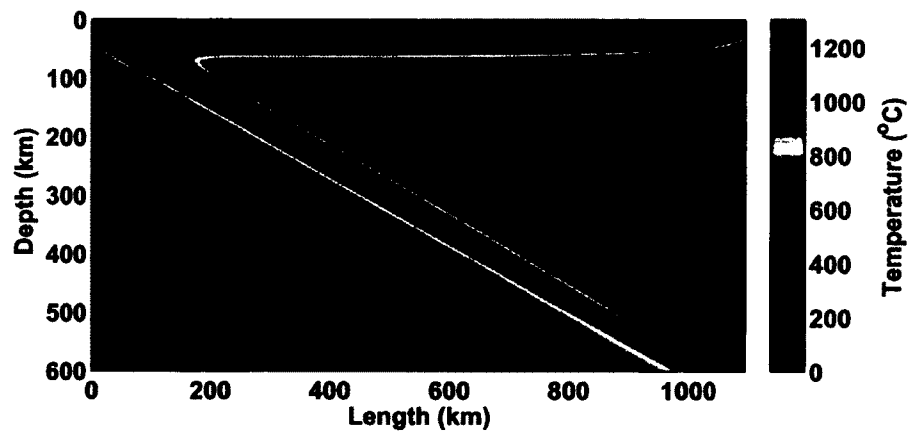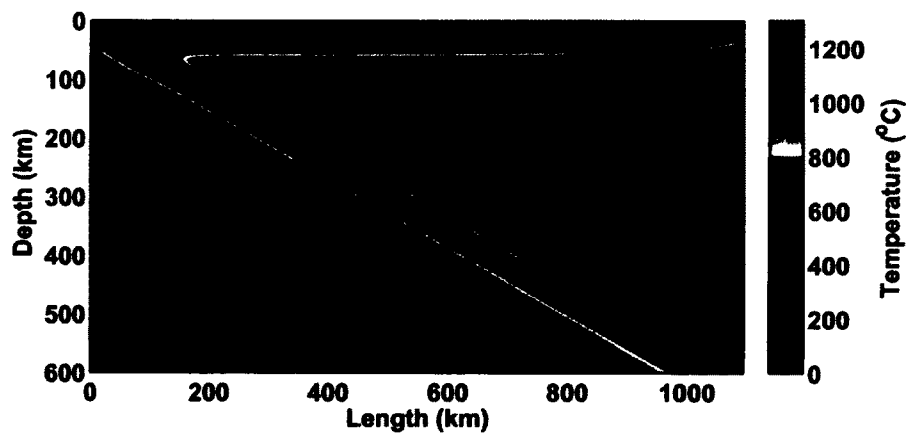
Figure 81. 10° Model predicted temperatures for various slab rates.
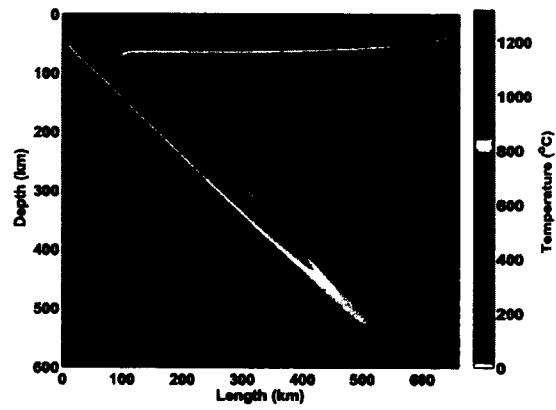
(a) 3cm/yr
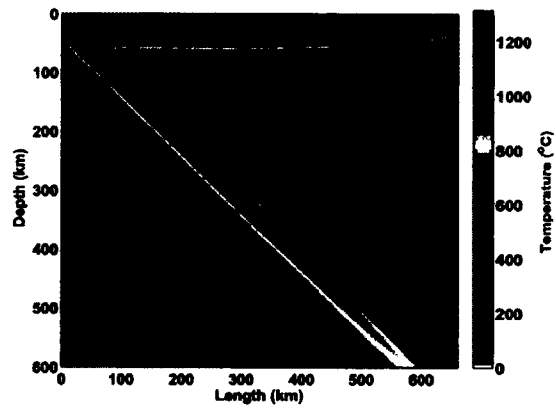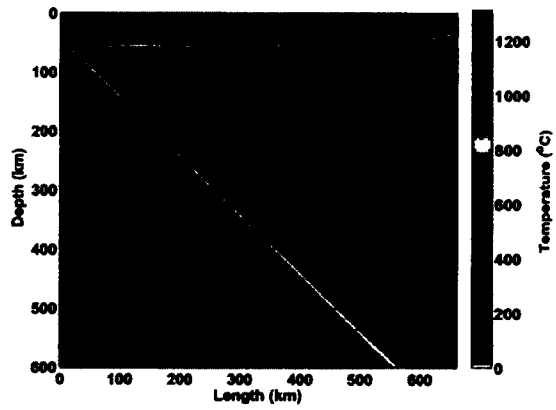

(b) 5cm/yr

(c) 7cm/yr

Figure 82. 30° Model predicted temperatures for various slab rates.

(a) 3cm/yr

(b) 5cm/yr

(c) 7cm/yr

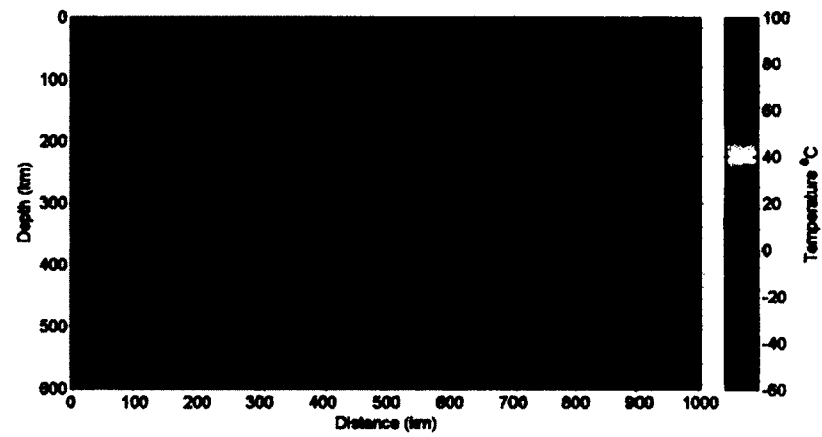**Figure 83.** 45° Model predicted temperatures for various slab rates.

difference between two temperature solutions for different coupling lengths, at the same angle and with a slab velocity of 5 cm/yr. For a 10° subduction angle, the temperature comparisons for Xfc70-Xfc60 and Xfc120-Xfc60 show little difference in the wedge, only approximately 10°C (Figure 84). However, for the slab, there is a large difference of about 60°C for Xfc120-Xfc60 (Figure 84b). The colder slab temperatures for the longer coupling length could correspond to more earthquakes at greater depths, since the slab would remain in the brittle failure regime for a longer period of time.

In contrast to the 10° model, for the 30° model temperature differences occur in the wedge as well as the slab for both Xfc70-Xfc60 and Xfc120-Xfc60 (Figure 85). The farther downslab from the corner point the coupling occurs, the warmer the temperature is at the coupling distance: For the Xfc120-Xfc60 comparison, the temperature difference is 100°C (Figure 85). In the wedge, a cooler region (up to 40°C less) develops upslab of the coupling distance as Xfc is increased (Figure 85b). The slab also has cooler temperatures as the coupling distance increases, similar to the 10° system. One implication of these results is that for a 30° system the coupling distance may be a strong control on how far inland, if at all, volcanoes may form, because an increase in coupling distance delays the temperature increase in the wedge and slab.

In the 45° model case, the longer the coupling distance, the warmer the temperature of the wedge is at the full couple depth (Figure 86). In temperature difference plots, cold lobes occur upslab of the coupling point. Both of these trends were predicted for the 30° case as well. However, temperature differences are more localized for the 45° model compared to the 30° model. This may indicate that the 45° system is less sensitive to coupling distance than the 30° case, potentially because of the increased flow in the corner described earlier (Figures 79 and 80). The greater flow in the 45° model brings an increased amount of warm mantle material through the corner. So, even when delaying the couple the extra material flow tends to homogenize wedge temperatures. Thus, higher flow rates could act to homogenize warm mantle temperatures. However, the system would still potentially have an increase in earthquakes, if the coupling distance was larger.

6.7.4 SUMMARY PLOTS OF MODEL RUNS

In this section, suites of model runs are summarized using the measures of wedge,

(a) Xfc70-Xfc60
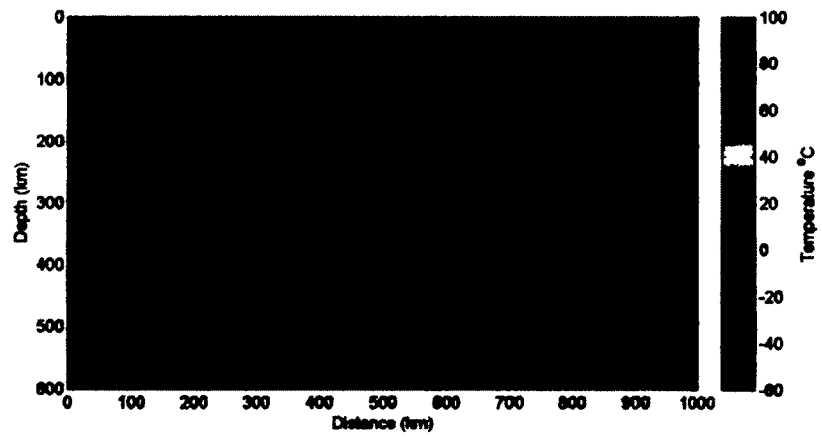
(b) Xfc120-Xfc60

Figure 84. 10° Model predicted temperatures comparison for different coupling values. The red x's are the locations used to calculate slab temperatures.
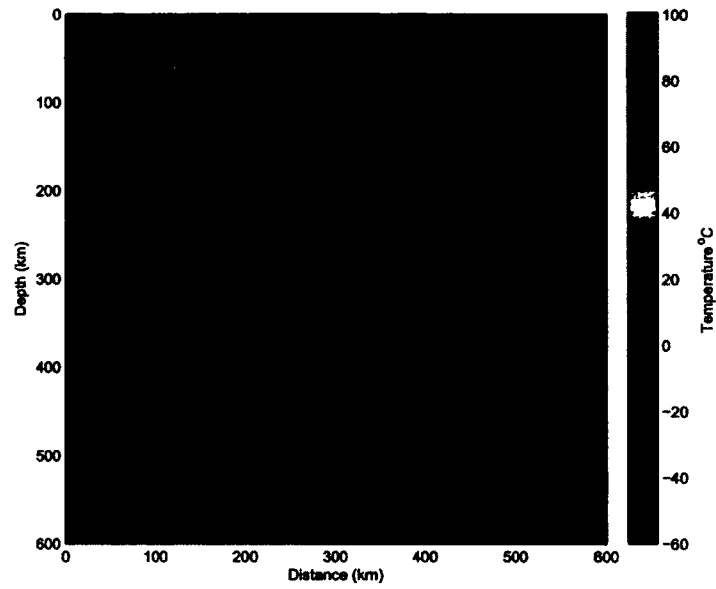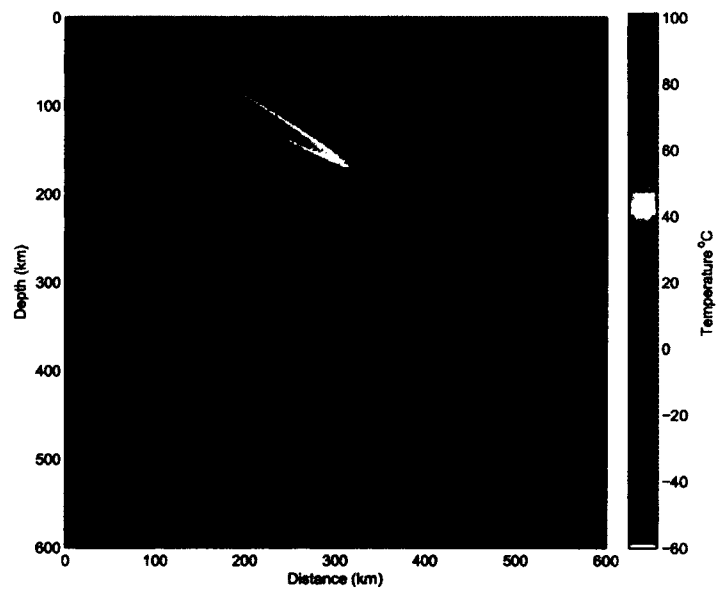
(a) Xfc70-Xfc60

(b) Xfc120-Xfc60

Figure 85. 30° Model predicted temperatures comparison for different coupling values. The red x's are the locations used to calculate slab temperatures.
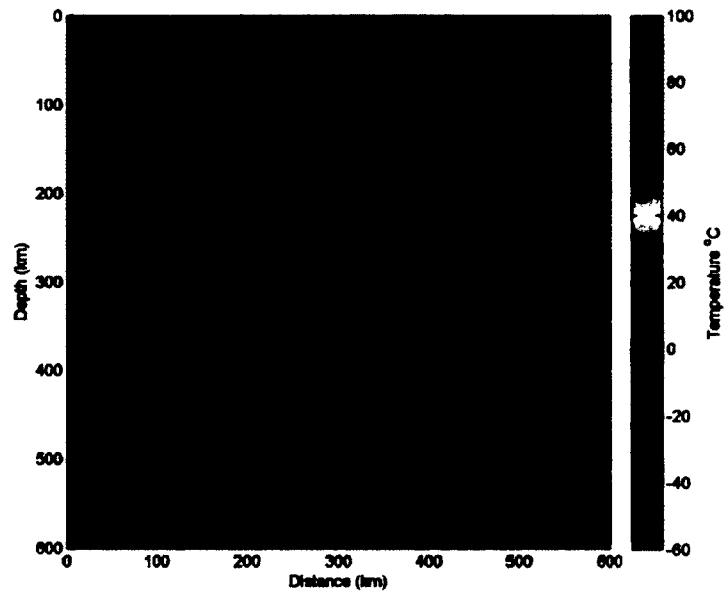
(a) Xfc70-Xfc60
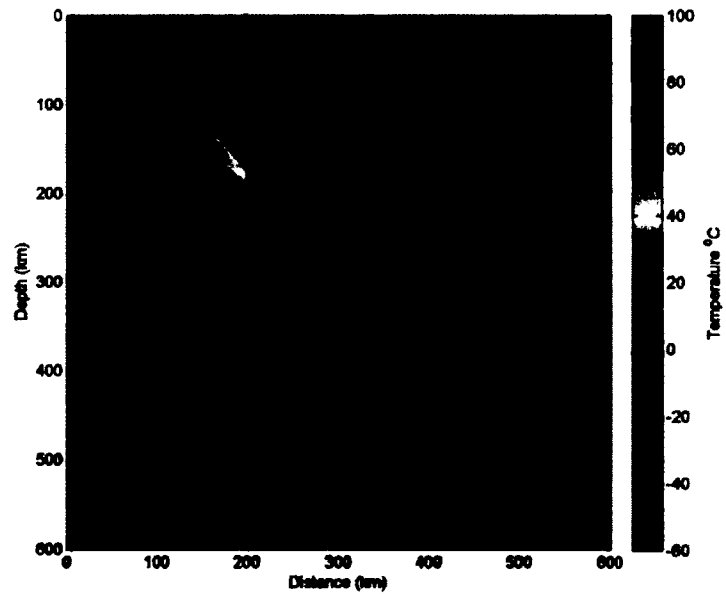
(b) Xfc120-Xfc60

Figure 86. 45° Model predicted temperatures comparison for different coupling values. The red x's are the locations used to calculate slab temperatures.

slab, and X60 point temperatures described above. General trends that emerge from the parameter space exploration are presented, and their geodynamic implications are discussed.

For the wedge, there is a direct relationship between subduction angle and temperature (T_{wedge}), over a wide range of subduction angles (10-45°) and coupling lengths (10-100 km) (Figure 87). For example, wedge temperature increases from $\sim$ 250°C for 10° subduction to $\sim$ 750°C for 45° subduction. The relationship between coupling distance and T_{wedge} for a given subduction angle is more complex. In the shallow-angle subduction zones (except 10°), the shorter the coupling length, the lower T_{wedge} . However, for steeper subduction angles like 45°, the smaller coupling lengths produce higher wedge temperature than the longer coupling lengths. For a 45° angle, wedge temperature is approximately 780°C for a coupling length of $\sim$20 km, but it is approximately 710°C for a coupling length of $\sim$100 km. The cross-over between the two coupling length trends occurs at 30°. For higher subduction angles, shorter coupling lengths allow for increased corner flow (higher quantity of warmer material) to move into the wedge. By delaying the couple, the velocity is slightly lower in the corner and less warm material flows into the corner region.

In the wedge temperature plot (Figure 87), the spread of T_{wedge} with coupling distance for a given angle is dependent on the subduction angle. For a 10° angle, the spread is very small (8°C). This is consistent with the temperature difference plots of Figure 84 which had very little temperature variation between different coupling lengths. However, for steeper angles (45°) the spread is much larger (70°C), which is also in agreement with the temperature difference plots of (Figure 86). The smaller spread for shallower angles (e.g. 10°) can be attributed to lower corner flow in the wedge, which causes the wedge to be colder overall and less responsive to velocity changes in the wedge. The small spread at 35° may be related to the transition from the shallower angles (where heat transfer in the wedge due to conduction in the wedge is relatively more important) to the larger angles (where heat transfer in the wedge due to conduction is relatively less important). At 35°, the longer couple distance is in the middle of the dots, which creates a smaller spread. Focusing on just the longer coupling distances at each angle in Figure 87 shows that the longer coupling distance systematically moves from hotter to colder temperatures and the inversion occurs at 35°.

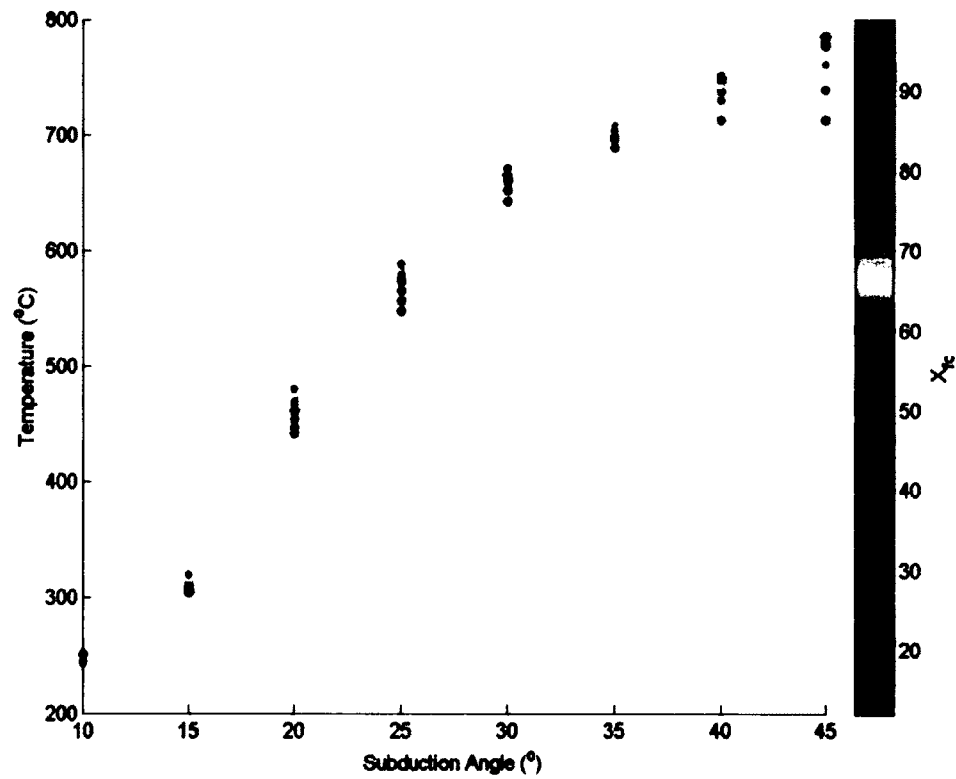For the slab, two methods were employed to examine temperature trends, the

Figure 87. Model predicted wedge temperatures, calculated from equation 27, for various angles and coupling lengths. Results shown are for a subduction velocity of 5 cm/yr.

single and multi-line methods. The methods are intended to help quantify the slab temperature structure near the slab-wedge corner (single-line method) as well as for the slab in general (multi-line method). In general, T_{slab} in the single-line slab method correlates positively with subduction angle (Figure 88). T_{slab} ranges from a low value of 320°C for a 15° angle, to 460°C for a 45° degree angle. The 10° model is an exception to this trend. It has a temperature of approximately 370°C. The 10° model may differ because a significant source of slab heating for this angle is from the mantle material beneath the slab.

As in the case of the wedge temperatures, the response of the single-line slab temperature to coupling distance at a given angle is complex. There is a cross-over between angles of 15° and 20°. For shallower angles, the shortest coupling lengths have the warmest temperatures, although the spread in temperatures as a function of coupling length is small (~ 10°C). For higher angles, the longer coupling lengths are warmer than the shorter lengths. For example, for a 30° subduction angle, the Xfc120 temperature is 385°C compared to 363°C for Xfc60. An exception is the 45° model, which shows the same trend as the 10 and 15° models of having the shortest coupling length being the warmest. For the 45° model, single-line T_{wedge} is 464°C for Xfc60 but 458°C for Xfc120.

These trends may be explained by how different coupling distances alter the material flow in the wedge, which indirectly affects the slab. Two effects of coupling length in the wedge can be to cause a cool spot to be generated upslab of the coupling point, and a warmer spot to develop at the coupling point. Since the single-slab T_{slab} is calculated at the couple point, when a warmer spot is built up at the coupling distance, the slab temperature will be higher. This is the effect seen from 20-40°. The shallow angles of 10° and 15° are not significantly influenced by the value of the coupling distance, and the cold spot generated by the delay is larger than the increase at the coupling point.

The second T_{slab} quantification method incorporates seven sampling lines (Figure 89). For the multi-line sampling method, the trend with subduction angle is from hot temperatures (583-593°C) at 10°, to cool temperatures (469-513°C) at 35°, the inversion value, and back to warmer temperatures (471-530°C) at 45° (Figure 89). The inversion arises because the slab is heated from below for a longer period when the angle is shallow. However, there is balance between heating from below and material flow in the wedge. As the angle increases the heating from below decreases
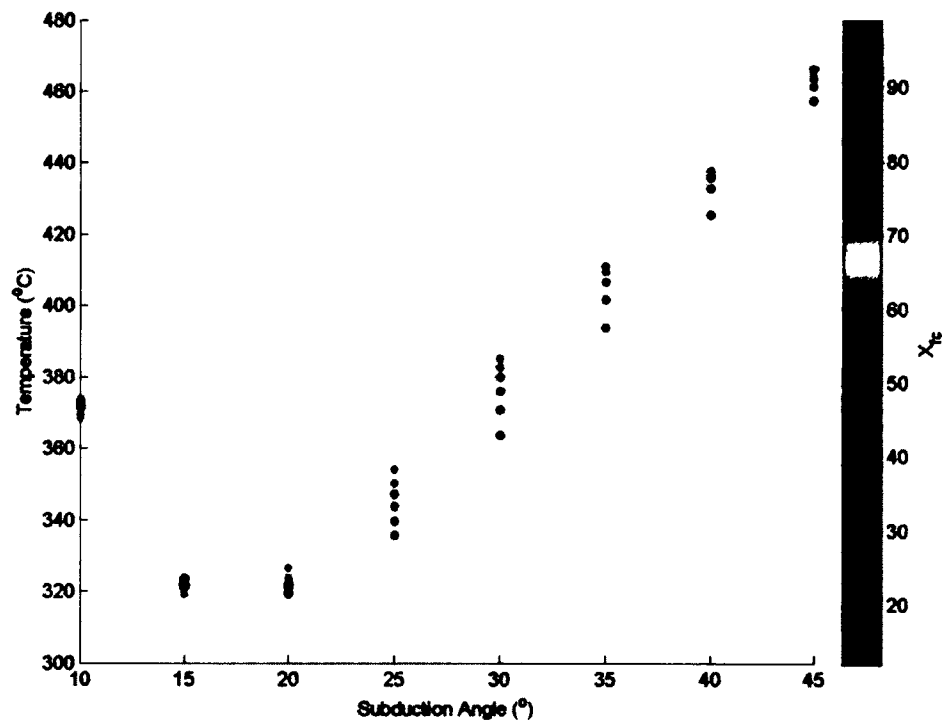
Figure 88. Model predicted single-line slab temperatures, calculated from equation 25, for various angles and coupling lengths. Results shown are for a subduction velocity of 5 cm/yr.

while the material flow in the wedge increases. The corner flow heating of the slab shows dominance for angles greater than 35°. This would imply that for the Nazca plate, the dominant mechanism for heating is from beneath the slab and not from wedge flow.

When a larger portion of the slab is sampled in the multi-line method, several features of the model suite become apparent. One feature involves the variation of T_{slab} with coupling length for a given angle. For all angles, the hottest temperatures occur at the shortest coupling distances. The second trend is that the temperature difference between the largest and smallest coupling distances increases with subduction angle, from 10°C at an angle of 10°, to 58°C at an angle of 45°. Compared to the single-line method, the multi-line method shows a larger response to change in coupling distance. For example, for a subduction angle of 30°, the temperature difference between the largest and smallest coupling distance was 21°C in the single-line method, while for the multi-line method, the difference was 38°C. The larger difference for the multi-line method may be due to the fact that the single-line method samples a limited region near the slab-wedge corner.

For the X60 point, the overall trend of temperature with subduction angle is similar to that of the slab (Figure 90). The inversion or inflection point in the predicted temperatures occurs at an angle of 25°. For a given angle, the X60 temperatures are higher for a shorter coupling distance. The X60 point, unlike the slab temperature measures, seems to be more sensitive to the coupling length even for small angles (10 and 15°), showing a variance of $\sim$20°C. This could be because the slab temperatures measures are averaged over a number of points.

As discussed earlier, the wedge and slab temperatures are sensitive to the velocity of the downgoing slab (Figures 91,92,93). For both the single-line and multi-line slab measures, increasing subduction velocity results in a decrease in T_{slab}. For example the multi-slab measure for a 30° subduction angle decreases from 521 to 509°C as velocity is increased from 3 cm/yr to 7 cm/yr (Figures 91,92). The slab temperature decrease with velocity can be attributed to plunging cold material downward faster, thus giving the material less time to heat up by either convection or conduction. The X60 point shows a similar trend to the slab for all angles (Figure 94).

The wedge temperatures show a more complex relationship with subduction velocity. For the 10° subduction angle, as the velocity increases the temperature decreases, from 345°C (3 cm/yr) to 278°C (7 cm/yr) (Figure 93). However, for 30 and
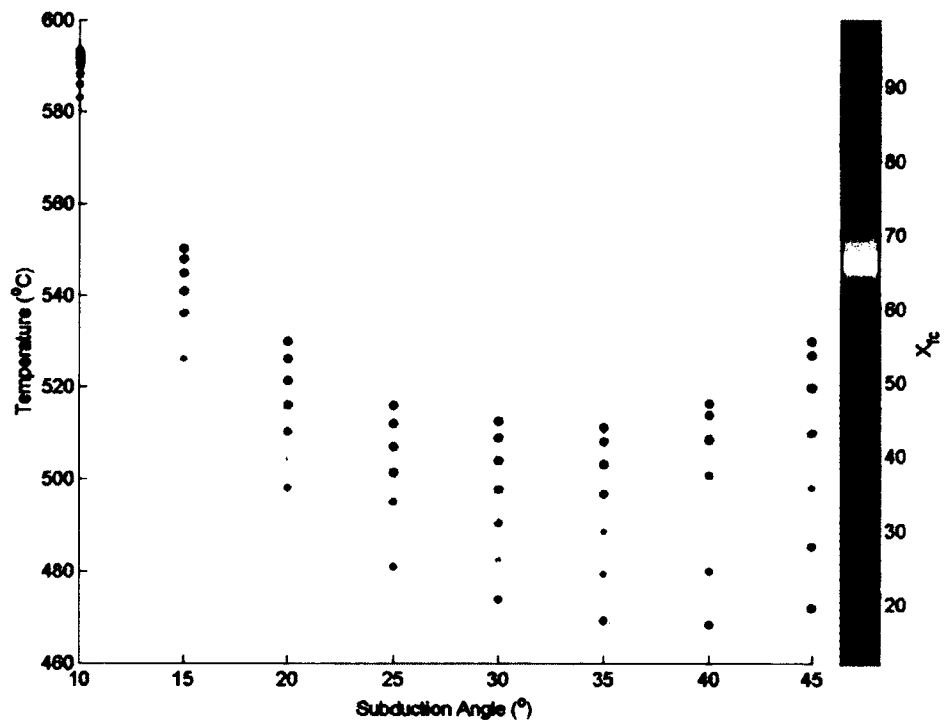
Figure 89. Model predicted multi-line slab temperatures, calculated from equation 25, for various angles and coupling lengths. Results shown are for a subduction velocity of 5 cm/yr.
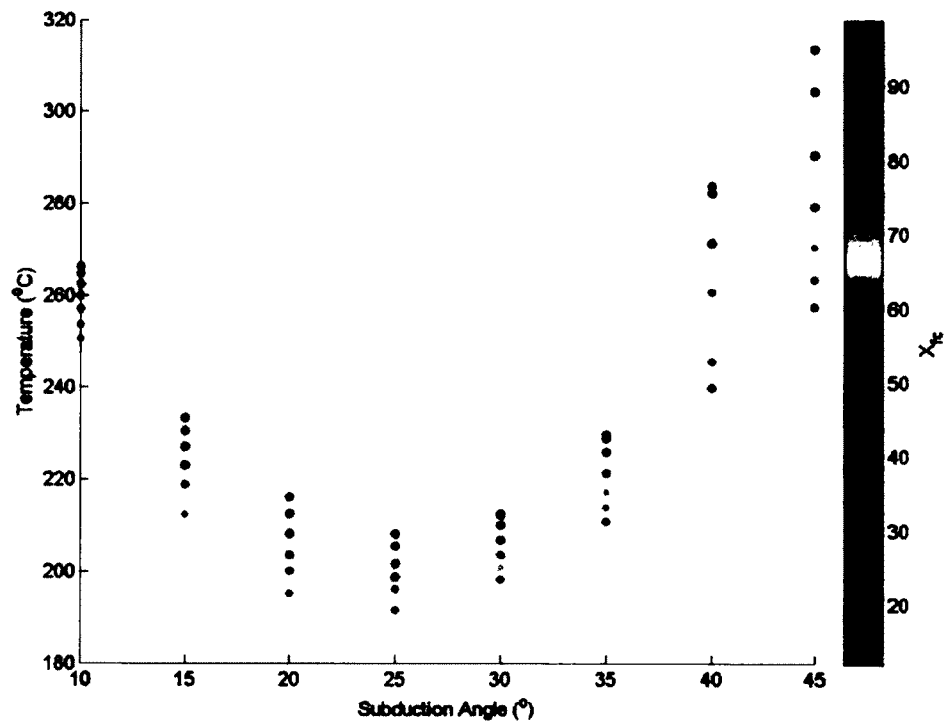
Figure 90. Model predicted X60 temperatures for various angles and coupling lengths. Results shown are for a subduction velocity of 5 cm/yr.

45° angles, when the slab velocity increases the temperatures increase, (i.e., for a 45° angle, from 675°C for 3 cm/yr to 843°C for 7 cm/yr). This result is related to a combination effect of slab heating from below and convection in the wedge. When the 10° slab subducts at higher velocities, the cooler slab from the faster subduction contributes to the cooling of the wedge. At the same time, corner flow pulls very little warm material into the wedge corner. For the higher angle slabs, the faster the velocity the more warm material is pulled further into the wedge.
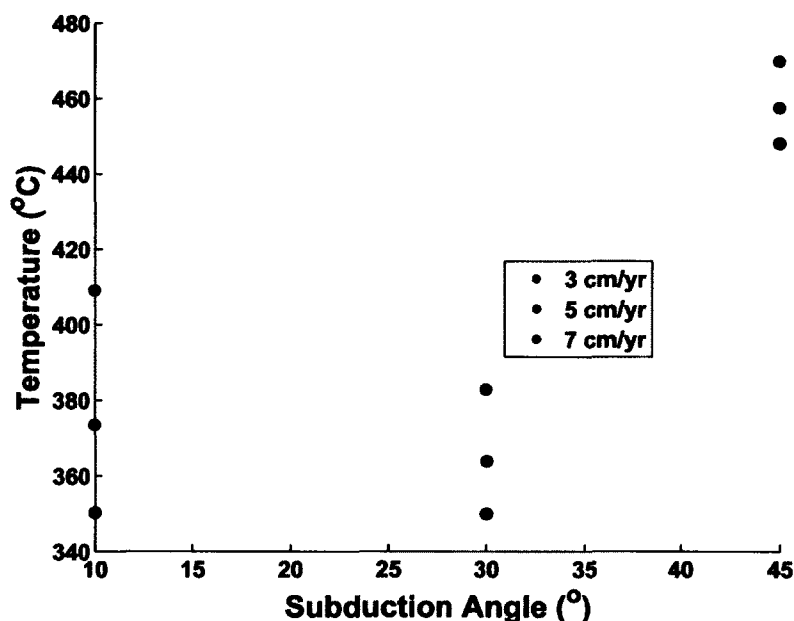
Figure 91. Model predicted single-line slab temperature comparison for varying subducting velocities and angles.

6.7.5 IMPLICATIONS FOR NAZCA SUBDUCTION GEODYNAMICS

One goal of this study was to better understand how each of the parameters investigated can influence the geodynamics of the Nazca subduction zone. As mentioned earlier, the models of most interest are the 10° and 30° simulations, which represent adjacent angles in the downgoing Nazca plate at S33°. The 10° model showed significant sensitivity to slab velocity. Varying slab velocity from 3 cm/yr to 5 cm/yr resulted in temperature changes in the wedge of as much as 67°C (Figure 91,92). The single-slab and X60 temperature measures also showed large responses to slab velocity, with temperature changes of up to 59°C in the slab and 63°C for the X60
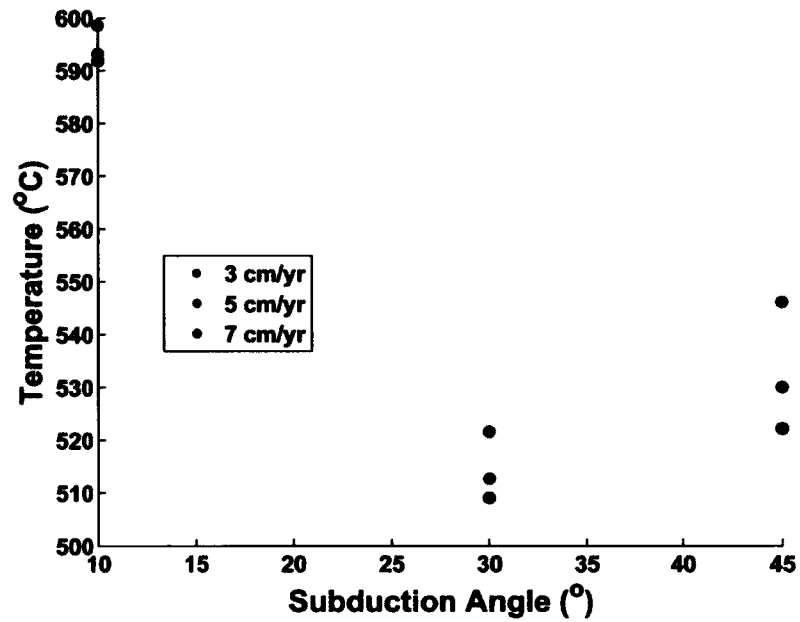
Figure 92. Model predicted multi-line slab temperature comparison for varying subducting velocities and angles.
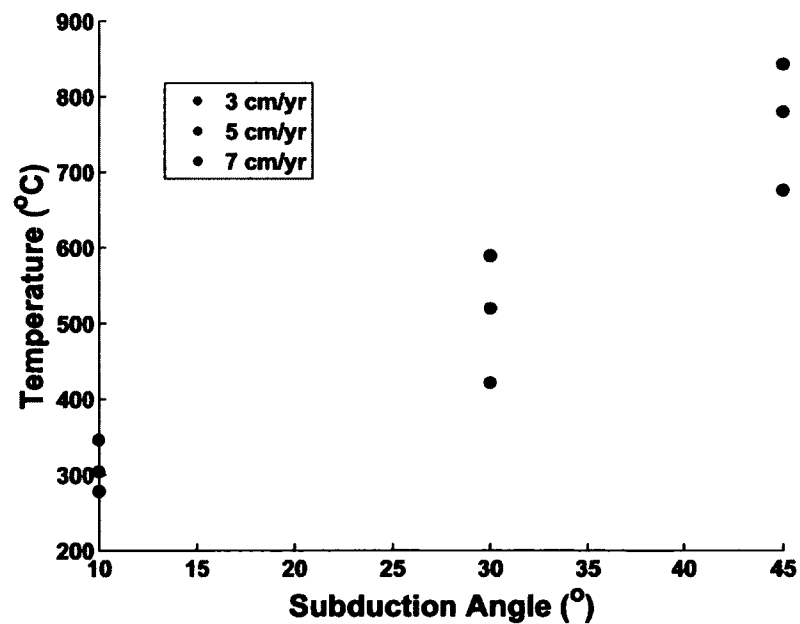
Figure 93. Model predicted wedge temperature comparison for varying subducting velocities and angles.
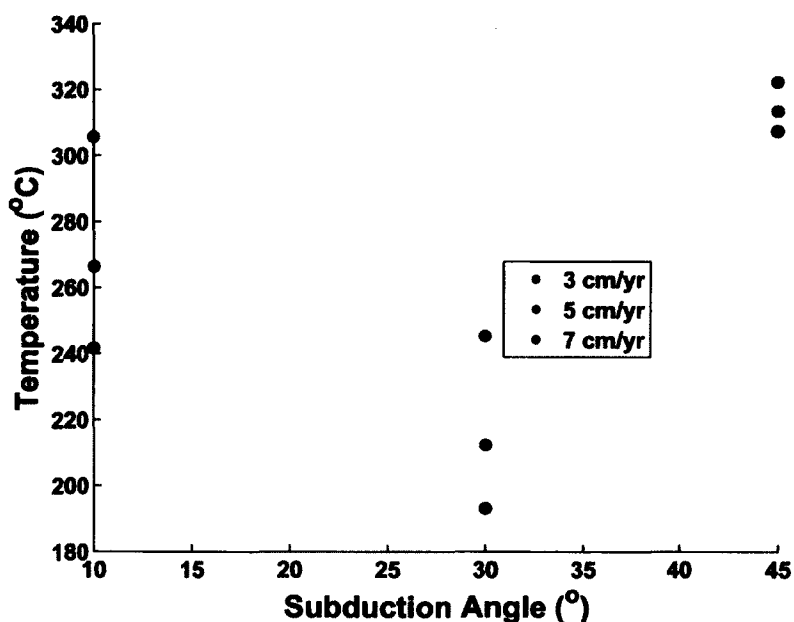
Figure 94. Model predicted X60 temperature comparison for varying subducting velocities and angles.

point. On the other hand, the 10° models are not sensitive to coupling length. As coupling length is varied, the spread in temperature predictions for the wedge, slab, and X60 point is a maximum of about 16°C (Figures 87-90).

For the 30° model, the multi-line T_{slab} is sensitive to the coupling length, with a temperature variance of 50°C over the range of coupling lengths modeled (Figure 89). The wedge also shows some sensitivity to coupling length with temperature results varying by 30°C (Figure 87). However, the parameter that impacts T_{wedge} the most is the slab velocity, with temperatures varying by as much as 190°C. The X60 and single-line slab temperatures showed less sensitivity to changing the velocity, with temperatures varying by about 40°C. The multi-slab temperature was the least responsive to velocity, with temperatures changing by only 12°C.

Overall, the largest changes in temperature came from varying the subduction angles themselves. The wedge temperature varied between the two angles by 500°C. The single-line slab and X60 temperatures changed by 70 and 60°C, respectively. Again, the multi-line method was least responsive to temperature variations, changing by only 20°C at most.

Thus, this study predicts that in a subduction zone such as the Nazca region,

where downgoing slabs of two different angles are juxtaposed, the greatest influence on predicted mantle temperature fields will be the slab angles. For example, in a three-dimensional model of the Nazca region where two boundaries of the model are proscribed to be 10° and 30° downgoing slabs, the interaction of the different subduction angles would likely impact the model more than the slab rate or coupling distance. Uncertainties in subduction rate of 1 or 2 cm/yr would probably not affect the general geodynamics of the system as much as uncertainties in slab angle.

6.8 CONCLUSIONS

This investigation uses a series of two-dimensional numerical models to quantify the sensitivity of subduction zone geodynamics (specifically, thermal fields) to subduction angle, subduction velocity, and coupling distance. The main conclusions of this investigation of are:

1. Subduction angle has the largest impact on model dynamics. Varying the subduction angle resulted in temperature variations of up to 500°C in the wedge. These variations result from the strong dependence of corner flow on subduction angle.

2. The second most important variable is the subduction rate, and the coupling distance influences the models least. Varying subduction rate and coupling distance resulted temperature changes of a 70°C or less in the wedge for a given angle. These relatively smaller changes are due to the angle dictating the overall corner flow regime; these other parameters cause variation within the angle.

3. In the subducting Nazca plate, where angles of 10° and 30° are adjacent, the juxtaposition of different angles is likely to be an important control on the geodynamics of the convergent margin. Uncertainties or errors in the velocity of the downgoing plate and the assignment of coupling distance are unlikely to qualitatively affect patterns of mantle temperature and mantle flow.

The results of this chapter can be expanded upon to a create a 3D numerical model. Knowing the influence the various parameters have in subduction zone dynamics will allow for a better understanding when choosing boundary values for a 3D system. The 3D model in chapter 7 is designed to study the transition zone slab that results from a multi-angle subduction process.

CHAPTER 7

3D NUMERICAL MODELS

In this chapter a 3D numerical model is used to explore the transition region between two different subducting angles. This work builds upon the results of chapter 6 through incorporating the model predicted temperature and flow solutions as boundary conditions. The results from the 3D calculations are used in analysis of the transition zone by brittle-ductile maps ands ductile-deformation mechanism maps. The model predicted results are also examined for changes in flow patterns due to the two subduction angle process. This chapter will be part of a paper submitted to a peer review journal in the Summer of 2012 with co-author J. Georgen.

7.1 ABSTRACT

The downgoing Nazca plate has adjacent subducting angles of 10° and 30°. A steady-state, 3D finite element numerical model is used to better understand the transition region between the juxtaposed angles. The model space is generated by using 2D solutions as boundary conditions for the trench-perpendicular "endcaps" of the numerical domain. The overall 3D model contains a rigid overlying plate, two subducting slabs (10° and 30°), and a mantle wedge with a geometry that changes in the z-direction. Models solve the conservation equations of mass, momentum, and energy, neglecting heat production and thermal buoyancy and assuming isoviscous mantle flow. Temperature solutions from the 3D models are used in calculations to quantify the brittle and ductile zones of the model domain and deformation mechanisms for the slab between the end caps. Three main conclusions can be drawn from the model and calculations. First, trench-parallel flow is predicted to occur during the subduction process. Also, the uppermost portion of the model space shows a continuous brittle section for distances of up to ~180-240 km perpendicular to the trench. Last, analysis of a region at a distance of 300 km from the trench suggests that the slab is mostly in an 'inelastic' state, with a small portion in power law creep.

7.2 INTRODUCTION

The downgoing Nazca plate around S33° has adjacent subduction angles of 10° and 30°. Seismic data from *Anderson et al.* [2007] show a clear distinction between these two angles over an along-trench distance of about 100 km. The purpose of this study is to investigate mantle geodynamics in the region of subduction angle transition using a 3D finite element numerical model. The 3D model is an extension of the 2D models discussed in chapter 6. It is generated by using 2D solutions as boundary conditions for the trench-perpendicular "endcaps" of the model domain.

Additionally, temperature solutions from the 3D models are used in calculations to quantify the brittle and ductile zones of the model domain. Brittle-ductile maps are plots that indicate where a system will fail by either a brittle mechanism or a ductile mechanism. Brittle strength laws are generally determined in laboratory settings, by measuring the fracture limits of a material like rock under different physical conditions to develop mathematical relations between stress and failure [*Byerlee*, 1978; *Sibson*, 1981]. Ductile stress rheological laws are determined with statistical mechanics and experimental data, and generally involve a power law relation [*Karato and Wu*, 1993; *Violay et al.*, 2010]. In this investigation, brittle and ductile stresses are calculated at each point in the 3D model, and the lower of the two values is assumed to be the applicable failure mechanism at that point [*Carminati et al.*, 2005; *Conder*, 2005; *Violay et al.*, 2010, 2012]. The patterns of deformation mechanism are then used to discuss the nature of the downgoing Nazca plate in the region where subduction angle transitions.

7.3 DESIGN OF 3D MODEL AND NUMERICAL METHODOLOGY

As mentioned above, the 3D model is created by using 2D solutions for 10° and 30° subduction zones as boundary conditions [*van Keken et al.*, 2002, 2008; *Conder*, 2005; *Peacock and Wang*, 1999; *Davies and Stevenson*, 1992; *Furukawa*, 1993; *Peacock and Wang*, 1999]. The total length of the model in the along-trench (z) direction is 48 km (Figure 95). The overall 3D model contains a rigid overlying plate, two subducting slabs (10° and 30°), and a mantle wedge with a geometry that changes in the z-direction. To reduce the computations required, a triangular slice with a 30° angle is cut out from the subducting slab. This region is of little interest in investigating Nazca subduction geodynamics, and the cut allows for a higher mesh

resolution in the wedge.
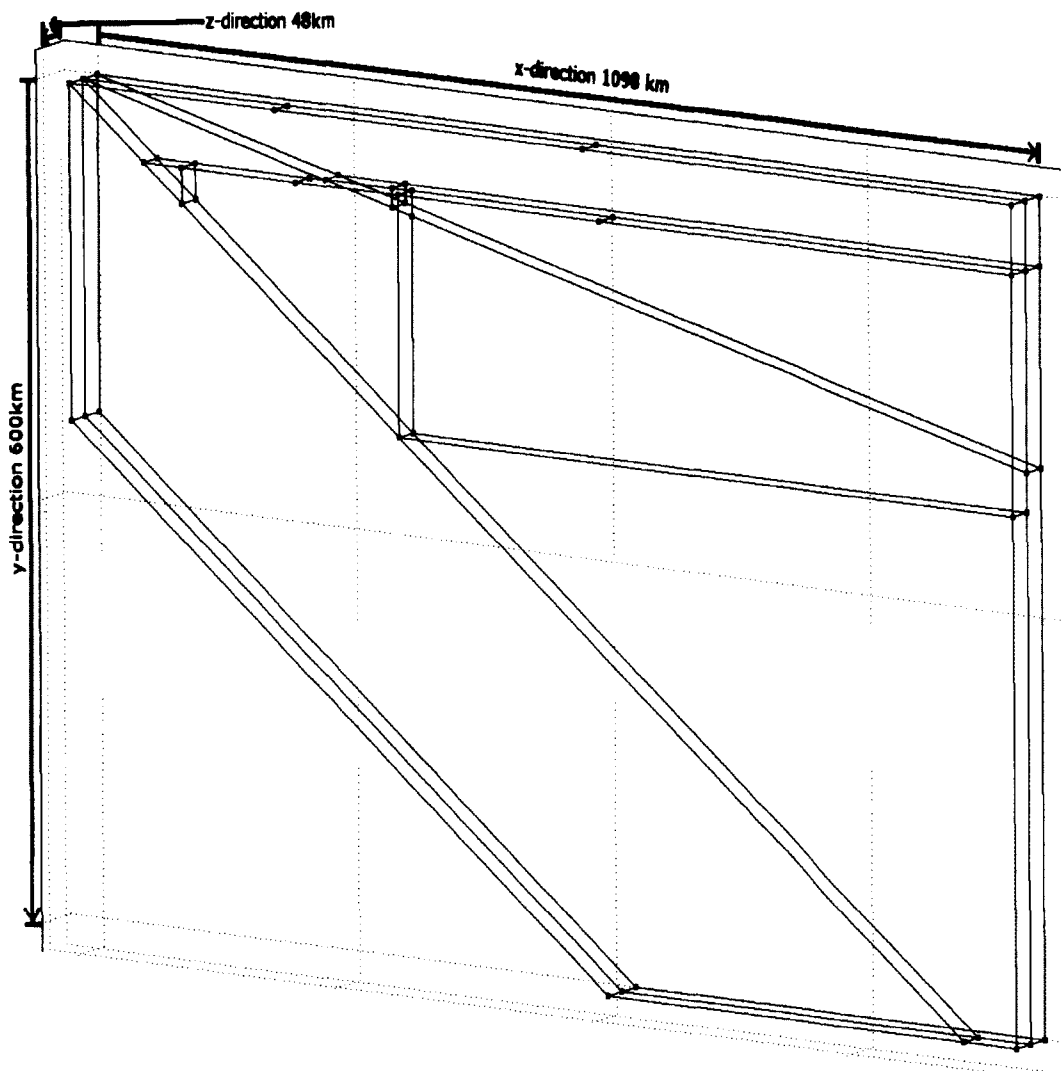
Figure 95. Numerical domain, showing two different subduction angles juxtaposed in a 3D model. Red arrowheads indicate direction of increasing value.

Similar to chapter 6, the non-dimensionalized, steady-state conservation equations for mass, momentum, and energy were solved using COMSOL Multiphysics finite element software with UMFPACK. Chapter 6 provides most of the details of the applicable the model equations and parameters, and only differences between the 2D and 3D models are discussed here. For example, boundary conditions used are similar to the 2D models in chapter 6, with a few exceptions. On the trench-perpendicular boundaries, the temperature solutions from the 2D models are used

for the conduction/convection boundary conditions (see chapter 6 Figures 78 and 79), and symmetry boundary conditions are used when solving the Navier-Stokes equations. Because of numerical constraints, the $10°$ boundary "endcap" in the 3D domain is a shorter subregion (with length 1098 km) of the original, larger, 2D model (which was over 3000 km long). Thus, for the wedge inflow/outflow boundary on the $10°$ side, the 2D model solutions were mapped to the length of the 3D model in the subduction-zone-perpendicular (x) direction. Several ridges (e.g. Nazca Ridge, Juan Fernandez Ridge, and Chile Rise) interact with the South American subduction boundary. Studies such as *Kelleher and McCann* [1976, 1977]; *Pilger* [1981] have investigated the potential effects of ridge subduction on convergent margin kinematics and dynamics. However, it is beyond the scope of the present study to include factors relating to ridge subduction, including buoyancy and changes in the crustal thickness of the downgoing oceanic plate.

The angle cut into the slab is assigned to be an inflow boundary, corresponding to a downgoing plate with subduction velocity of 7 cm/yr adjusted for the different subduction angles. The model is meshed so that the wedge zone has a resolution between 5-10 km. Resolution is 10 km elsewhere. This results in 119,000 tetrahedral elements in the numerical domain (Figure 96). Use of a coarser mesh with resolution ranging from 5-20 km yielded maximum temperature differences of $25°C$, which occurred in non-wedge regions for trench-perpendicular (x) distances of 270 km and greater. These relatively minor temperature differences (over the $1300°C$ range of the model) suggest that a mesh of 5-10 km is sufficient to capture the geodynamical processes of interest.

7.4 BRITTLE-DUCTILE TRANSITION TEMPERATURE

A brittle-ductile transition temperature may be calculated by comparing brittle strength to ductile stress at a given point. Two different approaches are used to determine brittle strength. The first uses Byerlee's law and the second is from Sibson *Byerlee* [1978]; *Sibson* [1981]. The ductile stress is calculated according to power-law relationships shown by *Karato and Wu* [1993]; *Violay et al.* [2010, 2012]; *Carminati et al.* [2005].

7.4.1 BRITTLE STRENGTHS

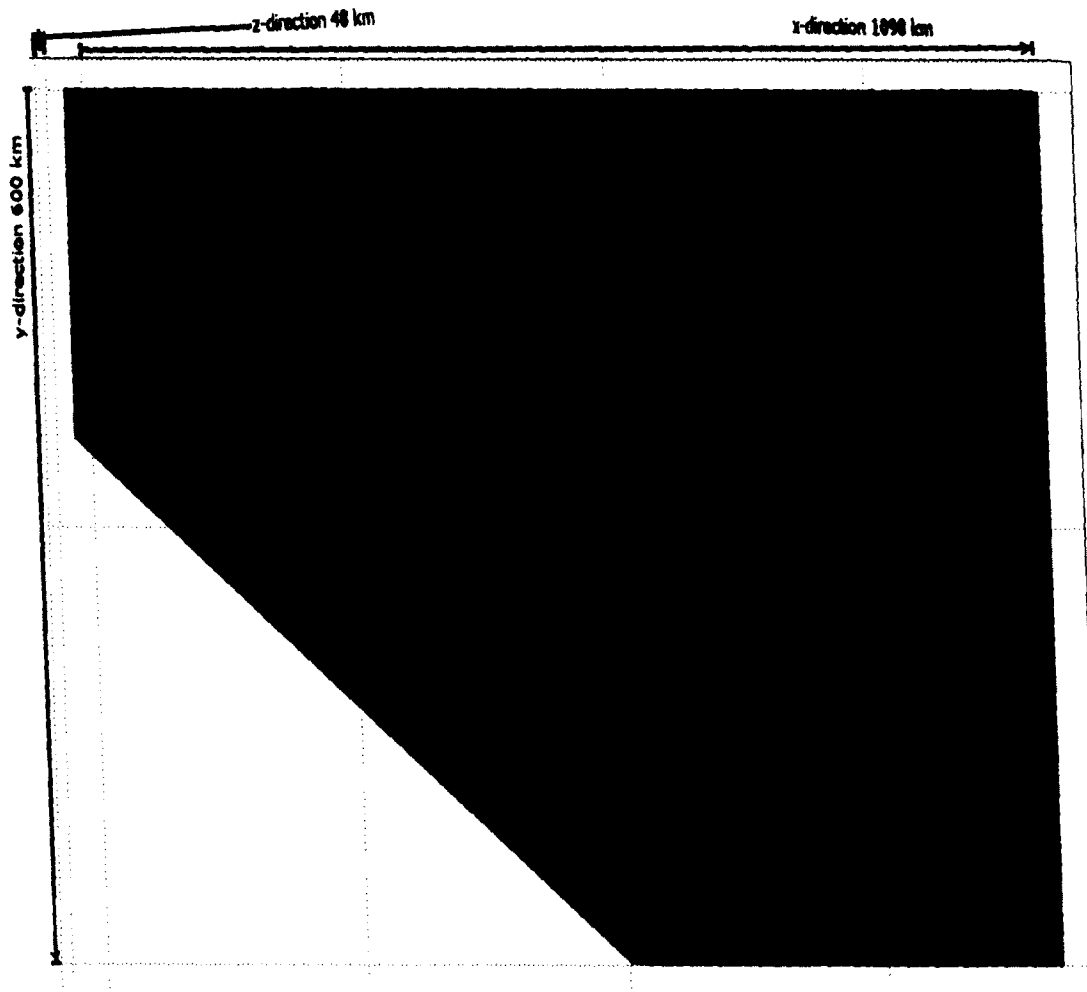*Byerlee* [1978] established a relationship between stress and faulting for various

Figure 96. Mesh used in 3D subduction model. Red arrowheads indicate direction of increasing value.

rock types, known as Byerlee's law. For normal stresses (σ_N) greater than 200 MPa, Byerlee's law is

$$\tau = (\sigma_1 - \sigma_3) = 50 + .60\sigma_n \tag{28}$$

Where τ is the brittle strength and σ_n is the normal stress. In this calculation, the overburden stress is used for the normal stress. The overburden stress is simply the pressure caused by the rock material overlying a given depth, and it is defined as

$$\sigma_n = \sigma_{yy} = \rho g y \tag{29}$$

where ρ is the density of the material (3300 kg m^{-3}), g is gravity (9.8 m s^{-2}), and y is the depth or height of material in meters.

The second method used to determine brittle strength is Sibson's law [Sibson, 1981], given in Equation 30 [Carminati et al., 2005]. This law is based on the Navier-Coulomb frictional criterion and it predicts a linear increase of yield stress with depth. In Sibson's law, β is a fault type parameter (assigned a value of 3), ρ is density (3300 kg m^{-3}), g is gravity (9.8 m s^{-2}), y is depth in meters, and λ is a pore-fluid pressure ratio, which is the ratio between fluid pressure and lithostatic load. λ is 0.4 for low fluid pressure and 0.8 for high fluid pressure. A low fluid assumption, or dry upper mantle, was used in this study.

$$\sigma_1 - \sigma_3 = \beta \rho g y (1 - \lambda) \tag{30}$$

7.4.2 DUCTILE STRESSES

Karato and Wu [1993] presented a relationship between strain rate $(\dot{\epsilon})$, shear stress (σ), pressure (P), grain size (d), and temperature (T) for mantle rock

$$\dot{\epsilon} = A(\frac{\sigma}{\mu})^n(\frac{b}{d})^m \exp\left(-\frac{Ea - PVa}{RT}\right) \tag{31}$$

where A is a pre-exponential factor, μ is the shear modulus, b is the length of the Burgers vector, n is the stress exponent, m is the grain size exponent, Ea is the activation energy, Va is the activation volume, and R is the gas constant. This equation can be modified to solve for σ as

$$\sigma = (\mu^n \frac{\dot{\epsilon}}{A}(\frac{d}{b})^m \exp\left(\frac{Ea - PVa}{RT}\right))^{\frac{1}{n}} \tag{32}$$

Equation 32 can be used to find stress for either the dislocation or diffusion creep regime, depending on the choice of constants as shown in Table 15 [Karato and Wu, 1993].

Table 15. Parameter Values for Diffusion Creep and Dislocation Creep in a Dry Upper Mantle from *Karato and Wu* [1993]

Quantity	Diffusion Creep	Dislocation Creep
Preexponential factor A, s^{-1}	8.7E(15)	3.5E(22)
Stress exponent n	1	3.5
Grain size exponent m	2.5	0
Activation Energy Ea, $kJmol^{-1}$	300	540
Activation Volume Va, m^3mol^{-1}	6E(-6)	2E(-5)
Shear Modulus G, MPa	80	80
Lattice Spacing b, nm	0.5	0.5
Grain Size h, mm	3	3
Gas Constant R, $JK^{-1}mol^{-1}$	8.3144	8.3144

The second method of calculating power creep stress from *Carminati et al.* [2005]; *Violay et al.* [2010, 2012] is given by

$$\dot{\epsilon} = D\sigma^n \exp\left(-\frac{Ea}{RT}\right) \tag{33}$$

The equation relates the strain rate ($\dot{\epsilon}$) to a material constant (D), stress exponent (n), activation energy (Ea), gas constant (R), and temperature (T). In this investigation, the value used for the strain rate comes from the kinematic models in chapter 5, and the other constants are given in Table 16 [*Carminati et al.*, 2005; *Violay et al.*, 2012].

Table 16. Parameter Values for Dislocation Creep from *Carminati et al.* [2005]; *Violay et al.* [2012]

Quantity	Violay	Carminati
Activation Energy Ea, $kJmol^{-1}$	456	449
Material Constant D, $(MPa^{-n}s^{-1})$	610	2430
Gas Constant R, $JK^{-1}mol^{-1}$	8.3144	8.3144
Stress exponent n	3.6	2.6

For each point in the model domain, the brittle-ductile transition is calculated according to each of the two brittle failure laws and each of the two power-law ductile

deformation equations. Thus, a total of four different brittle-ductile transition maps are determined for the 3D model. As mentioned above, the brittle-ductile transition is taken to be the lower of the two values (brittle failure vs. ductile stress).

7.5 RESULTS AND DISCUSSION

7.5.1 MODEL-PREDICTED TEMPERATURES AND FLOW FIELDS

Slices through the model domain along y-z (or trench-parallel) planes show how the predicted temperature and velocity fields of the subduction zone change with time (or, equivalently, distance away from the trench) (Figures 97-99). Slices are taken at 60 km intervals, and only the y-z components of mantle flow are shown. The model-predicted temperatures show a cool region with relatively complex geometry in between the 10° and 30° "endcaps." This cooler material is interpreted to correspond to the slab region between the two different subducting angles. It is clear that the model-predicted slab does not take a linear shape, because of viscous flow and material advection due to temperature gradients.

For the flow fields, close to x = 0 km, the y-z velocity only has components in the y-direction. However, as the distance from the trench increases to 60 km, temperature variations between the two subducting angles cause flow with a z-direction component to occur. The onset of a z-component velocity corresponds to the opening of the wedge on the 30° side of the model domain. The multi-directional flow is caused by the cooler 30° slab penetrating deeper earlier than the 10° slab. For distances greater than x = 60 km, there is always a z-component of velocity present.

Profiles extracted at constant depths quantify the variation of temperature throughout the model space (Figures 100-102). The constant-depth profiles can be interpreted to represent how the temperature of mantle material changes at a given depth through the course of the subduction process. The selected depths are 150, 200, 250, and 300 km. In general, depths shallower than 300 km show significant variations. For example, for 150 km depth at x = 120 km, subduction of the 30° slab is apparent as a ~100°C temperature decrease at z = 48 km (i.e., the 30° angle side of the model domain). The shallower 10° slab has little effect on the predicted temperature fields at this distance from the trench. By x = 240 km, there is a significant and roughly linear temperature variation of 800°C at a depth of 150 km. This large difference results from the center of the 30° subducting slab passing through

(a) x = 0 km

(b) x = 60 km

(c) x = 120 km

Figure 97. Model-predicted temperatures and y-z velocities for x-distances of 0-120 km from the trench. The left side of each panel (at z = 48 km) corresponds to the 30° subduction angle and the right side (at z = 0 km) to 10° subduction.
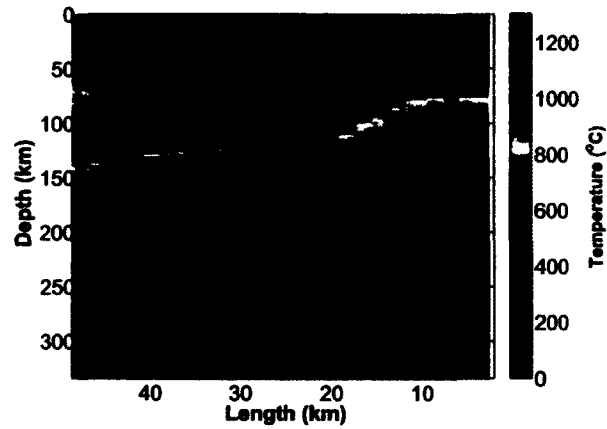
(a) x = 180 km
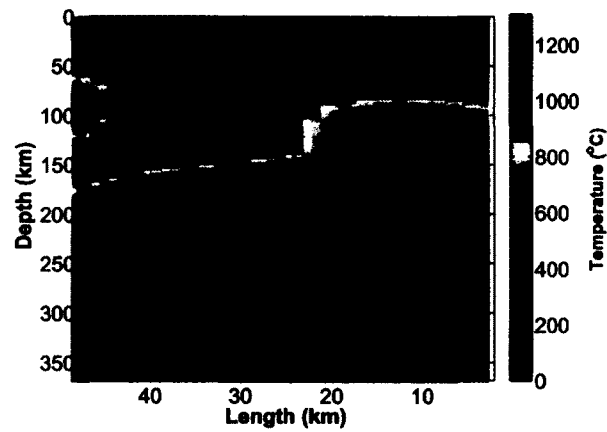
(b) x = 240 km
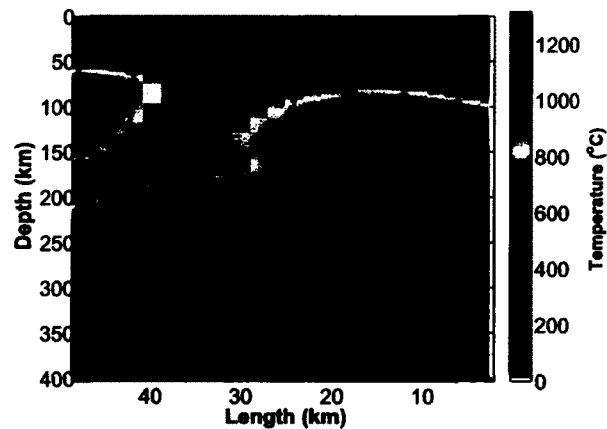
(c) x = 300 km

Figure 98. Model-predicted temperatures and y-z velocities for x-distances of 180-300 km from the trench. The left side of each panel (at z = 48 km) corresponds to the 30° subduction angle and the right side (at z = 0 km) to 10° subduction.
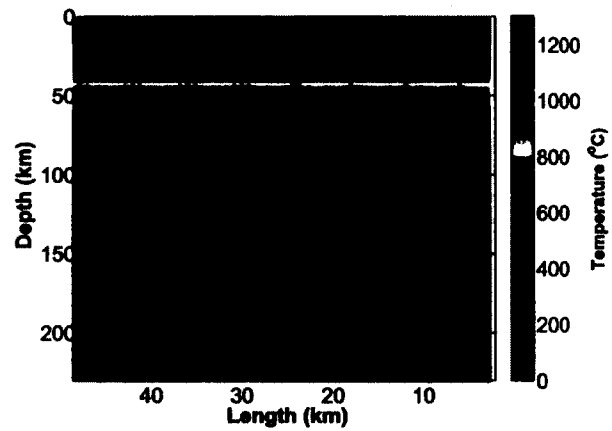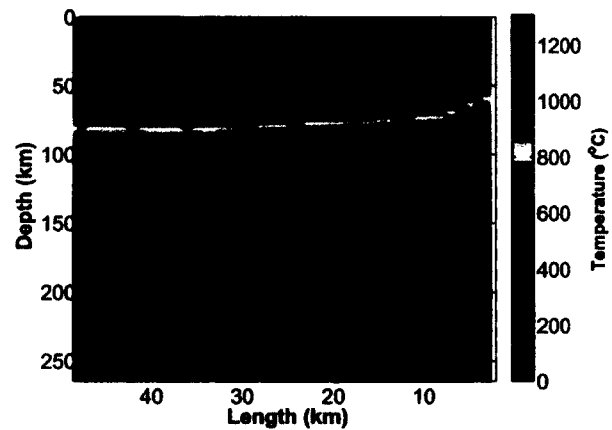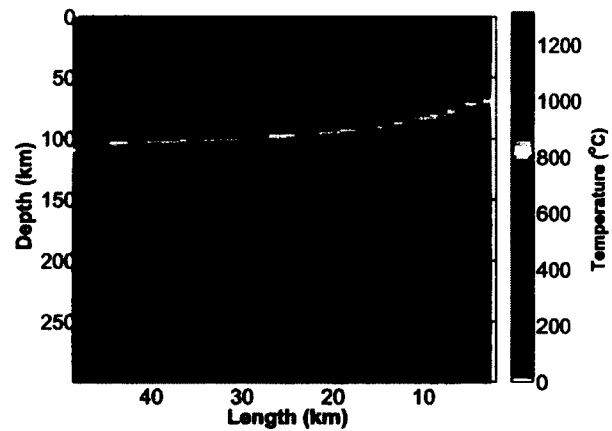
(a) x = 360 km

(b) x = 390 km

(c) x = 420 km

Figure 99. Model-predicted temperatures and y-z velocities for x-distances of 360-420 km from the trench. The left side of each panel (at z = 48 km) corresponds to the 30° subduction angle and the right side (at z = 0 km) to 10° subduction.
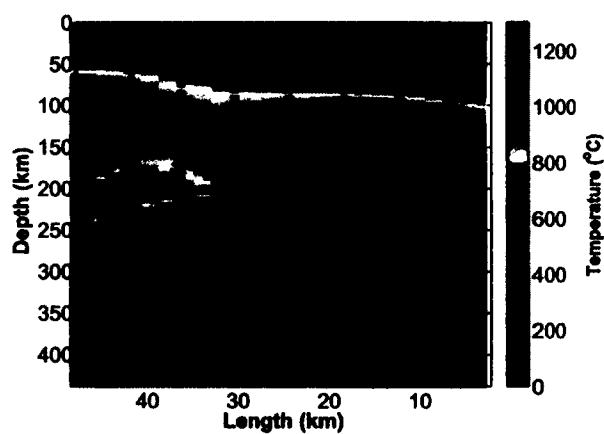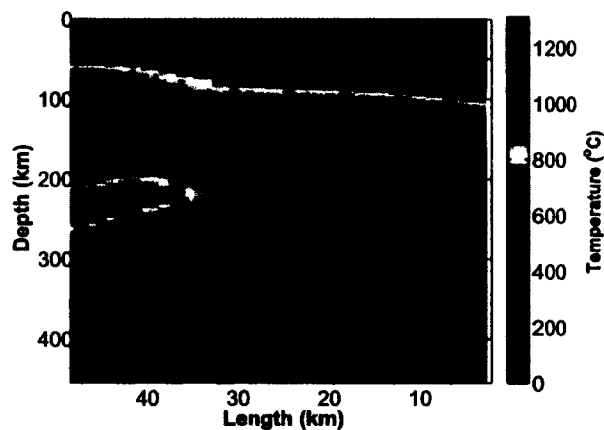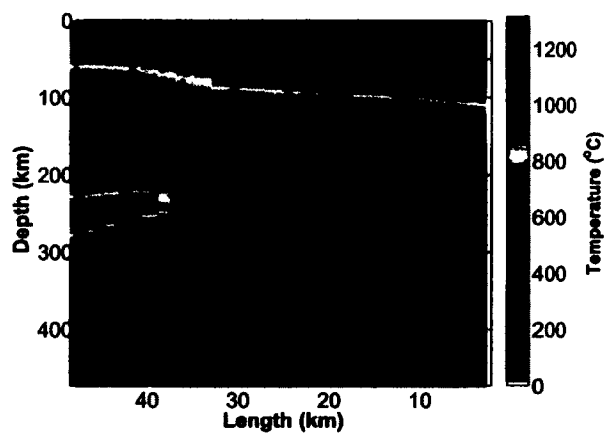
this plane.

At a trench-perpendicular distance of x = 300 km, however, there is no longer a roughly linear variation of the slab temperature profile at a depth of 150 km. The profile is relatively hot on the 10° subduction side (z = 0 km), reflecting hot material in the lower portions of the 10° slab. As the z value increases to 36 km the temperature decreases to 600°C, where the cold portion of the 30° subduction region is located. For greater along-trench (z) distances, the temperature begins to rise again, in accordance with the presence of the mantle wedge.

At x = 420 km, the subduction of the colder slab material on the 10° side of the model is evident depths of 150 km, as the temperature is 200°C cooler at z = 0 km for this x-distance than at x = 60 km or x = 120 km. The along-profile thermal variation is decreased because the majority of the 30° slab has moved past this depth. The minimum temperature along the profile, 1000°C, is still located at z = 36 km. Overall, the general pattern of temperature variations for 150 km depth is largely repeated for the other, greater depths, with the x-distance at which the maximum thermal variation along a given profile occurs increasing systematically as a function of the profile depth.

7.5.2 BRITTLE-DUCTILE MAPS

Brittle-ductile maps provide insight into the deformation mechanism of the mantle at a given point in the model domain. As mentioned above, brittle-ductile maps were made using all four combinations of brittle and ductile equations. The results from using equations 30 and 33 are shown in Figures 103-105, while the results from using equations 28 and 33 are shown in Figures 106-108. In both sets of plots, a continuous region of brittle material occurs between the two subducting angles in the top portion of the model, through a distance of 180 km from the trench. However, at x = 240 km, Figure 107 shows a ductile region forming at approximately y = 100 km and z = 35 km, while Figure 104 indicates a brittle region. For both cases, between x = 240-300 km, the top portion (y<100 km) of the model domain is predicted to undergo brittle failure, while greater depths are primarily ductile. Maintaining brittle failure to these depths is in good agreement with reported earthquake hypocenter locations. *Cahill and Isacks* [1992]; *Anderson et al.* [2007] both find earthquakes on the 30° side of subduction at these depths.

As the distance from the trench increases, the downgoing plate quickly becomes

(a) x = 0 km

(b) x = 60 km

(c) x = 120 km

Figure 100. Model-predicted temperatures at four depths (150 km, 200 km, 250 km, and 300 km) for x-distances of 0-120 km from the trench. The left side of each panel (at z = 48 km) corresponds to the 30° subduction angle, while the right side (at z = 0 km) corresponds to 10° subduction.

(a) x = 180 km
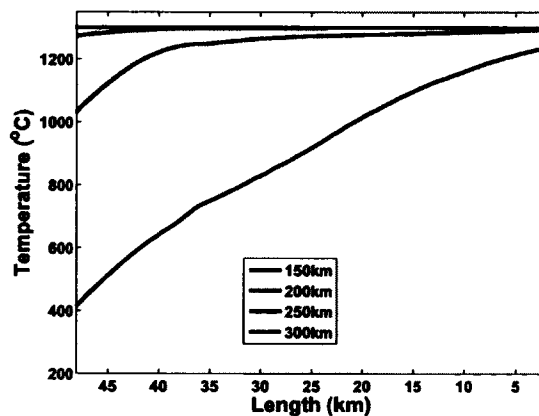
(b) x = 240 km
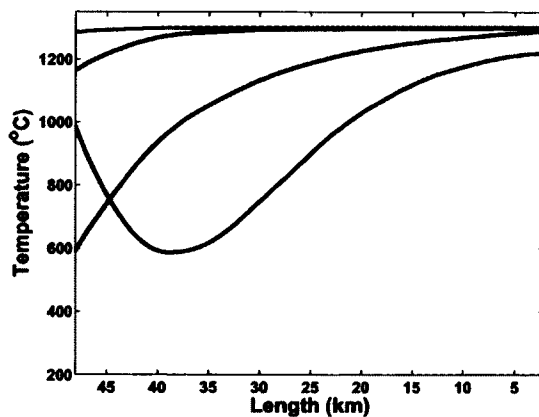
(c) x = 300 km

Figure 101. Model-predicted temperatures at four depths (150 km, 200 km, 250 km, and 300 km) for x-distances of 180-300 km from the trench. The left side of each panel (at z = 48 km) corresponds to the 30° subduction angle, while the right side (at z = 0 km) corresponds to 10° subduction.
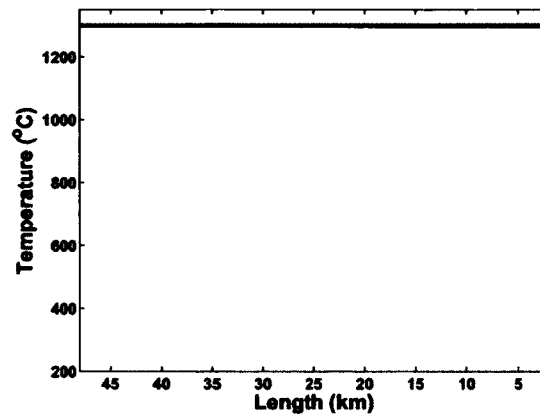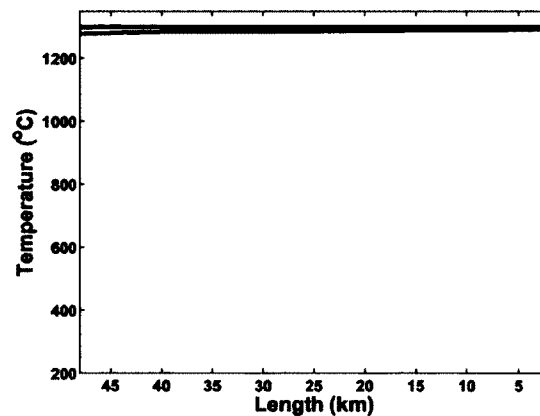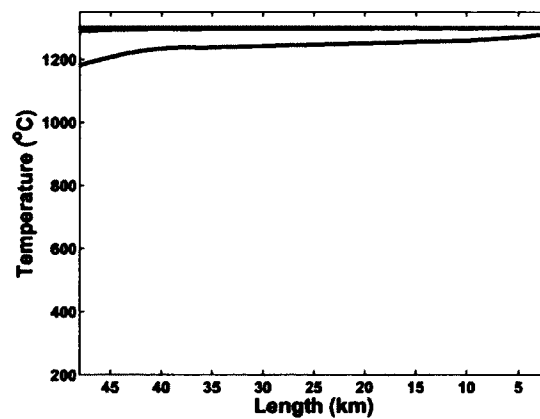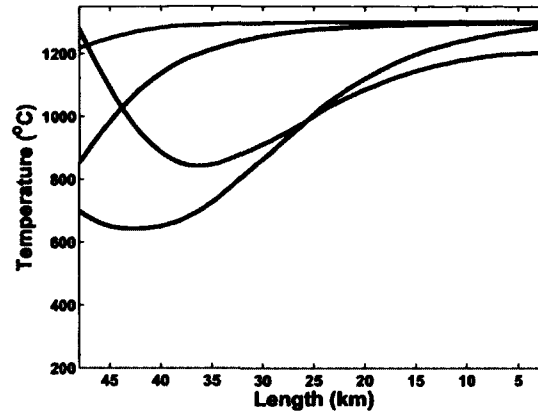
(a) x = 360 km
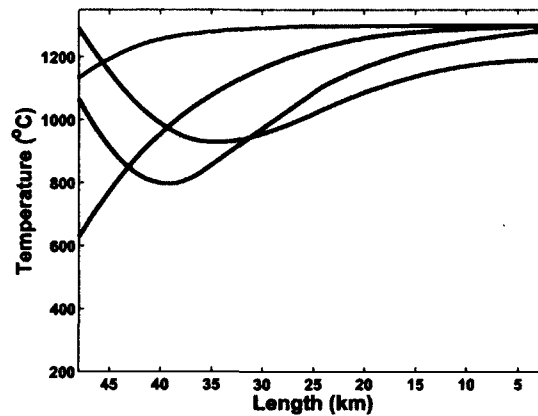
(b) x = 390 km
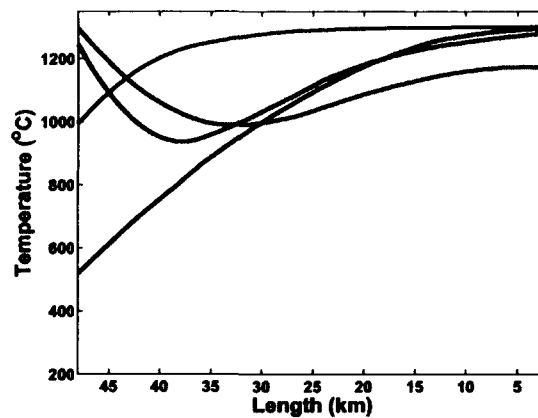
(c) x = 420 km

Figure 102. Model-predicted temperatures at four depths (150 km, 200 km, 250 km, and 300 km) for x-distances of 360-420 km from the trench. The left side of each panel (at z = 48 km) corresponds to the 30° subduction angle, while the right side (at z = 0 km) corresponds to 10° subduction.

ductile on the 30° side as the wedge continues to open and to provide hot mantle material to heat the top side of the slab. In Figure 108, the slab is predicted to be completely ductile by x = 360 km from the trench. However, Figure 105 shows that the 30° slab maintains a small region of brittleness over all x-distances modeled. It is possible that the conditions shown in Figures 103-105 may overestimate brittleness, because earthquakes are not reported to these depths on the 30° side of subduction [*Cahill and Isacks*, 1992; *Anderson et al.*, 2007].

7.5.3 DEFORMATION MECHANISM MAP FOR THE SUBDUCTING SLAB

Deformation mechanism maps can be used to show how a system deforms in response to stress (Figure 109). The deformation mechanism map is a plot of normalized stress versus homologous temperature (T_H) that is contoured for strain rate and divided into regions where different mechanisms dominate. The homologous temperature is the mantle temperature divided by the melting temperature of olivine, the dominant mineral in the mantle. The melting temperature of olivine was calculated from a linear function with depth provided in equation 17 (see chapter 5). Mantle temperature can be determined from the 3D model-predicted temperature solutions. The strain rates for the 2D systems were calculated previously (see chapter 5). Values obtained were $1.1 \times 10^{-14} s^{-1}$ and $2.35 \times 10^{-15} s^{-1}$.

To estimate the location of the slab in the model a linear interpolation is made between two slab depths of 54 km and 174 km, which represent the y-locations of the 10° and 30° downgoing plate segments for a subduction age of 4.3 m.y. (Figure 110). This is the amount of time required for the slab to move 300 km perpendicular to the trench, the distance the two-angle subduction covers, at a rate of 7 cm/yr. The function used in the interpolation is given by

$$y = -6km + 2.5(z)km \tag{34}$$

The resulting line is shown on a plot of the model-predicted temperatures at x = 300 km (Figure 110). The homologous temperatures calculated by extracting the model-predicted temperatures along this line are provided in Table 17.

Assuming an average strain rate of $2.35 \times 10^{-15} s^{-1}$, and using the calculated homologous temperatures, the interpolated slab line is predominantly in the 'plasticity' region in the deformation mechanism map of Figure 109 [*Ashby et al.*, 1977]. Part of

(a) x = 0 km
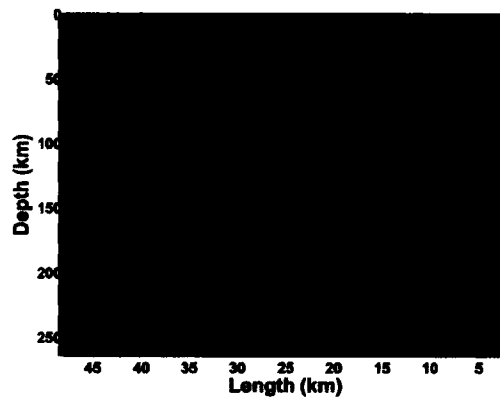
(b) x = 60 km
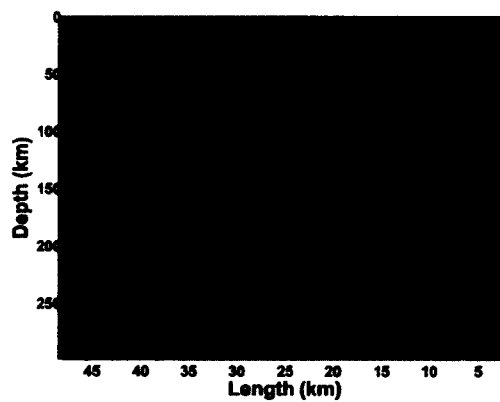
(c) x = 120 km

Figure 103. Brittle-ductile maps constructed using the rheological laws in equations 30 and 33 for x-distances of 0-120 km from trench. Blue and red indicate brittle and ductile regions, respectively. The left side of each panel (at z = 48 km) corresponds to the 30° subduction angle, while the right side (at z = 0 km) corresponds to 10° subduction.
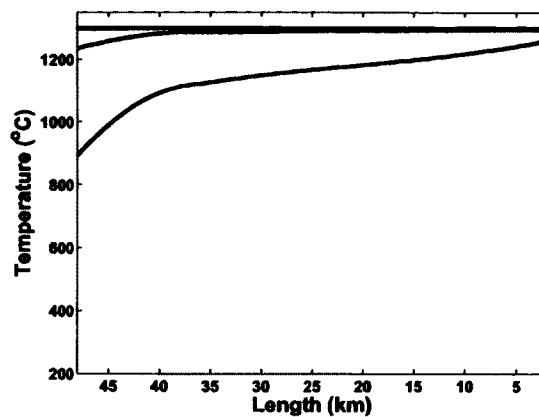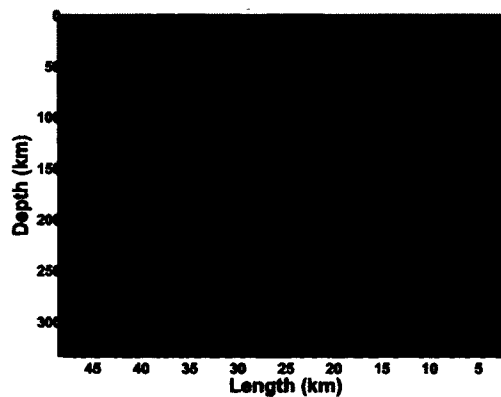
(a) x = 180 km
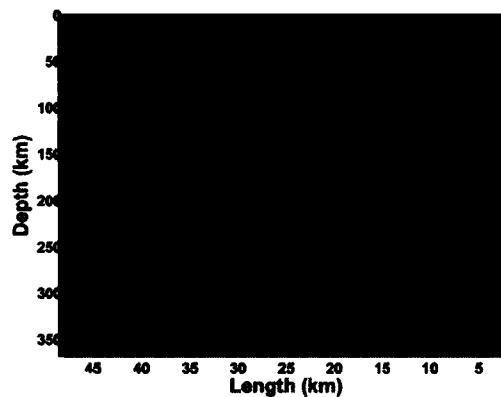
(b) x = 240 km
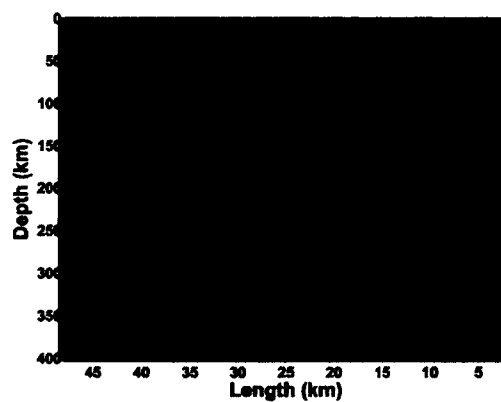
(c) x = 300 km

Figure 104. Brittle-ductile maps constructed using the rheological laws in equations 30 and 33 for x-distances of 180-300 km from trench. Blue and red indicate brittle and ductile regions, respectively. The left side of each panel (at z = 48 km) corresponds to the 30° subduction angle, while the right side (at z = 0 km) corresponds to 10° subduction.
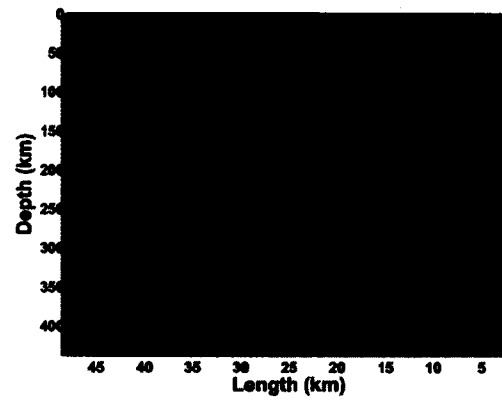
(a) x = 360 km
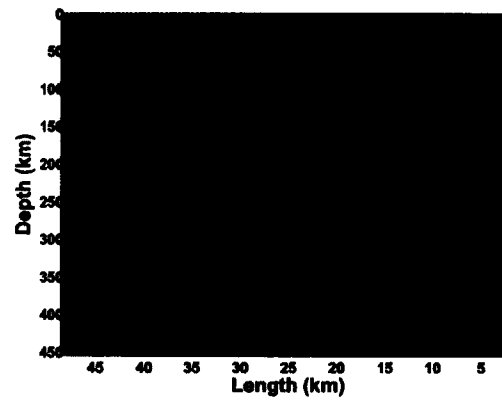
(b) x = 390 km
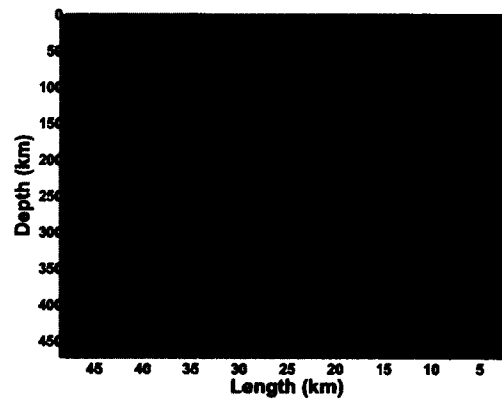
(c) x = 420 km

Figure 105. Brittle-ductile maps constructed using the rheological laws in equations 30 and 33 for x-distances of 360-420 km from trench. Blue and red indicate brittle and ductile regions, respectively. The left side of each panel (at z = 48 km) corresponds to the 30° subduction angle, while the right side (at z = 0 km) corresponds to 10° subduction.
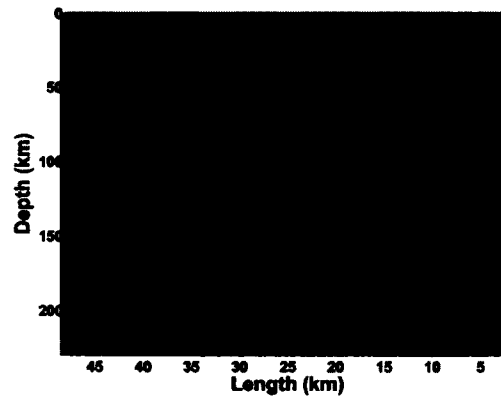
(a) x = 0 km
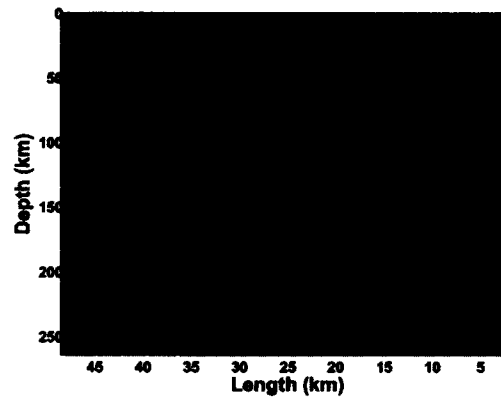
(b) x = 60 km
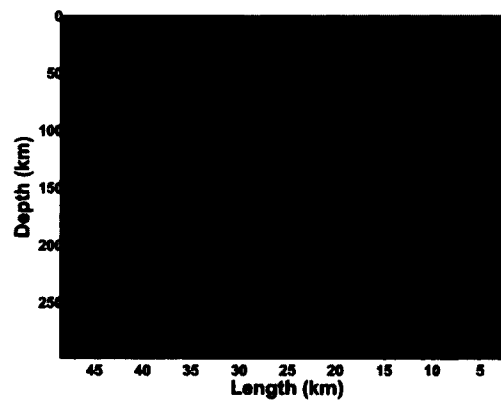
(c) x = 120 km

Figure 106. Brittle-ductile maps constructed using the rheological laws in equations 28 and 33 for x-distances of 0-120 km from trench. Blue and red indicate brittle and ductile regions, respectively. The left side of each panel (at z = 48 km) corresponds to the 30° subduction angle, while the right side (at z = 0 km) corresponds to 10° subduction.
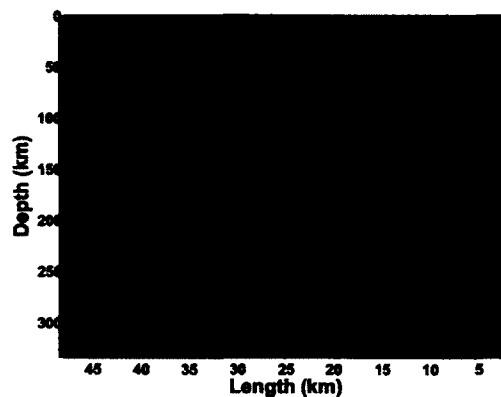
(a) x = 180 km
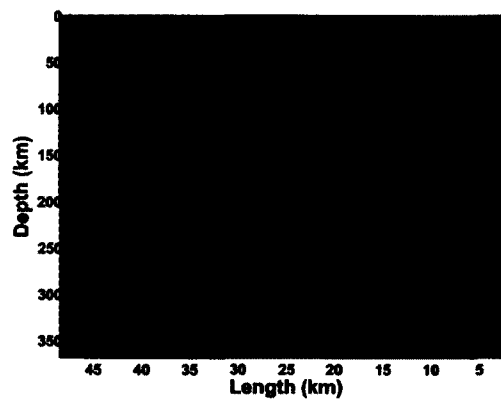
(b) x = 240 km
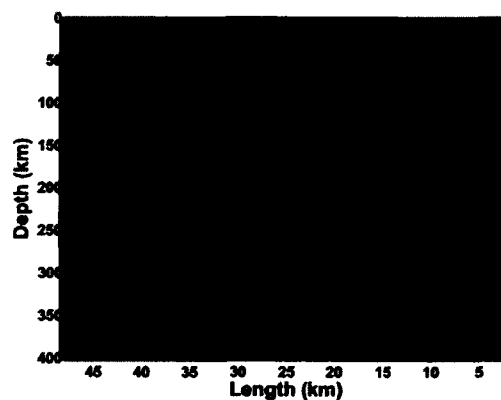
(c) x = 300 km

Figure 107. Brittle-ductile maps constructed using the rheological laws in equations 28 and 33 for x-distances of 180-300 km from trench. Blue and red indicate brittle and ductile regions, respectively. The left side of each panel (at z = 48 km) corresponds to the 30° subduction angle, while the right side (at z = 0 km) corresponds to 10° subduction.
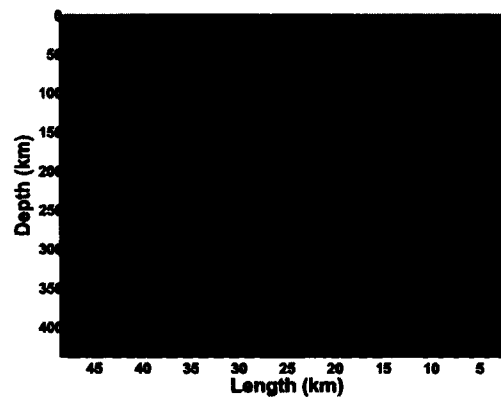
(a) x = 360 km
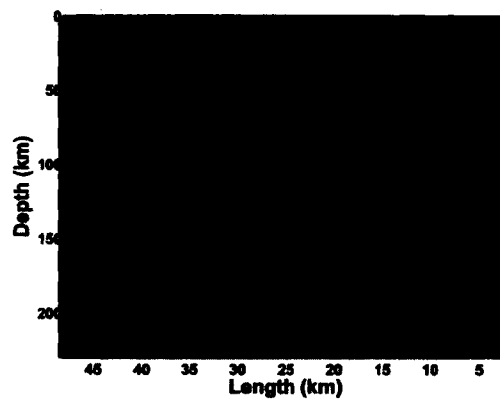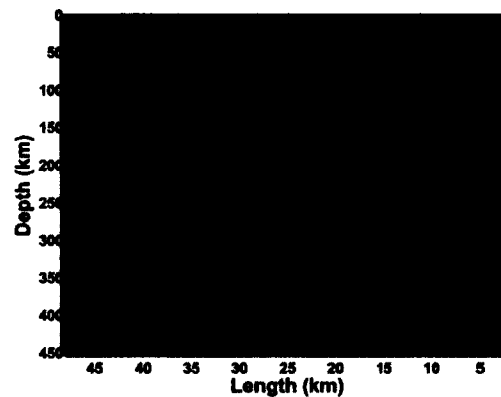

(b) x = 390 km
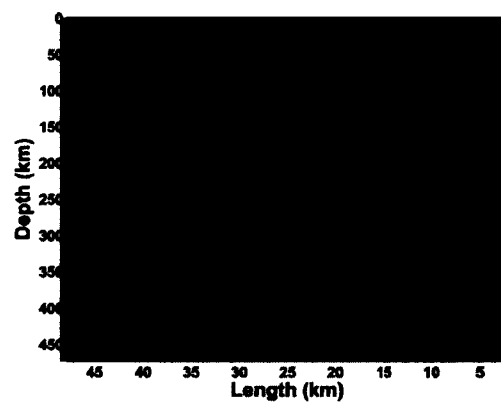
(c) x = 420 km

Figure 108. Brittle-ductile maps constructed using the rheological laws in equations 28 and 33 for x-distances of 360-420 km from trench. Blue and red indicate brittle and ductile regions, respectively. The left side of each panel (at z = 48 km) corresponds to the 30° subduction angle, while the right side (at z = 0 km) corresponds to 10° subduction.
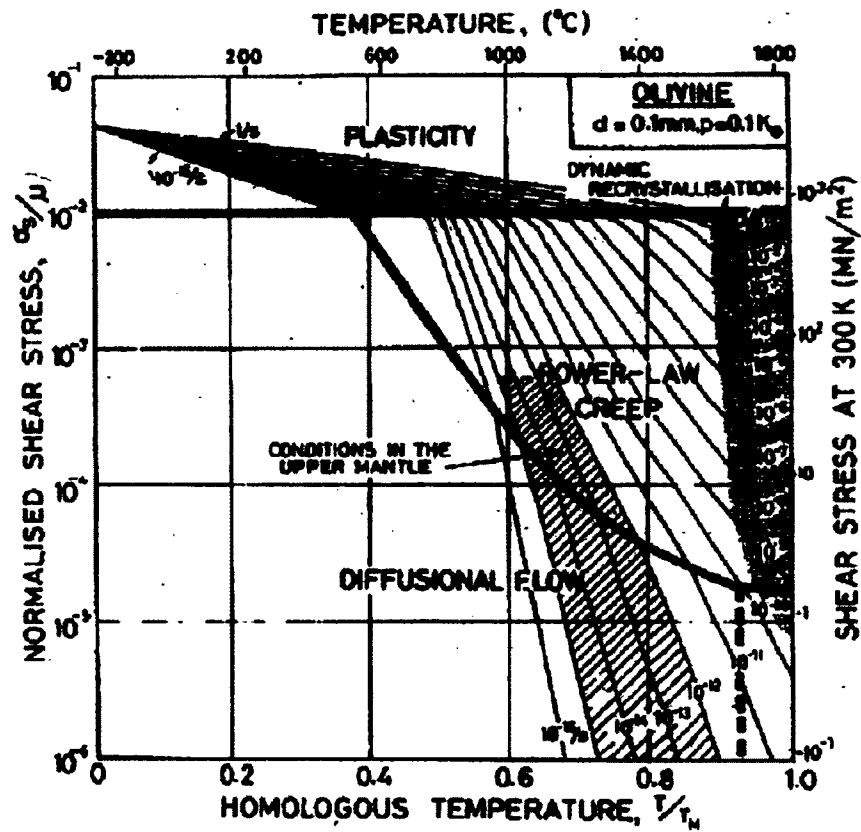
Figure 109. Deformation map across slab at x = 300 km. Red line shows the linear profile between angles has regions of brittle and ductile deformation occurring [*Ashby et al.*, 1977].

the line tracing out the deformation history of the slab goes between both brittle and ductile deformation mechanisms , which is in agreement with the brittle ductile maps of section 5.12. It be noted that the line drawn in Figure 110 does not go exclusively through the colder region which most likely defines the slab. The linear function is a useful approximation to give a first-order understanding of slab deformation. However, if the slab is instead defined based on an isotherm, then there would be discrepancies between the simple linear slab and the thermally-defined one. However, overall the results discussed here are in agreement with the kinematic model results in chapter 5 which had the slab in a non-ductile deformation state attributed to cataclastic flow.

Table 17. Homologous temperatures for linear slope profile at x = 300 km

Depth (km)	Along trench distance (z,km)	Temperature (K)	T_H
174	48	743	.299
162	42	820	.333
144	30	894	.368
132	24	1037	.431
114	18	1179	.503
84	12	1112	.482
72	6	929	.407
54	0	497	.221
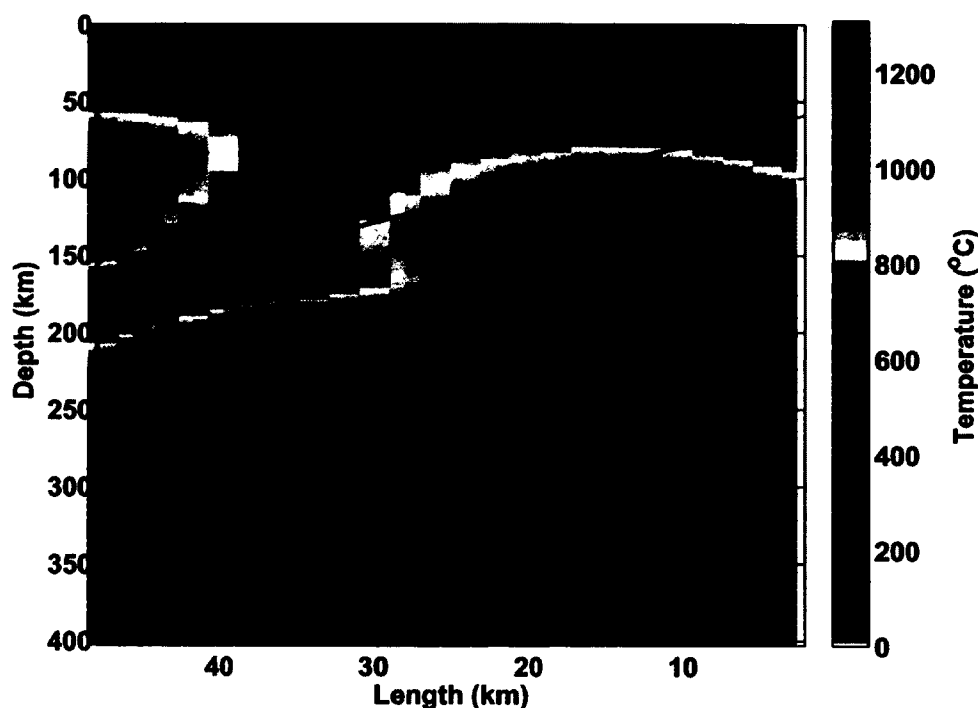
Figure 110. Linear interpolation for slab in 3D model.

7.6 CONCLUSIONS

1. Trench-parallel flow is predicted to occur during the subduction process. This viscous flow is a result of thermal gradients across the model space related to differential subduction of the two slab angles.

2. The uppermost portion of the model space shows a continuous brittle section for distances of up to ~180-240 km perpendicular to the trench. The variation in distance depends on which equations are used for the brittle-ductile transitions. After this distance, the plate can maintain continuity but may due so as a combination of brittle-ductile behavior.

3. The results of the linear profile, x = 300 km, used for the deformation mechanism map showed the slab to be mostly in an 'inelastic' state, with a small portion to be in power law creep. Overall these results are in good agreement with the mechanisms determined in chapter 5 which showed the slab to be deforming by cataclastic flow as well.

CHAPTER 8

CONCLUSIONS

In this thesis, several modeling and visualization techniques are used to explore the kinematics and dynamics of subduction zones. The geological regions studied are the Tonga and central Andean subduction zones, which both possess unique slab geometries. The modeling and visualization techniques include COLLADA models, kinematic modeling, and two- and three-dimensional finite element numerical models.

One visualization technique is building COLLADA models for both regions, using data mined from GeoMapApp (http://www.geomapapp.org) and the published literature. These data models led to questions about the general tectonic history of the Tonga region and slab deformation in the Andes. For Tonga, several scenarios are developed with animated COLLADA models. These models are designed to challenge the user to say "why" or "why not" based on geological and geophysical data. Construction of these engaging instructional resources blurred the boundaries between education and research as a new hypothesis emerged for the formation of the Tonga region.

The COLLADA models developed are also used in educational testing to understand their classroom learning benefits. In two studies, students' ability to learn with Google Earth lab activities is examined. The studies involve activities developed for Iceland and the animated COLLADA models for Tonga. The studies show positive learning gains regardless of gender or previous knowledge. That is, the findings suggest that Google Earth can be an effective learning tool for non-majors. Thus, Google Earth also has potential efficacy for scientific literacy on a broad scale. To expand on the effectiveness of Google Earth as a learning tool, the use of client-server-client communication is also discussed in this thesis. Such communications enable virtual field trip developers to produce more interactive, efficient, and engaging learning experiences.

To investigate the unique Nazca plate geometry at S33°, tear and shear kinematic models are developed. The tear model assumes two plates moving independently over

the zone, resulting in a gap or separation between the two plate segments. For the second model, heterogeneous simple shear is approximated using symmetrically nested slices of homogeneous simple shear. The models are used to calculate geophysical properties like strain rates and deformation mechanisms. The following conclusions are reached. First, the slab can accommodate two-angle subduction between 10° and 30° for the 300 km flat-slab distance, where the slab may deform by predominantly cataclastic flow. Second, the plate may thin to a thickness of 50 to 80 km as a result of this deformation, but a continuous plate should still be maintained.

To better understand the influence of parameters like subduction angle, slab velocity, and slab-wedge coupling on convergent margin geodynamics, a suite of numerical finite element models are created for general subduction cases. These models are not only used for the general 2D study of subduction processes but also as a framework for constructing 3D models of the Nazca plate at S33° as well. The 2D model results indicate that model-predicted temperatures show the greatest sensitivity to subduction angle. Subduction rate exerts the second most important control, while coupling length affects the model-predicted temperatures least. Thus, for the building of a 3D model that juxtaposes two downgoing slab angles, plate dip is likely to be an important control on the geodynamics of the convergent margin.

Finally, a 3D numerical model with two adjacent subduction angles of 10° and 30° is constructed to study the unique slab dip transition region at S33° in South America. The boundary conditions are selected based on or using the solutions of the appropriate 2D numerical models. The model-predicted temperatures and flow fields are then analyzed in a series of trench-parallel vertical depth slices, to create brittle-ductile maps and possible deformation mechanisms of the subducting slab. The subducting plate shows a continuous brittle section for a distance between 180-240 km perpendicular to the trench. Slab temperatures, determined using a simple linear depth profile, suggest the slab is mostly in a cataclastic flow state. This is in good agreement with the mechanisms determined with kinematic models.

BIBLIOGRAPHY

Allmendinger, R. W., and T. Gubbels (1996), Pure and simple shear plateau uplift, Altiplano-Puna, Argentina and Bolivia, *Tectonophysics*, *259*, 1–13, doi: 10.1016/0040-1951(96)00024-8.

Allmendinger, R. W., D. Figueroa, D. Snyder, J. Beer, C. Mpodozis, and B. L. Isacks (1990), Foreland shortening and crustal balancing in the Andes at 30° S latitude, *Tectonics*, *9*(4), 789–809, doi:10.1029/TC009i004p00789.

Alvarado, P., M. Pardo, H. Gilbert, S. Miranda, M. Anderson, M. Saez, and S. Beck (2009), Flat-slab subduction and crustal models for the seismically active Sierras Pampeanas region of Argentina, *Geol. Soc. Am. Mem.*, *204*, 261–278, doi: 10.1130/2009.1204(12).

American Association for the Advancement of Science (1993), *Benchmarks for Science Literacy*, Oxford Univ. Press, New York, NY.

Anderson, M., P. Alvarado, G. Zandt, and S. Beck (2007), Geometry and brittle deformation of the subducting Nazca plate, Central Chile and Argentina, *Geophys. J. Int.*, *171*, 419–434, doi:10.1111/j.1365-246X.2007.03483.x.

Arnaud, R., and M. C. Barnes (2006), *COLLADA: Sailing the Gulf of 3D Digital Content Creation*, A.K. Peters, Ltd., Wellesley, MA.

Ashby, M. F., R. A. Verrall, H. H. Schloessin, E. H. Rutter, K. H. G. Ashbee, S. H. White, S. A. F. Murrell, and A. Kelly (1977), Micromechanisms of flow and fracture, and their relevance to the rheology of the upper mantle, *Phil. Trans. R. Soc. Lond. A*, *288*, 59–95, doi:10.1098/rsta.1978.0006.

Barazangi, M., and B. L. Isacks (1976), Spatial distributions of earthquakes and subduction of the Nazca plate beneath South America, *Geology*, *4*, 686–692, doi: 10.1130/0091-7613(1976)4<686:SDOEAS>2.0.CO;2.

Batchelor, G. K. (1967), *An Introduction to Fluid Dynamics*, Cambridge Univ. Press, New York, NY.

Beck, S. L., and G. Zandt (2002), The nature of orogenic crust in the central Andes, *J. Geophys. Res.*, *107*, 52–53, 10B, doi:10.1029/2000JB000124.

Bednarz, S. W., G. Acheson, and R. S. Bednarz (2006), Maps and map learning in social studies, *Soc. Edu.*, *70*, 398–404.

Behn, M. D., G. Hirth, and P. B. Kelemen (2007), Trench-parallel anisotropy produced by foundering of arc lower crust, *Science*, *317*, 108–110, doi: 10.1126/science.1141269.

Bellahsen, N., C. Facenna, and F. Funiciello (2005), Dynamics of subduction and plate motion in laboratory experiments: insights into the "plate tectonics" behavior of the Earth, *J. Geophys. Res.*, *110*, B01401, doi:10.1029/2004JB002999.

Bevis, M. (1986), The curvature of Wadati-Benioff zones and the torsional rigidy of subducting plates, *Nature*, *323*, 52–53.

Bevis, M., and B. L. Isacks (1984), Hypocentral trend surface analysis: Probing the geometry of Benioff zones, *J. Geophys. Res.*, *89*(87), 6153–6170, B7, doi: 10.1029/JB089iB07p06153.

Billen, M. I. (2008), Modeling the dynamics of subducting slabs, *Ann. Rev. Earth Planet. Sci.*, *36*, 325–356, doi: 10.1146/annurev.earth.36.031207.124129.

Billen, M. I., and M. Gurnis (2001), A low viscosity wedge in subduction zones, *Earth Planet. Sci. Lett.*, *193*, 227–236, doi:10.1016/S0012-821X(01)00482-4.

Billen, M. I., and G. Hirth (2005), Newtonian versus non-Newtonian upper mantle viscosity: implications for subduction initiation, *Geophys. Res. Lett.*, *32*, 4, L19304, doi:10.1029/2005GL023457.

Billen, M. I., and G. Hirth (2007), Rheologic controls on slab dynamics, *Geochem. Geophys. Geosyst.*, *8*, 38, Q08012, doi:10.1029/2007GC001597.

Billen, M. I., M. Gurnis, and M. Simons (2003), Multiscale dynamic models of the Tonga-Kermadec subduction zone, *Geophys. J. Int.*, *153*, 359–388.

Black, A. A. (2005), Spatial ability and Earth Science conceptual understanding, *J. Geosci. Edu.*, *53*(4), 402–414.

Bodzin, A., and L. Cirucci (2009), Integrating geospatial technologies to examine urban land use change: A design partnership, *J. Geogr.*, *108*, 186-197, doi: 10.1080/00221340903344920.

Bodzin, A., D. Anastasio, and V. Kulo (2012), Designing Google Earth activities for learning earth and environmental science, in *Teaching Science and Investigating Environmental Issues with Geospatial Technology: Designing Effective Professional Development for Teachers*, edited by J. MaKinster, N. Trautmann, and M. Barnett, Springer, New York, NY.

Bonnardota, M. A., M. Régniera, C. Christovab, C. E. Ruellana, and E. Tric (2009), Seismological evidence for a slab detachment in the Tonga subduction zone, *Tectonophysics*, *464*(1-4), 84–99, doi:10.1016/j.tecto.2008.10.011.

Brickhouse, N. W. (1990), Teachers' beliefs about the nature of science and their relationship to classroom practice, *J. Teach. Educ.*, *41*(3), 53–62, doi: 10.1177/002248719004100307.

Britner, S. L. (2008), Motivation in high school science students: A comparison of gender differences in life, physical, and earth science classes, *J. Res. Sci. Teach.*, *45*(8), 955–970, doi:10.1002/tea.20249.

Brooks, W., and D. G. De Paor (2009), Construction and presentation of Google Earth models for undergraduate education, *Geol. Soc. Am. Abstracts with Programs*, *47*(7), 92.

Buckley, B. C., J. Gobert, P. Horwitz, and L. O'Dwyer (2010), Looking inside the black box: Assessments and decision-making in biologica, *Int. J. Learn. Technol.*, *5*(2).

Burkam, D. T., V. E. Lee, and B. A. Smerdon (1997), Gender and science learning early in high school: Subject matter and laboratory experiences, *Am. Educ. Res. J.*, *34*, 299–331, doi:10.2307/1163360

Butler, D. (2006), Virtual globes: the web-wide world, *Nature*, *439*, 776–778, doi: 10.1038/439776a.

Byerlee, J. D. (1978), Friction of rocks, *Pure Appl. Geophys.*, *5*(4-5), 615–626.

Cahill, T., and B. L. Isacks (1992), Seismicity and shape of the subducted Nazca plate, *J. Geophys. Res.*, *97*, 503–17, B12, doi:10.1029/92JB00493.

Carleton College (2012), Website, https://wiki.carleton.edu/download/attachments/ 12228613/Fig11.gif?version=1&modificationDate=1321753248000. Last accessed 07/07/2012.

Carminati, E., A. M. Negredo, J. L. Valera, and C. Doglioni (2005), Subduction-related intermediate-depth and deep seismicity in Italy: insights from thermal and rheological modelling, *Phys. Earth Planet. Int.*, *149*, 65–79, doi: 10.1016/j.pepi.2004.04.006.

Chase, C. (1978), Extension behind island arcs and motions relative to hot spots, *J. Geophys. Res.*, *83*, 5385–5387, B11, doi:10.1029/JB083iB11p05385.

Conder, J. A. (2005), A case for hot slab surface temperatures in numerical viscous flow models of subduction zones with an improved fault zone parameterization, *Phys. Earth Planet. Int.*, *149*, 155–164, doi:10.1016/j.pepi.2004.08.018.

Cruz, D., and S. D. Zellers (2006), Effectiveness of Google Earth in the study of geologic landforms, *Geol. Soc. Am. Abstracts with Programs*, *38*(7), 498.

Currie, C., K. Wang, R. Hyndman, and J. He (2004), The thermal effects of steady-state slab-driven mantle flow above a subducting plate: the Cascadia subuction zone and back-arc, *Earth Planet. Sci. Lett.*, *223*, 35–48, doi: 10.1016/j.epsl.2004.04.020

Dabbs, J. M., E. Jr., Chang, R. A. Strong, and R. Milun (1998), Spatial ability, navigation strategy, and geographic knowledge among men and women, *Evol. Hum. Behav.*, *19*(2), 89–98.

Dahl, J., S. W. Anderson, and J. C. Libarkin (2005), Digging into Earth Science: Alternative conceptions held by k-12 teachers, *J. Sci. Edu.*, *12*, 65–68.

Davies, J. H., and D. Stevenson (1992), Physical model of source region of subduction zone volcanics, *J. Geophys. Res.*, *97*, 2037–2070, B2, doi:10.1029/91JB02571.

De Paor, D. G. (1994), Modeling displacement and deformation in a single matrix operaiton, *J. Struct. Geol.*, *16*, 1033–1037, doi:10.1016/0191-8141(94)90085-X.

De Paor, D. G. (2007a), The world is (almost) round: An introduction to Google Earth science, *Frontmatter Technov.*, *1*(1), 10–11.

De Paor, D. G. (2007b), Embedding Collada models in geo-browser visualizations: A powerful tool for geological research and teaching, *Eos Trans. AGU*, *88*(52), IN32A–08.

De Paor, D. G. (2008a), Enhanced visualization of seismic focal mechanisms and centroid moment tensors using solid models, surface bump-outs, and Google Earth, *J. Virtual Explorer*, *29*, doi:10.3809/jvirtex.2008.00195.

De Paor, D. G. (2008b), Using Google SketchUp with Google Earth for scientific applications, Google Tech Talk (Dec.), San Francisco, CA. http://www.youtube.com/watch?v=6cVJqvsfxvo.

De Paor, D. G. (2008c), How would you move mount Fuji – and why would you want to?, Am. Geophys. Union Ann. Meeting (Dec.), San Francisco, CA.

De Paor, D. G. (2011a), Google Earth: Visualizing the possibilities for geoscience education and research, Geol. Soc. Am. Penrose Meeting (Jan.), Mountain View, CA.

De Paor, D. G. (2011b), Future implementation strategies for using Google Earth for geoscience education and presentation, Geol. Soc. Am. Penrose Meeting (Jan.), Mountain View CA.

De Paor, D. G., and A. Pinan-Llamas (2006), Application of novel presentation techniques to a structural and metamorphic map of the Pampean orogenic belt, Northwest Argentina, *Geol. Soc. Am. Abstracts with Programs*, *38*(7), 326.

De Paor, D. G., and S. J. Whitmeyer (2008), Collaborative research: Enhancing the geoscience curriculum using geobrowsers-based learning objects, Proposal NSF-CLLI #0837040, Washington, D.C.

De Paor, D. G., and S. J. Whitmeyer (2010), Geological and geophysical modeling on virtual globes using KML, COLLADA, and Javascript, *Comput. Geosci.*, *37*, 100–110, doi:10.1016/j.cageo.2010.05.003.

De Paor, D. G., and S. J. Whitmeyer (2011), Transforming undergraduate geoscience education with an innovative Google Earth-based curriculum, Am. Geophys. Union Fall Meeting (Dec.), San Francisco, CA, ED23, 1208428.

De Paor, D. G., and N. Williams (2006), Solid modeling of moment tensor solutions and temporal aftershock sequences for the Kiholo Bay earthquake using Google Earth with a surface bump-out, *Eos Trans. AGU*, *87*(52), S53E–05.

De Paor, D. G., D. C. Bradley, G. E. Eisenstadt, and S. M. Phillips (1989), The Arctic Eurekan orogen a most unusual fold and thrust belt, *Geol. Soc. Am. Bull.*, *101*, 952–967, doi:10.1130/0016-7606(1989)101<0952:TAEOAM>2.3.CO;2.

De Paor, D. G., J. Daniels, and I. Tyagi (2007), Five geo-browser lesson plans, *Eos Trans. AGU*, *88*, IN43A–0904.

De Paor, D. G., S. J. Whitmeyer, and J. Gobert (2008), Emergent models for teaching Geology and Geophysics using Google Earth, Am. Geophys. Union Ann. Meeting (Dec.), San Francisco, CA, ED09.

De Paor, D. G., W. Brooks, M. M. Dordevic, N. Ranashinge, and S. C. Wild (2009), Visualizing the 2009 Samoan and Sumatran earthquakes using Google Earth-based COLLADA models, *Eos Trans. AGU*, *90*(52), U13E–2088.

De Paor, D. G., S. Whitemeyer, and G. Watson-Papelis (2010a), Collaborative research: Virtual 4D field education in Google Earth, NSF-GEO #1034643.

De Paor, D. G., S. J. Whitemeyer, and J. Bailey (2010b), Collaborative research: Scaffolding undergraduate geoscience inquiry using new loggable Google Earth explorations, NSF-DUE #1022755.

De Paor, D. G., S. C. Wild, and M. M. Dordevic (2012a), Emergent and animated COLLADA models of the Tonga Trench and Samoa archipelago: Implications for geosciences modeling, education, and research, *Geosphere*, *8*(2), 491–506, doi: 10.1130/GES00758.1.

De Paor, D. G., S. C. Wild, and M. M. Dordevic (2012b), Movie, http://www.lions.odu.edu/org/planetarium/steve/GS/Movies/movie1.wmv Last accessed 07/07/2012.

De Paor, D. G., S. C. Wild, and M. M. Dordevic (2012c), Movie,
http://www.lions.odu.edu/org/planetarium/steve/GS/Movies/movie2.mov
Last accessed 07/07/2012.

De Paor, D. G., S. C. Wild, and M. M. Dordevic (2012d), Movie,
http://www.lions.odu.edu/org/planetarium/steve/GS/Movies/movie3.wmv
Last accessed 07/07/2012.

DeLaughter, J. E., S. Stein, C. A. Stein, and K. R. Bain (1998), Preconceptions
abound among students in an introductory earth science course, *Eos Trans. AGU*,
79, 429, doi:10.1029/98EO00325.

Dickerson, W., and W. Snyder (1978), Plate tectonics of the Laramide orogeny, in
*Laramide Folding Associated with Basement Rock Faulting in the Western United
States*, vol. 151, edited by V. Matthews, pp. 355–366, Geol. Soc. Am. Mem., Boul-
der, CO.

Digital-Planet (2011), Earth's interior, Website,
http://www.digitalplanet.org/DigitalPlanet/$New - June$.html.
Last accessed 07/07/2012.

Dordevic, M. M., and S. C. Wild (2012), Avatars and multi-student interactions in
Google Earth - based field experiences, in *Google Earth and Virtual Visualizations
in Geoscience Education and Research: Geological Society of America Special Pa-
per 492*, edited by S. Whitmeyer, J. Bailey, D. De Paor, and T. Ornduff, chap. 35,
Geol. Soc. Am., Boulder, CO, doi:10.1130/2012.2492(22).

Dordevic, M. M., D. G. De Paor, and S. J. Whitmeyer (2009), Understanding volcan-
ism on terrestrial planets and moons using virtual globes and COLLADA models,
Geol. Soc. Am. Abstracts with Programs, *41*(7), 260.

Dordevic, M. M., D. G. De Paor, S. J. Whitmeyer, and M. R. Beebe (2011), An-
imated COLLADA models and virtual field trips featuring volcanism in various
tectonic settings on planet Earth and other rocky planets and moons, *Geol. Soc.
Am. Abstracts with Programs*, *42*(5), 420.

Downs, R. M., and L. S. Liben (1991), The development of expertise in geography:
A cognitive-developmental approach to geographic education, *Ann. Assoc. Am.
Geogr.*, *81*, 304–327.

Eberle, M. A., O. Grasset, and C. Sotin (2002), A numerical study of the interaction between the mantle wedge, subducting slab, and overriding plate, *Phys. Earth Planet. Int.*, *134*, 191–202, doi:10.1016/S0031-9201(02)00157-7.

Espurt, N., P. Baby, S. Brusset, M. Roddaz, W. Hermoza, V. Regard, P. O. Antoine, R. Salas-Gismondi, and R. Bolanas (2007), How does the Nazca ridge subduction influence the modern Amazonian foreland basin?, *Geology*, *35*, 515–518, doi:10.1130/G23237A.1.

Espurt, N., F. Funiciello, J. Martinod, B. Guillaume, V. Regard, C. Faccenna, and S. Brusset (2008), Flat subduction dynamics and deformation of the south american plate: Insights from analog modeling, *Tectonics*, *27*, TC3001, doi: 10.1029/2007TC002175.

Fermann, E. J. (2006), Google Earth-based lessons and lab activities for earth science classes, Poster, Geol. Soc. Am. Ann. Meeting (Oct.), Philidelphia, PA.

Fowler, C. (Ed.) (2005), *The Solid Earth: An Introduction to Global Geophysics* (2nd ed.), Cambridge Univ. Press, New York, NY.

Frohlich, C. (1989), The nature of deep-focus earthquakes, *Ann. Rev. Earth Planet. Sci.*, *17*, 277–54, doi:10.1146/annurev.earth.17.1.227.

Fromm, R., G. Zandt, and S. Beck (2004), Crustal thickness beneath the Andes and Sierras Pampeanas at 30° S inferred from Pn apparent phase velocities, *Geophys. Res. Lett.*, *31*, 4, L06625 doi:10.1029/2003GL019231.

Furukawa, Y. (1993), Depth of the decoupling plate interface and thermal structure under arcs, *J. Geophys. Res.*, *98*, 20,005–20,013, B11, doi:10.1029/93JB02020.

Garrett, J. J. (2011), Ajax: A new approach to web applications, Website, http://www.adaptivepath.com/ideas/ajax-new-approach-web-applications Last accessed 07/07/2012.

GeoMapApp, M. S. D. S. (2012), Explore our planet with GeoMapApp, Website, http://www.geomapapp.org Last accessed 07/07/2012.

German, C. R., E. T. Baker, D. P. Connelly, J. E. Lupton, J. Resing, S. L. Prien, R. D. Walker, H. N. Edmonds, and C. H. Langmuir (2006), Hydrothermal exploration of the Fonualei rift and spreading center and the North East Lau spreading center, *Geochem. Geophys. Geosyst.*, *7*, Q11022, doi:10.1029/2006GC001324.

GIMP (2011), GIMP 2.6, Website,
www.gimp.org
Last accessed 07/07/2012.

Gobert, J. (2000), A typology of models for plate tectonics: Inferential power and barriers to understanding, *Int. J. Sci. Edu.*, *22*(9), 937–977, doi: 10.1080/095006900416857

Gobert, J. (2005a), Leveraging technology and cognitive theory on visualization to promote students' science learning and literacy, in *Visualization in Science Education*, edited by J. Gilbert, pp. 73–90, Springer-Verlag Publishers, Netherlands.

Gobert, J. (2005b), The effects of different learning tasks on conceptual understanding in science: teasing out representational modality of diagramming versus explaining, *J. Geosci. Edu.*, *53*, 444–455.

Gobert, J., S. C. Wild, and L. Rossi (2012), Testing the effects of prior coursework and gender on geoscience learning with Google Earth, in *Google Earth and Virtual Visualizations in Geoscience Education and Research: Geological Society of America Special Paper 492*, edited by S. J. Whitmeyer, J. E. Bailey, D. G. De Paor, and T. Ornduff, chap. 22, Geol. Soc. Am., Boulder, CO, doi:10.1130/2012.2492(35).

Gobert, J. D., and J. Clement (1999), Effects of student-generated diagrams versus student-generated summaries on conceptual understanding of causal and dynamic knowledge in plate tectonics, *J. Res. Sci. Teach.*, *36*, 39–53, doi: 10.1002/(SICI)1098-2736(199901)36:1<39::AID-TEA4>3.3.CO;2-9.

Gobert, J. D., and A. Pallant (2004), Fostering students' epistemologies of models via authentic model-based tasks, *J. Sci. Edu. and Tech.*, *13*, 7–22, doi: 10.1023/B:JOST.0000019635.70068.6f.

Goodchild, M. F. (2006), The fourth R: rethinking GIS education, *ArcNews*, *28*(3), 1.

Goodchild, M. F. (2008), The use cases of digital Earth, *Int. J. Digit. Earth*, *1*(1), 31–42, doi:10.1080/17538940701782528.

Google (a), Google Earth plug in, Website, http://earth.google.com/support/bin/answer.py?hl=en&answer=176145 Last accessed 07/07/2012.

Google (b), What is Google Earth?, Website, http://www.google.com/earth/explore/products/plugin.html Last accessed 07/07/2012.

Google (2012), Google Earth, Website, http://earth.google.com Last accessed 07/07/2012.

GSI (2004), Estimation of Pacific plate motion by GPS, Website, http://cais.gsi.go.jp/Virtual_GSI/Tectonics/Pacific_GPS/index.html Last accessed 07/07/2012.

Gudmundsson, O., and M. Sambridge (1998), A regionalized upper mantle (RUM) seismic model, *J. Geophys. Res.*, *103*, 7121–7136, B4, doi:10.1029/97JB02488.

Gurnis, M., and B. H. Hager (1988), Controls of the structure of subducted slabs, *Nature*, *335*(22), 317–321, doi:10.1038/335317a0.

Gutscher, M. A. (2002), Andean subduction styles and their effect on thermal structure and interplate coupling, *J. S. Am. Earth Sci.*, *15*, 3–10, doi:10.1016/S0895-9811(02)00002-0.

Gutscher, M. A., J. Malavielle, S. Lallemand, and J. Y. Collot (1999), Tectonic segmentation of the north Andean margin: impact of the Carnegie ridge collision, *Earth Planet. Sci. Lett.*, *170*, 155–156, doi:10.1016/S0012-821X(99)00060-6.

Hager, B. H. (1984), Subducted slabs and the geoid: constraints on mantle rheology and flow, *J. Geophys. Res.*, *89*, 6003–6015, B7, doi:10.1029/JB089iB07p06003.

Hall-Wallace, M. K., and C. M. McAuliffe (2002), Design, implementation, and evaluation of GIS-based learning materials in an introductory geoscience course, *J. Sci. Edu.*, *50*, 5–14.

Halpern, D. F., and M. L. LaMay (2000), The smarter sex: A critical review of sex differences in intelligence, *Educ. Psychol. Rev.*, *12*, 229–246.

Handelsman, J., D. Ebert-May, R. Beichner, P. Bruns, A. Chang, R. DeHaan, J. Gentile, S. Lauffer, J. Stewart, S. M. Tilghman, and W. B. Wood (2004), Scientific teaching, *Science*, *23*, 521–522, doi:10.1126/science.1096022.

Hart, S. R., M. Coetzee, R. A. Workman, J. Blusztajn, K. T. M. Johnson, J. M. Sinton, B. Steinberger, and J. W. Hawkins (2004), Genesis of the Western Samoa seamount province: age, geochemical fingerprint and tectonics, *Earth Planet. Sci. Lett.*, *227*(3-4), 37–56, doi:10.1016/j.epsl.2004.08.005.

Hasegawa, A., and I. S. Sacks (1981), Subduction of the Nazca plate beneath Peru as determined from seismic observations, *J. Geophys. Res.*, *86*(86), 4971–4980, B6, doi:10.1029/JB086iB06p04971.

Hickson, I. (2012), Html5, Website,
http://dev.w3.org/html5/spec/Overview.html
Last accessed 07/07/2012.

Holt, W. E. (1995), Flow fields within the Tonga slab determined from the moment tensors of deep earthquakes, *Geophys. Res. Lett.*, *22*(8), 989–992, doi: 10.1029/95GL00786.

Horwitz, P., J. Gobert, B. Buckley, and L. O'Dwyer (2010), Learning genetics with dragons: From computer-based manipulatives to hypermodels, in *Designs for Learning Environments of the Future: International Perspectives from the Learning Sciences.*, edited by M. J. Jacobson and P. Reimann, Springer Publishers, New York, NY.

Isacks, B., and P. Molnar (1969), Mantle earthquake mechanisms and the sinking of the lithosphere, *Nature*, *223*, 1121–1124, doi:10.1038/2231121a0.

Isacks, B., J. Oliver, and L. R. Sykes (1968), Seismology and the new global tectonics, *J. Geophys. Res.*, *73*(18), 229–246, doi:10.1029 /JB073i018p05855.

Ito, G., and J. Lin (1995), Oceanic spreading center-hotspot interactions: Constraints from along-isochron bathymetric and gravity anomalies, *Geology*, *23*(18), 657–660, doi:10.1130/0091-7613.

Jacobi, D., A. Bergeron, and T. Malvesy (1996), The popularization of plate tectonics: presenting the concepts of dynamics and time, *Public Underst. Sci.*, *5*, 75–100.

Jacobson, M. J., and P. Reimann (Eds.) (2010), *Designs for Learning Environments of the Future: International Perspectives from the Learning Sciences*, Springer Publishers, New York, NY.

Jenkins, A., M. Healey, and R. Zetter (2007), *Linking Teaching and Research in Disciplines and Departments*, Higher Education Academy, York, UK, http://www.heacademy.ac.uk/research/LinkingTeachingAndResearch_April07.pdf

Jordan, T. E., B. L. Isacks, R. W. Allmendinger, J. A. Brewer, V. A. Ramos, and C. J. Ando (1983), Andean tectonics related to geometry of subducted Nazca plate, *Geol. Soc. Am. Bull.*, *94*, 341–361, doi:10.1130/0016-7606(1983)94<341:ATRTGO>2.0.CO;2

json (1999), Introducing JSON, Website, http://www.json.org/ Last accessed 07/07/2012.

Kahle, J. B., L. H. Parker, L. J. Rennie, and D. Riley (1993), Gender differences in science education: Building a model, *Educ. Psychol.*, *28*, 379–404, doi: 10.1207/s15326985ep2804_6.

Kali, Y., and N. Orion (1996), Relationship between Earth Science education and spatial visualization, *J. Res. Sci. Teach.*, *33*, 369–391.

Kali, Y., N. Orion, and E. Mazor (1997), Software for assisting high school students in the spatial perception of geological structures, *J. Sci. Edu.*, *45*, 10–21.

KamLAND Collaboration, K. C. (2011), Partial radiogenic heat model for Earth revealed by geoneutrino measurements, *Nat. Geosci.*, *4*, 647–651, doi: 10.1038/ngeo1205.

Karato, S., and P. Wu (1993), Rheology of the upper mantle: A synthesis, *Science*, *260*(5109), 771–778, doi:10.1126/science.260.5109.771.

Karig, D. E. (1974), Evolution of arc systems in the Western Pacific, *Ann. Rev. Earth Planet. Sci.*, *2*, 51–78, doi:10.1146/annurev.ea.02.050174.000411.

Kay, S., and B. Coira (2009), Shallowing and steepening subduction zones, continental lithospheric loss, magmatism, and crustal flow under the Central Andean Altiplano-Puna plateau, in *Backbone of the Americas:Shallow Subduction, Plateau Uplift and, and Rigde and Terrane Collision:Geological Society of America Memoir*, edited by S. M. Kay, V. A. Ramos, and W. R. Dickenson, pp. 229–259, Geol. Soc. Am. Mem., Boulder, CO, doi:10.1130/2009.1204(11).

Kelleher, J., and W. R. McCann (1976), Buoyant zones, great earthquakes, and unstable boundaries of subduction, *J. Geophys. Res.*, *81*(26), 4885–4896, doi:10.1029/JB081i026p04885.

Kelleher, J., and W. R. McCann (1977), Bathymetric highs and development of convergent plate boundaries, in *Island Arcs, Deep Sea Trenches and Back Arc Basins, Maurice Ewing Series*, edited by M. Talwani and W. C. Pitman III, pp. 115–222, Am. Geophys. Union, Washington, D.C..

Kellogg, L. H., B. H. Hager, and R. D. van der Hilst (1999), Compositional stratification in the deep mantle, *Science*, *283*, 1881–1884, doi:10.1126/science.283.5409.1881.

Kendrick, E., M. Bevis, R. Smalley Jr., B. Brooks, R. Barriga Vargas, E. Lauría, and L. P. Souto Fortes (2003), The Nazca - South America euler vector and its rate of change, *J. S. Am. Earth Sci.*, *16*, 125–131, doi:10.1016/S0895-9811(03)00028-2.

Kincaid, C., and P. Olson (1987), An experimental study of subduction and slab migration, *J. Geophys. Res.*, *92*,832–13,840, B13, doi:10.1029/JB092iB13p13832.

Kincaid, C., and I. S. Sacks (1997), Thermal and dynamical evolution of the upper mantle in subduction zones, *J. Geophys. Res.*, *102*, 12,295–12, B6, doi:10.1029/96JB03553.

Kneller, E., P. van Kekan, K. Shun-ichiro, and J. Park (2005), B-type fabric in the mantle wedge: Insights from high-resolution non-Newtonian subduction zone models, *Earth Planet. Sci. Lett.*, *237*, 781–797, doi:10.1016/j.epsl.2005.06.049

Koppers, A. A. P., H. Staudigel, M. S. Pringle, and J. R. Wijbrans (2003), Short-lived and discontinuous intraplate volcanism in the south pacific: Hot spots or extensional volcanism?, *Geochem. Geophys. Geosyst.*, *4*,1089, 1–49, doi:10.1029/2003GC000533.

Kreemer, C. (2009), Absolute plate motions constrained by shear wave splitting orientations with implications for hot spot motions and mantle flow, *J. Geophys. Res.*, *114*, 18p., B10405, doi:10.1029/2009JB006416.

Larkin, J., and H. Simon (1987), Why a diagram is (sometimes) worth ten thousand words, *Cognitive Sci.*, *11*, 65–99, doi:10.1016/S0364-0213(87)80026-5.

Lau, S., and R. W. Roeser (2002), Cognitive abilities and motivational processes in high school students' situational engagement and achievement in science, *Edu. Assessment*, *8*, 139–162, doi:10.1207/S15326977EA0802_04.

Lawver, L. A., and J. W. Hawkins (1978), Diffuse magnetic anomalies in marginal basins: their possible tectonic and petrologic significance, *Tectonophysics*, *45*, 323–968, doi:10.1016/0040-1951(78)90167-1.

Lay, T., C. J. Ammon, H. Kanamori, L. Rivera, K. D. Koper, and A. R. Hutko (2010), The 2009 Samoa-Tonga great earthquake triggered doublet, *Nature*, *466*, 964–968, doi:10.1038/nature09214.

Libarkin, J. C. (2001), Development of an assessment of student conception of the nature of science, *J. Sci. Edu.*, *49*(5), 435–442.

Libarkin, J. C., and S. W. Anderson (2005), Assessment of learning in entry-level geoscience courses: Results from the geoscience concept inventory, *J. Sci. Edu.*, *53*(4), 394–401.

Linn, M. C., and A. C. Petersen (1985), Emergence and characterization of sex differences in spatial ability: A meta-analysis, *Child Dev.*, *56*, 1479–1498, doi: 10.2307/1130467.

Lisle, R. J. (2006), Google Earth: A new geological resource, *Geol. Today*, *22*(1), 29–32, doi:10.1111/j.1365-2451.2006.00546.x.

Lowe, R. (1993), Constructing a mental representation from an abstract technical diagram, *Learn. Instr.*, *3*, 157–179, doi:10.1016/0959-4752(93)90002-H.

Lupton, J. E., D. G. Pyle, W. J. Jenkins, R. Greene, and L. Evans (2003), Evidence for an extensive hydrothermal plume in the Tonga-Fiji region of the south Pacific, *Geochem. Geophys. Geosyst.*, *5*, Q01003, doi:10.1029/2003GC000607.

Maccoby, E. E., and C. N. Jacklin (1974), *The Psychology of Sex Differences*, Stanford Univ. Press, Palo Alto, CA.

Mahoney, J. J., and K. J. Spencer (1991), Isotopic evidence for the origin of the Manihiki and Ontong Java oceanic plateaus, *Earth and Planet. Sci. Lett.*, *104*, 196–210, doi:10.1016/0012-821X(91)90204-U.

Manea, V. C., M. Perez-Gussinye, and M. Manea (2012), Chilean flat slab subduction controlled by overriding plate thickness and trench rollback, *Geology*, *40*, 35–38, doi:10.1130/G32543.1.

Martin, D. J., and R. Treves (2008), Visualizing geographic data in Google Earth for education and outreach, Am. Geophys. Union Fall Meeting, San Francisco, CA, IN41B-1145.

Martinod, J., L. Husson, P. Roperch, B. Guillaume, and N. Espurt (2010), Horizontal subduction zones, convergence velocity and the building of the Andes, *Earth Planet. Sci. Lett.*, *299*, 299–309, doi:10.1016/j.epsl.2010.09.010.

Mc Donald, T. B., and D. G. De Paor (2008), Above Google Earth: Teaching and research applications of geobrowsers in atmospheric and ionospheric studies, *Geol. Soc. Am. Abstracts with Programs*, *40*(2), 9.

McConnell, D. A., D. N. Steer, K. D. Owens, J. R. Knott, S. Van Horn, W. Borowski, J. Dick, A. Foos, M. Malone, H. McGrew, L. Greer, and P. J. Heaney (2006), Using concept tests to assess and improve student conceptual understanding in introductory geoscience courses, *J. Sci. Edu.*, *54*(1), 61–68.

McDougall, I. (2010), Age of volcanism and its migration in the Samoa islands, *Geol. Mag.*, *147*, 705–717, doi:10.1017/S0016756810000038.

McGee, M. G. (1979), Human spatial abilities: Psychometric studies and environmental, genetic, hormonal and neurological influences, *Psychol. Bull.*, *86*, 889–918, doi:10.1037//0033-2909.86.5.889.

McKenzie, D. P. (1969), Speculations on the consequences and causes of plate motions, *Geophys. J. R. Astron. Soc.*, *18*, 1–32, doi:10.1111/j.1365-246X.1969.tb00259.x.

Millen, D. W., and M. W. Hamburger (1998), Seismological evidence for tearing of the Pacific plate at the northern termination of the Tonga subduction, *Geology*, *26*(7), 659–662, doi:10.1130/0091-7613(1998)026<0659:SEFTOT>2.3.CO;2.

Moores, E. M., and R. J. Twiss (1995), *Tectonics*, W. H. Freeman and Co., New York, NY.

Morgan, W. J. (1972), Deep mantle convection plumes and plate tectonics, *AAPG Bull.*, *56*, doi:10.1306/819A3E50-16C5-11D7-8645000102C1865D.

Muller, R. D., M. Sdrolias, C. Gaina, and W. R. Roest (2008), Age, spreading rates and spreading symmetry of the world's ocean crust, *Geochem. Geophys. Geosyst.*, *9*, Q04006, doi:10.1029/2007GC001743.

Mussett, A. E., and M. A. Khan (2008), *Looking into the Earth: An Introduction to Geological Geophysics*, Cambridge Univ. Press, Cambridge, UK.

NASA (2005), untitled, Website, http://www.nasa.gov/images/content/136215main_BMarbleStill.jpg Last accessed 07/07/2012.

National Research Council, U. S. (Ed.) (1996), *National Science Education Standards*, National Academy Press, Washington, D.C..

Okal, E. A., H. M. Fritz, C. E. Synolakis, J. C. Borrero, R. Weiss, P. J. Lynett, V. V. Titov, S. Foteinis, B. E. Jaffe, P. L. F. Liu, and I. C. Chan (2009), Field survey of the Samoa tsunami of 29 September 2009, *Seismol. Res. Lett.*, *81*(4), 577–591, doi:10.1785/gssrl.81.4.577.

Olbertz, D., M. J. R. Wortel, and U. Hansen (1997), Trench migration and subduction zone geometry, *Geophys. Res. Lett.*, *24*(3), 221–224, doi:10.1029/96GL03971.

Orion, N., D. Ben-Chiam, and Y. Kali (1997), Relationship between Earth-science education and spatial visualization, *J. Sci. Edu.*, *47*, 129–132.

Parker, R. L., and D. W. Oldenburg (1973), Thermal model of ocean ridges, *Nature*, *242*, 137–139, doi:10.1038/physci242137a0.

Parkhurst, D., K. Law, , and E. Niebur (2002), Modeling the role of salience in the allocation of overt visual attention, *Vision Res.*, *42*(1), 107–123, doi:10.1016/S0042-6989(01)00250-4.

Parsons, B., and J. Sclater (1977), An analysis of the variation of ocean floor bathymetry and heat flow with age, *J. Geophys. Res.*, *82*(5), 803–827, doi:10.1029/JB082i005p00803.

Patterson, T. C. (2007), Google Earth as a (not just) geography educational tool, *J. Geogr.*, *106*(4), 145–152, doi:10.1080/00221340701678032.

Peacock, S. (1991), Numerical simulation of subduction zone pressure-temperature-time paths: Constraints on fluid production and arc magmatism, *T. Phys. Sci. Eng.*, *335*, 341–353, doi:10.1098/rsta.1991.0050.

Peacock, S., and K. Wang (1999), Seismic consequences of warm versus cool subduction zone metamorphism: examples from northeast and southwest Japan, *Science*, *286*, 937–939, doi:10.1126/science.286.5441.937.

Pelletier, B., and J. M. Auzende (1996), Geometry and structure of the Vitiaz trench lineament (SW Pacific), *Mar. Geophys. Res.*, *18*, 305–335, doi:10.1007/BF00286083.

Pence, N., E. Weisbrot, S. J. Whitmeyer, D. G. De Paor, and J. Gobert (2010), Using Google Earth for advanced learning in the geosciences, *Geol. Soc. Am. Abstracts with Programs*, *42*(1), 115.

Pfiffner, O. A., and J. G. Ramsay (1982), Constraints on geological strain rates: Arguments from finite strain rates of naturally deformed rocks, *J. Geophys. Res.*, *87*, 311–321, B1, doi:10.1029/JB087iB01p00311.

Piburn, M. D., S. J. Reynolds, D. E. Leedy, C. M. McAuliffe, J. P. Birk, and J. K. Johnson (2002), The hidden Earth: Visualization of geologic features and their subsurface geometry, Nat. Assoc. Res. Sci. Teach. Ann. Meeting (Apr.), New Orleans, LA.

Pilger, R. H. (1981), Plate reconstructions, aseismic ridges, and low-angle subduction beneath the Andes, *Geol. Soc. Am. Bull.*, *92*, 448–456, doi:10.1130/0016-7606(1981)92<448:PRARAL>2.0.CO;2.

Rakshit, R., and Y. Ogneva-Himmelberger (2008), Application of virtual globes in education, *Geogr. Compass*, *2*(2), 1995–2010, doi:10.1111/j.1749-8198.2008.00165.x.

Rakshit, R., and Y. Ogneva-Himmelberger (2009), Teaching and learning guide for: Application of virtual globes in education, *Geogr. Compass*, *3*(4), 1579–1595, doi: 10.1111/j.1749-8198.2009.00246.x.

Ramos, V. A., and A. Folguera (2009), Andean flat slab subduction through time., in *Ancient Orogens and Modern Analogues*, vol. 327, edited by M. B., pp. 31–54, Geo. Soc. London Special Publication, London, UK., .

Ramos, V. A., E. O. Cristallini, and D. J. Pérez (2002), The Pampean flat-slab of the Central Andes., *J. S. Am. Earth Sci.*, *15*(1), 59–78, doi:10.1016/S0895-9811(02)00006-8.

Ramsay, J. (1967), *Folding and Fracturing of Rocks.*, McGraw-Hill, New York, NY.

Rashid, O., I. Mullins, P. Coulton, and R. Edwards (2006), Extending cyberspace: Location based games using cellular phones, *ACM Comput. Ent.*, *4*(1), doi: 10.1145/1111293.1111302, article 3C.

Reid, I., and H. R. Jackson (1981), Oceanic spreading rate and crustal thickness, *Mar. Geophys. Res.*, *5*, 165–172.

Rensink, R., J. O'Regan, and J. Clark (1997), To see or not to see: The need for attention to perceive changes in scenes, *Psychol. Sci.*, *8*(5), 368–373, doi:10.1111/j.1467-9280.1997.tb00427.x.

Reynolds, S. J., J. K. Johnson, M. D. Piburn, D. E. Leedy, J. A. Coyan, and M. M. Busch (2005), Visualization in undergraduate geology course, in *Visualization in Science Education*, edited by J. K. Gilbert, Springer Inc., Netherlands.

Rosenbaum, G., and G. S. Lister (2004), Neogene and quaternary rollback evolution of the Tyrrhenian sea, the Apennines and the Sicilian maghrebides, *Tectonics*, *23*, TC1013, doi:1010.1029/2003TC001518.

Ross, R. M., D. Duggan-Haas, R. Kissel, and C. Bessemer (2008), Why does the Earth look the way it does?, Website,
http://www.virtualfieldwork.org/Welcome.html
Last accessed 07/07/2012.

Roush, W. (2007), Second earth, *Technology Review (Jul./Aug.)*, 39–48.

Russo, R. M., J. C. VanDecar, D. Comte, V. I. Mocanu, A. Gallego, and R. E. Murdie (2010), Subduction of the Chile ridge: Upper mantle structure and flow, *GSA Today*, *20*(9), 4–10, doi:10.1130/GSATG61A.1.

Ryan, W. B. F., S. M. Carbotte, J. O. Coplan, S. O'Hara, A. Melkonian, R. Arko, R. A. Weissel, V. Ferrini, A. Goodwillie, F. Nitsche, J. Bonczkowski, and R. Zemsky (2009), Global multi-resolution topography synthesis, *Geochem. Geophys. Geosyst.*, *10*, Q03014, doi:10.1029/2008GC002332.

Sanchez, E. (2009), Innovative teaching/learning with geotechnologies in secondary education, *Edu. Tech. for a Better World*, *302*, 65–74, doi:10.1007/978-3-642-03115-1_7.

Sao Pedro, M. A., R. S. J. d. Baker, O. Montalvo, A. Nakama, and J. D. Gobert (2010), Using text replay tagging to produce detectors of systematic experimentation behavior pattern, Proceedings of the 3rd International Conference on Educational Data Mining, Pittsburgh, PA.

Schellart, W., J. Freeman, D. Stegman, L. Moresi, and D. May (2007), Evolution and diversity of subduction zones controlled by slab width, *Nature*, *446*, 308–311, doi:10.1038/nature05615.

Schellart, W. P., D. R. Stegman, R. J. Farrington, J. Freeman, and L. Moresi (2010), Cenozoic tectonics of Western North America controlled by evolving width of Farallon, *Science*, *329*, 316, doi:10.1126/science.1190366.

Schmelling, H., R. Monz, and D. C. Rubie (1999), The influence of olivine metastablility on the dynamics of subduction, *Earth Planet. Sci. Lett.*, *165*, 55–66, doi: 10.1016/S0012-821X(98)00249-0.

Schofield, N. J., and J. R. Kirby (1994), Position location on topographical maps: Effects of task factors, training, and strategies, *Cognition Instruct.*, *12*(1), 35–60, doi:10.1207/s1532690xci1201_2.

Schubert, G. (1992), Numerical models of mantle convection, *Ann. Rev. Fluid Mech.*, *24*, 359–94, doi:10.1146/annurev.fluid.24.1.359.

Segall, P., and C. Simpson (1986), Nucleation of ductile shear zones on dilatant fractures, *Geology*, *14*(1), 56–59, doi:10.1130/0091-7613(1986).

Selkin, P. A., D. G. De Paor, J. Gobert, K. B. Kirk, S. Kluge, G. A. Richard, and S. J. Whitmeyer (2009), Emerging digital technologies for geoscience education and outreach, *Geol. Soc. Am. Abstracts with Programs*, *47*(7), 165.

Sibson, R. H. (1981), Controls on low-stress hydro-fracture dilatancy in thrust, wrench and normal fault terrains, *Nature*, *289*, 665–667, doi:10.1038/289665a0.

Simpson, C., and D. G. De Paor (1993), Strain and kinematic analysis in general shear zones, *J. Struct. Geol.*, *15*(1), 1–20, doi:10.1016/0191-8141(93)90075-L.

Simpson, C., and D. G. De Paor (2010), Restoring maps and memoirs to four-dimensional space using virtual globe technology: A case study from the Scottish Highlands, in *Continental Tectonics and Mountain Building*, edited by R. D. Law, R. W. H. Butler, R. E. Holdsworth, M. Krabbendam, and R. A. Strachan, p. 335, Geol. Soc. London Special Publication, London, UK.

Simpson, C., S. J. Whitmeyer, D. G. De Paor, L. P. Gromet, R. Miro, M. A. Krol, and H. Short (2001), Sequential ductile through brittle reactivation of major fault zones along the accretionary margin of Gondwana in Central Argentina, in *The Nature and Tectonic Significance of Fault Zone Weakening*, edited by R. E. Holdsworth, R. A. Strachan, J. F. Macloughlin, and R. J. Knipe, pp. 233–254, Geol. Soc. London, London, UK.

Simpson, C., D. G. De Paor, M. R. Beebe, and J. Strand (2011), Transferring maps and data from pre-digital-era theses to Google Earth: A case study from the Vrede-fort dome, South Africa, in *Google Earth and Virtual Visualizations in Geoscience Education and Research: Geological Society of America Special Paper 492*, edited by S. Whitmeyer, J. Bailey, D. De Paor, and T. Ornduff, Geol. Soc. Am., Boulder, CO.

Smith, G. P., D. A. Wiens, K. M. Fischer, L. M. Dorman, S. C. Webb, , and Hilde-brand (2001), A complex pattern of mantle flow in the Lau backarc, *Science*, *292*(5517), 713–716, doi:10.1126/science.1058763.

SoftComplex (2010), Tigra slider control, Website,
http://www.softcomplex.com/products/tigra_slider_control/
Last accessed 07/07/2012.

Springer, M. (1999), Interpretation of heat-flow density in the Central Andes, *Tectonophysics*, *306*, 377–395, doi:10.1016/S0040-1951(99)00067-0.

Stadler, G., M. Gurnis, C. Burstedde, L. C. Wilcos, L. Alisic, and O. Ghattas (2010), The dynamics of plate tectonics and mantle flow: From local to global scales, *Science*, *329*(5995), 1033–1038, doi:10.1126/science.1191223.

Stahley, T. (2006), Earth from above, *Sci. Teach.*, *73*(7), 44–48.

Stegman, D. R., J. Freeman, W. P. Schellart, L. Moresi, and D. May (2006), Influence of trench width on subduction hinge retreat rates in 3-D models of slab rollback, *Geochem. Geophys. Geosyst.*, *7*, 22, Q03012, doi:10.1029/2005GC001056.

Stevenson, D. J., and J. S. Turner (1977), Angle of subduction, *Nature*, *270*(24), 334–336, doi:10.1038/270334a0.

Stout, D. L., and E. W. Bierly and J. T. Snow (1994), Scrutiny of undergraduate geoscience education: Is the viability of the geosciences in jeopardy?, Am. Geophys. Union Chapman Conference (Sept.), Washington, D.C., p. 55.

Sykes, L. R. (1966), The seismicity and deep structure of island arcs, *J. Geophys. Res.*, *71*(12), 2981–3006, doi:10.1029/JZ071i012p02981.

Syracuse, E. M., and G. A. Abers (2006), Global compilation of variations in slab depth beneath arc volcanoes and implications, *Geochem. Geophys. Geosyst.*, *7*(5), 1–18, Q05017, doi:10.1029/2005GC001045.

Syracuse, E. M., P. van Keken, and G. A. Abers (2010), The global range of subduction zone thermal models, *Phys. Earth Planet. Int.*, *183*, 73–90, doi: 10.1016/j.pepi.2010.02.004.

Tackley, P. J. (2000), Self-consistent generation of tectonic plates in time-dependent, three-dimensional mantle convection simulations, *Geochem. Geophys. Geosyst.*, *1*(1), 45, doi:10.1029/2000GC000036.

Tarantola, A. (1984), Inversion of seismic reflection data in the acoustic approximation, *Geophysics*, *49*, 1259–1266, doi:10.1190/1.1441754

Thompson, K., J. Keith, R. H. Swan, and W. K. Hamblin (2006), Linking geoscience visualization tools: Google Earth, oblique aerial panoramas, and illustrations and mapping software, *Geol. Soc. Am. Abstracts with Programs*, *38*(7), 325.

Tovish, A., G. Schubert, and B. P. Luyendyk (1978), Mantle flow pressure and the angle of subduction: non-Newtonian corner flows, *J. Geophys. Res.*, *85*, 5892–98, B12, doi:10.1029/JB083iB12p05892.

Trend, R. (2000), Conceptions of geological time among primary teacher trainees, with reference to their engagement with geosciences, history and science, *Int. J. Sci. Edu.*, *22*, 539–555, doi:10.1080/095006900289778.

Trimble (2012), Trimble sketchup, Website,
http://sketchup.google.com/intl/en/download/rubyscripts.html
Last accessed 07/07/2012.

Turcotte, D., and E. Oxburgh (1967), Finite amplitude convective cells and continental drift, *J. Fluid Mech.*, *28*, 29–42, doi:10.1017/S0022112067001880.

Turcotte, D., and G. Schubert (2002), *Geodynamics*, Cambridge Univ. Press, New York, NY.

USGS (2009a), Magnitude 8.1 Samoa Islands region., WebSite,
http://earthquake.usgs.gov/earthquakes/recenteqsww/Quakes/us2009mdbi.php.
Last accessed 07/07/ 2012.

USGS (2009b), Magnitude 8.1 Samoa Islands region., Website,
http://earthquake.usgs.gov/earthquakes/recenteqsww/
Quakes/us2009mdbi.php#scitech.
Last accessed 07/07/2012.

Uyeda, S., and H. Kanamori (1979), Back-arc opening and the mode of subduction, *J. Geophys. Res.*, *84*, 1049–1061, B3, doi:10.1029/JB084iB03p01049.

van der Hilst, R. (1995), Complex morphology of subducted lithosphere in the mantle beneath the Tonga trench, *Nature*, *374*, 154–157, doi:10.1038/374154a0.

van Keken, P., B. Kiefer, and S. Peacock (2002), High resolution models of sub-duction zones: implecations for mineral dehydration reactions and the transport of water into the deep mantel, *Geochem. Geophys. Geosyst.*, *3*, 1056, 1–20, doi: 10.1029/2007JB005190.

van Keken, P., C. Currie, S. D. King, M. D. Behn, A. Cagnioncle, J. He, R. F. Katz, S.-C. Lin, E. M. Parmentier, M. Spiegelman, and K. Wang (2008), A community benchmark for subduction zone modeling, *Phys. Earth Planet. Int.*, *171*, 187–197, doi:10.1016/j.pepi.2008.04.015.

van Kesteren, A. (2012), XMLHttpRequest, Website, http://www.w3.org/TR/XMLHttpRequest/ Last accessed 07/07/2012.

Vargas, C. A., P. Mann, and C. Borrero (2011), Field guides for excursions to the Nevado del Ruiz volcano and to the Romeral fault system (Colombia), in the frame of the neotectonics of arc-continent collision concepts, *Earth Sci. Res. J.*, *15*(1), 47–74.

Vassiliou, M. S., B. H. Hager, and A. Raefsky (1984), The distribution of earthquakes with depth and stress in subducting slabs, *J. Geodyn.*, *1*, 11–28, doi:10.1016/0264-3707(84)90004-8.

Violay, M., B. Gibert, D. Mainprice, B. Evans, P. Pezard, O. G. Flovenz, and R. As-mundsson (2010), The brittle ductile transition in experimentally deformed basalt under oceanic crust conditions: Evidence for presence of permeable reservoirs at supercritical temperatures and pressures in the Icelandic crust, Proceedings World Geothermal Congress (Apr.), Indonesia.

Violay, M., B. Gibert, D. Mainprice, B. Evans, J. Dautria, P. Azais, and P. Philippe (2012), An experimental study of the brittle-ductile transition of basalt at oceanic crust pressure and temperature conditions, *J. Geophys. Res.*, *117*, 1–23, B03213, doi:10.1029/2011JB008884.

Wada, I., and K. Wang (2009), Common depth of slab-mantle decoupling: Recon-ciling diversity and uniformity of subduction zones, *Geochem. Geophys. Geosyst.*, *10*(10), 36, Q10009, doi:10.1029/2009GC002570.

Wada, I., K. Wang, J. He, and R. D. Hyndman (2008), Weakening of the subduction interface and its effects on surface heat flow, slab dehydration, and mantle wedge serpentinization, *J. Geophys. Res.*, *113*, 15, B04402, doi:10.1029/2007JB005190.

Wagner, L. S., S. Beck, G. Zandt, and M. N. Ducea (2006), Depleted lithosphere,cold, trapped asthenosphere, and frozen melt puddles above the flat slab in central Chile and Argentina, *Earth Planet. Sci. Lett.*, *245*, 289–301, doi: 10.1016/j.epsl.2006.02.014.

Weiss, L. E. (1980), Nucleation and growth of kink bands, *Tectonophysics*, *65*, 1–38, doi:10.1016/0040-1951(80)90221-8.

Wernicke, J. (2009), *The KML handbook: Geographic Visualization for the Web*, Addison-Wesley, Boston, MA.

Whitmeyer, S. J., and D. G. De Paor (2008), Large-scale emergent cross sections of crustal structures in Google Earth, *Geol. Soc. Am. Abstracts with Programs*, *40*(6), 189.

Whitmeyer, S. J., and C. Simpson (2003), High strain-rate deformation fabrics characterize a kilometers- thick paleozoic fault zone in the Eastern Sierras Pampeanas, central Argentina, *J. of Struct. Geol.*, *25*, 909–922, doi:10.1016/S0191-8141(02)00118-9.

Whitmeyer, S. J., and C. Simpson (2004), Regional deformation of the Sierra de San Luis, Argentina: Implications for the paleozoic development of western Gondwana, *Tectonics*, *23*, 1–16, TC1005, doi:10.1029/2003TC001542.

Whitmeyer, S. J., M. Feely, D. G. De Paor, R. Hennessy, S. Whitmeyer, J. Nicoletti, B. Santangelo, J. Daniels, and M. Rivera (2009), Visualization techniques in field geology education: Modern Pedagogy and Original Research in Western Ireland, in *Field Geology Education: Historical Perspectives and Modern Approaches*, *Geol. Soc. Am. Special Paper*, *461*, 105–115.

Whitmeyer, S. J., J. Nicoletti, and D. G. De Paor (2010), The digital revolution in geologic mapping, *GSA Today*, *20*(4), 4–10, doi:10.1130/GSATG70A.1.

Whitmeyer, S. J., D. G. De Paor, J. Gobert, N. Pence, and E. Liz Weisbrot (2011), Enhancing the geoscience curriculum using geo-browser based learning objects, Presentation: CCLI/TUES Principal Investigators Conference, Washington, D.C., http://ccliconference.org/abstracts/638.

Wikipedia (2011), Monster milktruck, Website, http://en.wikipedia.org/wiki/Monster_Milktruck Last accessed 07/07/2012.

Wild, S. C., M. M. Dordevic, and D. G. De Paor (2011), Tonga, Website, http://www.lions.odu.edu/org/planetarium/steve/GS/API/ Last accessed 07/07/2012.

Wilson, J. T. (1973), Mantle plumes and plate tectonics, *Tectonophysics*, *19*(2), 149–164.

Yoshii, T. (1975), Regionality of group velocities of Rayleigh waves in the Pacific and thickening of the plate, *Earth Planet. Sci. Lett.*, *25*(3), 305–312, doi:10.1016/0012-821X(75)90246-0.

Zandt, G. M., J. Leidig, J. Chmielowski, D. Baumont, and X. Yuan (2003), Seismic detection and characterization of the Altiplano-Puna magma body, Central Andes, *Pure Appl. Geophys.*, *160*, 789–807, doi:10.1007/PL00012557.

Zhong, S., and M. Gurnis (1992), Viscous flow model of a subduction zone with a faulted lithosphere: long and short wavelength topography, gravity and geoid, *Geophys. Res. Lett.*, *19*(18), 1991–1894, doi:10.1029/92GL02142.

Zhong, S., and M. Gurnis (1994), Controls on trench topography from dynamic models of subducted slabs, *J. Geophys. Res.*, *99*, 15,683–15,695, B8, doi: 10.1029/94JB00809.

Zhong, S., and M. Gurnis (1996), Interaction of weak faults and non-Newtonian rheology produces plate tectonics in a 3-D model of mantle flow, *Nature*, *383*, 245–247, doi:10.1038/383245a0.

APPENDIX A

STUDY 1 - ICELAND PRE- AND POST-TEST

NSF-TUES: Pre-post Test, Nov 2010

Note: Your score in this test will not affect your grade.

Study ID number:........................... Circle one: pre / post

Q1 What is your previous experience of the geology or geography of Iceland?

(i) I have no significant previous study experience

(ii) I did a class project about the geology or geography of Iceland

(iii) I participated in a real field trip or a holiday visit

(iv) I am Icelandic or lived in Iceland for an extended period

Q2 Where is Iceland relative to the Arctic Circle?

(i) Iceland lies entirely south of the Arctic Circle

(ii) Iceland lies entirely north of the Arctic Circle

(iii) The Arctic Circle touches the northern coast or offshore islands

(iv) The Arctic Circle touches the southern coast or offshore islands

(v) The Arctic Circle goes through the center of Iceland

Q3 Trace the location of Iceland in pencil or felt pen on this map:

Figure 111. Regional Iceland Map.

Q4 If you camped out in northern Iceland in mid-summer and looked at the northern ocean horizon close to midnight, what would you expect to see, weather permitting?

(i) Continuous sunshine

(ii) Continuous darkness

(iii) Darkness except for a brief period of twilight

(iv) Sunshine except for a brief period of twilight

Q5 If you camped out in southern Iceland in mid-winter and looked at the southern ocean horizon close to midday, what would you expect to see, weather permitting?

(i) Continuous sunshine

(ii) Continuous darkness

(iii) Darkness except for a brief period of twilight

(iv) Sunshine except for a brief period of twilight

Q6 Outside of city and town limits, Iceland is...

(i) Predominantly forested in fir trees

(ii) Predominantly industrialized

(iii) Predominantly farmed for cereal crops

(iii) Predominantly undeveloped land

Q7 Ho much of Iceland is covered in ice all year round?

(i) about 99%

(ii) more than 75%

(iii) about 50%

(iv) less than 25%

(iv) about 1%

Q8 What is the principle rock type seen in Iceland?

(i) limestone

(ii) basalt

(iii) granite

(iv) marble

Q9 Which best describes the geological origins of Iceland?:

(i) Iceland sits on top of both a deep mantle plume and a divergent plate boundary

(ii) Iceland is a fragment of continental crust, like Britain and Ireland, that detached from the European margin during North Atlantic spreading

(iii) Iceland is a volcanic island arc forming above a subduction zone

(iv) Iceland is a huge floating mass of ice drifting very slowly away from Greenland

Q9 What does a glacier look like?:

(i) A river of rapidly flowing ice

(ii) a mass of pure white ice

(iii) a mixture of ice with lots of dirty rock

APPENDIX B

STUDY 2 - TONGA PRE- AND POST-TEST

NSF-TUES: Pre-post Test, Nov 2010

Note: Your score in this test will not affect your grade.

Study ID number:............................ **Circle one: pre / post**

Q1 What is your previous experience of the geology or geography of American-Samoa/Tonga?

(i) I have no significant previous study experience

(ii) I did a class project about the geology or geography of American-Samoa/Tonga

(iii) I participated in a real field trip or a holiday visit

(iv) I am Native to or lived in the American-Samoa/Tonga region for an extended period

Q2 Where is American-Samoa/Tonga region relative to Equator?

(i) American-Samoa/Tonga region lies entirely south of the Tropic of Capricorn

(ii) American-Samoa/Tonga region lies entirely north of the Tropic of Capricorn

(iii) The Tropic of Capricorn touches the northern part of the American-Samoa/Tonga

(iv) The Tropic of Capricorn touches the southern part of the American-Samoa/Tonga

(v) The Tropic of Capricorn goes through the center of the American-Samoa/Tonga region

Q3 Circle the location of the Samoa-Tonga region in pencil or felt pen on this map:
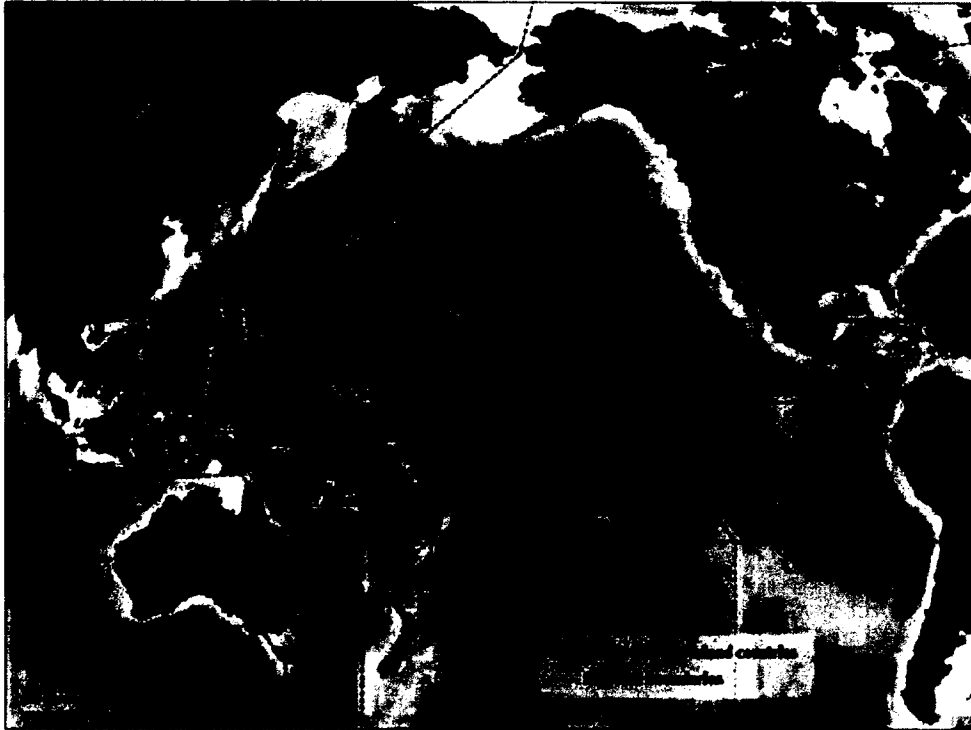

Figure 112. Pacific Rim Map.

Q 4 Study this sketch map where:
A, B = two converging tectonic plates.
V = line of volcanic islands,
T = line of ocean trench
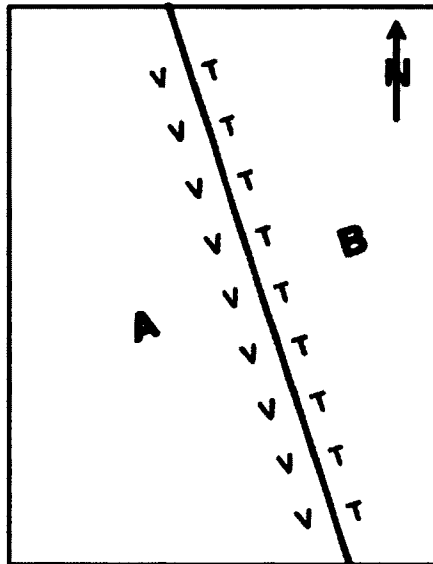
Based on the map view above which cross section below describes the relative plate motion between A and B? Circle cross section (i) or cross section (ii).
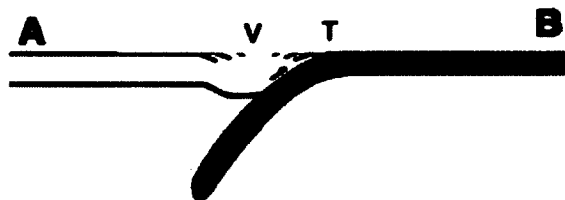
Above: cross section (i) A is moving east and subducting under B

Below: cross section (ii) B is moving west and subducting under A
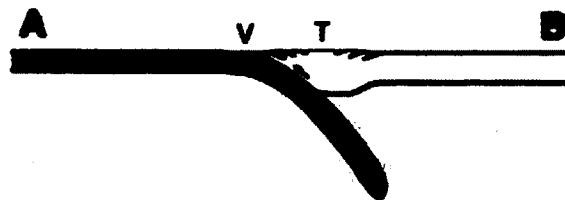
Q5 Which of the following pictures shows the earthquake pattern for the American-Samoa/Tonga region. Where A represents the Australian Plate and B is the Pacific plate. Plate B moves under Plate A.

With ● being deep earthquakes

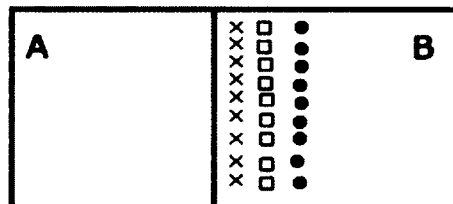[] Are medium depth earthquakes
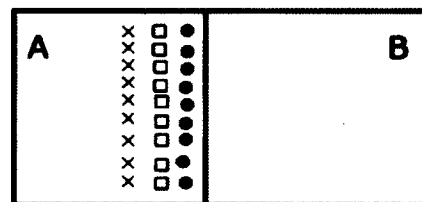
And X representing shallow earthquakes
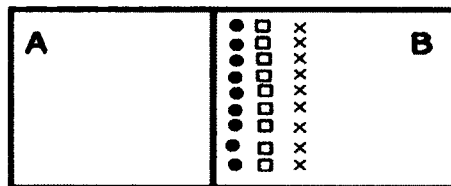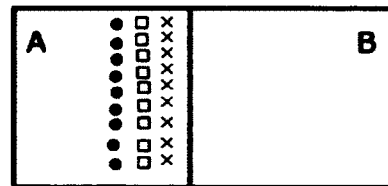
(a) i   (b) ii

(c) iii   (d) iv

Q6 The Tonga trench's motion relative to the Pacific plate is

(i) Moves forward with the Pacific plate.

(ii) Stationary (trench does not move).

(iii) Moves against Plate Motion.

(iv) There is no such thing as the Tonga trench.

Q7 Which volcanic arc is closer to a trench?

(i) Active Arc closer and Dormant arc further.

(ii) Dormant Arc closer and Active Arc further.

Q8 A Convergent Plate Boundary is described as

(i) two tectonic plates slide by each other side by side

(ii) two tectonic plates move apart from each other

(iii) two tectonic plates moving together but they slam into each other

(iv) two tectonic plates moving together but one goes under the other

Q9 Put the two events in the correct order

(i) trench rollback occurs then spreading ridge forms

(ii) spreading ridge forms and then trench rollback occurs

Q10 Where is new ocean crust formed?

(i) Trench

(ii) Volcanic Arc

(iii) Spreading Ridge

(iv) Island Chains

Q11 Put the events in the correct order, using 1 for the first and 4 for the last

Tear Point Forms -

Spreading Ridge Forms -

Trench Rollback-

Trench Forms-

APPENDIX C

COMSOL QUANTIFICATION

C.0.1 NAVIER-STOKES

To verify the COMSOL solutions a comparison to a analytic solution will be made. The Navier-Stokes equations for fluid flow can be checked against the analytic corner flow solution by *Reid and Jackson* [1981] using the corner flow equations developed by *Batchelor* [1967]. The corner flow model is set up by having a rigid plate slide against a stationary plate at an angle as shown in Figure 113.
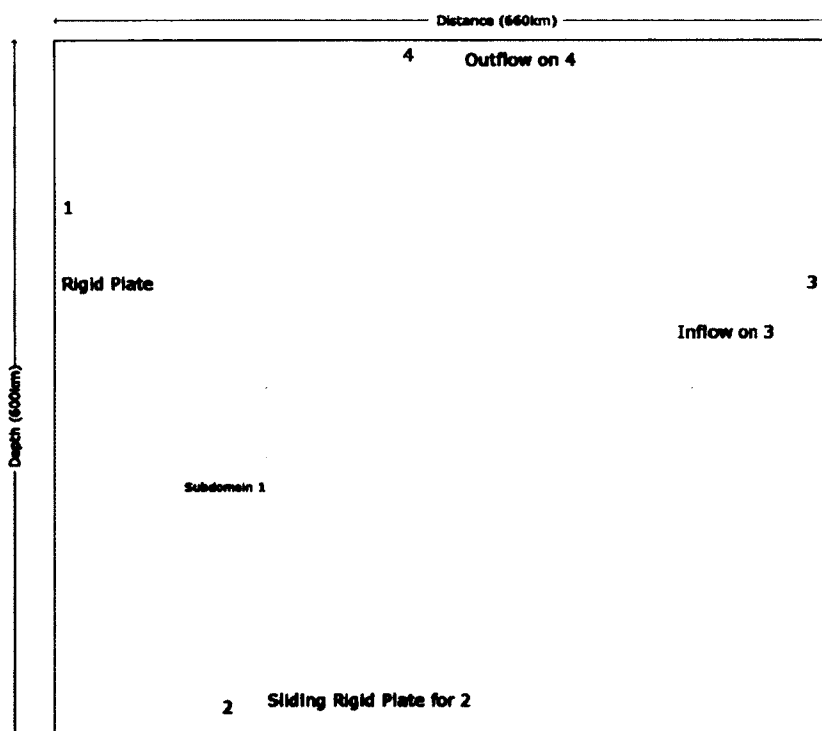

Figure 113. Boundary Conditions in COMSOL for code-verification.

The analytic solution for the x and y velocity components is

$$V_x = A(B + C\tan^{-1}(\frac{y}{x}) + \frac{x^2 + xyC}{x^2 + y^2}) \tag{35}$$

and

$$V_y = A(-\tan^{-1}(\frac{y}{x}) + \frac{Cy^2 + xy}{x^2 + y^2}) \tag{36}$$

The constants are dependent on the angle between the plates for 90° the constants are

- $A = \frac{4U}{\pi^2 - 4}$

- $B = -\frac{\pi^2}{4}$

- $C = \frac{\pi}{2}$

The velocities may be analytically solved for and compared to the COMSOL flow field solutions.

The COMSOL model used for the verification was developed using the non-dimensional Navier-Stokes equation. The model was a 1.1x1 size with a length scale of 600 km. Figure 113 shows the model set-up with the four boundary conditions. The sub-domain setting used a homogeneous medium of non-dimensionalized density with a value $\frac{1}{Pr}$ and all forces set to 0. The only particle motion is due from the shearing of the mobile wall which has a non-dimensional velocity of 1308.

The COMSOL velocity solutions are exported on a predefined 6 km spaced x-y grid, shown in Figure 114, which allows direct comparison of the analytical to model predicted velocities seen in Figure 115. The grid consists of over 11000 points. The method of comparing error is to take the absolute value of the difference between the model predicted and analytic value. This results in a total difference of 1900 for V_x values and 3400 for V_y values. A plot of the V_x and V_y differences is shown in Figures 116 and 117. The differences arise in the upper right corner while the Batchelor Solution has free boundaries and the COMSOL solution has a zero-pressure point in the upper corner, this causes a swirl to develop where the Batchelor solution has straight flow, see Figures 114 and 115 . This discrepancy caused in the upper corner is a far-model effect which does not impact the lower left corner where the actual physics of interest, the corner flow, takes place. As can be seen in Figures 116 and 117 there is a buffer of 500 km between the corner and region where the swirl develops. The effect of the corner swirl was tested in tow subduction models as well, one model was the normal model used and a second had a velocity patch on an exit boundary. The models had different velocities near the exit boundaries, but the same solutions in the corner. Thus, the physics of the COMSOL solution for the Navier-Stokes equations can be used with confidence.
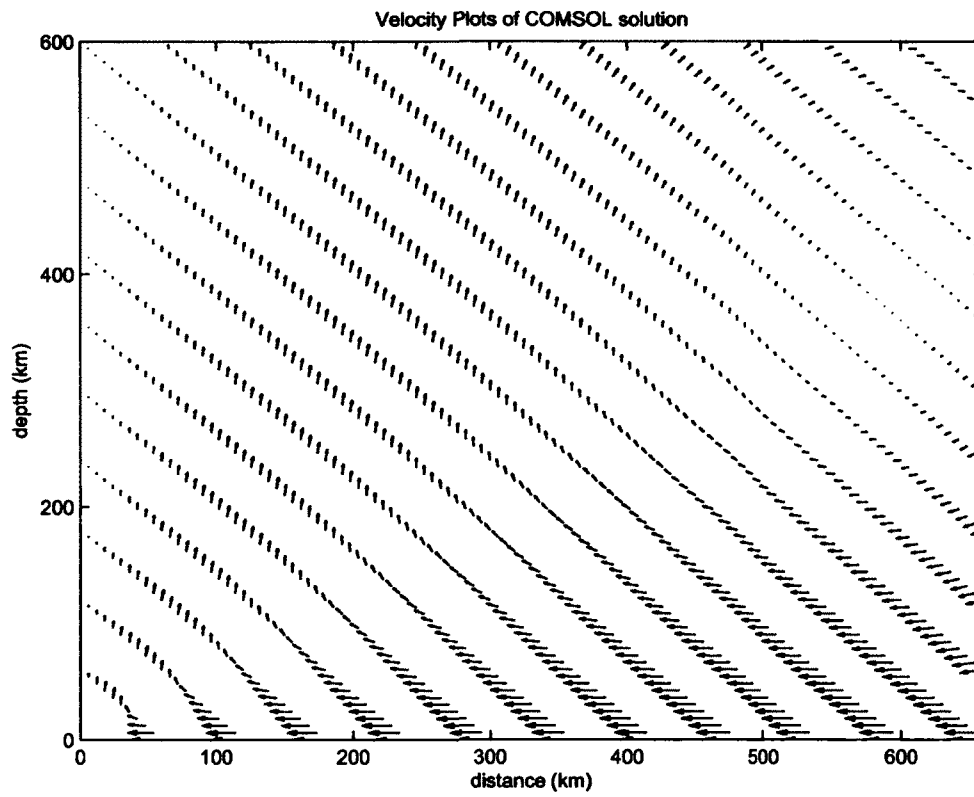
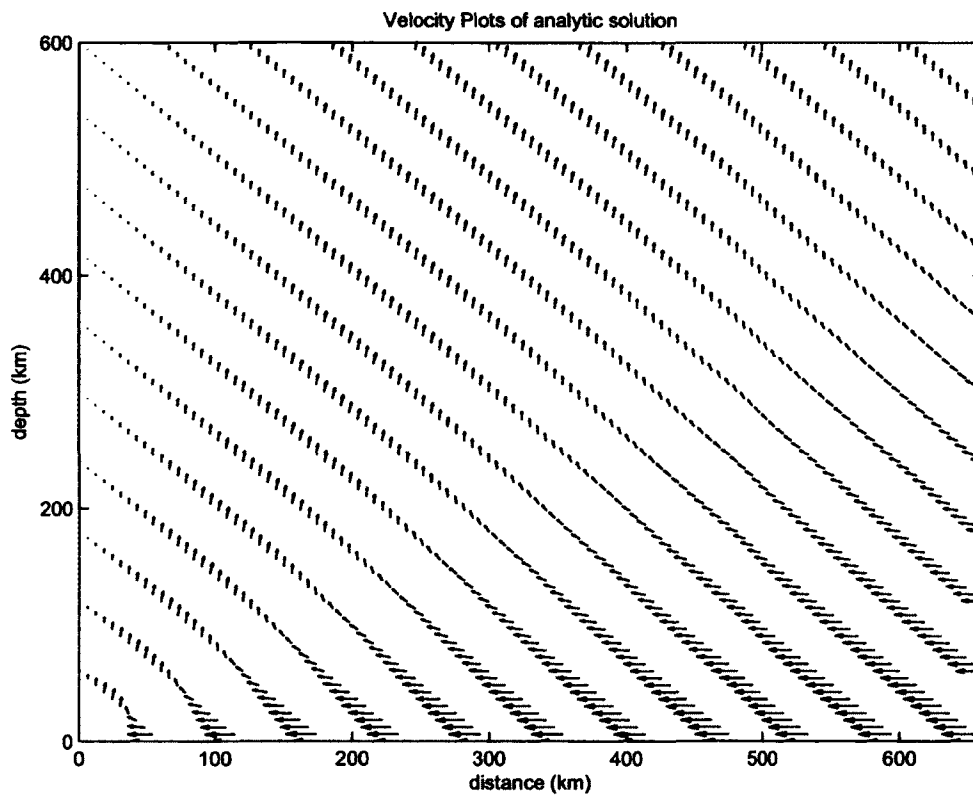**Figure 114.** Velocity Field from the COMSOL solution for corner flow in a 90° set-up.

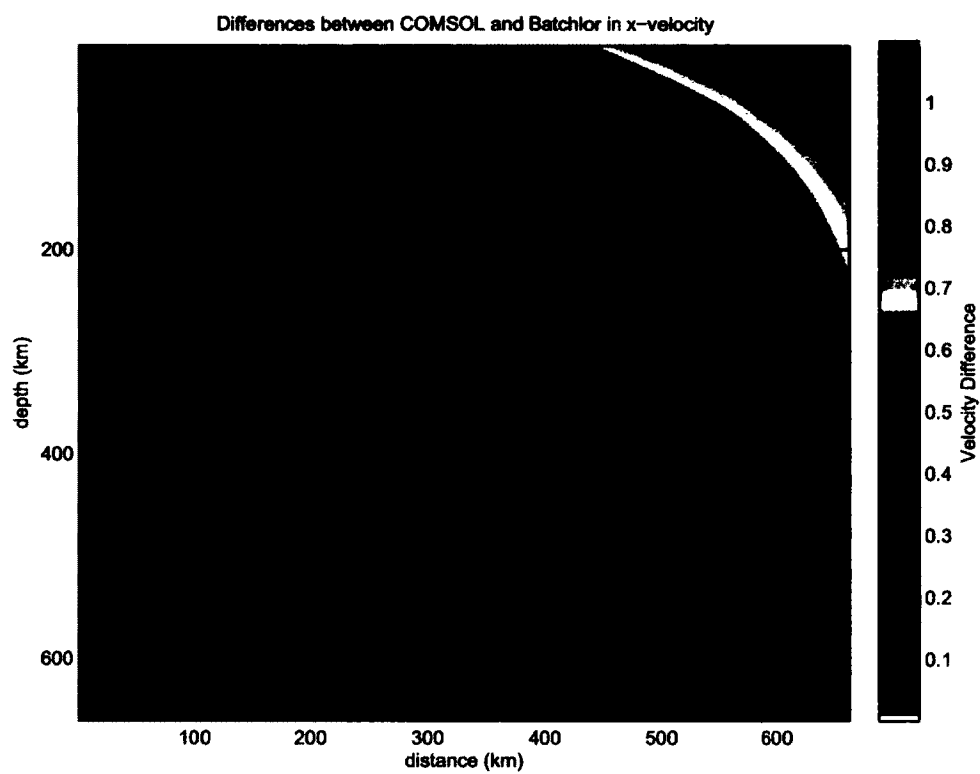**Figure 115.** Velocity Field from the Batchelor solution for corner flow in a 90° set-up.

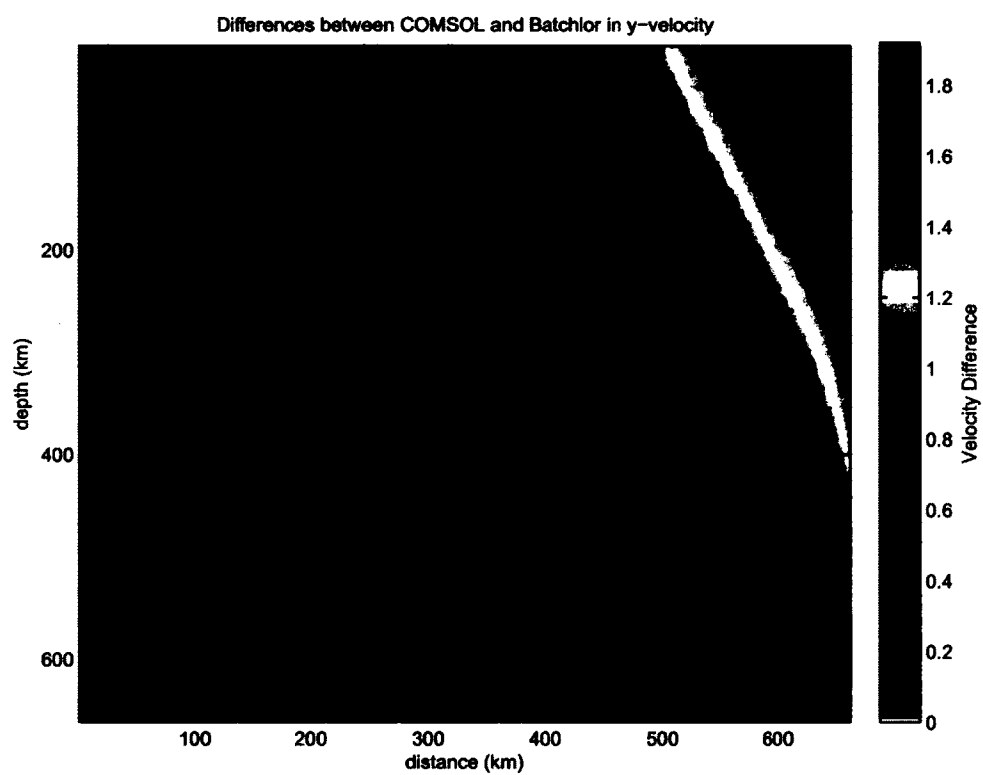**Figure 116.** Differences in V_x between analytic and COMSOL solution

Figure 117. Differences in V_y between analytic and COMSOL solution

C.0.2 CONDUCTION-CONVECTION

The conduction-convection physics code of COMSOL is checked by comparing the results to the analytic solution of the half-space cooling model based on the age of the plate [*Turcotte and Oxburgh*, 1967; *Parsons and Sclater*, 1977]

$$T(x = 0, y) = T_s + (T_0 - T_s)erf(\frac{y}{2\sqrt{\kappa\tau}}) \tag{37}$$

where surface temperature T_s is the temperature at y=0 (273 K), mantle reference temperature $T_0 = 1573$ K, τ is the plate age in seconds, and κ is thermal diffusivity $(0.7272 \times 10^{-6}m^2s^{-1})$ [*van Keken et al.*, 2008]). The plate age is found by taking the length of the model, 660 km, and dividing by the plate velocity, 7 cm/yr, and then converting to seconds. A temperature profile vs. depth may then be created and compared to the model-predicted temperature profile of the same value.

The conduction convection model has the boundary condition shown in Figure 118.

This verification has a temperature dependent buoyancy force term added by

$$F_y = (T(x) - T_0)\rho \tag{38}$$

where T_0 is the reference temperature of 1573K, ρ is the density 3300 kgm^{-3}, and T(x) is the model temperature at the point. Using these parameters the model predicted temperature solutions are given in Figure 119 and 120.

The plots of the temperature profiles for x=0 from the model predicted results and equation 37 for y=0 to 600 km are very similar, see Figure 121.

The largest temperature difference is 36°C, with an expected value of 904° C, which results in a 4% error. Temperature differences range from 9-36°C over a length of 54 km, which is small compared to the size of the model and to the reference temperature of 1300°C. This agreement allows the use of the convection-conduction equations in COMSOL with confidence.
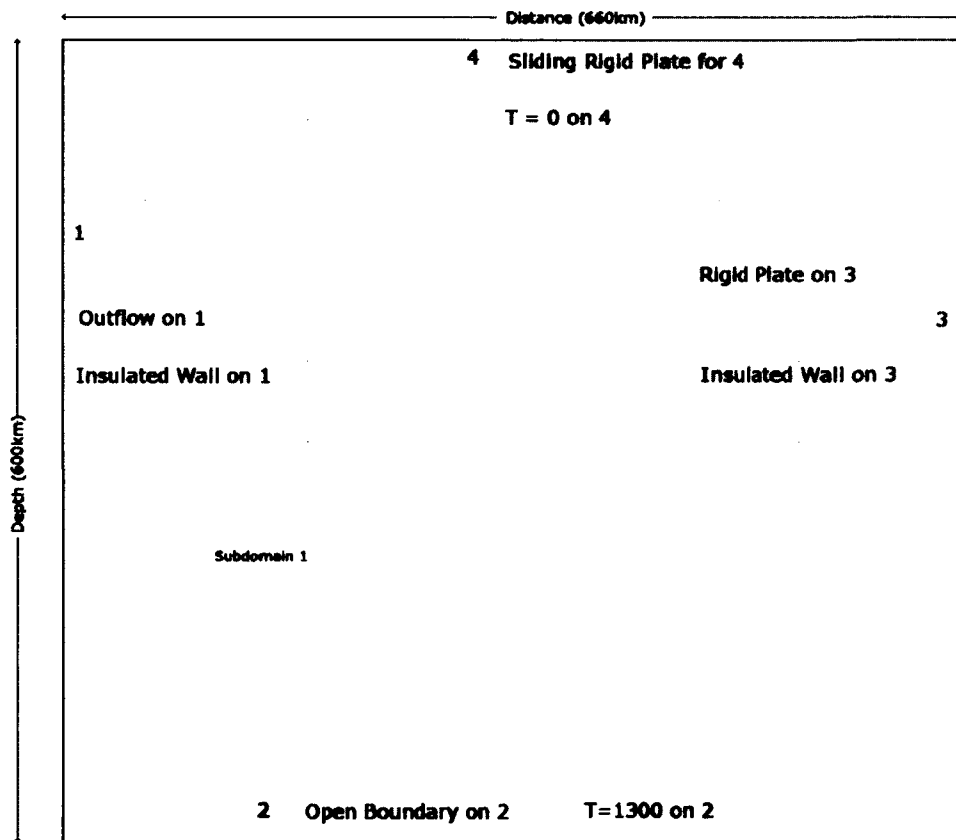
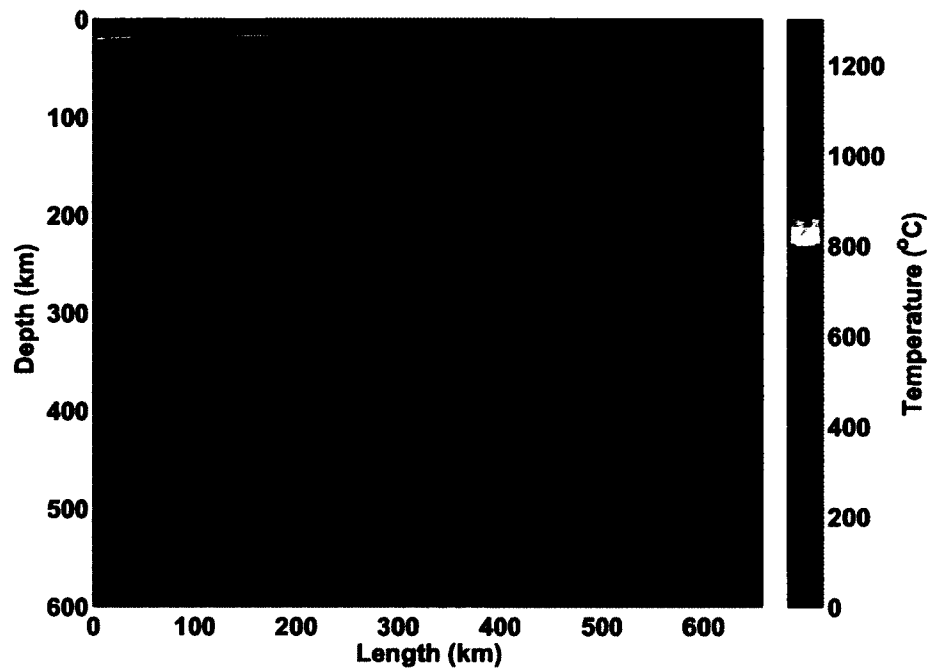**Figure 118.** Boundary conditions for conduction convection code check.

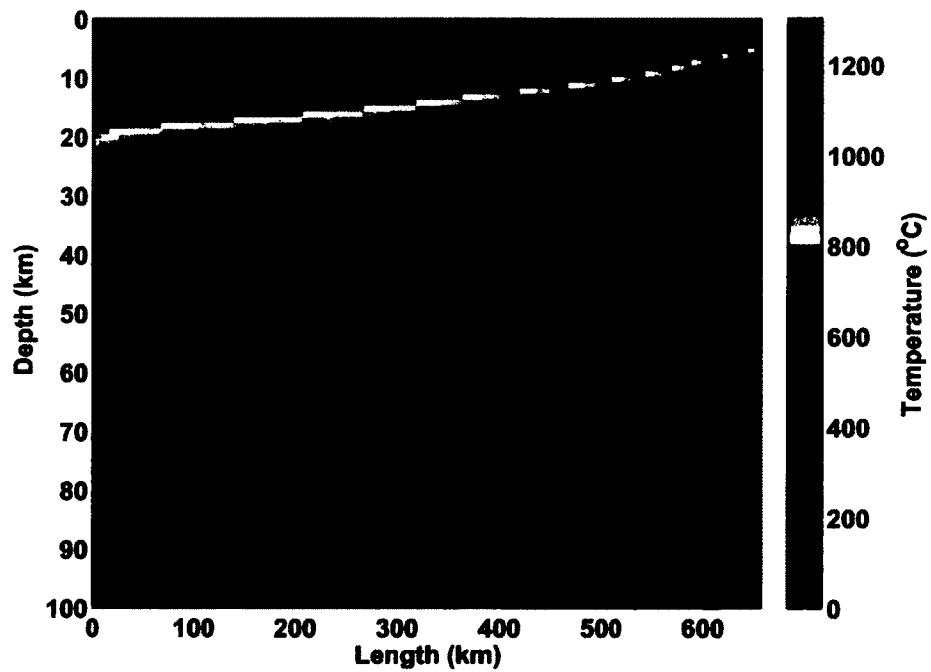**Figure 119.** Model-predicted temperatures for buoyant driven flow.

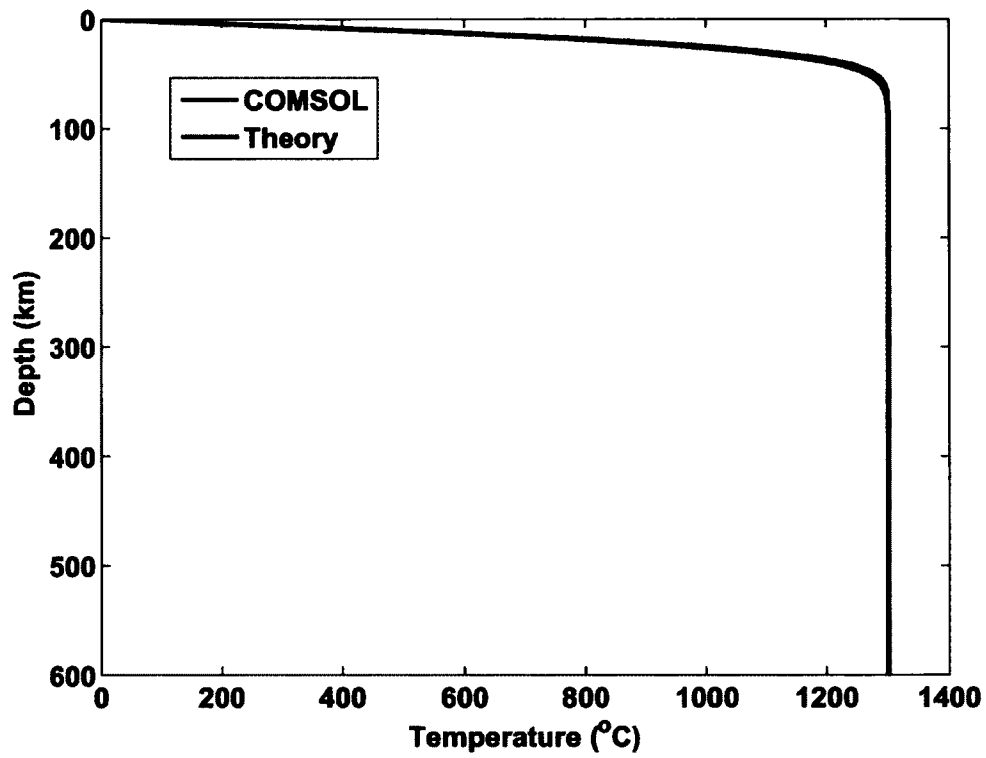**Figure 120.** Zoom in of top 100 km of buoyant flow results.

Figure 121. Temperature profiles for COMSOL model predicted temperatures at x=0 and half-space cooling model (Theory).

VITA

Steven Wild

Department of Physics

Old Dominion University

Norfolk, VA 23529

Education:

Old Dominion University, Norfolk, VA, **M.S.** Physics, May 2009

Indiana University, Bloomington, IN, **M.S.** Chemistry, May 2000

Baldwin-Wallace College, Berea, OH, **B.S.** Physics, June 1996

Recent Experience:

Old Dominion University, Norfolk, VA

Teaching Assistant - physics and astronomy 2007-2012

Research Assistant - geophysics 2009-2012 Hamilton College, Clinton, NY

Google Earth module developer August 2011

Recent Publications:

Dordevic, M. M., and S.C. Wild (2012), Avatars and multi-student interactions in Google Earth-based virtual field experiences, in *Google Earth and Virtual Visualizations in Geoscience Education and Research: Geological Society of America Special Paper 492*, edited by Whitmeyer, S. J., J.E. Bailey, D. G. De Paor, and T. Ornduff, T., chap.35, Geological Society of America, doi:10.1130/2012.2492(22).

Gobert, J., S. Wild, and L. Rossi (2012), Testing the effects of prior coursework and gender on geoscience learning with Google Earth, in *Google Earth and Virtual Visualizations in Geoscience Education and Research: Geological Society of America Special Paper 492*, edited by Whitmeyer, S. J., J.E. Bailey, D. G. De Paor, and T. Ornduff, T., chap.22, Geological Society of America, doi:10.1130/2012.2492(35).

De Paor, D. G., S. C. Wild, and M. M. Dordevic (2011), Emergent and animated COLLADA Models of the Tonga Trench and Samoa Archipelago: Implications for Geoscience Education and Research., *Geosphere, 8*(2), 491-506, doi:10.1130/GES00758.1.